From particle tracking to counting tomography

F. Cassol

AIX-MARSEILLE UNIVERSITÉ
ECOLE DOCTORALE 352
UMR 7346
CENTRE DE PHYSIQUE DES PARTICULES DE MARSEILLE

Habilitation à Diriger des Recherches

Discipline : Physique

Franca CASSOL

From particle tracking to counting tomography

Soutenue le 11/4/2018 devant le jury :

Cristinel DIACONU	CPPM	Examinateur
Benjamin GUILLET	CERIMED	Rapporteur
Sébastian JAN	CEA	Rapporteur
Jean-Michel Létang	INSA	Examinateur
Christian Morel	CPPM	Tuteur
Françoise Peyrin	ESRF	Rapporteur

Contents

Introduction

This dissertation describes my research activity and that of the students that I tutored inside the interdisciplinary group imXgam (imagerie X et gamma)[a] of CPPM (Centre de Physique de Particules de Marseille). It concerns the last ten years of my career which have mainly been focused on technology transfer inside an interdisciplinary context. The previous years were dedicated to fundamental physics research in neutrino physics[b] and astrophysics[c] and in accelerator physics[d], as reflected in my publication list.
I would like to stress that, besides my work, this dissertation aims to report a successful project conceived and developed by a group of people with different background and education (physicists, engineers, biologists) which joined together to achieve a common research goal.

Context

CPPM is a Joint Research Unit (UMR) of Aix-Marseille University and IN2P3 (Institut National de Physique Nucléaire et de Physique des Particules) of CNRS (Centre National de la Recherche Scientifique) which has the aim "to promote and unify research activities in the fields of nuclear physics, particle and astroparticle physics"[e]. Among others, its mission is the development of new particle detectors through various R&D (Research and Development) programs, often within international collaborations. During the nineties, the largest site for detector building was at the LHC (Large Hadron Collider) at CERN (European Organization for Nuclear Research) in Geneva (Switzerland). On that occasion, CPPM played a major role in the development of new tracking detectors suitable for addressing the challenges posed by the high energy and high luminosity specifications of the new hadron collider. In particular, a large group of physicists and engineers joined the ATLAS (A Toroidal LHC ApparatuS) experiment and took part in the design and construction of its vertex detector, which was developed using the *hybrid pixel technology* based on the recent progress made in semiconductor technology and microelectronics. Following the success of this project, Pierre Delpierre, one of the leading ATLAS engineers, founded a new research team at CPPM specifically dedicated to the transfer of the hybrid pixel technol-

[a] http://imxgam.in2p3.fr.
[b] From 1994 to 1998, at the CHORUS (CERN Hybrid Oscillation Research apparatUS) experiment at CERN.
[c] From 1998 to 2001, at the ANTARES (Astronomy with a Neutrino Telescope and Abyss environmental RESearch project) neutrino detector in the Mediterranean Sea, off the coast of Toulon.
[d] From 2001 to 2006, at the H1 experiment at HERA (Hadron Elektron Ring Anlage), Hamburg.
[e] http : //www.in2p3.fr/presentation/politique/statuts_missions_en.htm.

Figure A: Logo of the interdisciplinary research team imXgam of CPPM.

ogy towards *X-ray imaging*. This transfer was indeed promising and demanded by other disciplines, such as material science or biomedical imaging. The new team had therefore a clear *interdisciplinary vocation*, involving the collaboration between particle physicists, synchrotron radiation physicists, biologists and engineers specialized in electronics, mechanics and software. With the arrival of Prof. Christian Morel as team leader in 2005, the structure of the team was definitely established. It was at that time that I joined the project, attracted by its innovative research goals, aiming at making other disciplines to benefit from particle physics developments and promoting the transfer of knowledge between scientists acting within different fields. Shortly after, we baptized the group with the name of *imXgam* for imaging with X and gamma and selected its logo, shown in Figure A, as the result of a competition open to all CPPM members. In 2010, Pierre Delpierre, together with other imXgam members, founded a CPPM spin off company, called imXPAD, dedicated to the commercial promotion of the hybrid pixel technology XPAD (X-ray pixel chip with Adaptable Dynamics) that was developed at CPPM. The imXPAD company, active till December 2016, has been a faithful partner of the imXgam team in several research projects and a valid support in the search for grants for our PhD students.

Research activity and supervision of students

In this context, my activity has been centered on the research studies performed for exploring, characterizing and qualifying the XPAD hybrid pixel detectors as counting detectors for tomographic imaging. The field has been mainly related to X-ray imaging for preclinical research but, thanks to the versatility of the XPAD hybrids, the topic of neutron tomography could also be explored. The first steps towards X-ray photon counting tomography were performed with a micro-CT (micro-Computed Tomography) scanner prototype, called PIXSCAN I, equipped with a camera based on the XPAD2 version of the hybrids, whereas the full characterization of the detectors was achieved with the micro-CT prototype PIXSCAN II and several cameras based on the XPAD3 version of the chip. Our last results are at present carried out with the ultimate version of the PIXSCAN series, the PIXSCAN-FLI, that will soon be installed at CERIMED (Centre Européen de

Recherche en Imagerie MEDicale). Neutron tomography could be accessed during a full-time secondment of one year at the HZB (Helmholtz Zentrum Berlin) in Germany, where I could have access to a cold neutron beam.
The research activity described in this document has been performed in collaboration with students actively involved in the PIXSCAN project, for which I assured the technical coordination. In general, the student participation has been a fundamental resource, not only for each concrete contribution, but also for the charge of doubts, questioning, ideas and enthusiasm brought by each of the student to the project. Here the list of the students that worked fully or partially under my supervision inside the PIXSCAN project:

- Didier Benoit, Master Thesis, supervised (Benoit 2007)
- Rana Koury, PhD student, co-supervised with Prof. C. Morel (Khoury 2008)
- Charles Hemmer, Master Thesis, surpervised (Hemmer 2008)
- Hamid Ouamara, PhD student, co-supervised with Prof. C. Morel (Ouamara 2013)
- Loriane Portal, Master Thesis, supervised (Portal 2014)
- Mathieu Dupont, PhD student, advised (Dupont 2014)
- Carine Kronland-Martinet, PhD student, advised (Kronland-Martinet 2015)
- Margaux Hamonet, PhD student, advised (Hamonet 2016)
- Loriane Portal, PhD student, co-supervised with Prof. C. Morel (2014-)

Plan

This document is organized in such a way that the *Main Body* (Chapters 1 to 3) introduces and summarizes the goals, the development and the results of my research activity, guiding the reader towards published articles which describe the studies in detail and are collected in Section *Articles*.
The plan follows mainly a temporal order. In Chapter 1, after a brief historical introduction of hybrid pixel detectors and their transition from particle tracking to X-ray imaging applications, we describe the XPAD hybrids and their evolution. Chapter 2 illustrates all the work related to the setup of our first micro-CT scanner prototype, the PIXSCAN I, and the results obtained with the first photon counting X-ray camera fully developed at CPPM. Then, Chapter 3 goes through all the studies performed in order to evaluate the potential of the last version of the XPAD hybrids, mainly for X-ray imaging in biomedical researches (both in standard absorption and in spectral tomography) but also in neutron tomography with a cold neutron beam. We finish with some conclusions and perspectives.

1. Hybrid pixels detectors

Hybrid pixel detectors result from the outstanding effort started in the late eighties to develop two dimensional detectors able to face the high particle density (10-100 particles per collision) and rate (10-100 MHz) delivered by future accelerators, and also to permit unambiguous detection of short-living particles ($\sim$1 ps), which requires spatial accuracies of some tens of microns.
The most advanced tracking detectors at that time were silicon microstrip detectors, which, like hybrid pixels, are semiconductor diode detectors but with a linear structure: the signal coming from the fully depleted high resistivity sensor is read by an array of linear diode elements (Figure 1.1) and two planes of microstrip detectors, rotated by 90^{o}, or double-sided strips are necessary in order to get the position of a track passing through them. This configuration is however affected by the so called "ambiguity problem" which appears when more than one particle crosses the same diode, as schematically shown in Figure 1.2, and does not permit to unambiguously associate a track to a hit when the rate and/or the track density become too high.
The idea of pixel detectors has been first expressed by Heijne et al. 1988 in an article with the suggestive title *The silicon micropattern detector: a dream?* Indeed, at that time, all the driving elements for the successive developments were already there: the coming need for fast two-dimensional detectors with detection elements of around $100\ \mu\mathrm{m} \times 100\ \mu\mathrm{m}$, an established experience with silicon microstrip detectors, which had demonstrated to be a solid and faithful technology for particle tracking, and, last but not least, the accessibility of compact circuits thanks to the development of the ASIC (Application Specific Integrated Circuit) technology, which enabled the integration of some component of the front-end readout in compact chips. In this context, the RD19 collaboration at CERN started a wide R&D program on the development of *hybrid and monolithic* silicon micropattern detectors in 1990. Indeed, the processing technology had been derived from the standard CMOS (Complementary Metal-Oxide Semicon-

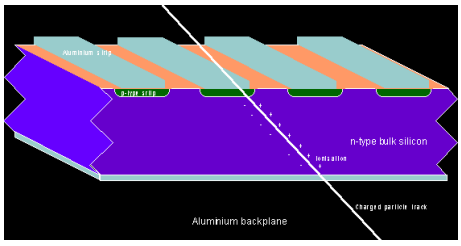

Figure 1.1: Scheme of a single-side silicon strip detector (©CERN).

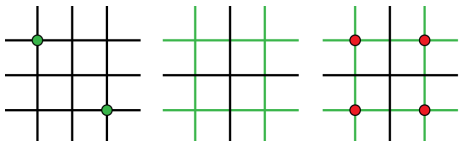

Figure 1.2: Ambiguity problem exemplification.

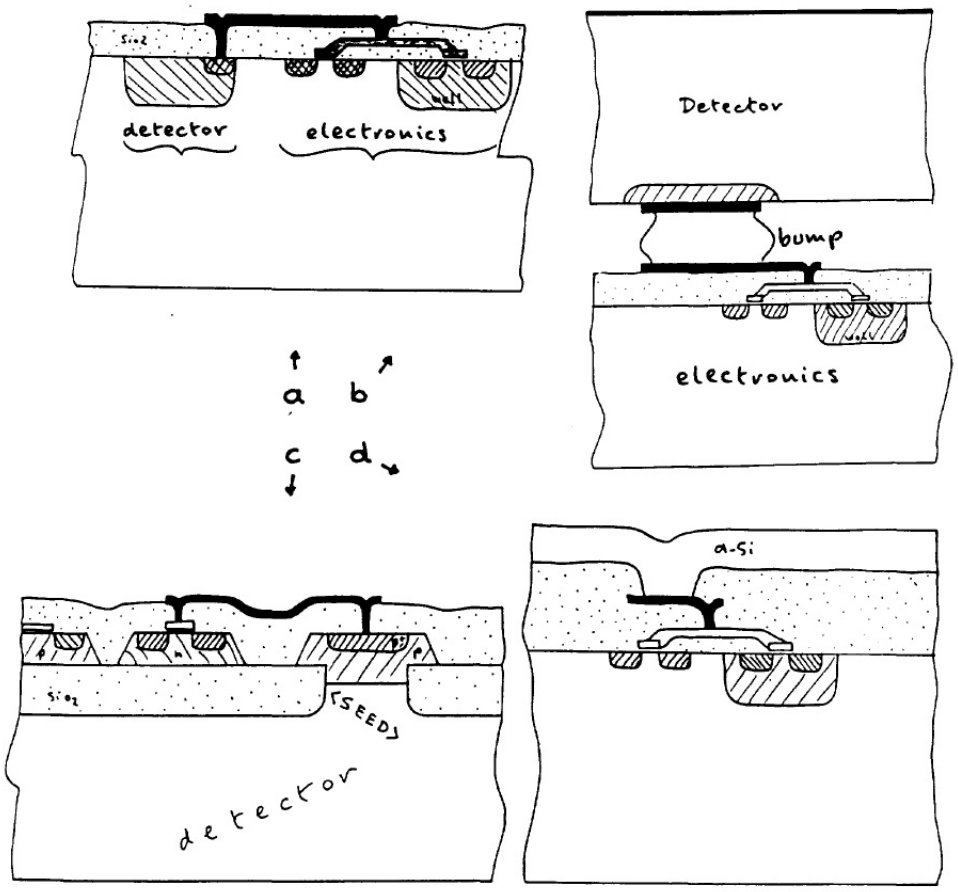

Fig.1 Cross section showing various detector-readout interconnect techniques [8]:
a) Monolithic integration of electronics within the detecor substrate
b) Hybrid integration of different chips using bump bonding
c) Monolithic integration of electronic circuits in a Silicon top layer, grown On an Insulating oxide (SOI), using seed openings. The substrate is the high-resistivity detector chip.
d) The detector layer is a thin amorphous Si layer, deposited on top of the insulating oxide, which may be useful for of highly ionizing particles or visible/ultraviolet light. The substrate is a regular Si chip, containing the readout electronic circuits.

Figure 1.3: Monolithic and hybrid pixel designs from the RD19 Proposal (Beusch et al. 1990).

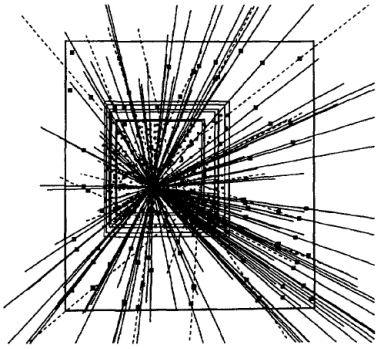

Figure 1.4: WA97 event with 153 reconstructed tracks in the pixel tracking chamber (CERN 1997).

ductor) technology, but it was still not evident whether the micropattern detectors would have been *monolithic*, with detector and signal processing located in the same piece of silicon, or *hybrid*, with the sensor and the readout chip separated and interconnected. Figure 1.3 presents monolithic and hybrid pixel schemes taken into consideration in the original RD19 Proposal (Beusch et al. 1990).
The history rapidly showed that the hybrid concept was the easiest solution to implement and in 1995, after several R&D phases, the fixed target heavy ion collision experiment WA97, at the Omega facility at CERN, was equipped with a telescope of seven pixel planes that permitted the detection of very high density events, as the one shown in Figure 1.4. Shortly after, in 1996, the DELPHI (Detector with Lepton, Photon and Hadron Identification) experiment at the LEP (Large Electron Positron Collider) has been the first collider detector equipped with hybrid pixels: two crowns of hybrid pixels were added to the microstrip vertex detector in order to increase the forward and backward acceptance, as schematically presented in Figure 1.5. Following the great success of this technology, all the LHC experiments were then equipped with a pixel vertex detector.

1.1. Working principle

Hybrid pixel detectors are semiconductor radiation detectors. Their working principle exploits the physics of semiconductors and the progress made by the electronics industry since the mid-20th Century, as well as the processes of interaction of radiation in matter. Several text books are available on the subject (see, for example, Knoll 2010, Rossi et al. 2006 and Lutz 2007). We only summarize in this section the main elements useful for an easy comprehension of the described work and propose in Appendix A a brief recall of the key elements of

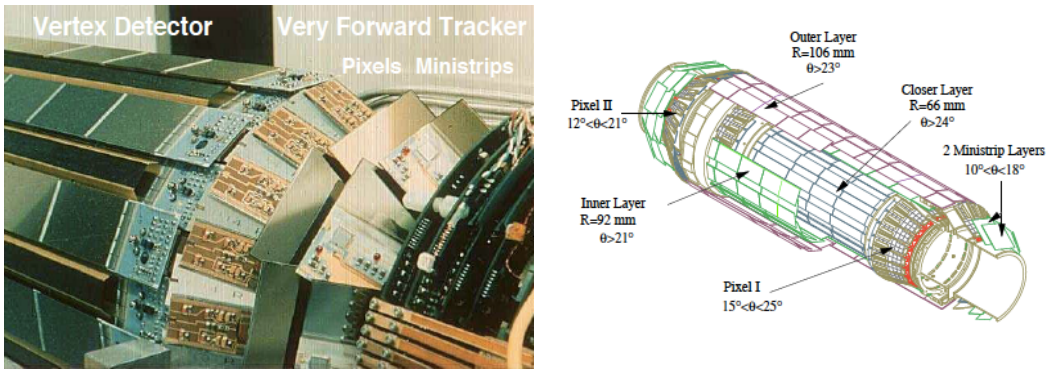

Figure 1.5: Picture and layout of DELPHI's Silicon Tracker, both end-caps are equipped with pixel detectors (Becks et al. 1997).

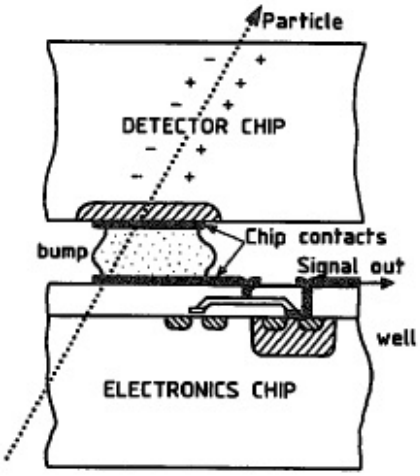

Figure 1.6: One of the first schemes of the hybrid pixel concept (Campbell et al. 1990).

semiconductor physics.
Figure 1.6 presents a schematic view of a hybrid pixel, taken from one of the first articles which considered these devices for particle tracking (Campbell et al. 1990). It clearly illustrates the "hybrid pixel" concept: the sensor chip is separated from the readout chip but connected through a bump bonding realized by using the flip-chip technology, which is derived from processes used in microelectronic circuit fabrication. Conducting balls of a few tens of micrometers, deposited on metallic sockets, guarantee a sufficiently narrow interspace between the pixels, as shown in Figure 1.7. The material of the sensor can be silicon but also a semiconductor with higher atomic number, like CdTe or AsGa, which have the advantage of assuring a higher detection efficiency for hard X-rays (> 20 keV). Particles interacting inside the sensor generate free charge carriers (holes and electrons) that are collected under the action of an electric field

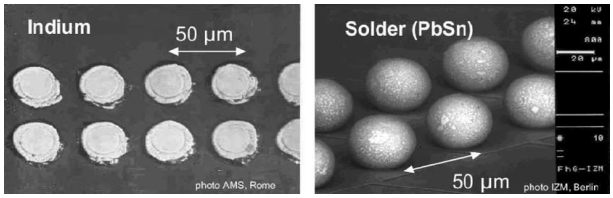

Figure 1.7: Examples of Indium and Solder bump rows (Wermes 2003).

through proper electric contacts. The low resistivity of the sensors does not permit in general to use simple Ohmic contacts, because a too high leakage current would be generated. The usual solution is to create a region inside the electric field that is depleted from free charge carriers, which can be achieved through reversed-biased junctions acting as blocking contacts. If the sensor semiconductor is silicon, the diode is generally given by a pn-junction. Otherwise, in the case of higher resistivity semiconductors, like CdTe, a reduction of the leakage current can be obtained with metal on semiconductor contacts (Schottky)[a]. We briefly recall in Appendix B the basic elements of these two types of junctions, which have both been employed in our studies.
The front-end electronics behind each pixel transforms the charges coming from the sensor to an exploitable signal. Figure 1.8 presents the classical components of a readout chip: charges are transformed either in a voltage or in a current, the signal is then amplified, eventually filtered, and finally digitized by a discrimination stage. The further processing of the data depends on the final application, which can belong to various research fields as described in the next Section.

[a]The resistivity of CdTe permits to use also Ohmic contacts.

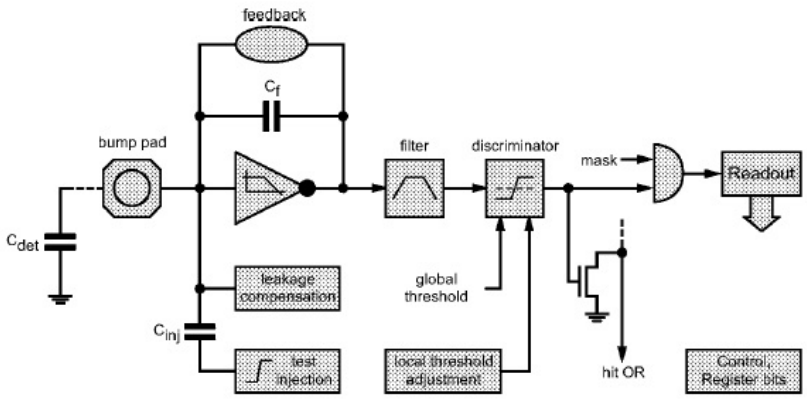

Figure 1.8: Components behind a pixel in a generic readout chip (Rossi et al. 2006).

1.2. From particle physics to X-ray imaging

After the successful operation of hybrid pixels in particle physics experiments, several groups started, at the end of the nineties, to explore their use for X-ray photon counting applications, such as biomedical imaging or material research with X-ray diffraction (Wermes 2003). Their potential for single photon counting detection was already addressed, since γ sources were usually used for the calibration of the thresholds of the pixels of the particle trackers. At that point, the main topics under investigation were the following:

- **The readout chip had to be adapted to imaging purposes**, in particular, the external trigger used in particle tracking for starting the data recording had to be replaced by a counter in each pixel, being read out at the end

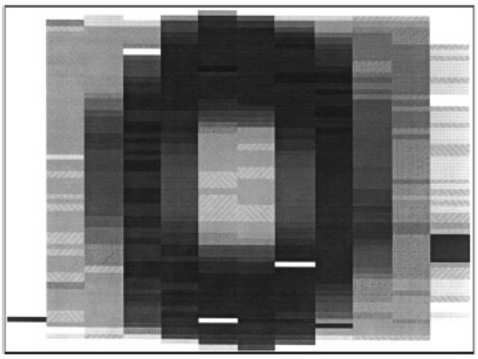

Figure 1.9: Shadow image of a nut from a $^{241}\mathrm{Am}$ source, taken with a modified version of the ATLAS tracker readout chip (Blanquart et al. 1998).

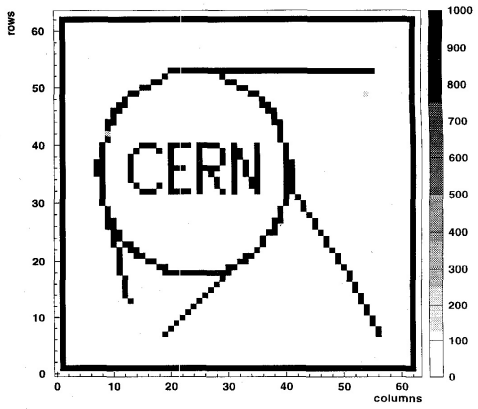

Figure 1.10: Image of test pulses (applied 1000 times to every pixel) which were following a pattern reproducing the CERN logo, acquired with one of the first squared pixel readout chips developed for single photon counting (Campbell et al. 1997).

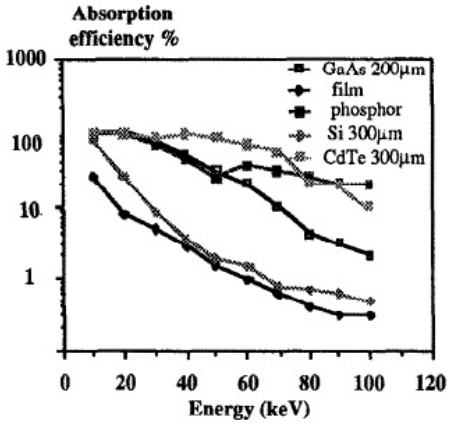

Figure 1.11: Comparison of the absorption efficiency of different detector media in the X-ray radiology energy range (Via et al. 1997).

of each exposure frame. The Bier&Pastis chip, developed for the ATLAS detector at CERN, was among the first readout chips modified in order to add counting capability to every pixel (Fischer et al. 1998). Figure 1.9 shows the X-ray image of a nut taken with a first prototype.

- **New readout designs with squared pixels had to be developed** because the rectangular shape of the pixels, generally used in particle tracking for increasing the spatial resolution in the bending direction of the magnetic field, was not suitable for X-ray imaging. One of the first single photon counting readout chips with squared pixels ($170\ \mu\mathrm{m} \times 170\ \mu\mathrm{m}$) was developed using building blocks of the Omega3 chip (Campbell et al. 1997). Figure 1.10 shows a first acquisition performed with test pulses repetitively applied to every pixel following a pattern corresponding to the CERN logo.

- **The possibility of choosing the sensor material was a key feature of hybrid pixels when used for photon detection**, permitting to optimize the detector efficiency for the energy of the detected photons. A first test of this peculiarity, directly intended for medical imaging, was performed by bump bounding GaAs sensors to the Omega3 chip developed by the RD19 collaboration at CERN (Via et al. 1997). Figure 1.11 shows the comparison of absorption efficiencies of different detector media, which were taken as reference for that preliminary work.

Following the above mentioned guidelines, in the beginning of the 2000s, several research teams and spinoff companies started the development of original and fully adapted ASICs, eventually bump bounded to several types of semiconductors. Table 1.1 presents a recent review of readout chips developed for photon counting, listed together with their main parameters. Among them, the XPAD chip developed at CPPM to build single photon counting X-ray cameras

Name	Matrix	Channel size (μm²)	Energy thresholds	Peaking time (ns)	Buttable sides	Technology (μm)	Specific information	References
Medipix3 *(1)*	256x256	55x55	2	120	3	0.13	Fine Pitch mode, Single Pixel mode, Compatibility with Through Silicon Vias (TSVs)	[33,34,35,36]
Medipix3 *(2)*	256x256	55x55	2	120	3	0.13	Fine Pitch mode, Charge summing and hit allocation algorithm, TSVs	[33,34,35,36]
Timepix3 *(3)*	256x256	55x55	10bits	30	3	0.13	Data push mode, Time-over-Threshold (ToT) energy measurement, charge sharing correction possible off-chip	[37]
Pixirad Pixie II *(4)*	512x476	52x60	2	300	2	0.18	Hexagonal pixels, equivalent pixel pitch of 55.6μm	[38]
Samsung PC *(5)*	128x128	60x60	3	NS	0	0.13	On-pixel successive approximation Analog to Digital Converter (ADC)	[39]
Pixirad Pixie III *(6)*	512x402	62x62	2	125	2	0.16	Large area ASIC (31.7x25mm²), Charge summing algorithm	[40]
Eiger *(7)*	256x256	75x75	1	30	3	0.25	Radiation hard electronics design	[41]
PXD23K (AGH) *(8)*	128x184	75x75	2	48	3	0.13		[42]
X-Counter PC *(9)*	256x256	100x100	2	NS	3	NS	Charge summing algorithm	[43]
PXD18K (AGH) *(10)*	96x192	100x100	2	30	3	0.18		[44]
FPDR90 (AGH) *(11)*	40x32	100x100	2	28	3	0.09		[45]
AGH_Fermilab *(12)*	18x24	100x100	2	48	0	0.04	Charge summing algorithm	[46]
Medipix3 *(13)*	128x128	110x110	8	120	3	0.13	Spectroscopic mode, Single Pixel mode, TSVs	[33,34,35,36]
Medipix3 *(14)*	128x128	110x110	8	120	3	0.13	Spectroscopic mode, Charge summing algorithm, TSVs	[33,34,35,36]
XPAD3 *(15)*	80x120	130x130	2	150	3	0.25		[47,48]
Pilatus 2 *(16)*	60x97	172x172	1	110.00	3	0.25	Radiation hard design	[49,50]
Pilatus 3 *(17)*	60x97	172x172	1	110.00	3	0.25	Radiation hard design, instant retrigger technology	[51]
Telesystems *(18)*	40x40	200x200	4	300-500	3	0.25		[52]
Dosepix *(19)*	16x16	220x220	16	300	3	0.13	ToT energy measurement, 16 digital thresholds	[53]
Siemens PC *(20)*	64x64	225x225	2	20	NS	NS	Pile-up trigger method	[54,55,56,57]
Hexitec *(21)*	80x80	250x250	14bits	2000	3	0.35	Digitization of pulse amplitude with off-chip ADC, TSVs	[58]
CIX 0.2 *(22)*	8x8	500x250	1	NS	1	0.35	Simultaneous charge integration and photon counting measurement	[59,60]
Philips Chromaix *(23)*	16x16	300x300	4	20	2	0.18		[61]
Ajat-0.35 (PC) *(24)*	32x64	350x350	1	1000	3	0.35		[62,63]
Ajat-0.35 (ADC) *(25)*	32x64	350x350	64	1000	3	0.35	On-pixel ADC	[62,63]
DxRay-Interon *(26)*	16x16	500x500	4	10	NS	NS		[2,64]
Ajat-0.5 *(27)*	44x22	500x500	2	1000-2000	3	0.35		[65]

Table 1.1: Review of readout chips developed for photon counting hybrid pixel detectors (Ballabriga et al. 2016).

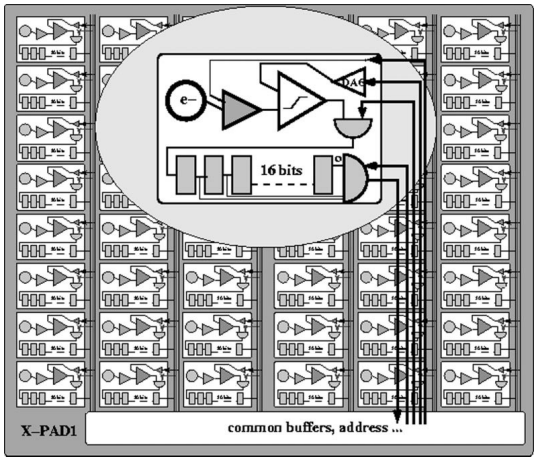

Figure 1.12: Schematic diagram of the XPAD1 chip: each analog circuit amplifies, discriminates and stores the signal in a 16-bit counter (Berar et al. 2002).

for preclinical imaging in micro-CT systems and for X-ray diffraction imaging at synchrotron facilities.

Next sections concern only the XPAD hybrid pixel detectors, our results are placed in the context of parallel developments from other teams in the final chapter *Conclusions and perspectives*.

1.3. The XPAD detectors

The history of the single photon counting chip XPAD starts with its first version, the XPAD1, thanks to the synergy between the CPPM engineers that were contributing to the development of hybrid pixel detectors for the DELPHI and ATLAS experiments at CERN and the physicists of the Institut Néel of CNRS operating at the D2AM beamline at ESRF (European Synchrotron Radiation Facility) (Ferrer et al. 1998), which were looking for X-ray cameras well adapted to synchrotron radiation sources. It followed an improved version of the chip in 2002, the XPAD2, tested for biomedical imaging applications in our first micro-CT prototype, the PIXSCAN I. Then, in 2006, in collaboration also with the engineers of the detector group at SOLEIL (Source Optimisée de Lumière d'Energie Intermédiaire du LURE), a main re-design of the chip was carried out, the XPAD3.1, which had pixels of smaller size ($130\ \mu\mathrm{m} \times 130\ \mu\mathrm{m}$) and was used to build the camera of our second micro-CT prototype, the PIXSCAN II. Finally, the last version of the chip, the XPAD3.2, manufactured in 2009, is employed in our present cameras. A review of the XPAD development can be found in Pangaud et al. 2010. We recall here only the key elements of these different versions.

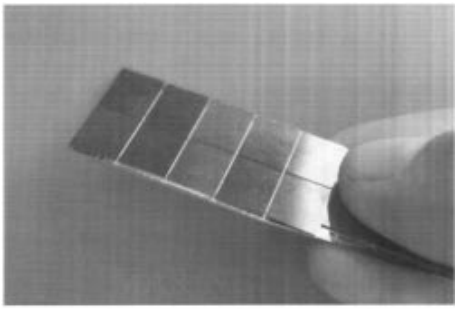

Figure 1.13: Ten DELPHI silicon diodes bump-bonded to the XPAD1 chips (Delpierre et al. 2002).

1.3.1. XPAD1

The XPAD1 chip (Blanquart et al. 2000) was conceived with the specific goal of improving photon counting in crystallography experiments with respect to standard CCD (Charge-Coupled Devices) cameras. The new detector was designed on the base of precise requests (Delpierre et al. 2001, Delpierre et al. 2002) :

1. Adjustable/tunable pixel per pixel threshold
2. Continuous counting during the exposure
3. Maximum counting rate $\sim 10^7$ photons/s/pixel
4. Noise $<$ 1 photon/hour/pixel
5. Dynamic range $> 10^9$
6. Readout time $<$ 3 ms/frame

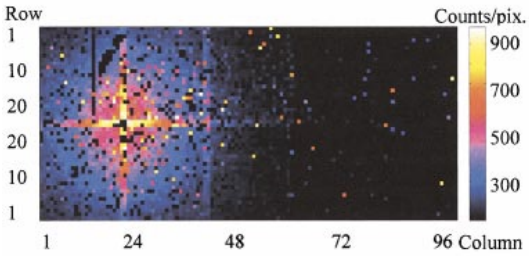

Figure 1.14: Image of a ^{90}Sr source place in front of the XPAD1 module, in the middle of four chips (Delpierre et al. 2001).

The chip, manufactured in the AMS 0.8 μm CMOS process, consisted in an array of 24×25 pixel elements of $330\ \mu\mathrm{m} \times 330\ \mu\mathrm{m}$ which could fit the already existing $300\ \mu$m thick DELPHI silicon sensor. If the chip size, fixed by the pre-existing diodes, was intended to change, the pixel design had already all the key elements which would be kept for the successive versions of the chip. It was based on three parts: the pixel matrix, the bottom-of-column logic and the slow control. An external readout and memory board with an Altera programmable chip completed the system. Each pixel had its own counting line with an analog part, which provided the signal amplification and discrimination, followed by an overflow adjustable counter, as schematized in Figure 1.12. Data transport towards the bottom of the chip was performed by a scanner based readout, which was scanning the 16-bit counter overflows of the pixels and was adding those to 16-bit counters in the external memory board. The readout was clocked externally by a 33 MHz clock provided by the data acquisition system (PCI standard). At the end of the exposure frame, the time to read the image was around 1 ms. A 10 chip detector prototype was setup, shown in Figure 1.13, for a total sensitive area of $4.0\ \mathrm{cm} \times 1.6\ \mathrm{cm}$. The tests at the D2AM beamline were rather promising (Berar et al. 2002) but an unexpected large dispersion of the signal amplification was observed, which did not permit the correct adjustment of the threshold for all the pixels, thus resulting in a high number of not counting pixels as shown in the image of Figure 1.14. Moreover, some logical errors in the circuit conception and the high noise, induced by the large capacitance of the DELPHI diodes, suggested to move rapidly to a new version of the chip and of the sensors.

1.3.2. XPAD2

The research activity described in this document starts with the XPAD2 chip, which, although keeping the same design as the XPAD1, was conceived to solve the encountered problems (Boudet et al. 2003) and to setup a first large surface camera for preclinical imaging (Delpierre et al. 2007b). Eight XPAD2 chips have been bump bonded on newly realized $500\ \mu$m thick silicon diodes (by Canberra, Belgium), mounted in tiles in order to obtain the $6.8\ \mathrm{cm} \times 6.5\ \mathrm{cm}$ hybrid pixel camera shown in Figure 1.15. The hybrids were much better performing than the first XPAD1 prototype, but still an excessive dispersion of the thresholds was observed, which from the beginning did not allow to configure simultaneously more than 85% of the pixels and limited its usage to energies higher than 15 keV. Nevertheless, the camera was successfully tested for crystallography studies at ESRF (Basolo et al. 2005) and then mounted in our first micro-CT prototype, the PIXSCAN I, that is described in Chapter 2.

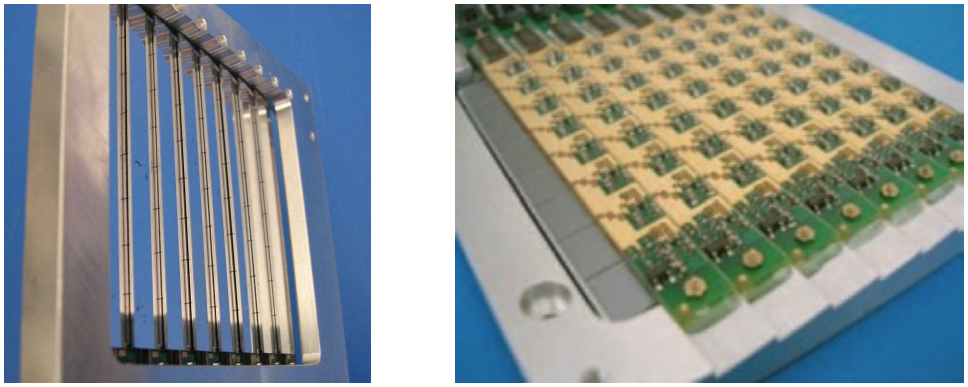

Figure 1.15: The 8 module XPAD2 detector.

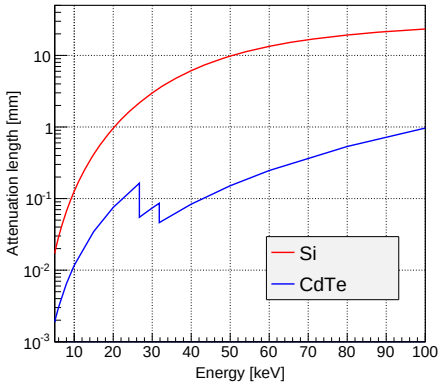

Figure 1.16: Total attenuation length of Si and CdTe (NIST).

1.3.3. XPAD3

The XPAD3.1 version consisted in a major redesign of the chip based on the new IBM 0.25 μm technology, which allowed to reduce the pixel size to $130\ \mu\mathrm{m} \times 130\ \mu\mathrm{m}$. For this new design, the possibility of using a sensor material different than silicon was exploited and CdTe sensors were also planned from the very beginning. This material assures a much higher X-ray detection efficiency, by virtue of its much shorter attenuation length, as shown in Figure 1.16. On the other hand, CdTe has some drawbacks with respect to silicon: it is difficult to produce large surface sensors ($\gg 1\ \mathrm{cm}^2$), the crystals are very fragile and they easily present dislocation walls which tend to trap the signal charges, generating polarization effects that induce spatial non-uniformities in the images and a drift of the sensor response over time (Bell et al. 1974). Table 1.2 compares the main properties of both semiconductors. The chips were then originally split in two types: the XPAD3.1-S (S standing for silicon), accepting positive charges from the sensor, was dedicated to synchrotron research in the $5 - 35\ \mathrm{keV}$ energy range, using a single comparator (threshold), while the XPAD3.1-C (C standing

	Si	CdTe
Atomic number (Z)	14	48 (Cd) 52 (Te)
Density $[g/cm^3]$	2.33	6.2
Energy gap $[eV]$	1.12	1.4
Energy/e-hole pair $[eV]$	3.62	4.4
Intrinsic resistivity $[\Omega\ cm]$	$3.2 \cdot 10^5$	$\sim 10^9$
Intrinsic carrier concentration $[cm^{-3}]$	$1.45 \cdot 10^{10}$	10^7
Electron mobility $[cm^2/(Vs)$	1450	1000
Hole mobility $[cm^2/(Vs)$	450	80
Electron lifetime $[s]$	10^{-4}	10^{-6}
Hole lifetime $[s]$	10^{-4}	10^{-6}

Table 1.2: Main properties of Si and CdTe at 300 K.

for CdTe), accepting negative charges, was optimized for biomedical imaging in the $5 - 60$ keV energy range, using two comparators in order to select an energy window (Pangaud et al. 2007b). Unfortunately, the C circuit had some major working problems and could not be used (Pangaud et al. 2007a). Therefore, the S circuit was employed both for the silicon and the CdTe (Schottky) sensors (Basolo et al. 2008).
One XPAD3.1-S hybrid consists of 9600 (120×80) pixels, bump bonded to the readout circuit, which is schematically shown in Figure 1.17. In the analog part, the signal is converted to a current and compared to a threshold in the selection stage. The energy threshold is set globally for all pixels by a 8-bit DAC and then locally adjusted for each pixel by a 6-bit DAC, which permits to reduce the offset dispersion. The selection stage feeds a 12-bit counter with overflow reading, deep enough to guarantee photon counting rates up to 10^6 photons/pixel/s. Table 1.3 presents the measured characteristics of the circuit.
The XPAD3.1-S chip bump-bonded to Si sensors has been the building block for several photon counting X-ray cameras of different sizes. The smallest camera was composed of a single chip (1.6 cm $\times$ 1.1 cm), intermediate-size modules were based on a single Si sensor (7.5 cm $\times$ 1.6 cm) bump-bonded to 7 contiguous chips, while large surface cameras (7.5 cm $\times$ 11.4 cm) were formed of 8 modules tiled one above the others, as shown in Figure 1.18. The circuits bump bonded to CdTe sensors were employed only for tests and permitted some first direct comparisons between Si and CdTe sensors. In total, three large surface cameras (500 kpixels) have been produced, one for each of the collaborating institutes (CPPM, D2AM, SOLEIL), and successfully employed at synchrotron beamlines for crystallography and at CPPM for biomedical imaging in a new micro-CT scanner, the

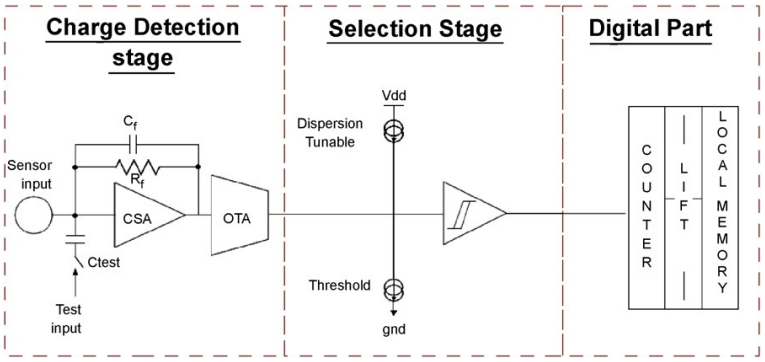

Figure 1.17: XPAD3-S circuit pixel chain: the signal is first converted to a voltage by the charge sensitive amplifier (CSA), then to a current signal by the transconductance amplifier (OTA) and finally compared to the threshold in the selection stage (Pangaud et al. 2008).

Table 1.3: Characteristics of the XPAD3.1-S chip (Pangaud et al. 2010).

Number of pixels	9600 (80 × 120)
Pixel size	130 μm × 130 μm
Chip size	1.56 cm × 1.04 cm
Input polarity	Hole collection
Power	< 70 μW/pixel
Selectivity mode	Single threshold
Non linearity	$< 10\%$ over 35 keV
Counting rate	10^6 photons/pixel/s
Readout time	2 ms/frame
Global electronic noise	< 140 e^-
Threshold adjustment resolution	50 e^- rms
Minimum threshold	5 keV

PIXSCAN II, described in Chapter 3 together with all the characterization studies related to this version of the chip.

The improved XPAD3.2 circuit design, manufactured in 2009, had for main purpose to increase the range of the threshold linearity up to 60 keV, which is useful for spectral imaging with hard X-ray energies using CdTe sensors. As for XPAD3.1, a S version accepting positive charges and a (revisited) C version accepting negative charges were conceived in order to test CdTe sensors both with Ohmic contacts (e^- collection) and Schottky contacts (e^- or hole collection) (Buton et al. 2014). Recently, single chip XPAD3.2/CdTe hybrids (mainly Schottky contacts for hole collection) have been employed to build modules of 7 contiguous chips by mechanically assembling single hybrids, hold by mono-blocks of graphite, as shown in Figure 1.19 (Cassol et al. 2015a, full text at page 130).

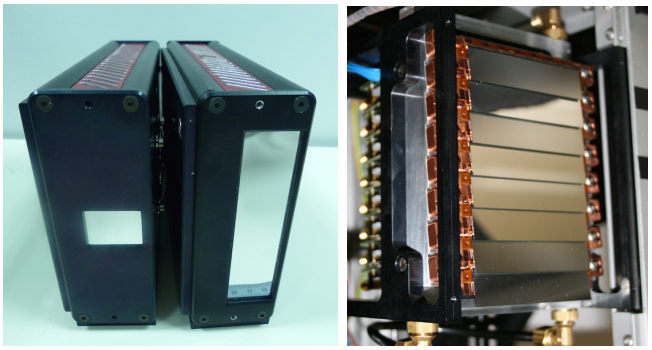

Figure 1.18: Pictures of X-ray cameras based on the XPAD3.1-S/Si detector.

These latter were also used to assemble a large camera of 8 modules. The camera and the modules are planned to be employed for biomedical longitudinal studies. In parallel to this, a large XPAD3.2/Si camera (8 modules) has been purchased from the company imXPAD in order to equip the newly developed PIXSCAN-FLI scanner, to be used for biomedical imaging in lower energy ranges.

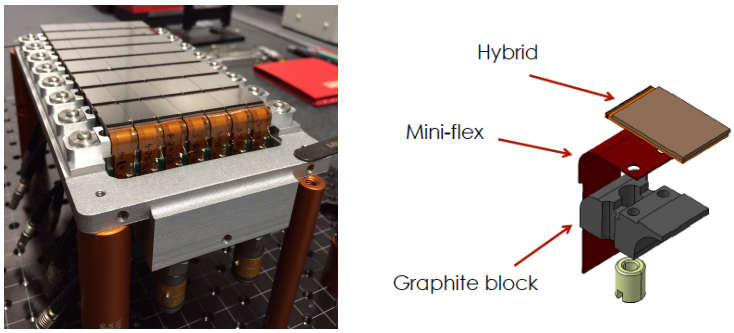

Figure 1.19: Picture of the camera based on the XPAD3.2/CdTe hybrids (left) and CAD design of the graphite block holding a hybrid (right).

2. Towards counting tomography with the XPAD2 hybrids

Our first steps towards photon counting tomography have been performed with the XPAD2 camera, which, after being successfully tested at synchrotron beamlines, has been dedicated to investigations in biomedical imaging. The low counting efficiency of silicon sensors for hard X-ray[a] suggested to limit the studies to the field of *preclinical research* which employs small animals for in-vivo longitudinal studies. In particular, we targeted mouse imaging that can be performed with low energy radiation, similarly to mammography scanners (< 60 kVp). The possibility of mouse surveys with non invasive imaging tools represents not only a great help for the precision and reliability of biomedical studies, but also aims at reducing the number of employed animals. In fact, without imaging, the different stages of the pathology must be obtained by sacrificing animals at every step, which requires a larger starting sample. With this in mind, we setup a micro-CT scanner for mice, called PIXSCAN, in collaboration with the research team of biologists of IBDM (Institut de Biologie du Développement de Marseille) led by Geneviève Rougon.
The main question we wanted to answer at that time was: does a hybrid pixel detector minimize the noise in X-ray images? A positive answer would mean an increase of low contrast sensitivity at low delivered dose and therefore would provide the opportunity to safely perform longitudinal studies thanks to minimizing the impact of the radiations on the mouse metabolism. This was indeed the main objective of our biologist colleagues.

The first scanner prototype, the PIXSCAN I, took data from 2005 to 2008 and its characterization was the topic of the MSc dissertation of D. Benoit (Benoit 2007), the PhD dissertation of R. Khoury (Khoury 2008) and the MSc dissertation of C. Hemmer (Hemmer 2008).

2.1. Setting-up of the micro-CT scanner PIXSCAN I

The scanner, described in Delpierre et al. 2007a (full text at page 56) and shown in Figure 2.1, is composed of the XPAD2 camera, a X-ray tube[b] and a rotating table on which the animal, under anesthesia, is placed in vertical position. The system is contained inside an iron box. The distances source-detector and

[a] The photon absorption efficiency of 500 μm thick silicon sensors is below 10% for energies above 30 keV (Benoit 2007).
[b] A Molybdenum target tube, MCBM 65B-50 Mo, RTW, Berlin, Germany.

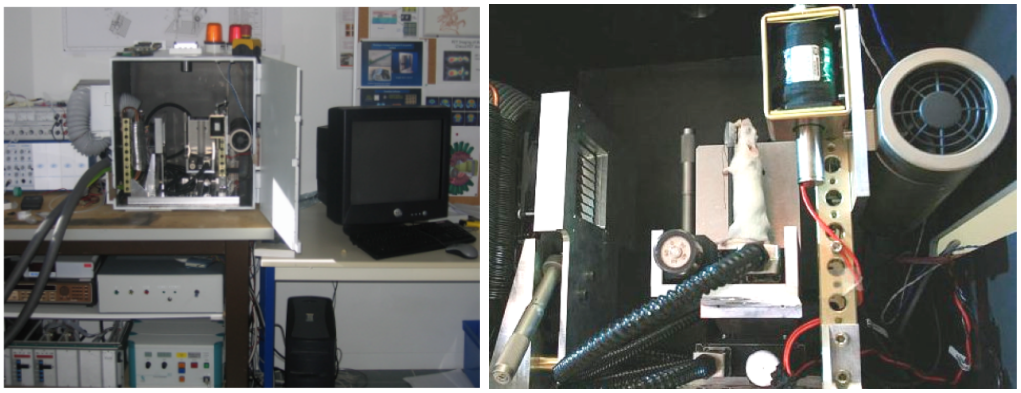

Figure 2.1: The PIXSCAN I scanner (©Camille Moirenc).

source-imaged object are 286 mm and 137 mm, respectively, corresponding to a magnification of around 2.1.
The challenge for this first system was not only the study of the new camera, but also to develop all the tools necessary for the setting up of a correctly working tomographic imaging system and for its full characterization, which was a new research field for us. The data taking and processing included the following main steps:

1. **Geometrical calibration of the scanner:** the geometry, which describes all the distances and angles between the system components, could be estimated with a sub-pixel precision of around 30 μm (Khoury et al. 2009).

2. **Tomographic acquisition:** typically 360 projection images were acquired, rotating the table supporting the imaged object with steps of one degree.

3. **Resampling of the projection images**: raw projections were resampled in order to take into account the tiled geometry of the camera and the gaps between the modules.

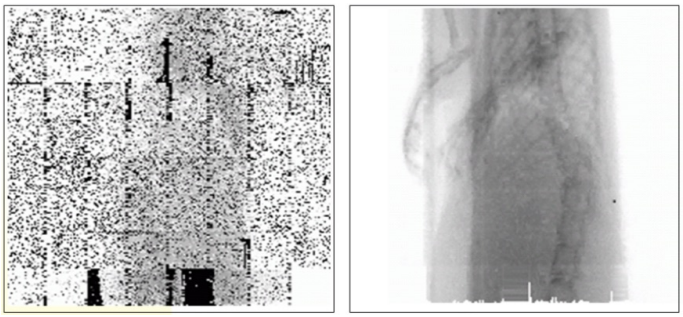

Figure 2.2: Raw projection of a mouse (left) and image sent to the reconstruction after resampling and interpolation of the pixel values (right) (Khoury 2008).

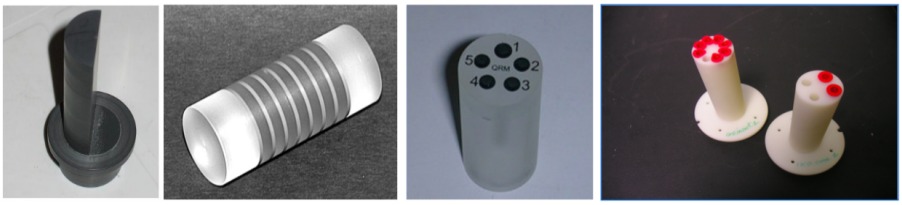

Figure 2.3: Phantoms used for the PIXSCAN characterization, from left to right: a spatial resolution phantom (based on the "edge method"), a phantom Defrise (QRM, Germany) for the evaluation of the reconstruction distortions, a linearity phantom (QRM, Germany) and two home made low contrast phantoms filled with iodine solutions at different concentrations.

4. **Interpolation of defective pixels**: faulty pixels received an estimated value from the spline-interpolation of their neighbor pixel values.

5. **Tomographic reconstruction**: it was performed with a FDK-based algorithm for cone beam tomography developed at CREATIS (Centre de Recherche en Acquisition et Traitement de l'Image pour la Santé) (Valton 2007).

From the beginning, the system was limited by a high percentage of defective pixels ($\sim 25\%$), partly due to the already mentioned threshold dispersion which did not allow their proper calibration ($\sim 20\%$) and partly to defective behaviors that gradually appeared, most probably caused by the mechanical and irradiation stresses induced with time. Figure 2.2 shows the raw projection of a mouse and the processed final image sent to the reconstruction after re-binning and interpolation of the pixel values.

2.1.1. Figures of merit and delivered dose

An important step of the project has been the identification of valid figures of merit for a full characterization of the system. In particular, we decided to evaluate the scanner response linearity, the spatial resolution[c], the noise, the low contrast detectability of small objects and the distortions induced by tomographic reconstruction. For this, several phantoms were developed or acquired, of which some are shown in Figure 2.3.
For what concerns the dose delivered to the animal, this camera was penalized by the high pixel threshold dispersion, which limited its optimal use to energies greater than $20\ \mathrm{keV}$. Typically, the X-ray tube was set to a voltage of 60 kVp and a current of 0.5 mA, and a filter with 6 mm of Aluminum was employed in order to absorb the low energy component of the spectrum, as shown in Figure

[c]Estimated through the LSF (Line Spread Function) and the MTF (Modulation Transfer Function).

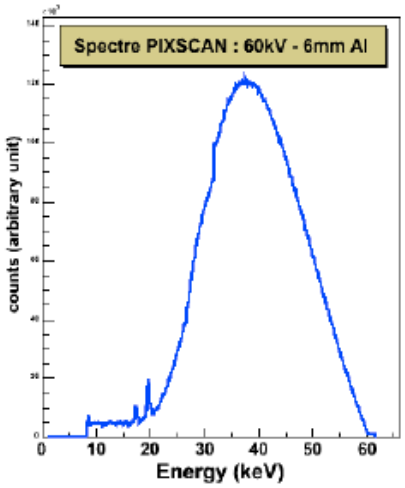

Figure 2.4: Typical X-ray spectrum employed in the PIXSCAN I scanner (Hemmer 2008).

2.4. The resulting dose rate was $290 \pm 24\ \mu\mathrm{G/s}$ and the photon counting rate was $\sim 10000\ \mathrm{photon/pixel/s}$. A compromise between dose and noise reduction was reached with acquisitions of 1.2 s per projection image, corresponding in principle to a total dose of about 125 mGy per scan (360 projection images). However, the system had an incompressible dead time per scan (mainly due to data transfer) of around seven minutes, which resulted in a real dose delivered per tomographic image of about 260 mGy. An accurate study of different radiation qualities employed in this scanner and the corresponding dose rates can be found in Hemmer 2008.

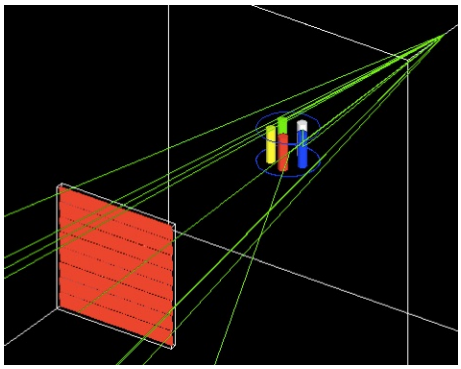

Figure 2.5: GATE illustration of a simulated scan of a linearity phantom.

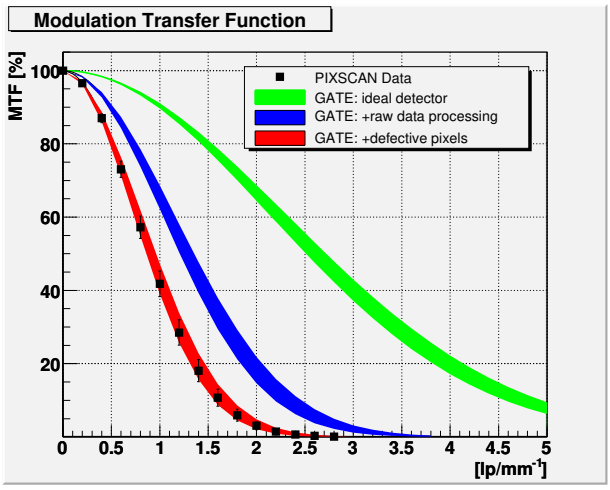

Figure 2.6: MTF (Modulation Transfer Function), data and Monte Carlo simulation in the case of an ideal flat detector (green line), a tiled detector (blue line) and a tiled detector with defective pixels (red line), as observed with the XPAD2 camera (Cassol et al. 2009b, p. 61).

2.1.2. Monte Carlo simulation

In order to verify the data processing chain and to disentangle intrinsic performance features from the limitations induced by the great number of defective pixels, we have performed both an analytical and a full Monte Carlo simulation of the system (Cassol et al. 2009b, full text at page 61). The Monte Carlo simulation was developed in the frame of the GATE package, developed and maintained by the OpenGATE Collaboration[d], which was dedicated at that time only to the simulation of PET (Positron Emission Tomography) systems. In 2006, we became members of the Collaboration and contributed by extending the code to simulating CT scanners (Jan et al. 2011, full text at page 94). As an example, Figure 2.5 shows the GATE illustration of a simulated scan of the linearity phantom.

2.1.3. Results

Thanks to the above described tools, a complete comprehension of the scanner behavior and of its limits could be achieved. In particular, we could explain the unexpected poor spatial resolution of $\sim 500\ \mu$m[e] with respect to the reconstructed pixel dimension of $\sim 170\ \mu$m, which had to be attributed mainly to the adopted resampling procedure and partly to the successive pixel interpolations. Figure 2.6 illustrates how the measured MTF is well reproduced by the Monte Carlo simulation when all effects are included. For the rest, the scanner behaved

[d] http://www.opengatecollaboration.org.

[e] Given by the FWHM (Full Width at Half Maximum) of the LSF (Line Spread Function).

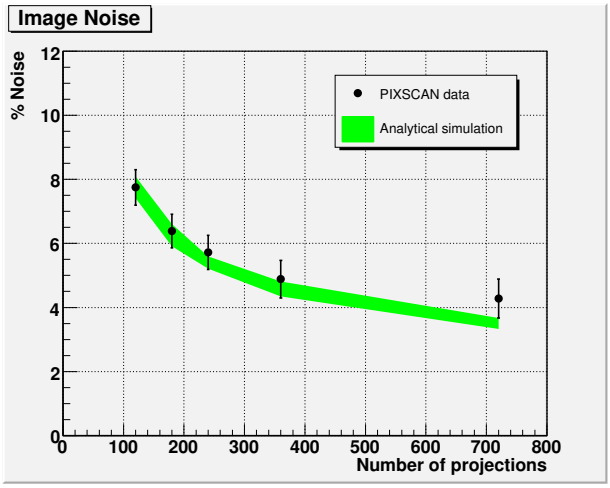

Figure 2.7: Simulated and measured noise in tomographic acquisitions as a function of the number of projections (Cassol et al. 2009b, p. 61).

as expected: its response was linear with respect to the attenuation coefficient and the image noise could be fairly well reproduced by a simulation that included only statistical noise, as shown in Figure 2.7.
For what concerns the low contrast detectability, we developed cylindrical phantoms with two conical inserts, in order to study detectability as a function of the object diameter. One conical insert was filled with an iodine solution corresponding to the desired contrast with respect to the phantom material and the other one was kept empty, in order to precisely determine the cone diameter in each transverse slice, as shown in Figure 2.8. Figure 2.9 compares data against an analytical simulation for three different delivered doses. In general, a detectability limit at 25 HU was identified, independently of the insert diameter and of the dose, probably related to an incompressible noise associated to the

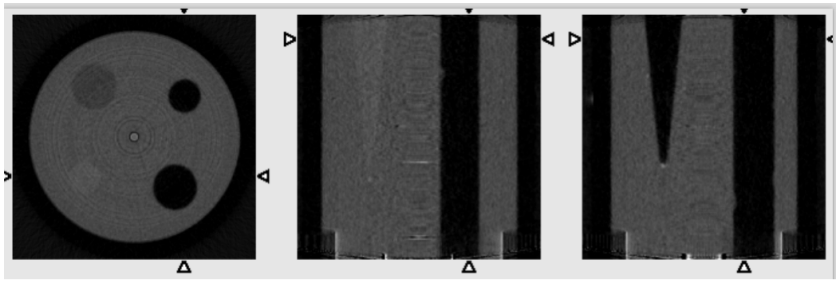

Figure 2.8: Reconstructed slices of an original low contrast phantom. One conical insert is filled with the iodine solution corresponding to the desired contrast with respect to the phantom material. Two cylindrical inserts are also present, one of which being filled with water for the conversion to HU (Hounsfield Unit).

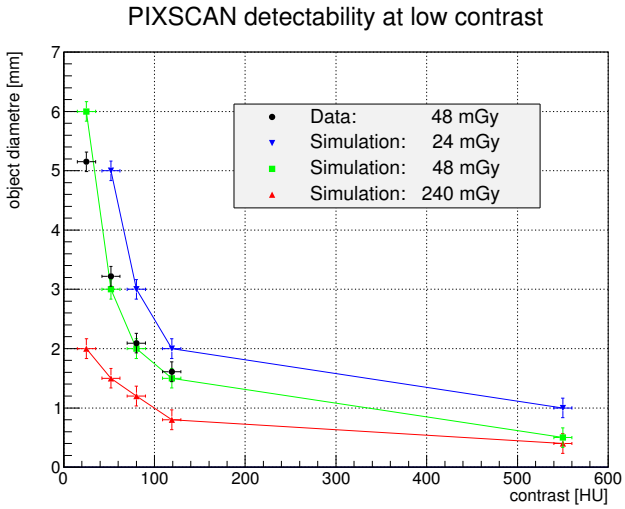

Figure 2.9: Measured and analytically simulated low contrast detectability as function of the imaged object diameter, contrast and delivered dose.

detector calibration and to the data processing and reconstruction.
Finally, the scanner has been used by our biologist colleagues for lung cancer development studies (Debarbieux et al. 2010, full text at page 84) and for angiographic imaging with injection of an iodinated contrast agent, as shown for example in Figure 2.10. In both cases, the results were very promising but still unsatisfactory for what concerned the image homogeneity, which was in part severely affected by the interpolation process and prevented to distinguish small structures ($< 500\ \mu\mathrm{m}$).

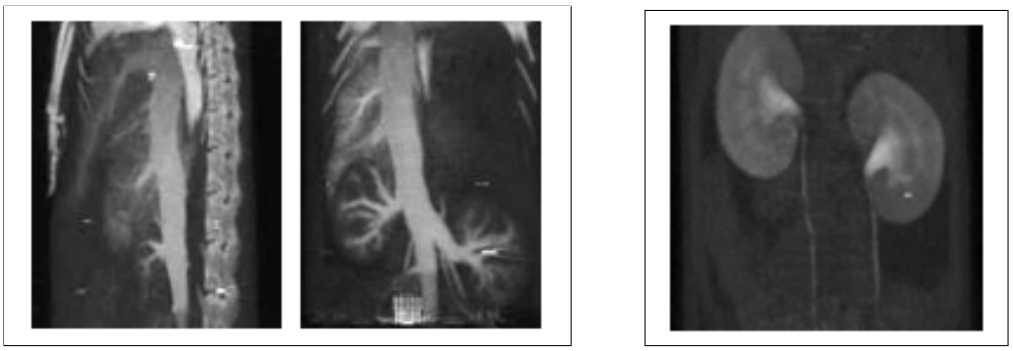

Figure 2.10: MIP (Maximum Intensity Projection) of mice acquisitions taken after the injection an iodinated contrast agent (400 mL of Iomeron 400), with the animal sacrificed immediately (left) or 5 minutes (right) after injection (Khoury 2008).

2.2. Conclusions

The PIXSCAN I scanner demonstrated the feasibility of developing a micro-CT system with hybrid pixel detectors. The intrinsic limitations of the XPAD2 camera, such as its large pixel size, the broad threshold dispersion and its high percentage of defective pixels, together with the still preliminary data processing, did not allow the achievement of totally satisfying results and a clear answer to our questions at that time. Nevertheless, the scanner permitted to acquire a solid knowledge of all the procedures necessary for the setup and characterization of a micro-CT system, to identify weak points in our data treatment and, last but not least, to realize first biomedical studies with a hybrid pixel X-ray photon counting camera.

Following the commissioning of a new detector based on the XPAD3.1 version of the chip, a second micro-CT scanner, the PIXSCAN II, was built with the goal of clearly answering the question mentioned in the beginning of this chapter, but also new and ambitious ones that are described in the next chapter.

3. Counting tomography results with the XPAD3 hybrids

The move towards the XPAD3.1 version of the chip represented a leap in quality of our project for two main raisons: the $130\ \mu\mathrm{m}$ pixel size allowed to reach tomographic spatial resolutions below $100\ \mu m$, which permitted to better address the research goals of our biologist colleagues, and the properly working pixel energy threshold opened the door to new imaging modalities exploiting spectral information of the detected X-rays. These new modalities, called *spectral imaging*, started to be largely investigated in the late 2000s when several photon counting detectors with one or more thresholds per pixel became available. In this context, the main questions at that point were:

- Does the use of hybrid pixels allow to minimize the noise in biomedical images?
- Is it feasible to perform spectral imaging with a single energy threshold as available with the XPAD3 chips?

We first proceeded by estimating the X-ray detection performance of single XPAD3.1 hybrids, as described in Section 3.1. Then, we looked for positively answering the above questions in the context of the PIXSCAN II scanner equipped with a large surface camera based on XPAD3.1/Si hybrids. The encouraging results brought us to the last phase of our project, where the potential of these detectors is exploited for preclinical researches performed with XPAD3.2 cameras equipped either with CdTe or Si sensors and installed in the newly developed PIXSCAN-FLI scanner. Many of these studies, summarized in Section 3.2, have been performed in the context of PhD or MSc dissertations (Ouamara 2013, Dupont 2014, Portal 2014, Kronland-Martinet 2015, Hamonet 2016, Portal 2014-). Finally, the last section of this chapter (Section 3.3) reports on the possibility of using hybrid pixels for neutron tomography, which revealed to be possible thanks to the astonishing versatility of this type of detectors.

3.1. Imaging performance of the hybrids

Before considering any tomographic result, we decided to verify the performance of the XPAD3 hybrids in the detection of X-ray beams and to compare them with published results of more standard cameras (Cassol et al. 2009a, full text at page 67). This study, which specifically targeted biomedical imaging issues, was performed with single XPAD3.1-S chips bump bounded either to Si or CdTe sensors.

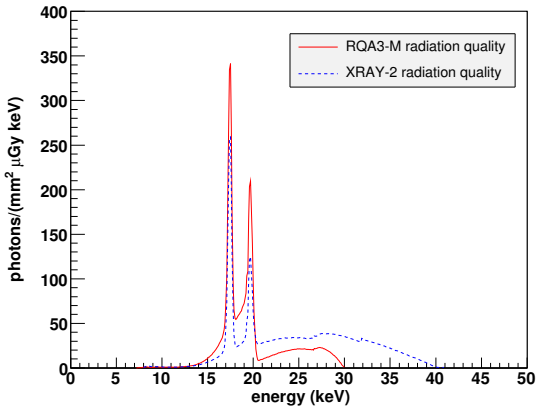

Figure 3.1: Spectra used for the XPAD3.1-S hybrids characterization (Cassol et al. 2009a, p. 67).

Figure 3.1 shows the employed radiation qualities: a standard mammography beam (RQA3-M) which can be easily taken as reference and a published micro-CT beam (XRAY-2) in order to compare with other detectors. Several figures of merit have been evaluated at different exposure doses, both with a minimal energy threshold, close to the chip noise (5 keV), and with a higher threshold, set at 18 keV. Details are given in the article at page 67. Here we simply like to notice that the main results can all be deduced from the DQE (Detection Quantum Efficiency) estimated for the different cases and defined as

$$\mathrm{DQE}(f) = \frac{(\mathrm{MTF}(f))^2}{K_a \times Q \times \mathrm{NPS}(f)}$$

where f is the frequency, MTF the Modulation Transfer Function, NPS the Noise Power Spectrum, K_a the measured air kerma at the detector surface (in μGy) and Q is the photon fluency at the detector per unit exposure (in photons mm^{-2} $\mu\mathrm{Gy}^{-1}$). Figure 3.2 presents the measured DQE for both the Si and the CdTe sensors, the two thresholds and three delivered doses. Considering the 5 keV threshold at low delivered doses (corresponding to less than 5000 photons/pixel), the value of $\mathrm{DQE}(0)$ reflects the photon absorption efficiency of the sensors[a], which indicates that no extra noise adds to the images and that both the Si and CdTe sensors follow a pure Poisson statistics. By increasing the dose, some additional noise starts to appear, which reduces the DQE values. This is almost negligible in the case of the Si sensors, but significant in the case of the CdTe sensors. These latter need also to be corrected for a slight drift of counts over time. Considering the 18 keV threshold, the DQE is smaller, resulting from the lower detection

[a] Estimated, for the RQA3-M radiation, 42% and 98% for the Si and the CdTe sensor, respectively.

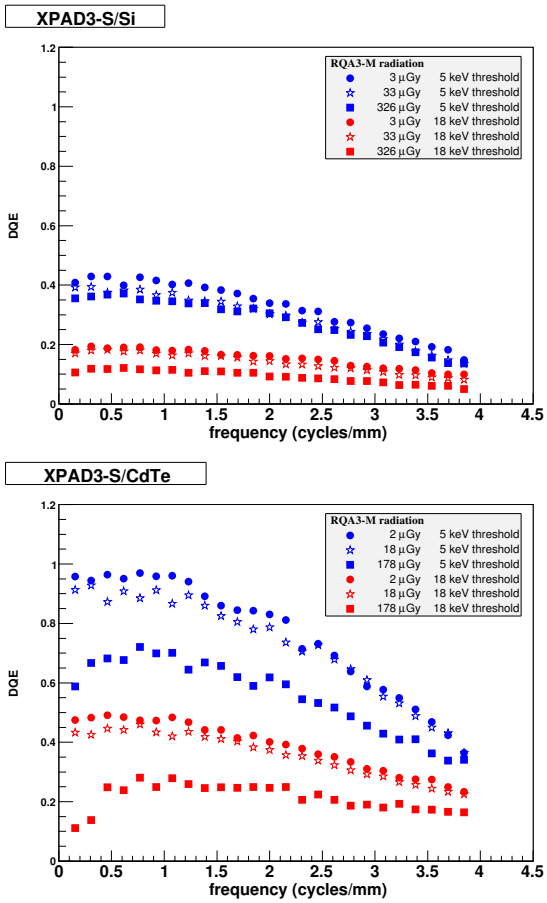

Figure 3.2: DQE of XPAD3.1-S/Si (top) and XPAD3.1-S/CdTe hybrids (bottom) for different exposures and threshold settings with the radiation quality RQA3-M of Figure 3.1 (Cassol et al. 2009a, p. 67).

efficiency. Its flatter shape at higher frequencies is due to the better spatial resolution, hence higher MTF, induced by the rejection of the low energy signals generated by the sharing of charges between neighboring pixels.

Charge sharing not only affects the spatial resolution, but also the detection efficiency of the hybrids. In fact, near the pixel borders, charges are split between pixels and signals can be lost or double counted, depending on the threshold level. In order to precisely evaluate this phenomenon for the XPAD3 hybrids, we performed a dedicated measurement campaign at the D2AM beamline at ESRF and developed a specific Monte Carlo simulation, which includes the main sources of charge migrations and could well reproduce the data (Cassol et al. 2011b, full text at page 115). If we model the spectrum measured by a pixel for an incident photon energy E_0 as the sum of an unsplitted Gaussian charge

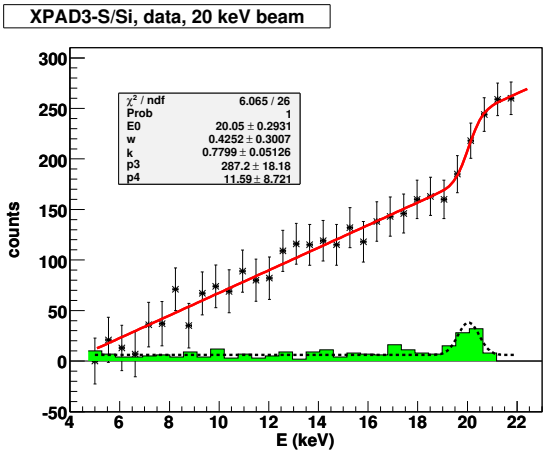

Figure 3.3: Counts of one pixel for an energy threshold scan (star points) with a beam of 20 keV. The derivative (dashed line) of the fit (full line) gives the energy spectrum as measured by a XPAD3.1-S/Si hybrid. The simulated spectrum (green histogram) reproduces the flat energy component at low energies due to charge sharing between pixels (Cassol et al. 2011b, p. 115).

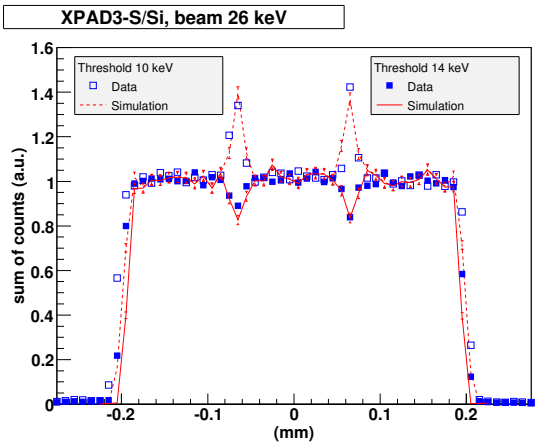

Figure 3.4: Sum of counts on three pixels for a 26 keV beam scan centered on one pixel row of a XPAD3.1-S/Si hybrid (Cassol et al. 2011b, p. 115).

component $\mathrm{n_p}(\mathrm{E}, \mathrm{E_0})$ and of a constant charge sharing component $\mathrm{n_{cs}}(\mathrm{E}, \mathrm{E_0})$

$$\mathrm{n}(\mathrm{E}, \mathrm{E_0}) = (1 - k)\ \mathrm{n_p}(\mathrm{E}, \mathrm{E_0}) + k\ \mathrm{n_{cs}}(\mathrm{E}, \mathrm{E_0}) \tag{3.1}$$

the charge sharing probability k was measured to be around 0.8 both for the Si and CdTe sensors, as illustrated in Figure 3.3, which presents the fit of a threshold scan for one XPAD3.1-S/Si pixel. For what concerns the detection efficiency, Figure 3.4 shows the lost or double counts at the border of the pixels

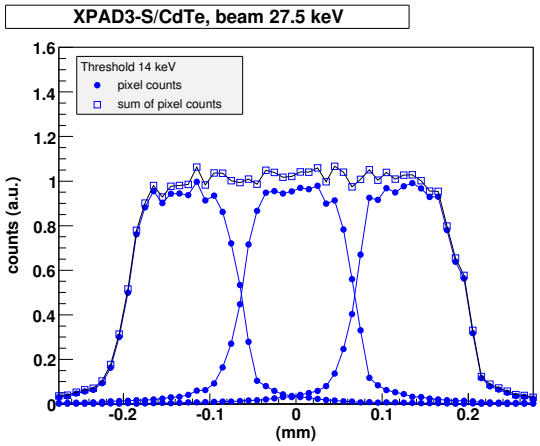

Figure 3.5: Counts and sum of counts on three pixels of a XPAD3.1-S/CdTe hybrid for a 27.5 keV beam scan. The threshold, which is close to half of the beam energy, guarantees an uniform global response between the pixels. (Cassol et al. 2011b, p. 115).

for two narrow beam scans with different energy thresholds, one above and one below half the beam energy. If the threshold is set at half the beam energy, the efficiency is uniform throughout the pixel border because only one of the pixels receives enough signal to pass the threshold, as shown in Figure 3.5 for a XPAD3.1-S/CdTe hybrid. In general, we could conclude that the relative large pixel size keeps the charge sharing effect at an acceptable level, which does not significantly degrade the spatial resolution (see also Cassol et al. 2009a, p. 67).

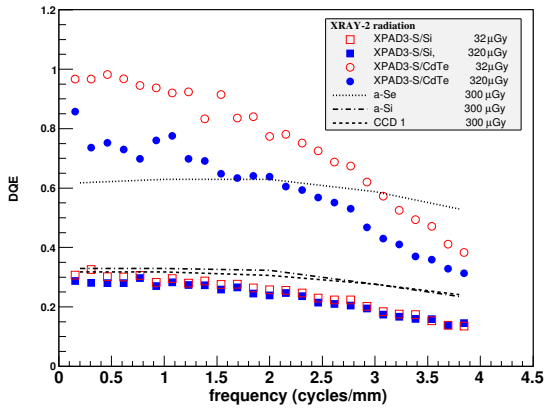

Figure 3.6: Comparison between the DQE of the XPAD3.1-S hybrids and an amorphous selenium detector (a-Se), an amorphous Si detector (a-Si) and a CCD camera with a GOS scintillator screen (CCD) (Cassol et al. 2009a, p. 67).

Figure 3.7: Picture of the PIXSCAN II scanner.

Finally, Figure 3.6 illustrates a direct comparison of the hybrids with other devices under equivalent radiation conditions. The XPAD3.1-S/Si detector presents a stable DQE (independent of the exposure level) which is however rather low, due to the low Si sensor absorption efficiency. Therefore, this detector is not really competitive in dose reduction with respect to other devices. It guarantees however a noise entirely driven by statistics, which can be very useful in low contrast studies when the delievered dose is not a problem. On the contrary, the CdTe hybrids show a less stable response due to the progressive appearance of noise with increasing exposures. Nevertheless, they can assure a maximal DQE for low exposures, which appears very promising for low dose preclinical longitudinal studies.

3.2. Preclinical imaging with the micro-CT scanner PIXSCAN II

Despite the results of the previous section, the production of a large CdTe detector was still under investigation at that point, mainly due to the difficulty of growing uniform CdTe crystals. Instead, we could dispose of a large XPAD3.1-S/Si camera, produced in the context of the XPIX consortium[b] together with two other cameras employed by our colleagues on the beamlines at ESRF and SOLEIL. Therefore our next step was to characterize the imaging performance of this new $7.5\ \mathrm{cm} \times 11.4\ \mathrm{cm}$ detector installed in the PIXSCAN II scanner (Cassol et al. 2016, full text at 154). This time, in parallel to standard absorption tomography, we paid attention to spectral tomography in order to obtain a first proof of principle of its feasibility with a single threshold detector, as well as to optimize the results.

[b] http://imxgam.in2p3.fr/xpix.php.

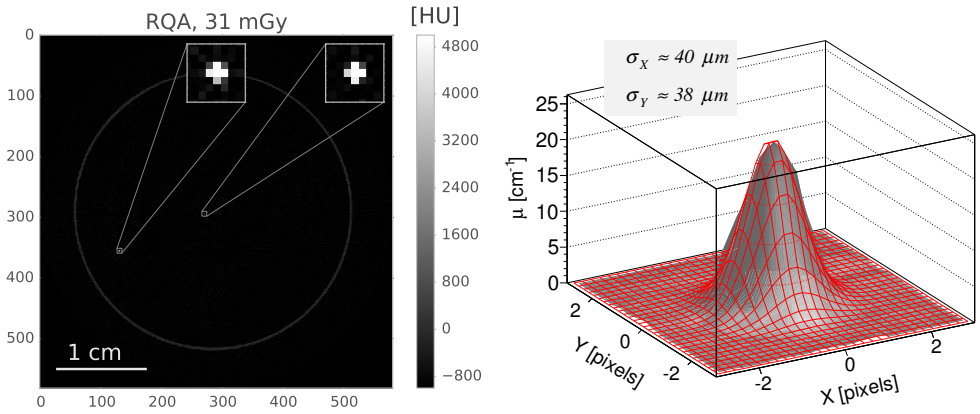

Figure 3.8: Transverse slice of the phantom composed of two tungsten wires of $25\ \mu\mathrm{m}$ diameter employed for the estimation of the PSF (left) and its measured PSF for the central wire (right) (Cassol et al. 2016, p. 154).

3.2.1. Standard absorption tomography

The scanner, shown in Figure 3.7, was similar to the PIXSCAN I, but with a longer source-detector distance ($\sim 440\ \mathrm{mm}$) and a standard magnification of 1.85[c]. It disposed both of a molybdenum and a tungsten target X-ray tube, alternatively installed in the scanner lead/steal shielding box.
In the light of the PIXSCAN I experience, great efforts were put in optimizing the data processing. In particular, the internal tiled geometry of the detector was directly incorporated in the back projection core of the code and the resampling procedure, responsible for a significant loss of spatial resolution in the PIXSCAN I, was suppressed. This guaranteed a spatial resolution of $\sim 92\ \mu\mathrm{m}$ (FWHM), slightly larger than the reconstructed pixel size of $70\ \mu\mathrm{m}$, as it can be seen in Figure 3.8, which presents the PSF (Point Spread Function) measured by imaging a vertical tungsten wire of $25\ \mu\mathrm{m}$ diameter. Such a high resolution, which can be improved by increasing the magnification, permits to visualize small details of the mouse anatomy, as for example the nasal septum of Figure 3.9.
For what concerns the noise of tomographic images, the scanner behaved as expected. Both the image variance and the NPS (Noise Power Spectrum) were close to the results expected from a detector affected only by statistical noise. The detectability at low contrast showed again a limit at 25 HU for objects with a size of few mm and for a count statistics of at least 10,000 detected photons/pixels. In general, this amount of counts was set as a standard in order to have good quality images. This fixed the minimal dose per scan to few hundreds mGy (de-

[c]The magnification could be varied from 1.4 to 2.8 by changing the distance between the rotation axis and the source.

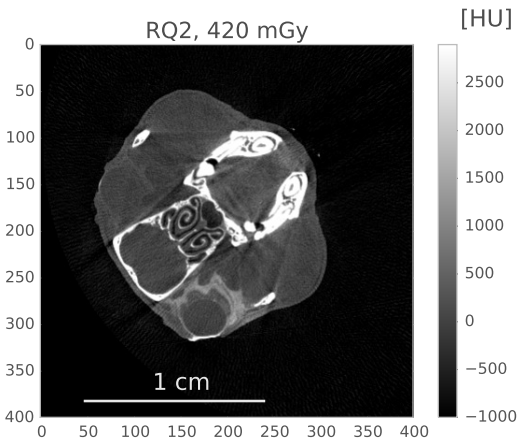

Figure 3.9: Transverse slice of a mouse head acquired with a magnification of 2.6 (Cassol et al. 2016, p. 154).

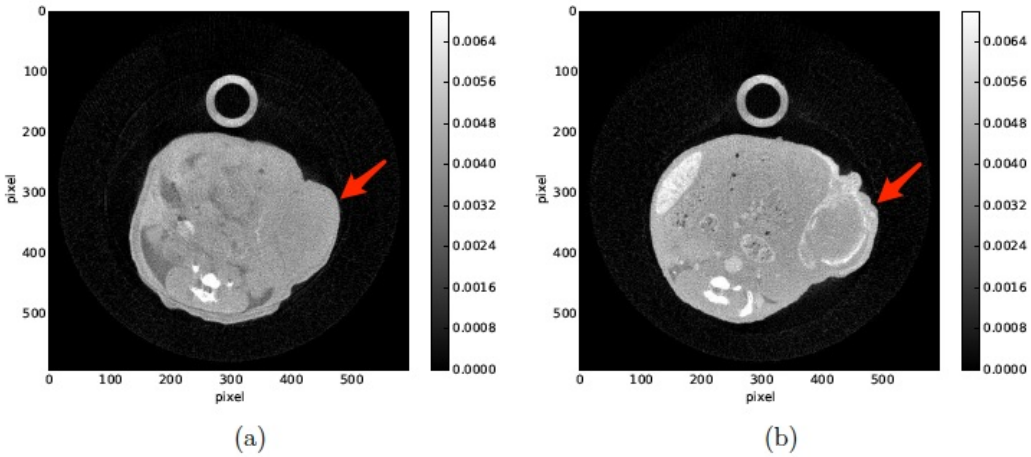

Figure 3.10: Transverse slices of a mouse with a cancer lesion (indicated by the red arrow) before (left) and after (right) injection of liposomes NanoVista charged with a 70 mg/mL iodine solution (Kronland-Martinet 2015).

pending on the radiation quality) to get satisfying results.
The PIXSCAN II scanner has been used for first in vivo biomedical studies with iodinated contrast agents by C. Kronland-Martinet (Kronland-Martinet 2015). These agents, generally employed for enhancing the contrast of the vascular system, were used in an innovative way for tumor detection. The idea was to detect the inflammation associated to the tumors by visualizing the macrophages around the lesions after their ingestion of the agent, which is identified by the macrophages as a foreign substance. Figure 3.10 presents one of the most

promising results obtained with liposomes[d] NanoVista charged with 70 mg/mL of iodine.

3.2.2. Spectral tomography

Photon counting detectors have the remarkable advantage, with respect to charge integration devices, of giving some access to the detected photon energy. This motivated the development of new imaging modalities, exploiting spectral information in order to achieve material decomposition thanks to the dependence, specific to each element, of the attenuation coefficient on the X-ray energy (Riederer and Mistretta 1977, Roessl and Proksa 2007). In particular, we considered the so called *K-edge method* which permits to recognize elements having their K-edge energy within the photon spectrum by comparing images taken within two energy windows, one above and one below the K-edge value. As the XPAD3 chip is equipped with only one threshold, one energy window is obtained by subtracting before reconstruction two acquisitions taken with the pixel thresholds set at the window lower and upper bound. Therefore, the K-edge image of one chemical element requires in general three acquisitions taken with the pixel thresholds set at the K-edge value and at the interval ΔE_- and ΔE_+, below and above the K-edge, respectively.
We demonstrated the feasibility of the method by imaging phantoms containing solutions of two elements: iodine and silver, which have K-edge energies at 33.2 and 25.5 keV, respectively (Cassol et al. 2013, full text at 124). Figure 3.11 shows the attenuation coefficient of the imaged solutions as a function of energy, together with the selected energy intervals. Standard absorption tomography does not permit to distinguish between the silver and the iodine solutions, and other materials constituting the phantom (see Figure 3.12), whereas the K-edge images, obtained by subtracting the reconstructed scans acquired within the two energy windows, permit to enhance a specific element thanks to the increase of the attenuation coefficient above its K-edge value, as shown in Figure 3.13.
Following this first proof of principle, several tests have been performed on mice, mainly employing iodinated contrast agents[e], as in the example of Figure 3.14, where coronal slices of a mouse reconstructed within the two energy windows and the corresponding K-edge image are shown.
Nevertheless, we were not totally satisfied with our results because the above described procedure has some limitations for in vivo imaging: the necessity of acquiring three successive scans implies a multiplication of the dose delivered to the animal, which is not suitable for longitudinal studies. Moreover, the subtrac-

[d] A liposome is a spherical vesicle having at least one lipid bilayer. It can be used as a vehicle for administration of nutrients and pharmaceutical drugs (Wikipedia).
[e] Preliminary tests with silver nanoparticles showed a high toxicity for this element, which demanded further studies (Kronland-Martinet 2015).

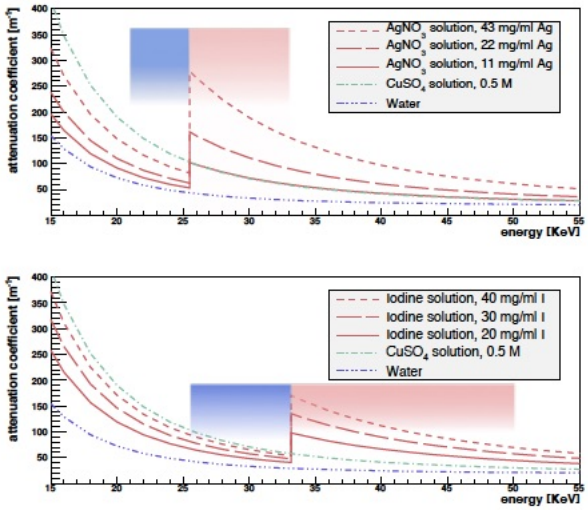

Figure 3.11: Expected attenuation coefficients of silver and iodine solutions imaged considering energy windows (indicated by the color gradients) below and above the K-edge energy (Cassol et al. 2013, p. 124).

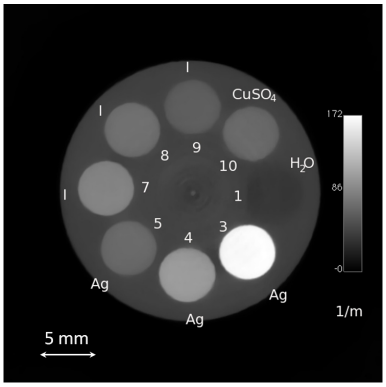

Figure 3.12: Transverse slice of a phantom with inserts filled with water (No. 1), silver nitrate solutions (No. 3-5), iodine solutions (No. 7-9) and a copper sulphate solution (No. 10) (Cassol et al. 2013, p. 124).

tion of images acquired successively induces the appearance of artifacts caused by unavoidable movements of the animal during the scans. The femur shadows in the K-edge image of Figure 3.14 are a typical example of this kind of artifacts.

Composite pixels

In order to reduce these effects, we explored the possibility of performing K-edge imaging with a single acquisition by considering larger 3×3 composite pixels where the thresholds are set at three different levels, following alternate pat-

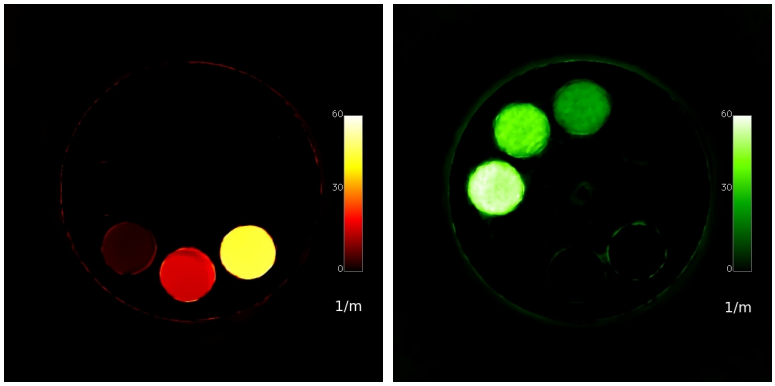

Figure 3.13: K-edge images of silver (left) and iodine (right) solutions: these appear as positive CT numbers on the subtraction of the images acquired within two energy windows around the corresponding K-edge values (Cassol et al. 2013, p. 124).

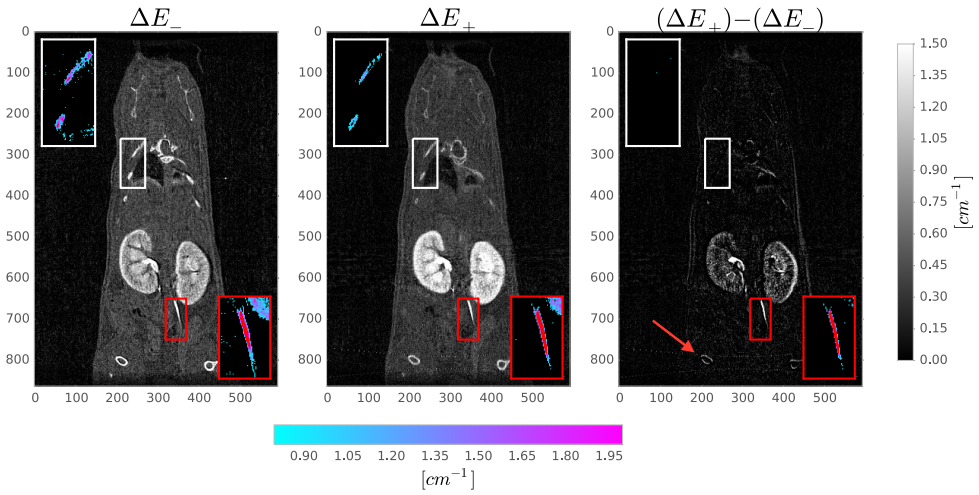

Figure 3.14: Coronal slices of a mouse sacrificed after injection of an iodinated contrast agent. From left to right: slice reconstructed in the low energy window, in the high energy window and K-edge image (subtraction of the second slice from the first one). The rectangles show zooms of two ribs and of the ureter. The arrow indicates an example of shadows, which appear in the K-edge image as a result of small movements of the animal during the acquisitions (Cassol et al. 2016, p. 154).

terns, as in Figure 3.15. The image associated to a given threshold is then directly derived from this single scan by assigning to each large pixel ($390\ \mu\mathrm{m} \times 390\ \mu\mathrm{m}$) the average of the counts measured by the pixels set at the corresponding threshold inside the composite pixel. As an example, Figure 3.16 shows the MIP of a

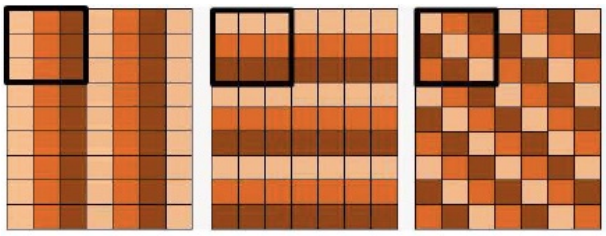

Figure 3.15: Three possible patterns for composite pixel imaging. Each color corresponds to a threshold level and the black square indicates the composite pixel size used for the K-edge image (Kronland-Martinet 2015).

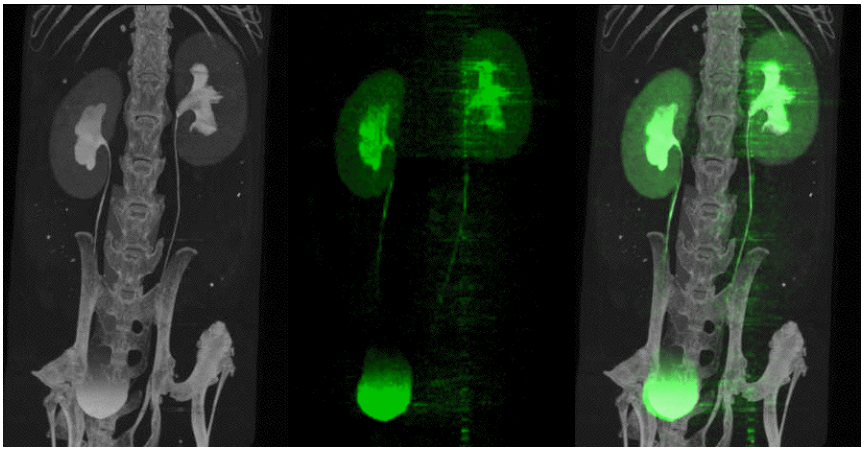

Figure 3.16: Coronal MIP (Maximum Intensity Projection) of a standard tomography image with a pixel size of $130\ \mu m$ (left), K-edge composite pixel image with a pixel size of $390\ \mu m$ (center) and their overlap (right). The mouse was previously injected with an iodinated contrast agent (Kronland-Martinet 2015).

K-edge image obtained with the pixels thresholds following a column pattern. The mouse was injected with a iodinated contrast agent ($200\ \mu$L of Visipaque 320) and sacrificed 20 minutes after injection. The composite pixel method pays obviously the prize of a reduced spatial resolution, which however remains sufficient in several preclinical studies.

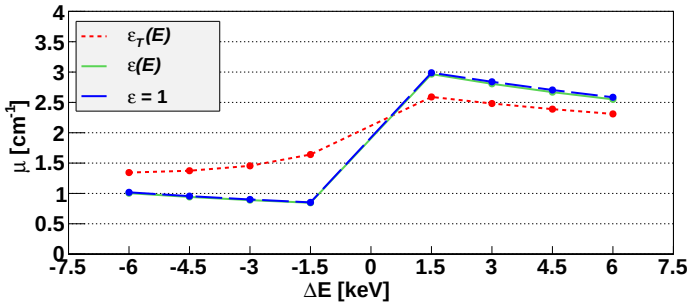

Figure 3.17: Attenuation coefficients of an iodine solution (0.630 M) measured in energy windows of width ΔE around the iodine K-edge for three simulated detector efficiencies: efficiency 100%, $\mathcal{E} = 1$, efficiency of a Si sensor when the threshold is set just above noise, $\mathcal{E}(E)$, and efficiency of a real Si sensor, which depends on the threshold, $\mathcal{E}_T(E)$. Simulated data (Cassol et al. 2015b, p. 139).

High-Z sensors

Another direct way for reducing both the delivered dose and the movement artifacts is to increase the detector efficiency by considering high-Z sensors, which

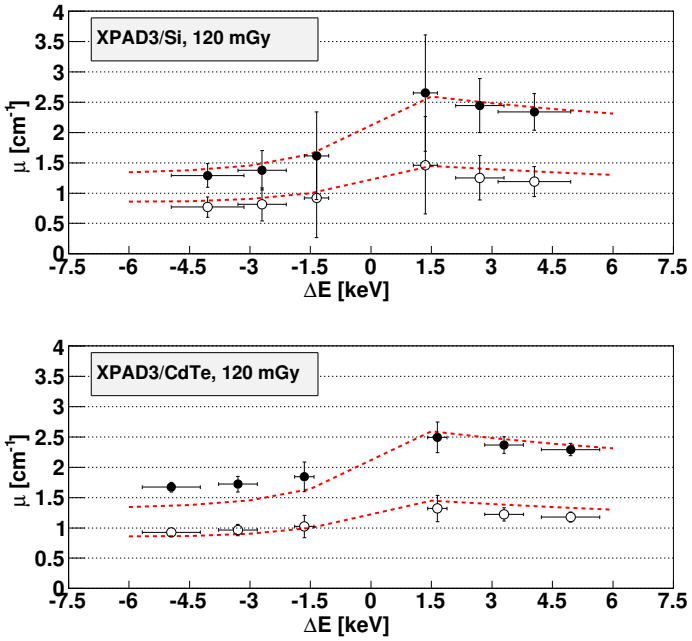

Figure 3.18: Reconstructed attenuation coefficients of two iodine solutions (full markers: 0.630 M, empty markers: 0.315 M) as measured by the XPAD3.2/Si (top) and the XPAD3.2/CdTe at equivalent dose. The dashed lines corresponds to the XPAD3.2/Si simulated response (Cassol et al. 2015b, p. 139).

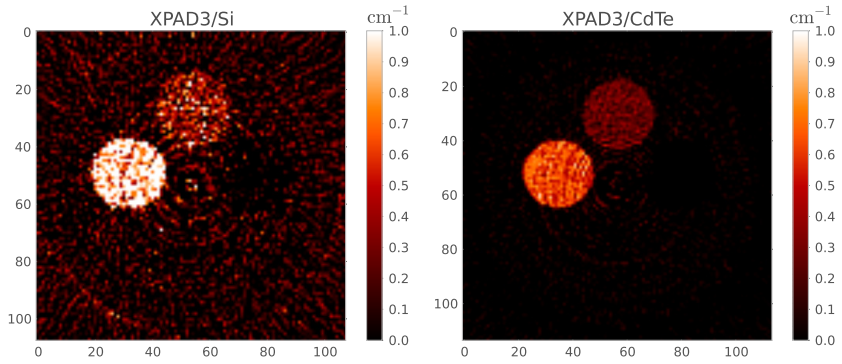

Figure 3.19: K-edge transverse slices of two iodine solutions (0.630 M and 0.315 M) reconstructed from data acquired with the XPAD3.2/Si detector (left) and the XPAD3.2/CdTe detector (right) (Cassol et al. 2015b, p. 139).

allow to fully exploit the photon flux and to reduce the acquisition time. Furthermore, the increase of the sensor efficiency permits to access harder X-rays, hence to employ contrast agents with K-edge values at higher energies, like Ba or Gd, which have K-shell values at 37.4 keV and 50.2 keV, respectively. Given our previous experience with CdTe sensors, we considered this high-Z material in order to verify the improvements that it could provide to spectral imaging. In the context of the MSc dissertation of L. Portal (Portal 2014), we have performed a direct comparison of XPAD3.2 chips bump bonded to Si or CdTe sensors while considering the K-edge imaging of iodine solutions (Cassol et al. 2015b, full text at 139). A first interesting result of this study was to point out that charge sharing represents a main cause of contrast degradation in K-edge images. As seen in Section 3.1, the sharing of charges between adjacent pixels entails a dependence of the detection efficiency on the threshold. Therefore, the number of detected photons inside an energy window (which is estimated by subtracting two acquisitions at two different thresholds) does not strictly correspond to the detected photon flux. As a consequence, the reconstructed attenuation coefficients in the energy windows are distorted and unfortunately in the direction of reducing the contrast between them. This is clearly visible in the simulation results of Figure 3.17, which consider three energy windows of different widths around the iodine K-edge: the contrast between the negative and positive windows (corresponding to windows below and above the K-edge) is much worse when the simulation takes into account the correct pixel efficiency (red points in the Figure). Real data confirmed this result for Si sensors and showed that CdTe sensors present even a stronger loss of contrast with respect to an ideal detector, as shown in Figure 3.18 for two iodine solutions. As a consequence, even if CdTe sensors had an efficiency ~ 11 times higher[f], the associated improvement

[f] In the case of a common preclinical beam and thresholds set at 33.2 keV.

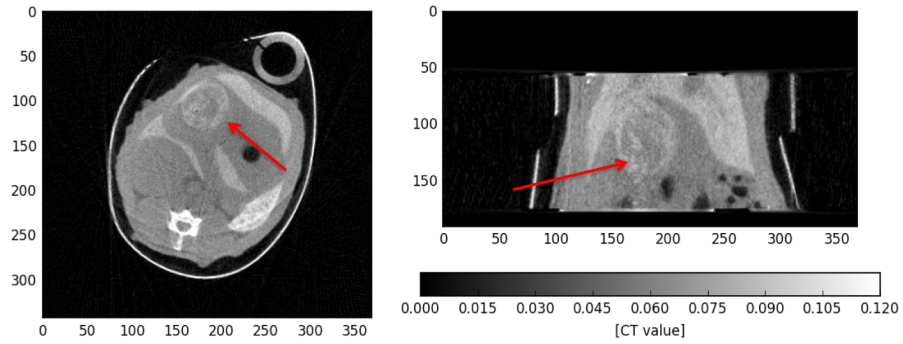

Figure 3.20: Large liver tumour imaged with a XPAD3.2/CdTe module after 100 mL injection of $\mathrm{ExiTron}^{\mathrm{TM}}$ nano 12000. The liver and the spleen are highly contrasted. (Portal et al. 2017a).

of the CNR (Contrast-to-Noise Ratio) in the K-edge image[g] was only twice. Figure 3.19 presents the K-edge image obtained, in identical conditions, with the two sensors: the XPAD3.2/Si image is more noisy, due to the lower detected statistics, but clearly presents a higher signal thanks to the higher contrast, as already indicated by Figure 3.18. Nevertheless, CdTe sensors have to be preferred in longitudinal studies because they permit to reach a given CNR with a lower delivered dose.

3.2.3. Longitudinal studies

In the light of the previous results, L. Portal started in 2014 a PhD work with the goal of performing longitudinal studies for in vivo monitoring of liver tumors (hepatocellular carcinoma) in mice by the mean of both the standard absorption and the K-edge imaging approach with XPAD3.2/CdTe detectors. This study, which is currently ongoing, has been developed in close collaboration with the group of biologists of IBDM led by Flavio Maina, who is searching for drugs that inhibit tumor development (Fan et al. 2015). The idea was to provide our colleagues with a new, unprecedented for them, imaging tool while completing our R&D program in spectral imaging by comparing in vivo standard absorption and K-edge imaging of tumors together with keeping the delivered dose to minimal values ($<$ 20 mGy per scan). For this, a hepatospecific contrast agent has been selected, which permits to enhance the contrast of the liver tissue so as to visualize the tumors as a low contrasted mass inside the organ. We chose $\mathrm{ExiTron}^{\mathrm{TM}}$ nano 12000, which is based on long-lasting barium charged nanoparticles and permits to enhance the liver contrast by a factor 4 for several weeks after a single retro-orbital injection ($4\ \mu\mathrm{L/g}$ body weight). Furthermore this contrast agent

[g]For a given ROI (Region of Interest), CNR is defined with respect to water as $\mathrm{CNR} = (\mu_{\mathrm{ROI}} - \mu_{\mathrm{H_2O}})/\sigma_{\mathrm{H_2O}}$.

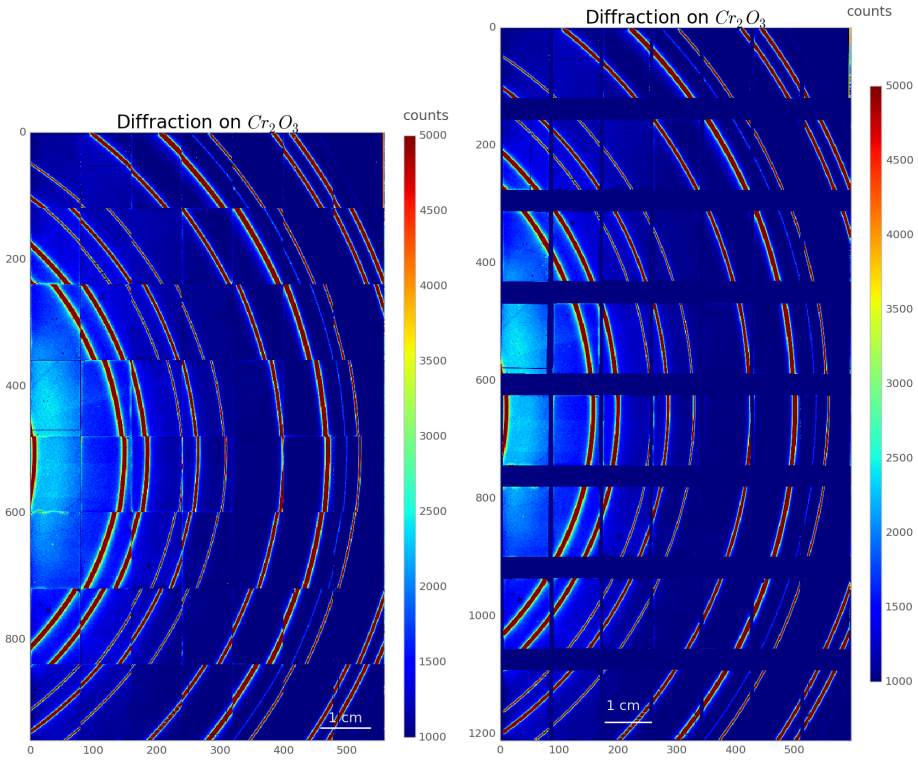

Figure 3.21: Beam (25.5 keV) diffraction by Cr_2O_3 crystals: raw image (left), image after applying a correction for the internal geometry of the camera (right) (Cassol et al. 2015a, p. 130).

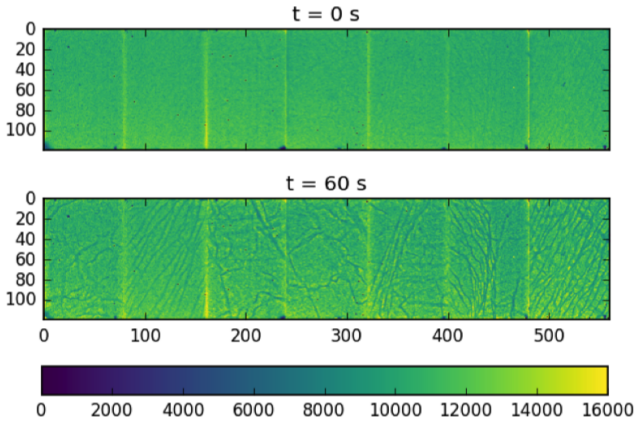

Figure 3.22: Appearing of polarization effects in the XPAD3.2/CdTe module after 60 s of data taking (Portal et al. 2017b).

allows to perform K-edge imaging of barium, which has a K-shell binding energy of 37.4 keV, easily accessible with CdTe sensors.
We could dispose at that time of one CdTe module based on Schottky hybrids

Figure 3.23: The PIXSCAN-FLI scanner.

(cf. Section 1.3.3) that permitted to successfully image our first tumors, as illustrated in Figure 3.20. We planned also to use the large CdTe camera that was successfully tested on synchrotron beamlines, but that is available at CPPM only one third of the time since it is shared with our collaborators at ESRF and SOLEIL. Figure 3.21 presents one of the first diffraction images acquired with the camera (Cassol et al. 2015a, p. 130), which demonstrates a satisfying image quality, but also dead spaces between the single mono-blocks assembled in modules. The Schottky CdTe hybrids were however known to be affected by a drift of the counts over time due to the progressive accumulation of charges along the crystal defects, which caused the appearance of image non-uniformities after a few minutes of data taking (Buton et al. 2014). In the beginning, the polarization was rather slow, amounting to only few % over tens of minutes, and it could be easily corrected by performing periodical HV (High Voltage) resets, every ten minutes, which caused the rapid dispersion of the space charges and the recovery of the correct counting rate. Unfortunately, with the aging of the CdTe module,

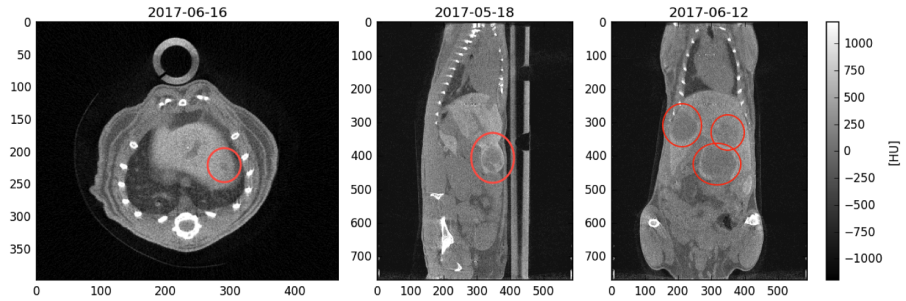

Figure 3.24: Transverse (left), coronal (center) and sagittal (right) tomographic slices of small, medium and large tumors acquired with a XPAD3.2/Si camera after a 100 mL injection of ExiTron$^{\mathrm{TM}}$ nano 12000 (Portal et al. 2017b)

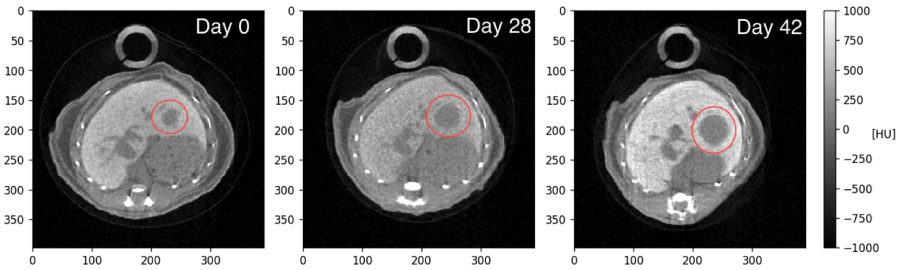

Figure 3.25: Longitudinal liver tumour monitoring with the XPAD3.2/Si camera: progression of the tumour volume with time (Portal et al. 2017b).

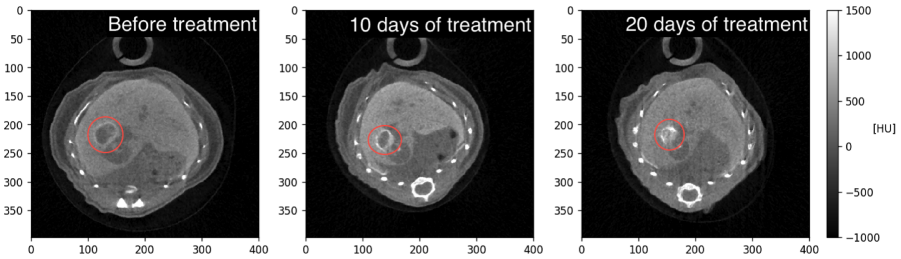

Figure 3.26: Longitudinal liver tumour monitoring with the XPAD3.2/Si camera: regression of the tumour volume induced by a targeted therapy (Portal et al. 2017b).

the image degradation arose ever more rapidly, thus requiring HV resets about every ten seconds, which in turn became incompatible with low dose imaging, because each reset would involve a corresponding dead time during the scan. Figure 3.22 shows the non-uniformity appearance after only 60 s of data taking, in the last period of employment of the module. The reason for this detector degradation, which is somehow related the detector operating temperature, is still under investigation. However, we could verify that this phenomenon does not appear with CdTe sensors with Ohmic contacts, which then will have to be preferred for the construction of CdTe hybrids.

In order to carry on our imaging program, motivated also by the requirements of our biologist colleagues, we have decided to go back to Si sensors and to use the new XPAD3.2/Si camera delivered by imXPAD and installed in the micro-CT system PIXSCAN-FLI, which was recently developed at CPPM for CERIMED. This scanner, which is shown in Figure 3.23, represents the final evolution of the PIXSCAN series. It permits to maximize the dose reduction by minimizing the acquisition dead time, thanks to its data taking on the fly, which is performed with continuous rotation of the imaged object. Figure 3.24 shows some examples of tumour images of excellent quality obtained with a delivered dose of ~ 180 mGy. A clear advantage of this camera with respect to the CdTe mod-

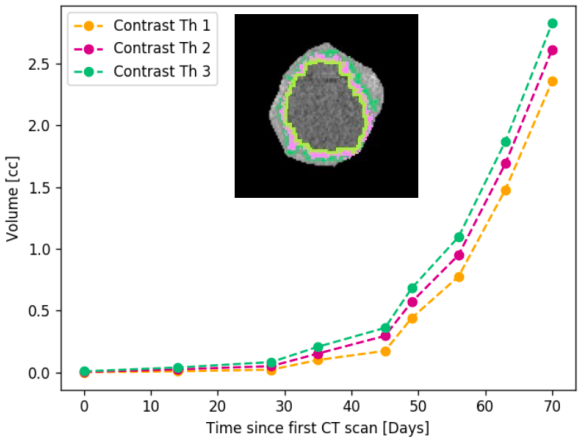

Figure 3.27: Tumour volume estimation by mean of contrast thresholds: Th 1/2/3 = 75/50/25 % of the liver tissue contrast (Portal et al. 2017b).

ules is the possibility of obtaining full body images without vertical dead spaces, which is particularly useful in the case of multiple or big volume tumours. Then, we could successfully follow over several weeks a cohort of mice affected by hepatocellular carcinoma in order to determine the dynamics of the tumour evolution and to evaluate the lesion regression induced by the innovative targeted therapy developed by our colleagues at IBDM. Figure 3.25 shows an example of evolving tumour and Figure 3.26 the example of a tumor regression under the effect of the administered drugs. A semiautomatic segmentation method based on predefined contrast thresholds has been developed in order to quantify the tumour volume in a stable and reproducible way. An example of tumour evolution measured with three different thresholds is presented in Figure 3.27. The estimated volumes are pretty independent of the threshold values. Tumors with diameter greater then 3 mm could be easily visualized and appeared to have an exponential growth with an average doubling time of around 20 days. The test of the therapy was also very successful, with a significative regression of the tumour volume (> 50%), followed by a steady state for several weeks. Moreover, we could observe an intriguing increase of contrast around the tumors after treatment, whose interpretation has been the object of a Declaration of Invention at SATT Sud-Est[h]. The complete results of this promising research will be soon described in the PhD work of L. Portal (June 2018), together with some preliminary conclusions related to the K-edge R&D program.

[h]F. Cassol, F. Maina, R. Doro, "Tumour response to treatment, anticancer therapy, immune response following cancer treatment, immuno-therapies, macrophages", Reference SATT: 979. Reference CNRS: DI10955-01.

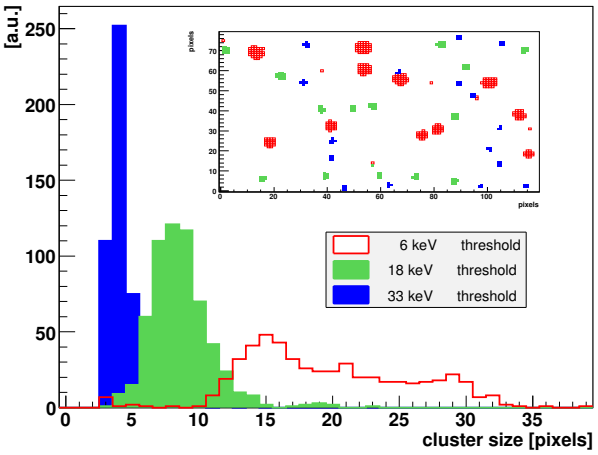

Figure 3.28: Alpha signals and their size distribution for 1.7 MeV alphas measured at three different pixel thresholds (Cassol et al. 2011a, p. 118).

3.3. Neutron tomography

In parallel to the above described studies and following the attempt of other solid state detector producers, we decided to also investigate the performance of the XPAD3 hybrids for neutron tomography, which represents an imaging technique complementary to X-ray tomography because of the difference between the interactions of X-rays and neutrons in matter. Neutron tomography is in fact suitable for the imaging of light elements typical of organic materials, especially when surrounded by heavy elements that preclude X-ray but not neutron transmission, thanks to their low heavy elements interaction cross section. For example, the imaging of hydrogen in fuel cells or organic rests in archeological fossils are good topics for neutron tomography. The characteristics of the XPAD3 hybrid like its pixel size, dynamic range and its readout speed suggested that it could be a performing neutron detector, provided we could identify a suitable neutron converter.

The achievement of this study (Cassol et al. 2011a, full text at page 118) demanded both the easy access to neutron beams and a gain of expertise in neutron detection. For that, we have set up a collaboration with the Imaging Group of HZB, led by Prof. John Banhart, which had free access to the BER II nuclear reactor. The project was then planned in the context of a full-time secondment of one year that I spent at HZB from August 2009 to August 2010 (Cassol and Morel 2009, full text at page 88).

We decided to choose a thin layer of $^{6}\mathrm{LiF}$ as neutron converter, which was deposited on a $500\ \mu\mathrm{m}$ thick polished silicon wafer and placed in close contact with a XPAD3/Si hybrid. The induced nuclear reaction is

$$^{6}\mathrm{Li} + \mathrm{n} \rightarrow \alpha(2.05\ \mathrm{MeV}) +^{3}\mathrm{H}(2.72\ \mathrm{MeV}) \tag{3.2}$$

The alpha and tritium particles are produced back to back, thus only one of those reaches the detector. Their range in Si is very short ($\mathrm{R}_{\alpha} = 8.6\ \mu\mathrm{m}$ and $\mathrm{R}_{^3\mathrm{H}} = 44.1\ \mu\mathrm{m}$), assuring a 100% detection efficiency even with low bias voltages ($V_{bias} > 10\ V$). Due to the ion high ionization power, the response of the hybrids is a cluster of counting pixels, as shown in Figures 3.28 in the case 1.7 MeV alphas. The cluster size was measured to be dependent both on the pixel threshold and on the particle energy.

The optimal converter thickness is given by the convolution of the neutron interaction probability, shown in Figure 3.29 for several beam energies, and the charged particle escape probability, that decreases with the amount of material to be crossed. Figure 3.30 shows the measured efficiency as a function of the converter thickness in the case of a 7.3 meV neutron beam and the estimated Monte Carlo prediction for the three beams considered in Figure 3.29. In all cases, the efficiency is maximal for a converter thickness of $6 - 7\ \mathrm{mg/cm^2}$ and remains below 10%.

Finally, we could perform a first tomographic scan at a cold neutron beam with a single XPAD3.2/Si hybrid by imaging a tooth, as shown in Figure 3.31. This result, despite the non-uniformity of the converter due to the home-made deposition procedure, was very encouraging, thus demonstrating that this type of detectors can be easily converted to neutron detection by simply developing a removable converter adaptable to any detection surface.

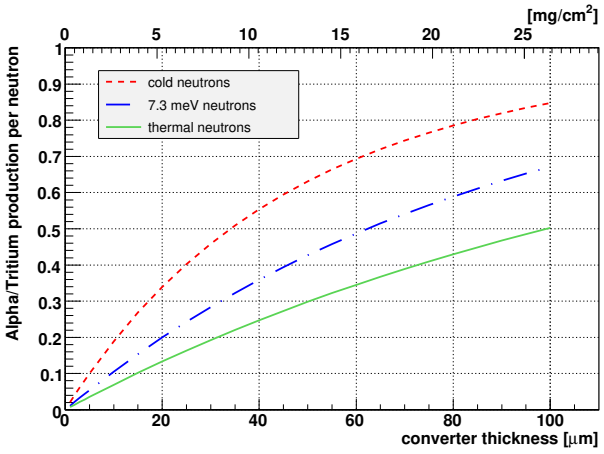

Figure 3.29: Production of alpha/tritium particles simulated with MCNP as a function of the $^{6}\mathrm{LiF}$ converter thickness for a cold, a thermal and $7.3\ \mathrm{meV}$ neutron beam. (Cassol et al. 2011a, p. 118).

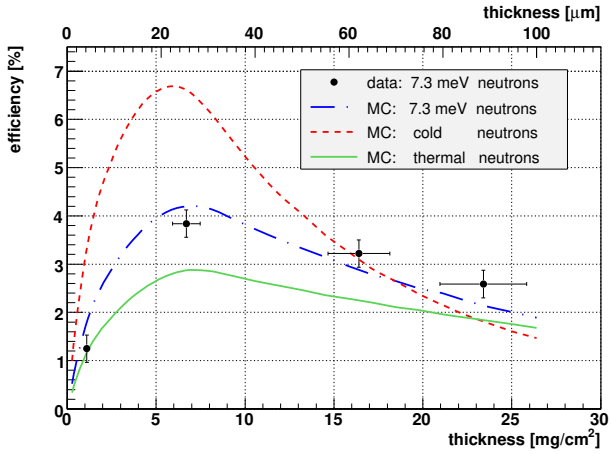

Figure 3.30: Neutron detection efficiency as a function of the $^{6}\mathrm{LiF}$ thickness for measured and simulated data (Cassol et al. 2011a, p. 118).

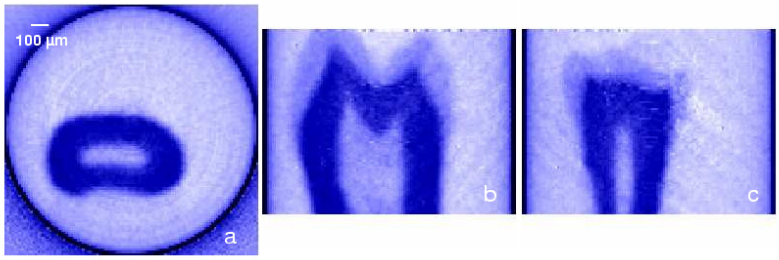

Figure 3.31: Transverse (a), coronal (b) and sagittal (c) slices of the reconstructed scan of a tooth with a XPAD3.2/Si detector irradiated by a cold neutron beam (Cassol et al. 2011a, p. 118).

Conclusions and perspectives

The previous chapters have described our research program and the results obtained in tomographic imaging with the XPAD hybrid pixel detectors, which were in our case mainly dedicated to X-ray imaging for biomedical research. We would like to conclude by setting the described activity into perspective.

All the teams that started to develop hybrid pixel detectors for X-ray imaging during the late nineties were motivated by the same idea of producing *noise free detectors*, which came naturally by the transition from charge integration to pulse counting systems. Indeed, by detecting only photons that create a signal above a certain threshold, it is possible to reject electronics noise just by setting the threshold at a sufficiently high value. This, not only allows to perform long lasting imaging with full noise rejection, but also permits to give the same weight to every photon, independently from its energy. This is not possible in charge integrating devices, where higher energy photons have a higher weight in the signal formation. Moreover, single photon counting gives access to an ideally infinite detection dynamic provided that the counter is deep enough, which immediately appeared quite appealing, particularly for X-ray diffraction imaging. An other evident advantage of the new technology was the *hybrid concept*, which means to move from *indirect detection devices*, as in the standard imaging systems, to *direct detection devices*, where the electrical signal is directly generated by the X-ray deposited energy. This one step detection was believed to improve spatial resolution as well as to permit optimization of the detection efficiency.
The XPAD1 and XPAD2 chips were born in this context, so as other similar chips, like the MEDIPIX chip developed at CERN (Campbell et al. 1998) or the PILATUS chip developed at PSI in Switzerland (Brönnimann et al. 2001). All these ASICs were characterized by rather large pixel sizes ($> 150\ \mu\mathrm{m}$) and one single threshold per pixel. It was in this context that we also set up the PIXSCAN I scanner, which had the merit to be one of the first functional micro-CT scanner based on a large hybrid pixel camera without dead spaces (thanks to the tiled modules).
Then, starting from the mid-two thousands, more focus has been put on the spectroscopic capability of counting detectors, which at best can be achieved with multiple counters. Indeed, the acquisition of images in several energy bins not only permits to access material decomposition (Alvarez and Macovski 1976), but also to suppress beam hardening effects and to reduce image signal-to-noise ratio by assigning energy dependent weights to photons in the different channels (Cahn et al. 1999). For what concerns material decomposition, particular attention has been payed to K-edge spectral tomography that allows to recognize a specific heavy element inside the imaged object (Riederer and Mistretta 1977, Roessl and Proksa 2007). This, together with the intense development of

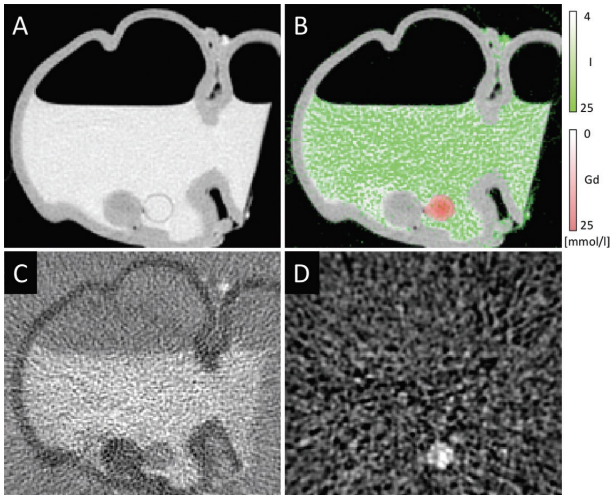

Figure 3.32: Multiple K-edge spectral imaging of a colon phantom with the Philips photon counting prototype. A) Conventional CT scan. B) Conventional CT scan (image in A) with overlay of iodine (green) and gadolinium (red). C) Iodine image. D) Gadolinium image (Muenzel et al. 2017).

targeted biomarkers based on heavy metal nanoparticles, has opened the door towards the innovative concept of both *functional and anatomical X-ray tomography* (Clark and Badea 2014, Li et al. 2014). The XPAD3 chip was developed in this context, and its C version was designed to provide two thresholds per pixels for spectral studies, similarly to the MEDIPIX2 chips (Campbell 2011) or the PIXIRAD chip developed in Italy by a team of INFN (Bellazzini et al. 2013). This ASIC generation was characterized by smaller pixel sizes ($< 150\ \mu$m) and two thresholds per pixel, which permitted to access first spectral results. This is also the period of the PIXSCAN II scanner that, despite the impossibility of benefiting from the two thresholds (the C version of the chip did not worked properly), has been successfully employed for first K-edge spectral tomography and could demonstrate that hybrid pixel detectors permit to access statistical noise tomography.

Then, in parallel to this academic effort, several companies started to emerge with the intent of commercializing hybrid pixel detectors principally for biomedical and synchrotron research imaging: XPAD was commercialized by imXPAD[i], PILATUS by Dectrics[j], PIXIRAD by PiXrad[k] and the Medipix detectors by several companies, as for example MARS Bioimaging[l] or Advacam[m]. Soon after,

[i] Now by Cegitek, www.cegitek.com.
[j] https://www.dectris.com
[k] http://www.pixirad.com
[l] https://www.marsbioimaging.com
[m] http://advacam.com

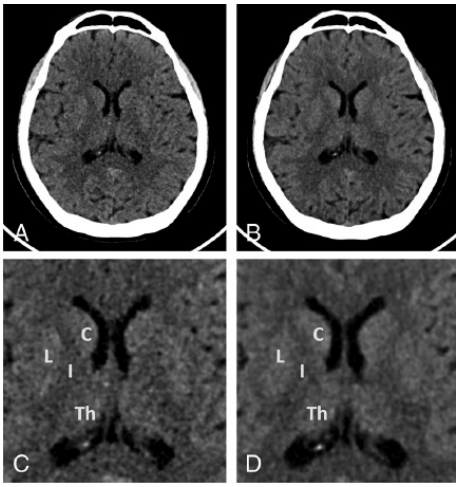

Figure 3.33: Brain image of a 59-year-old woman from an energy integrating device (left) and the SIEMENS photon counting prototype (right), both detectors are mounted on the same gantry (Pourmorteza et al. 2017).

large industrial companies, mainly focused on human applications, started also to grow interest on the photon counting concept, which with its lower signal-to-noise ratio and its flexible type of energy bins promised to be better performing than the already well-established dual energy technique (Taguchi and Iwanczyk 2013). This, based on dual spectrum methods (fast switching or dual source) or on sandwich-type detectors (with the upper layer detecting the low energy part of the spectrum and the lower layer the upper energy part) already permitted to achieve some spectral imaging with standard cameras (Faby et al. 2015).

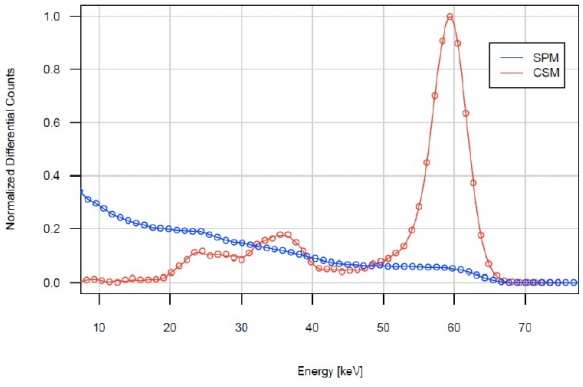

Figure 3.34: Spectrum measured with (red) and without (blue) charge sharing correction for a 2 mm thick CdZnTe sensor connected to the MEDIPIX3 chip with a 110 μm pixel pitch (Ballabriga et al. 2016).

Hence, during the last decade, companies like Philips (Steadman et al. 2017) or Siemens (Yu et al. 2016) have started their own developments on photon counting, in close contact with academic institutes and hospitals. Also, new companies emerged based on the specific development of photon counting detectors for human imaging, e.g. dxRay, inc.[n], whose detectors are installed in GE Healthcare scanners (Cho et al. 2014). The challenge for human applications is to achieve enough detection efficiency (generally obtained with CdTe or CdZnTe sensors, but also with edge-on silicon strips, i.e. DxRay), enough containing rate (up to 10^9 photons mm^{-2} s^{-1}) and multiple energy bins, which has been accessed both with multiple thresholds (i.e. Philips) and with the composite pixel concept (i.e. Siemens). At present, all these developments are already deployed in hospital contexts, though still in R&D phase. Figure 3.32 shows an example of multiple K-edge imaging obtained with the Philips prototype installed at ISC in Lyon, which is equipped with five counters (Muenzel et al. 2017). Particularly interesting is also the direct comparison between a standard integrating device and a photon counting detector that is extensively performed on human subjects with the SIEMENS prototype (Bluemke 2017). Figure 3.33 illustrates for example a direct comparison of human brain scans acquired with the two devices, images are then evaluated by expert radiologists with blinded readings (Pourmorteza et al. 2017).
In parallel to the effort towards multiple energy channels, large attention has recently been put on the optimization of the detector response in each channel, which is particularly critical in the case of small pixel sizes, where charge sharing and fluorescence emission can strongly modify the detector energy response (Xu et al. 2011). Energy response correction has been achieved in the last hybrid pixel generations both directly at the ASIC level, as for the MEDIPIX3 (Ballabriga et al. 2013) or the PIXIRADIII (Bellazzini et al. 2015), or offline, as for the TIMEPIX3 (Poikela et al. 2014). Figure 3.34 shows for example the MEDIPIX3 detector response with and without charge sharing correction in the case of a 2 mm thick CdZnTe sensor.
In absence of resources for the design of a new multi-threshold/energy response-corrected version of the XPAD chip, we decided to complete our program with the set up of a large CdTe camera in order to correct for one of the main limit of our previous Si cameras, i.e. the detection efficiency. Then, the construction of the PIXSCAN-FLI scanner finally equipped with both a Si and a CdTe camera has permitted to successfully employ the XPAD photon counting detectors in a full biomedical research project.
The upcoming move of PIXSCAN-FLI to the imaging platform CERIMED (end 2018) and overall the awareness that photon counting imaging is nowadays a central issue not only for biomedical but also for human tomography bring us to consider the PIXSCAN project and the technology transfer program that we

[n] http://www.dxray.com

started more than one decade ago as successfully achieved. Further technological developments are still necessary but can be carried from now on by the industrial actors in the field, which have at this point a better insight of the clinical world and probably easier access to larger financial resources to continue the program. The imXgam group is now moving towards new challenges at the frontiers of the present technology and for my part I am moving back towards fundamental research with a new fascinating imaging project, CTA (Cherenkov Telescope Array), which plans to image the universe with photons at the highest ever detected energies in order to localize the still mysterious sources of high energy cosmic rays (Consortium et al. 2017).

Articles

Available online at www.sciencedirect.com
ScienceDirect
Nuclear Instruments and Methods in Physics Research A 571 (2007) 425–428
NUCLEAR INSTRUMENTS & METHODS IN PHYSICS RESEARCH Section A
www.elsevier.com/locate/nima

PIXSCAN: Pixel detector CT-scanner for small animal imaging

P. Delpierre[a,*], F. Debarbieux[d], S. Basolo[a], J.F. Berar[b], A. Bonissent[a], N. Boudet[b], P. Breugnon[a], B. Caillot[b], F. Cassol Brunner[a], B. Chantepie[a], J.C. Clemens[a], B. Dinkespiler[a], R. Khouri[a], I. Koudobine[a], V. Mararazzo[d], C. Meessen[a], M. Menouni[a], C. Morel[a], C. Mouget[b], P. Pangaud[a], F. Peyrin[c], G. Rougon[d], D. Sappey-Marinier[c], S. Valton[c], E. Vigeolas[a]

[a]*Centre de Physique des Particules de Marseille(CPPM), IN2P3/CNRS, Université de la Méditerranée, France*
[b]*CNRS Grenoble & D2am CRG, France*
[c]*CREATIS, UMR-CNRS-5515, INSERM-U630, Lyon, France*
[d]*Institut de Biologie du Développement de Marseille Luminy (IBDML), France*

Available online 9 November 2006

Abstract

The PIXSCAN is a small animal CT-scanner based on hybrid pixel detectors. These detectors provide very large dynamic range of photons counting at very low detector noise. They also provide high counting rates with fast image readout. Detection efficiency can be optimized by selecting the sensor medium according to the working energy range. Indeed, the use of CdTe allows a detection efficiency of 100% up to 50 keV. Altogether these characteristics are expected to improve the contrast of the CT-scanner, especially for soft tissues, and to reduce both the scan duration and the absorbed dose. A proof of principle has been performed by assembling into a PIXSCAN-XPAD2 prototype the photon counting pixel detector initially built for detection of X-ray synchrotron radiations. Despite the relatively large pixel size of this detector ($330 \times 330\,\mu m^2$), we can present three-dimensional tomographic reconstruction of mice at good contrast and spatial resolution. A new photon counting chip (XPAD3) is designed in sub-micronique technology to achieve $130 \times 130\,\mu m^2$ pixels. This improved circuit has been equipped with an energy selection circuit to act as a band-pass emission filter. Furthermore, the PIXSCAN-XPAD3 hybrid pixel detectors will be combined with the Lausanne ClearPET scanner demonstrator. CT image reconstruction in this non-conventional geometry is under study for this purpose.

PACS: 85.40.Bh; 87.59.−e; 42.50.Ar

Keywords: Hybrid pixels; Photon detector; Photon counting; CT-scanner

1. Introduction

Imaging systems dedicated to small animal imaging are now recognized as important tools for both cancer and genomic researches. Actually, these new imaging systems allow non-invasive visualization of tissues in rodents, which is of considerable interest to follow evolution of tumors and related therapeutic actions, but also to screen large population of genetically modified animals. One of these modalities, the CT-scanner is a very promising technique since it is a fast and relatively low cost means to characterize tissues organization and skeleton abnormalities. Moreover, tumors and vascular system can also be visualized on live animals after injection of contrast agents. The aim of the PIXSCAN project is to develop a CT-scanner offering optimized contrast resolution in soft tissues of mice. In a later stage, plans are to combine this CT scanner with a Positron Emission Tomography (PET) scanner, to allow simultaneous PET/CT imaging of small animals.

The originality of our approach resides in the use of hybrid pixel detectors. These detectors have been devel-

*Corresponding author. Tel.: +33 491827200; fax: +33 491827299.
E-mail address: delpierre@cppm.in2p3.fr (P. Delpierre).

0168-9002/$ - see front matter © 2006 Elsevier B.V. All rights reserved.
doi:10.1016/j.nima.2006.10.126

oped at CPPM for vertex trackers of high-energy physics experiments (DELPHI, ATLAS, CERN, Geneva), and for this reason they are optimized for photons detection and counting. They offer high detection efficiency with low noise and practically infinite dynamic range. In addition, image acquisition and image readout can be done at very high rate (up to 500 Hz). These properties are expected not only to improve contrast resolution of images as compared with images obtained with standard CCD-based detectors, but also to allow reduction of irradiation dose during a scan.

To evaluate the benefits of hybrid pixel detectors in the context of small animal imaging, we have built a large surface detector with the XPAD2 chips [1] and have assembled a first prototype of CT-scanner (named PIXSCAN-XPAD2). We present here the first projection images and corresponding tomographic reconstructions acquired from living mice with the PIXSCAN-XPAD2 system. These encouraging results led us to build an improved version of detector based on the new XPAD3 chip, with enhanced robustness and reproducibility across repeated imaging sessions. Accurate double-energy threshold has been implemented as a new feature to allow narrow energy windowing at the detector level.

Because XPAD3 circuits have been designed to fit with $130 \times 130\,\mu m^2$ pixels, the new version of PIXSCAN using XPAD3 will also benefit from improved spatial resolution. We are currently designing equipment to improve mouse conditioning and are studying the optimal configuration to combine the XPAD3 detector with a small animal PET scanner.

2. The XPAD2 detector

The XPAD2 detector is built using the XPAD2 chip [1]. This chip includes 600 pixels of $330 \times 330\,\mu m^2$. It includes a charge amplifier, a discriminator and a 15 bits counter. 8 XPAD2 are bump-bonded on a $65 \times 8 \times 0.5\,mm^3$ silicon sensor. Because each chip presents photon insensitive areas on its periphery, these 8 modules have been mounted like tiles, to minimize the dead area. This procedure resulted in a $6.5 \times 6.8\,cm^2$ detector of 36,800 pixels, as shown in Fig. 1. Thanks to a fast readout system, the full detector can be read in less than 2 ms. This detector has been tested on the D2AM beam of the ESRF (Grenoble) synchrotron in the context of X-ray experiments for material sciences. Both its very large dynamic range and fast readout could be demonstrated and appreciated since experiment duration was shortened as much as 10–100 times as compared to the standard protocol [2].

3. Fabrication of the PIXSCAN

To evaluate the performances of the XPAD2 hybrid pixel detector for small animal imaging, we have built a very simple CT-scanner prototype. It consists of a step-by-step rotating animal holder placed between a fixed X-ray source and the fixed X-ray detector. To maximize the body region imaged at once, we have used a wide conic beam aperture X-ray source (60 kV, 30 W, 0.8 mA; Rontgentek, SEPH, France) with an emission spot of $50 \times 50\,\mu m^2$. This configuration illustrated in Fig. 2 allows for three dimensional (3D) tomographic imaging of half of the mouse body at once.

The system is installed inside a shielding box made of 5 mm thick iron plates to protect users from radiations. Most mechanical actions have been remote controlled: in particular, mouse is held on a remotely controlled rotating platform with an adjustable angular step (microcontrol, France) and this platform can also be remotely translated to bring the mouse out of the beam for white calibration image acquisition. Finally, an external remote shutter has been installed in front of the source to perform the black calibration image.

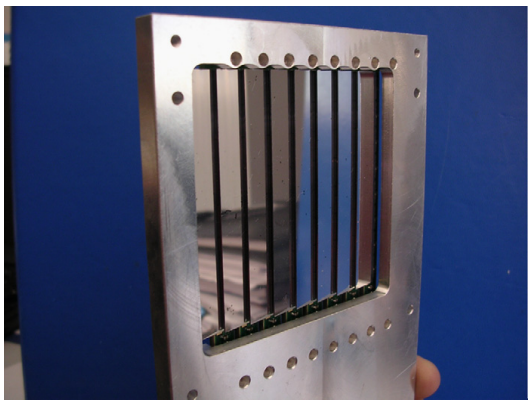

Fig. 1. The XPAD2 detector.

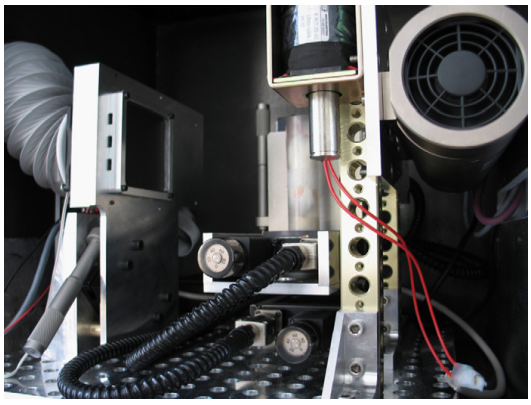

Fig. 2. The PIXSCAN ready for the scan of a mouse.

Fig. 3. Mouse holder.

4. Mouse conditioning

Mice were anesthetized using intraperitoneal injection of urethane at a dose of 1.5 g/kg. They were then placed freely breathing in the imaging system. A 2 cm diameter plexiglas cylinder was first used to contain mouse body. But although body and legs were nicely maintained this way, images turned out to be blurred due to the surrounding plexiglas shell. The image quality was improved with the animal hung by a mouth piece along a carbon axis, with mouse bump supported on the base (Fig. 3). An extra piece of plastic foil was wrapped around the trunk of the animal to avoid movements of the paws during rotation. Advantage of the method resides in the fact that tomographic reconstruction is minimally degraded by mouse support.

5. Detector tuning and image processing

Before any image acquisition, pixels threshold have to be adjusted one by one. To this end the same electric charge is first injected via the calibration capacitor at the input of the analog front end. Threshold adjustment is then finalized using the X-ray source photoelectric peaks as references. Several black calibration images (no object and source blocked) are acquired and averaged to obtain the map of unstable oscillating pixels. Similarly several white calibration images (no object but source opened) are used to map non-working pixels with constant output. All defective pixels (oscillating and non-counting) are masked for calculation of the tomographic reconstruction.

The white calibration image is also used to normalize each mouse projection image, thereby compensating for residual threshold misalignment after calibration. Normalization is done by dividing each mouse image by the white calibration image. Images are then interpolated to compensate for bad pixels and further filtered using a standard median. Fig. 4 gives an example of the images after processing.

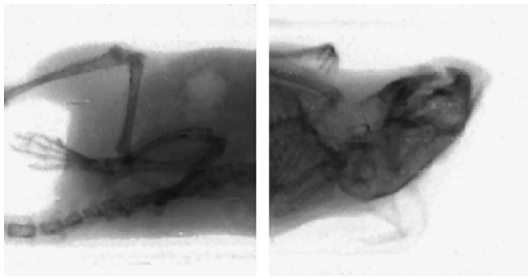

Fig. 4. Examples of images (projections) of a mouse.

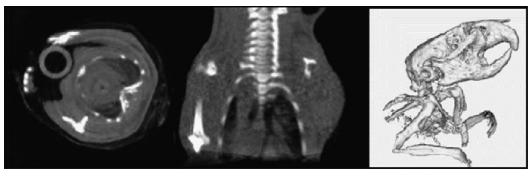

Fig. 5. Tomographic reconstruction of mice images. Left: horizontal slice of a mice thorax, middle: coronal slice, right: bone surface image of a mouse head and thorax.

6. 3D tomographic reconstruction

3D tomographic reconstruction of the mouse body at best possible resolution given the detector pixel size requires about 400 cone beam projections. For convenience, we acquired one image per degree (360 images per scan). These images have then been processed using a FDK-based reconstruction algorithm for cone beam tomography provided by CREATIS (RecFDK). Examples of mouse tomographic images are presented in Fig. 5. For these images, the mouse was alive and held hung anesthetized on its carbon tube (seen on the left part of the horizontal slice in Fig. 5). Although images are still preliminary and can still be improved by corrections taking into account some defects of the detector such as the geometrical tile and gap effects, high absorption contrast can be seen between the air-filled lungs (dark) and the dense spine and rib bones (white) on the horizontal and coronal slices.

7. Geometrical parameters

Geometrical parameters are determined precisely using a 2 cm diameter cylinder with three small metal balls glued on its surface at known positions. Centers of the balls can be easily determined from the projections by fitting an ellipse on high contrast edges. The fitted position of the ellipses are then used to map the trajectories of the center of the spheres. These trajectories are finally used to determine the exact position of the detectors and of the source with regards to the rotation axis. This is done by

minimizing the residuals between the measured position and the estimated positions of the balls for each rotation angle, using the least mean square method. The resulting mean dispersion is about 10 μm.

8. Prospects

A new version of the PIXSCAN (named PIXSCAN-XPAD3) is under development with the aim to improve the spatial resolution and to make full body scans with a larger detector. To this, we have designed a new chip named XPAD3 [3] with pixels of $130 \times 130\,\mu m^2$, precise threshold adjustment, and very fast frame readout (<2 ms). Moreover, the XPAD3 has been equipped with an energy selection circuit to act as a band-pass emission filter. We expect this feature to be useful in the presence of iodinated contrast agents. Indeed, one would be able to select an energy window lower and higher than the iodine photoelectric absorption jump and, by image subtraction, to enhance the contrast of the regions containing iodine.

The size of the XPAD3 is $10 \times 17\,mm^2$. Modules of seven chips will be built on silicon and eight modules will be assembled to form a detector of $12 \times 7.5\,cm^2$. This XPAD3 detector will replace the XPAD2 to build the PIXSCAN-XPAD3. Moreover in this PIXSCAN, the photon detector and the source will rotate around the mouse support.

To improve the detection efficiency we will also build modules with CdTe, but they will be smaller due to the lack of large size CdTe wafers. Modules of two chips will be built and 3×4 modules will be assembled to form a $6 \times 6\,cm^2$ detector.

Beside the development of these XPAD3 detector, tests of simultaneous detection of X and γ- rays are done with the ClearPET demonstrator [4] and the XPAD2 detector, to study the feasibility of a simultaneous PET/CT for small animal imaging. CT image reconstruction in this non-conventional geometry is under study for this purpose [5].

References

[1] P. Delpierre, et al., IEEE Trans. Nucl. Sci. NS-49 (4) (2002) 1709.
[2] J.F. Bérar, et al., J. Appl. Crystallogr. 35 (2002) 471.
[3] P. Pangaud, et al., XPAD3: A new photon counting chip for X-ray CT-Scanner, presented at this conference.
[4] M. Rey, et al., Measured and simulated specifications of the Lausanne ClearPET scanner demonstrator, in Conferernce Record of the IEEE Medical Image San Juan, Puerto Rico, October 2005.
[5] S. Valton,Evaluation of tomographic reconstruction methods for small animal microCT and microPET/CT, presented at this conference.

PUBLISHED BY IOP PUBLISHING FOR SISSA
RECEIVED: *March 11, 2009*
REVISED: *March 12, 2009*
ACCEPTED: *May 7, 2009*
PUBLISHED: *May 19, 2009*

4th INTERNATIONAL CONFERENCE ON IMAGING TECHNOLOGIES IN BIOMEDICAL SCIENCES,
FROM MEDICAL IMAGES TO CLINICAL INFORMATION - BRIDGING THE GAP,
22–28 SEPTEMBER 2007,
MILOS ISLAND, GREECE

2009 JINST 4 P05012

Simulation of PIXSCAN, a photon counting micro-CT for small animal imaging

F. Cassol Brunner,[1] **R. Khoury, D. Benoit, C. Meessen, A. Bonissent and C. Morel**

Centre de Physique des Particules de Marseille (CPPM), CNRS-IN2P3 and Université de la Mediterranée Aix-Marseille II,
163 Avenue de Luminy, 13288 Marseille, France

E-mail: cassol@cppm.in2p3.fr

ABSTRACT: A main challenge in the development of new detectors is the achievement of a satisfactory comprehension of the instrument behaviour. We present the simulation work developed to understand and characterize an innovative micro-CT scanner. The PIXSCAN scanner is a photon counting device based on hybrid pixel detectors. Its working principle is expected to improve the contrast for soft tissues and to reduce both the scan duration and the dose absorbed by the animal. A prototype of the scanner, PIXSCAN-XPAD2, has been assembled and studied in order to achieve a proof of principle of the system. Simulations by analytical and Monte Carlo methods of the prototype and of the evaluation phantoms have been developed to ensure a satisfactory comprehension of the data. The Monte Carlo simulation was based on the GATE package. It included the complete simulation of photon propagation in matter, together with the modelling of the source spectrum, the scanner geometry and the sensor response. The analytical simulation is much more approximate, but its merit is the rapidity which permits fast preliminary results. Several figures of merit are studied and show good agreement with real data. Hence, the developed simulations can be used as a valid tool for the estimation of the ultimate PIXSCAN performances, in terms of spatial resolution, contrast measurement and dose reduction.

KEYWORDS: X-ray detectors; Models and simulations; Computerized Tomography (CT) and Computed Radiography (CR)

[1]Corresponding author.

doi:10.1088/1748-0221/4/05/P05012

Contents

2009 JINST 4 P05012

1 Introduction

The design of particle physics experiments and their data analysis make largely use of simulation software. This permits in fact to optimize the construction of detectors by reproducing all particle interactions in the sensors, and consequently the expected output signal.

Moreover the correct simulation of a system allows the unfolding of the different components that act on the detector response, hence providing a complete understanding of the data. This paper describes the simulations of PIXSCAN-XPAD2 [1], a micro-CT scanner for small animals. The good agreement between data and simulation validates the use of these tools for the design and data analysis of the next version of the scanner, PIXSCAN-XPAD3 [2].

2 PIXSCAN-XPAD2 scanner

The PIXSCAN-XPAD2 is a cone beam micro-CT scanner demonstrator for small animals. The system consists of a rotating platform placed between an X-ray source[1] and the photon detector. The mouse stands on the platform (fixed to a mouse holder), while the platform rotates 360°, step by step (typically, 1°/step). One X-ray cone beam projection of the object is acquired at each angle. The photon sensor is based on hybrid pixel detectors that were originally developed for high-energy physics experiments [3]. The sensitive surface is about $6.5 \times 6.8\,\mathrm{cm}^2$ and includes 8 modules tiled as shown in figure 1, for a total of 36,800 pixels of $330 \times 330\,\mu\mathrm{m}^2$. The whole set of projections

[1] 60 kV, 0.8 mA, 50 W, Mo target (Rontgentek, SEPH, France).

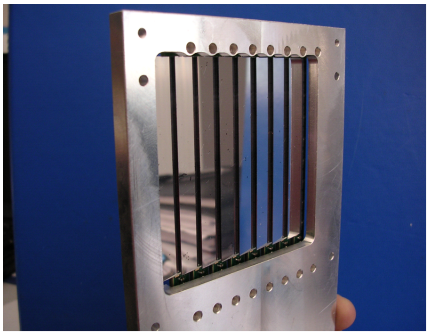

Figure 1. The XPAD2 detector.

needs to be numerically processed before reconstruction. The pixel response must be normalized. After geometrical calibration of the detector [4], the cone beam projection is mapped to a plane geometry, as required by the image reconstruction algorithm. Defective pixels are masked,[2] while a neighbouring pixel interpolation permits to fill the dead areas. Finally, a FDK-based reconstruction algorithm for cone beam tomography (supplied by CREATIS) is applied to reconstruct 3D images from the cone beam projections.

3 Scanner simulation

Two different simulation models were developed to reproduce the scanner data. A rather simple analytical model guarantees fast, but approximated results, whereas a Monte Carlo simulation, based on GATE [5], supplies a very accurate description of the system. Both simulations reproduce in detail the scanner geometry. Their output has a format that is identical to real data and follows the same numerical processing. Several evaluation phantoms of known geometry and material composition are simulated.

3.1 Analytical simulation

The model is based on the well known formula of propagation of photons in matter: $I = I_o \times e^{-\mu d}$. The intensity I of the beam measured by a pixel is defined by the initial beam intensity I_o, the attenuation coefficient μ of the material along the beam path, and the path length d. $e^{-\mu d}$ is determined by connecting the source to the center of each pixels and calculating the length of the ray in every phantom material. Statistical noise is added afterwards by introducing a Gaussian smearing to the pixel response, corresponding the typical scan statistics[3] of 6000 photons/pixel.

3.2 Monte Carlo simulation

The simulation is developed in the framework of the GATE package. X-rays are generated by a $50 \times 50\,\mu m^2$ square source, while reproducing the real source spectrum. All interaction processes

[2] The prototype chip XPAD2 has about $\sim 25\%$ of its pixels that are oscillating or non counting.

[3] The scan statistics is defined by the counts per pixel in absence of objects between the source and the detector.

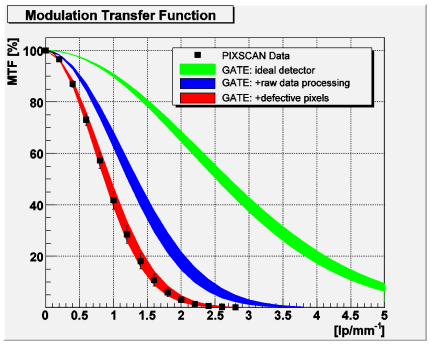

Figure 2. Modulation Transfer function study.

of photons and electrons in matter are modeled. As for real data, only photons that deposite more than 15 keV in the detector are counted. Due to the long simulation time, the statistics available for the Monte Carlo projections is limited to 3000 photons/pixel.

4 Data-simulation comparison

Several figures of merit are established to estimate the performance of PIXSCAN-XPAD2. This section presents the first results obtained from the scanner and their comparison with the simulation data.

4.1 Spatial resolution

The Modulation Transfer Function (MTF) and Line Spread Function (LSF) of the system are derived using the "edge method" procedure, as described in [6]. A half cylinder of PVC (12 mm radius) is used as phantom. The Full Width at Half Maximum (FWHM) of the LSF is assumed as index of the spatial resolution. A real data scan, in standard conditions, gives $\sim 500\,\mu$m. This value is well reproduced by both simulations, hence allowing to understand the resolution degradation factors. The simulation results show in fact that an ideal detector (not requiring raw data processing) guarantees a spatial resolution equal to the voxel size of the reconstructed image,[4] i.e. $\sim 165\,\mu$m; the present raw data processing (as applied to XPAD2 before reconstruction) degrades the resolution by more than a factor 2 to $\sim 350\,\mu$m. Finally the introduction of defective pixels (equivalent to an increase of dead areas) permits to reproduce correctly the XPAD2 measurements, which achieved a spatial resolution of $\sim 500\,\mu$m. Figure 2 shows the evolution of the MTF for the above described situations, as reproduced by the Monte Carlo simulation.

4.2 Detector noise

The same phantom as in 4.1 is used to estimate the image %Noise

$$\%Noise = \frac{\sigma_{\mathrm{PVC}}}{CT_{\mathrm{PVC}} - CT_{\mathrm{air}}}$$

[4]The image voxel size is half the detector pixel size due to the magnification fan beam effect of 2.

2009 JINST 4 P05012

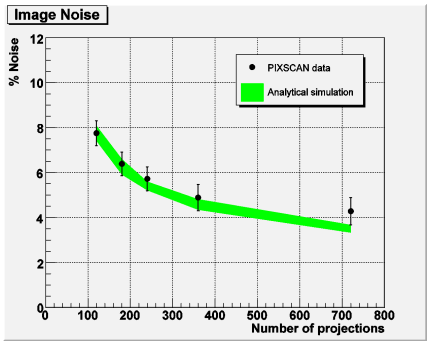

Figure 3. PIXSCAN-XPAD2 noise.

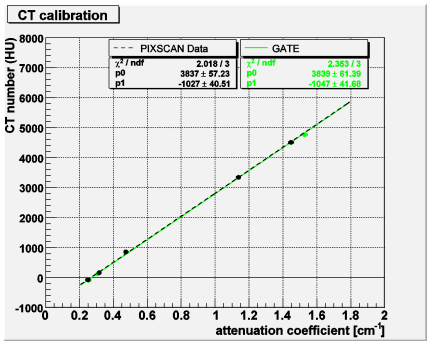

Figure 4. PIXSCAN calibration function.

with σ_{PVC} and CT_{PVC}, the mean and the standard deviation of the image CT values inside the PVC phantom, while CT_{air} is the average CT value in air. Both the analytical and Monte Carlo simulations reproduce correctly the measured data. Figure 3 shows, for example, the evolution of the noise versus the number of projections measured during a complete rotation of the scanner, compared to the analytical simulation results.

4.3 CT linearity

The linearity of the scanner is estimated using a phantom (QRM-MicroCT-HA) of epoxy resin having cylindrical inserts at various densities of calcium hydroxyapatite. Figure 4 shows the match between data and Monte Carlo simulation. The linear fit represents the scanner calibration function. It permits to associate an attenuation coefficient value to each grey level of the reconstructed image.

2009 JINST 4 P05012

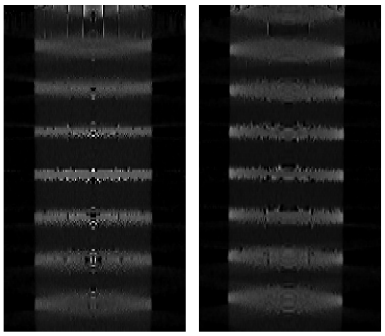

Figure 5. Tomographic image distortions: analytical simulation (left) and measured data (right).

4.4 Tomographic distortions

The back-projection FDK algorithm induces distortions in the image. They increase when moving away from the central plane perpendicular to the rotation axis and containing the source. A phantom after Defrise (QRM-MicroCT-MD) was imaged and simulated. Again, the simulations reproduce correctly the data, as shown in figure 5 in the case of the analytical model.

5 Prospects

The new version of the scanner, PIXSCAN-XPAD3, will be ready soon. This prototype has less then 1% defective pixels and the scanner aims at a spatial resolution of $\sim 70\,\mu$m. The analytical and Monte Carlo simulations described in this paper will be used to optimize and assess the new system design. Moreover, the knowledge acquired on the XPAD2 data will help us in developping the new data processing, with the aim to limit as much as possible the degradation of the spatial resolution.

Acknowledgments

This work was supported by the French National Agency for Research (ANR) under Grants Nos. ANR-05-CEXC-013 and ANR-06-CIS6-004-04.

References

[1] P. Delpierre et al., *PIXSCAN: Pixel detector CT-scanner for small animal imaging*, *Nucl. Instrum. Meth.* **A 571** (2007) 425.

[2] P. Pangaud et al., *XPAD3: a new photon counting chip for X-ray CT-scanner*, *Nucl. Instrum. Meth.* **A 571** (2007) 321.

[3] P. Delpierre et al., *Large surface X-ray Pixel detector*, *IEEE Trans. Nucl. Sci.* **49** (2002) 1709.

[4] R. Khoury et al., *A Geometrical Calibration Method for the PIXSCAN*, presented at 4^{th} *International Conference on Imaging Technologies in Biomedical Sciences*, Milos Island, Greece, September 22–28 2009.

[5] S. Jan et al., *GATE: a simulation toolkit for PET and SPECT*, *Phys. Med. Biol.* **49** (2004) 4543.

[6] M. Bentzen, *Evaluation of the spatial resolution of a CT scanner by direct analysis of the edge response function*, *Med. Phys.* **10** (1983) 579.

2009 JINST 4 P05012

IOP PUBLISHING PHYSICS IN MEDICINE AND BIOLOGY

Phys. Med. Biol. **54** (2009) 1773–1789 doi:10.1088/0031-9155/54/6/024

Imaging performance of the hybrid pixel detectors XPAD3-S

F Cassol Brunner, J C Clemens, C Hemmer and C Morel

Centre de Physique des Particules de Marseille (IN2P3-CNRS and Université de la Mediterannée), 13288 Marseille, France

E-mail: cassol@cppm.in2p3.fr

Received 29 August 2008, in final form 27 January 2009
Published 3 March 2009
Online at stacks.iop.org/PMB/54/1773

Abstract

Hybrid pixel detectors, originally developed for tracking particles in high-energy physics experiments, have recently been used in material sciences and macromolecular crystallography. Their capability to count single photons and to apply a threshold on the photon energy suggests that they could be optimal digital x-ray detectors in low energy beams such as for small animal computed tomography (CT). To investigate this issue, we have studied the imaging performance of photon counting hybrid pixel detectors based on the XPAD3-S chip. Two detectors are considered, connected either to a Si or to a CdTe sensor, the latter being of interest for its higher efficiency. Both a standard 'International Electrotechnical Commission' (IEC) mammography beam and a beam used for mouse CT results published in the literature are employed. The detector stability, linearity and noise are investigated as a function of the dose for several imaging exposures (∼0.1–400 μGy). The perfect linearity of both detectors is confirmed, but an increase in internal noise for counting statistics higher than ∼5000 photons has been found, corresponding to exposures above ∼110 μGy and ∼50 μGy for the Si and CdTe sensors, respectively. The noise power spectrum (NPS), the modulation transfer function (MTF) and the detective quantum efficiency (DQE) are then measured for two energy threshold configurations (5 keV and 18 keV) and three doses (∼3, 30 and 300 μGy), in order to obtain a complete estimation of the detector performances. In general, the CdTe sensor shows a clear superiority with a maximal DQE(0) of ∼1, thanks to its high efficiency (∼100%). The DQE of the Si sensor is more dependent on the radiation quality, due to the energy dependence of its efficiency its maximum is ∼0.4 with respect to the softer radiation. Finally, we compare the XPAD3-S DQE with published curves of other digital devices in a similar radiation condition. The XPAD3-S/CdTe detector appears to be the best with the highest DQE at low frequency, although

some improvements are expected to reduce the increase of noise with the counts statistics and to guarantee a better stability of the detector response.

(Some figures in this article are in colour only in the electronic version)

1. Introduction

Hybrid pixels represent a new generation of digital x-ray detectors for which photon counting replaces the energy integration of standard radiography systems (Mikulec 2003). The novel approach induces several advantages (Yorkston 2007), the extremely low noise and the possibility of setting an energy threshold for the detected photon being the most significant ones for medical imaging systems.

Several systems have recently been developed by research groups or companies, such as the Medipix collaboration[1] (Medipix 1, Medipix 2 and Medipix 3 detectors (Llopart *et al* 2001, Giersch 2005)), the Dectris Ltd[2] (Pilatus detector (Broennimann *et al* 2005)) and the Nova R&D Inc.[3] (DANA detector (Tumer *et al* 2006)). In this paper, we investigate the imaging performance of hybrid pixel x-ray detectors based on the XPAD3-S chip (Pangaud *et al* 2007) developed by the imXgam research group[4]. This chip is connected either to a 500 μm thick Si or to a 700 μm thick CdTe sensor. Single XPAD3-S chip prototypes have already been tested at synchrotron facilities (Pangaud *et al* 2008). They demonstrate high potential in material science and macro-crystallography experiments, thanks to their high maximum counting rate (2×10^6 photons pixel^{-1} s^{-1}), fast read out (2 ms frame^{-1}) and dynamic range (0.01–10^6 photons pixel^{-1} s^{-1}).

The challenges of x-ray computed tomography (CT) for *in vivo* mouse imaging applications (and radiological detectors in general) are however different, the dose reduction and the soft tissue contrast being the most difficult to achieve. It is believed that the reduced noise of single photon counting systems could supply optimal imaging performances in low dose small animal CT imaging. The possibility of setting an energy threshold for the detected photons could also permit the use of dual energy techniques with contrast agents (Le Duc *et al* 2000) or energy-resolved imaging (Shikhaliev 2008).

The stability, linearity and noise of the detectors are first investigated. Then, standard figures of merit, namely the noise power spectrum (NPS), the modulation transfer function (MTF) and the detective quantum efficiency (DQE) are measured under different exposure conditions and threshold settings. As far as possible, the standards defined by the International Electrotechnical Commission (IEC) are followed.

2. Materials and methods

2.1. Detectors

Two XPAD3-S circuits are used, connected either to a Si (XPAD3-S/Si) or to a CdTe sensor (XPAD3-S/CdTe). The sensor thicknesses are 500 and 700 μm, respectively. A detailed description of the XPAD3-S chip can be found in Pangaud *et al* (2008) and Basolo *et al*

[1] http://medipix.web.cern.ch.
[2] http://www.dectris.com.
[3] http://www.novarad.com.
[4] http://imxgam.in2p3.fr.

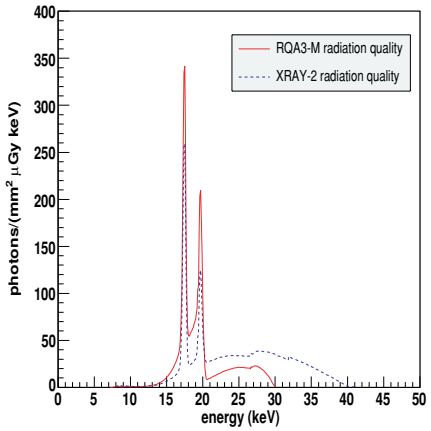

Figure 1. Spectra of the two considered radiation qualities, normalized to the estimated fluence (cf table 1).

(2008). Both detectors are composed of 9600 pixels with a 130 μm $\times$ 130 μm pixel pitch (Δ_{pix}), organized in a 80 $\times$ 120 matrix. The pixel energy threshold is alternatively set to $\sim$5 keV, which is the minimum usable threshold, or to $\sim$18 keV in correspondence with one of the source photoelectric peaks (cf 2.2). This last value is chosen in order to maximize the discrimination operated by the threshold on the spectrum and to verify its influence on the detector noise (NPS) and on the spatial resolution (MTF). Indeed, high thresholds are not interesting in standard imaging, due to the lost of detected photons, but they can be used in non-standard imaging techniques, such as dual energy techniques with contrast agents (Le Duc *et al* 2000) or energy-resolved imaging (Shikhaliev 2008). The chips are mounted on an evaluation board placed in front of the x-ray source, at about 14 cm from the source.

2.2. X-ray source

A wide cone beam aperture x-ray source with a molybdenum target and a 50 μm $\times$ 50 μm emission spot has been used (MCBM 65 B-50, RTW, Berlin, Germany). Two radiation qualities are considered: the standard IEC mammography beam RQA3-M (IEC 61267 2005), well suited for small animal imaging and perfectly adapted to our source, and a harder beam (here further called XRAY-2) that tries to be close to one of the x-ray qualities used by Goertzen *et al* in comparisons between several x-ray detectors for mouse CT imaging (Goertzen *et al* 2004). This radiation is produced to compare the XPAD3-S performance to other detectors in equivalent beam conditions. Table 1 summarizes the main characteristics of the two beams, as measured in this study. The source spectra (figure 1) have been acquired with an XR100T spectrometer (Amptek, Inc., Bedford, USA) corrected for the detector efficiency following the procedure described in Maeda *et al* (2005), with the support of a Monte Carlo simulation (cf section 2.3). The exposure at the detector surface is measured with the semiconductor detector DIADOS T60004 (PTW, Freiburg, Germany), placed close to the XPAD3-S position before any data taking and then removed. A correction is applied to take into account the

Table 1. Measured x-ray beam qualities (the tabulated values are given in brackets).

Quality	kV	Filter (mm)	HVL (mm Al)	Fluence (photons $mm^{-2}\mu Gy^{-1}$)
RQA3-M	30	0.03 Mo + 2 Al	0.64 (0.62[a])	5166 (5303[a])
XRAY-2	40	1.9 Al	0.85 (0.85[b])	6723 (6775[b])

[a] IEC 61267 (2005).
[b] Goertzen *et al* (2004).

Table 2. Estimated absorption detector efficiency.

Radiation quality	Detectors	
	XPAD3-S/Si	XPAD3-S/CdTe
RQA3-M	42%	98%
XRAY-2	27%	98%

slight difference in the distance from the source. A maximum error of 7% is estimated for the dose measurement. The photon fluence (table 1) on the detector surface (photons mm^{-2}) is obtained by the measured counting rate of the XPAD3-S/Si detector, corrected for the absorption efficiency (table 2), as estimated by the Monte Carlo simulation, and for the charge sharing effect as described in section 2.4. Finally, the half-value layer (HVL) of the beams is directly measured placing aluminum filters (minimal thickness of 100 μm) in front of the source shutter.

2.3. Monte Carlo simulation

A simple Monte Carlo simulation is developed in the framework of the GATE package (Jan *et al* 2004). X-rays are generated by a 50 μm × 50 μm square source, while reproducing the real source spectrum. All interaction processes of photons and electrons in matter are modeled. The chip is simply described by its sensor and, as for real data, only photons that deposit more than the threshold energy are counted. The modelization of charge sharing effect is not included.

2.4. Charge sharing correction

Hybrid pixel detectors are affected by charge sharing (Mathieson *et al* 2002). This effect influences not only the spatial resolution and the measured energy spectrum, but also the detector count rate. We estimate the charge sharing probability in the XPAD3S-Si detector, following the formulation proposed by Ponchut (2008) for the Medipix2 system. The measured spectrum, for an incident energy E_0, is the sum of an unsplit charge component $n_p(E, E_0)$ and of a charge sharing component $n_{cs}(E, E_0)$:

$$n(E, E_0) = (1 - k)n_{\mathrm{p}}(E, E_0) + kn_{\mathrm{cs}}(E, E_0). \quad (1)$$

For $n_{\mathrm{p}}(E, E_0)$ a Gaussian distribution is assumed with a width w (associated with energy dispersion due to the pixel noise), as a result $n_{\mathrm{cs}}(E, E_0)$ is constant and equal to $1/E_0$ for $E < E_0$, finally k represents the charge sharing probability. The XPAD3S-Si chip has been exposed to diffused monochromatic synchrotron beams of energy 14, 20 and 22 keV (ESRF

D2AM beam line). The integral of the energy spectrum is acquired changing the threshold $E_{\rm th}$ from the noise level, $E_{\rm N} \sim 5$ keV, up to the beam energy. The integral of equation (1) fits the data nicely and permits the estimation $k = 0.747$, an average over 100 pixels and three energies (0.745, 0.741 and 0.754 for the 14, 20 and 22 keV beams, respectively).

It is then possible to quantify the influence of the charge sharing on the pixel counts. We assume that the global chip efficiency is equal to the absorption efficiency if $E_{\rm th} = E_0/2$ (neither double counting nor photon losses are induced by charge sharing). For a given threshold, $E_{\rm th}$, the efficiency of the detector is then weighted by the term $1/(1 - \epsilon_{\rm cs})$, where

$$\epsilon_{cs}(E_0) = \frac{k}{E_0}(E_0/2 - E_{\rm th}). \tag{2}$$

In the case of the RQA3-M and XRAY-2 beams, the charge sharing induces 18% and 19% double counted photons for $E_{\rm th} = 5$ keV and loss of 28% and 22% measured photons for $E_{\rm th} = 18$ keV. The effective pixel efficiency corrected for the charge-sharing effect is given by the ratio of the absorption efficiency estimated by Monte Carlo and the charge-sharing correction $(1 - \epsilon_{\rm cs})$. The fluences estimated from the XPAD3-S/Si count rate by using this effective pixel efficiency are in good agreement with the tabulated values (table 1). Unfortunately, no monochromatic data are available for the XPAD3-S/CdTe detector.

2.5. Data correction

The inequalities in pixel normalization due to a slight dispersion of the pixel thresholds and the presence of defective pixels require a preliminary image correction. The chosen protocol respects the prescription given by standard IEC (IEC 62220-1-2 2007).

For each studied configuration a series of 100 frames ($F_k, k = 0, \ldots, 99$) is acquired. Because there were defective pixels in the border of the detector that were mainly related to damage occurring to the bump bonds during the manipulations, only the central part of the images (76×116 pixels for XPAD3-S/Si and 66×80 pixels for XPAD3-S/CdTe) is considered. The image resulting from the average of the 100 frames is taken as calibration reference (Cal). A pixel in the frame F_k at position (x, y) is tagged as defective if

$$\mathrm{Cal}(x, y) = 0 \qquad \text{dead pixel} \tag{3}$$

$$|\mathrm{Cal}(x, y) - \overline{\mathrm{Cal}}| > 4\sigma_{\rm Cal} \qquad \text{globally noisy pixel} \tag{4}$$

$$(F_k(x, y) - \overline{\mathrm{Cal}}) > 4\sigma_{\rm Cal} \qquad \text{locally noisy pixel,} \tag{5}$$

where $F_k(x, y)$ is the pixel content in the frame number k, while $\overline{\mathrm{Cal}}$ and $\sigma_{\rm Cal}$ are the mean and the sigma of a Gaussian fit of the calibration image Cal. The percentage of defective pixels in the selected part of the frame is ∼1% and ∼15% for the Si and CdTe sensors, respectively. In the case of the CdTe detector, a second-order polynomial fit, Pol(k), of the frame average counts versus the frame number k is also performed, in order to correct the images for a slight shift over time (cf section 3.1). Finally, the pixel normalization for a frame F_k is defined as

$$\mathrm{XPAD3-S/Si:} \quad N_k(x, y) = F_k(x, y)/\mathrm{Cal}(x, y) \cdot \overline{\mathrm{Cal}} \tag{6}$$

$$\mathrm{XPAD3-S/CdTe:} \quad N_k(x, y) = F_k(x, y)/\mathrm{Cal}(x, y) \cdot \overline{\mathrm{Cal}} - \mathrm{Pol}(k). \tag{7}$$

With the exception of the stability study, all presented results refer to images corrected as described above.

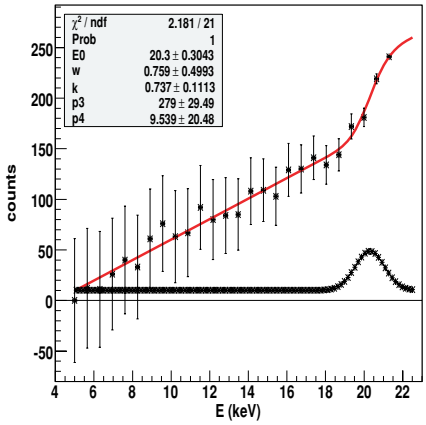

Figure 2. Integral of the energy spectrum as measured by one XPAD3-S/Si pixel for a monochromatic beam of energy $E_0 = 20$ keV. On the bottom, the derivative of the fitted curve represents the measured beam spectrum, as described by equation (1).

2.6. Detector stability, linearity and noise

The detector stability is studied by looking at the average pixel count as a function of the frame number, before any image correction. The average is obtained as the mean of a Gaussian fit of the count histogram, in order to neglect the effects of strongly defective pixels placed in the tails of the distribution.

The linearity and the noise of the detectors are also investigated. The XPAD3-S chip is expected to have a linear response as a function of the dose and, in the absence of external noise sources, a Poisson distribution of the counts. This behavior has been verified with two series of measurements.

(i) The dose is incremented by increasing the acquisition time from very short values (0.01 s) to times beyond any reasonable *in vivo* CT scan (50 s). The RQA3-M beam is used.
(ii) The dose is incremented by increasing the x-ray tube current from 12 μA to 700 μA, keeping a short acquisition time (0.5 s). The XRAY-2 beam is used.

The two sets of measurements permit the separation of the effects associated with the time from those linked to the count statistics. The considered doses span from the lowest interesting limit, $\sim$0.07 μGy, equivalent to a few counts per pixel, to maximal values acceptable in radiography, $\sim$400 μGy, equivalent to $\sim 10^4$ (10^5) counts per pixel for the Si (CdTe) sensor.

2.7. Modulation transfer function (MTF)

The MTF of the systems is estimated by the analysis of a sharp edge profile as proposed by several authors and demanded by the IEC standard (IEC 62220-1-2 2007). A 100 μm thick lead test device, embedded in 2 mm Plexiglas (Reinhold Funk, Erlangen, Germany), is fixed just in front of the detectors. The angle between the lead edge and the pixel matrix is kept in

the range 2°–3° and is measured by a coordinate measuring machine (Mitutoyo, Japan) with a precision of ∼0.1°. The edge spread function (ESF) is obtained by a projection of the pixel counts in the one-dimensional direction perpendicular to the edge. The procedure proposed by Flynn and Samei (1998) is followed for the edge analysis and the line spread function (LSF) derivation. The ESF is presampled in a sub-pixel spatial bin of width $\Delta s = 0.1\Delta_{\text{pix}}$. Each bin content, ESF_i, is then locally smoothed replacing its value with the result of a 4° polynomial fit centered on the bin i and extended over the window $[i-8, i+8]$. Each point inside the window is strongly weighted by a Gaussian function centered on $i = 0$ with $\sigma = \sqrt{8}$.

The LSF is then obtained by a $[-1, 0, 1]$ kernel differentiation of the ESF:

$$\text{LSF}_i = (\text{ESF}_{i+1} - \text{ESF}_{i-1})/2\Delta s. \tag{8}$$

A Hanning filter with a window width of $2.5\Delta_{\text{pix}}$ is then applied to smooth fluctuations in the tail of the LSF, not directly related to the edge response of the device. The numerical differentiation of the edge profile permits the derivation of a LSF that faithfully describes the spatial resolution of the pixels. Finally, the MTF is calculated as the fast Fourier transform of the LSF after a zero padding procedure that guarantees an oversampled MTF with frequency $f = 0.02/\Delta_{\text{pix}}$ mm^{-1}, as suggested by the IEC standard. For each configuration, 100 frames with the test device are acquired and the average of the 100 estimated MTF is considered as an index of the system spatial resolution.

2.8. Noise power spectrum (NPS)

The NPS is estimated on the base of flat-field images (no object between the source and the detector) acquired in each of the configurations. The frames are corrected as in equations (6) and (7). All identified defective pixels are replaced by a random value following a Poisson distribution with mean equal to the frame mean value ($\overline{N_k}$). The two-dimensional NPS is obtained from the corrected frames (N'_k) as

$$\text{NPS}_k(u, v) = \frac{|\text{FFT}(\delta_k(x, y))|^2}{NM}(\Delta_{\text{pix}})^2, \tag{9}$$

where u and v denote the spatial frequency along the horizontal and vertical axes, N and M correspond to the number of columns and rows in the frame, Δ_{pix} is the pixel size and FFT is the fast Fourier transform of $\delta_k(x, y)$, which represents the normalized variation of pixel (x, y) in frame N'_k

$$\delta_k(x, y) = \frac{N'_k(x, y) - \overline{N'_k}}{\overline{N'_k}}. \tag{10}$$

The one-dimensional $\text{NPS}_k(f)$ along the u-axis is obtained by averaging $\text{NPS}_k(u, v)$ such that $\sqrt{u^2 + v^2} \in [f - f_{\text{int}}, f + f_{\text{int}}]$, with $f_{\text{int}} = 0.01/\Delta_{\text{pix}}$ and $v \in [-7, 7]$, excluding the axis (IEC 62220-1-2 2007). Finally, a global $\text{NPS}(f)$ is estimated as average of the $\text{NPS}_k(f)$ obtained by the 100 flat acquisitions acquired for each configuration.

2.9. Detective quantum efficiency (DQE)

The DQE is defined as (Goertzen *et al* 2004)

$$\text{DQE}(f) = \frac{(\text{MTF}(f))^2}{K_a \times Q \times \text{NPS}(f)},$$

where K_a is the measured air kerma at the detector surface (in μGy) and Q is the photon fluence at the detector per unit exposure (in photons mm^{-2} μGy^{-1}). The estimation of Q has been performed on the base of the XPAD3-S counting rate corrected for the detector efficiency (cf section 2.2).

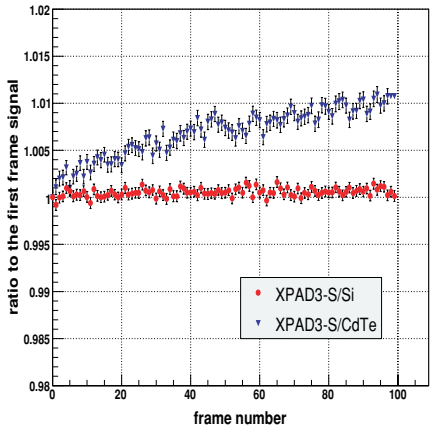

Figure 3. Count stability over 100 frames (RQA3-M beam, 5 keV threshold, 4 s frame^{-1}, 15′ total time acquisition).

3. Results

3.1. Detector stability, linearity and noise

The detector stability has been studied in several configurations. Figure 3 shows typical behavior in the case of a pixel threshold set at 5 keV. The Si sensor always presents a very stable response during the successive 100 frames, while the CdTe sensor has a global drift of the pixel counts of about 1%. This effect, already described in Basolo *et al* (2008), is under investigation and can easily be corrected as described in section 2.5. The effects of the data correction on the pixel count distribution are presented in figure 4, in the case of the Si sensor. Similar results are obtained for the CdTe sensor.

Both detectors present perfect linearity in the considered exposure range. This is shown in figures 5 and 6, where the linear fits also permit estimation of the efficiency ratios of the two sensors for both the radiations in consideration that are in fair agreement with the Monte Carlo simulations (cf table 2).

The most important feature of hybrid pixels is the single photon counting that, associated with the low electronics noise, can guarantee a high signal-to-noise ratio, especially at low count rates. In fact, for such detectors the noise must follow a Poisson statistics. Figures 7 and 8 show the root mean square versus the mean pixel count for the Si and CdTe detectors, respectively. The ideal Poisson behavior is given by the dashed line. Data from both the time increasing and the current increasing series are plotted (cf section 2.6). The dose scale on the top of the figures refers to the RQA3-M radiation (used for the time increasing series). For count numbers lower than ∼5000 photons pixel^{-1}, the detectors have a RMS perfectly compatible with the Poisson distribution down to very low exposures. For higher count numbers both detectors present an increase of the noise. This appears, in the case of the RQA3-M beam, at doses above ∼110 μGy for the Si sensor and above 50 μGy for the CdTe sensor, due to its

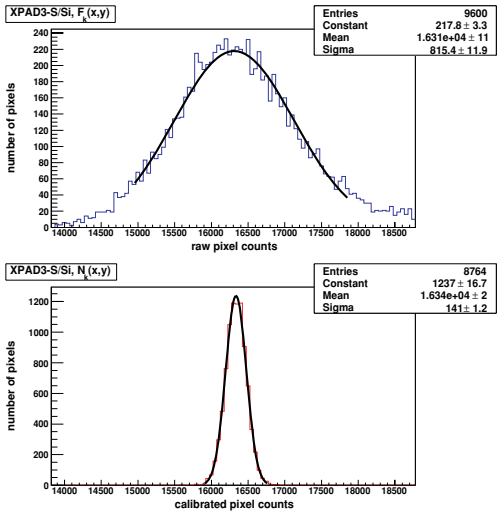

Figure 4. Effect of the data correction on the pixel count distribution in the case of a flat-field image taken with the RQA3-M beam and the Si sensor (326 μGy). Top image: before corrections. Bottom image: after corrections.

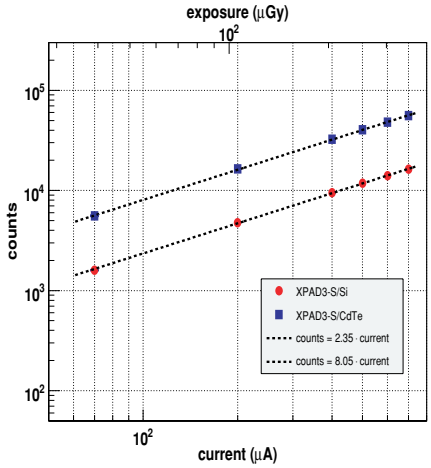

Figure 5. XPAD3-S linearity as a function of the source current (XRAY-2 beam quality).

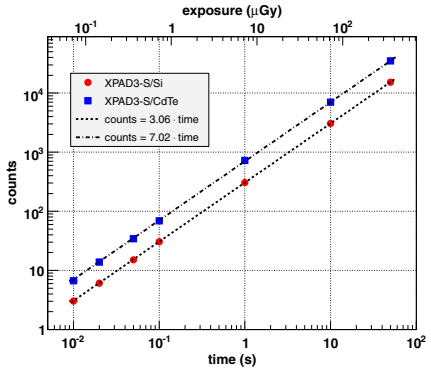

Figure 6. XPAD3-S linearity as a function of the acquisition time (RQA3-M beam quality).

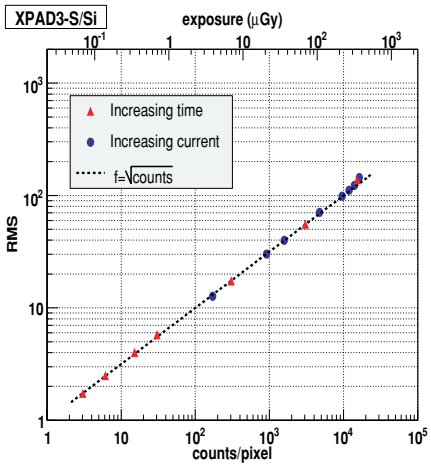

Figure 7. Root mean square versus pixel mean count of the XPAD3-S/Si detector. The pixel statistics is increased changing the acquisition time (red points) or the x-ray tube current (blue points).

higher efficiency. This noise increase is likely to be due to the slight difference in threshold adjustment from pixel to pixel that becomes the dominant source of pixel-to-pixel fluctuation at high count numbers (when Poisson noise becomes negligible). The XPAD3-S/CdTe detector presents also a certain dependence on the acquisition time since the two series of measurements give slightly different results (the (red) triangles of figure 8 follow a steeper curve than the

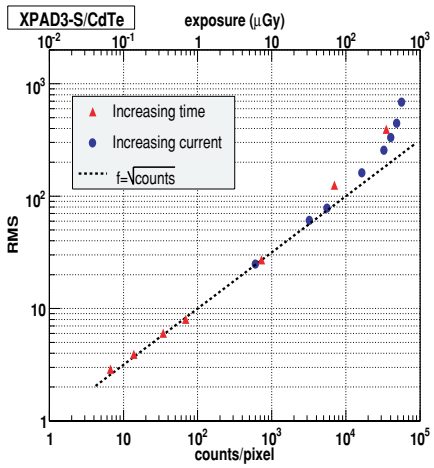

Figure 8. Root mean square versus pixel mean count of the XPAD3-S/CdTe detector. The pixel statistics is increased changing the acquisition time (red triangles) or the x-ray tube current (blue circles).

(blue) circles). This is probably associated with the instability of the CdTe sensor over time (cf 3.1).

3.2. MTF

The ESF is found to be independent of the sensor (Si or CdTe) and of the exposure. The edge shape is affected mostly by the pixel energy threshold as shown in figure 9 in the case of the CdTe sensor with the RQA3-M beam quality. In fact, at lower thresholds the charge sharing between neighboring pixels implies a larger ESF and a brighter LSF due to double counting of the photons incident near the pixel borders. Figure 10 compares the LSF measured corresponding to the two thresholds of 5 and 18 keV. The Gaussian form obtained at higher threshold is enlarged and deformed when a low threshold is set. This corresponds to an artificial increase of the pixel dimension. The spatial resolution, described by the MTF, is consequently deteriorated, as shown in figures 11 and 12 for the two detectors.

3.3. NPS

The results of section 3.1 about the detector noise are confirmed by the NPS curves. Figures 13 and 14 show the NPS of the detectors corresponding to the two threshold settings. The RQA3-M beam quality is used and three different doses are investigated by increasing the exposure time over two orders of magnitude, from 0.04 s per frame to 4 s per frame. In order to help in the comprehension of the noise quality, the NPS curves of an ideal detector are also plotted. They are obtained by the Monte Carlo simulation of images with Poisson counting statistics. For each different configuration, the mean value of the calibration image, $\overline{\mathrm{Cal}}$, is assumed as the mean of the ideal Poisson distribution. In general, the Poisson behavior of both

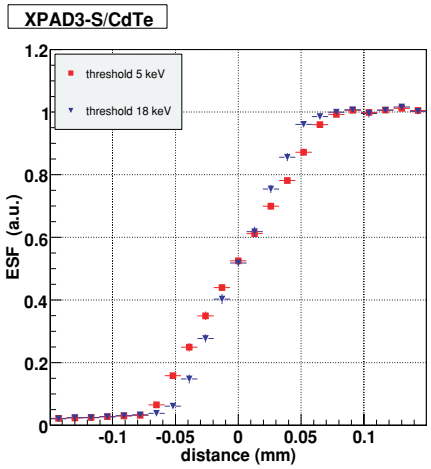

Figure 9. Smoothed ESF of XPAD3-S/CdTe and two threshold settings (RQA3-M beam quality).

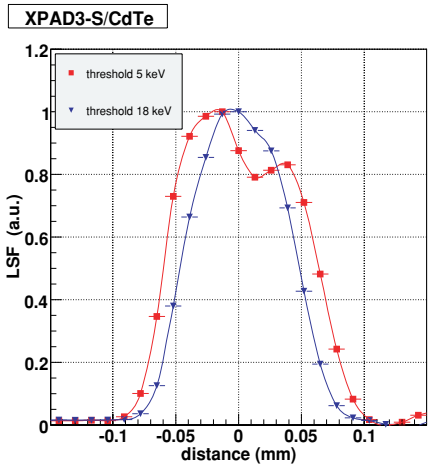

Figure 10. LSF of XPAD3-S/CdTe and two threshold settings (RQA3-M beam quality) .

detectors for doses under 50 μGy is confirmed. For longer exposures, an increase of the noise is observed, stronger at higher threshold. In this case, the CdTe sensor presents even visible count non-uniformities in the images that induce a NPS peaked at low frequencies (figure 14, right).

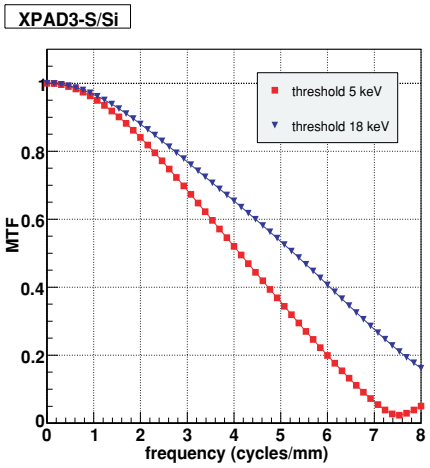

Figure 11. MTF of XPAD3-S/Si at two different pixel energy threshold settings (RQA3-M beam quality).

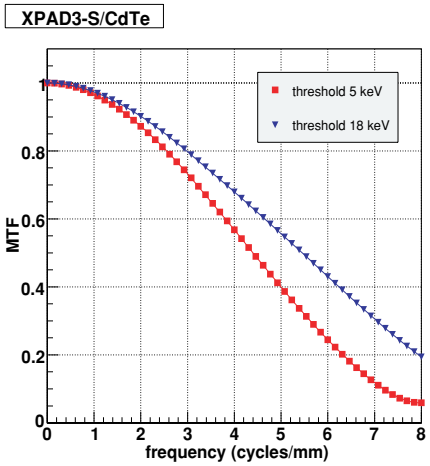

Figure 12. MTF of XPAD3-S/CdTe at two different pixel energy threshold settings (RQA3-M beam quality).

3.4. DQE

Because the MTF is very stable as a function of the exposure and of the radiation quality, the DQE of the XPAD3-S detectors is mostly influenced by their noise and detection efficiency.

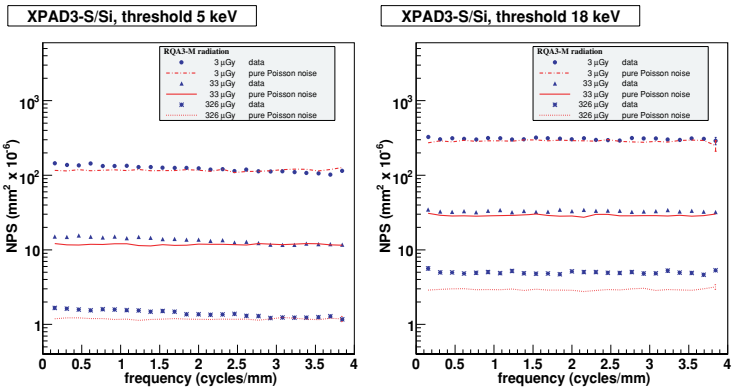

Figure 13. NPS of the XPAD3-S/Si detector with a pixel threshold at 5 keV (left) and at 18 keV (right).

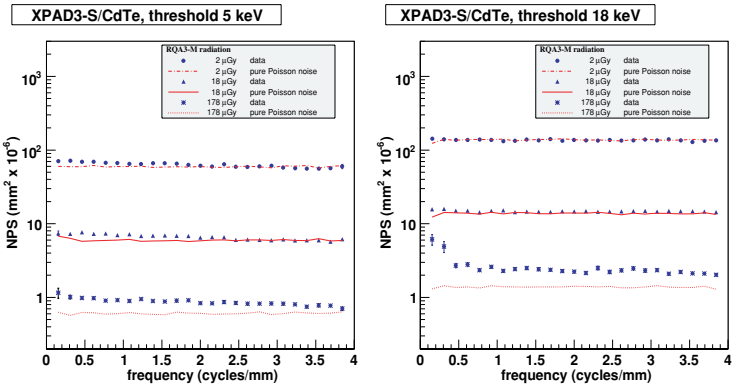

Figure 14. NPS of the XPAD3-S/CdTe detector with a pixel threshold at 5 keV (left) and at 18 keV (right).

Figure 15 compares the DQE of both detectors for the different exposures and threshold settings, in the case of the RQA3-M beam quality. The first striking point is the much higher DQE of the CdTe sensor, thanks to its higher efficiency. As expected, a degradation of the DQE is observed at higher exposures and more clearly for the CdTe sensor than for the Si sensor. The high threshold dramatically reduces the DQE due to the fall in efficiency. The maximum value of the DQE is obtained at low threshold and for reduced doses, where no additional noise is observed. Finally, we present a comparison between the DQE of the hybrid pixels

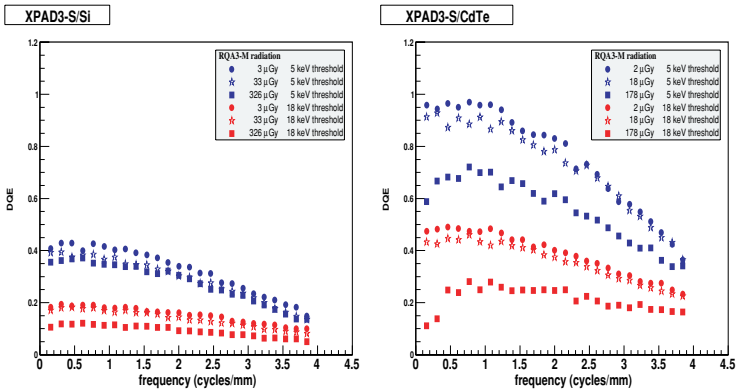

Figure 15. DQE of XPAD3-S/Si (left) and XPAD3-S/CdTe (right) for different exposures and threshold setting with the radiation quality RQA3-M.

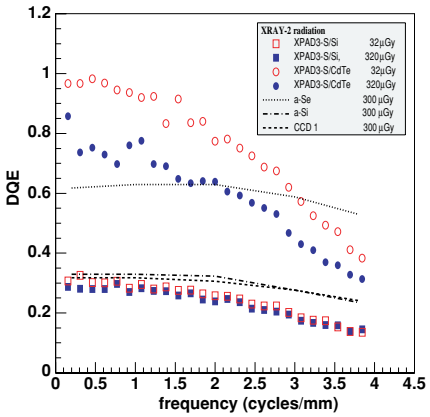

Figure 16. Comparison between the DQE of the XPAD3-S detectors and the detectors studied by Goertzen *et al* (2004) with similar radiation quality.

and the results published by Goertzen *et al* (2004) relative to an amorphous selenium detector (a-Se)[5], an amorphous silicon detector (a-Si)[6] and a CCD camera with a GOS scintillator screen (CCD)[7]. All devices are studied with a beam quality close to XRAY-2. Figure 16 shows the approximated curves of Goertzen *et al* (black lines) and those of the XPAD3-S

[5] Thermotrex Inc., San Diego, CA, 66 μm $\times$ 66 μm pixel size.
[6] Palo Alto Research Center. Palo Alto, CA, 75 μm $\times$ 75 μm pixel size.
[7] Dalsa Life Sciences, Tucson, AZ, 67.55 μm $\times$ 67.55 μm.

detectors for two different exposures (open and full points). The faster decrease of the DQE at higher frequency for XPAD3-S is normal and is related to the bigger pixel size. XPAD3-S/Si has a rather low DQE due to its reduced efficiency with this beam quality. XPAD3-S/CdTe presents a DQE similar to the a-Se detector for the higher exposure, but it is clearly better for a lower dose when the noise is controlled.

4. Conclusion

The imaging performance of a new generation of x-ray detectors has been investigated. Two XPAD3-S hybrid pixel devices have been studied for typical small animal CT radiations and exposures. Several figures of merit have been used for a detailed examination of the potentiality of these detectors in pre-clinical imaging. Both prototypes demonstrate an optimal noise suppression for count statistics under ∼5000 photons pixel^{-1}, corresponding to doses lower than ∼110 μGy and ∼50 μGy for the Si and CdTe sensors, respectively. Under these conditions, both devices work as ideal detectors with Poisson noise given by their counting efficiency. Moreover, the setting of the threshold on the detected photon energy does not affect the noise. This is very promising for the application of dual energy contrast techniques and for the improvement of lesion detectability at low contrast and/or low dose by the use of statistical tomographic reconstruction algorithms. The spatial resolution results are mainly limited by the pixel size and, secondarily, by the threshold setting. The MTF is in all cases greater than 0.6 at the Nyquist frequency given by the pixel dimensions (3.8 cycles mm^{-1}). Finally, the low noise guarantees an optimized DQE, with DQE(0) close to 1 for the CdTe sensor, better than several other x-ray detectors. The Si sensor appears to be less performing (DQE(0) $\leqslant$ 0.4), due to its limited detection efficiency at the chosen beam energies. An increase of the sensor thickness and/or a reduction of the beam HVL could however easily improve the DQE for this sensor.

A small animal CT demonstrator is actually under construction. It will be based on the XPAD3-S/Si detector with a global detection surface of 8 cm × 12 cm, corresponding to eight modules of seven chips tiled together (Chantepie *et al* 2008). The potentialities of hybrid pixel detectors for mouse CT imaging will be then directly tested on phantoms and mice in order to evaluate the ultimate benefits of this innovative technology for pre-clinical imaging.

Acknowledgments

This work was supported by the French National Agency for Research (ANR) under grant no ANR-05-CEXC-013. The authors would like to thank Jean-François Bérar and Nathalie Boudet for providing access to the D2AM beam line at ESRF and for their support. Finally, they would also like to thank all the members of the XPIX collaboration (CPPM, SOLEIL, D2AM-ESRF) involved with the development of the XPAD3 detector.

References

Allison J 2007 Geant4: a simulation toolkit *Nucl. Phys. News* **12** 20–4

Basolo S *et al* 2008 A 20 kpixels CdTe photon-counting imager using XPAD chip *Nucl. Instrum. Methods Phys. Res.* A **589** 268–74

Broennimann C *et al* 2005 The Pilatus 1M detector *J. Synchrotron Radiat.* **13** 120–30

Chantepie B *et al* 2008 The XPAD3 detector: a fast hybrid pixel detector for small animal x-ray imaging *Proc. Int. Conf. on Optical Complex Systems, OCS'08, Cannes* pp 107–8

Flynn M J and Samei E 1998 A method for measuring the presampled MTF of digital radiographic systems using and edge test device *Med. Phys.* **25** 102–13

Flynn M J and Samei E 1999 Experimental comparison of noise and resolution for 2k and 4k storage phosphor radiography systems *Med. Phys.* **26** 1612–23
Giersch J 2005 Medical quantum x-ray imaging with 2D detectors *Nucl. Instrum. Methods Phys. Res.* A **551** 125–38
Goertzen L *et al* 2004 A comparison of x-ray detectors for mouse CT imaging *Phys. Med. Biol.* **49** 5251–65
IEC 61267 2005 Medical diagnostic x-ray equipment—radiation conditions for use in the determination of characteristics p 85
IEC 62220-1-2 2007 Determination of the detective quantum efficiency—detectors used in mammography p 59
Jan S *et al* 2004 GATE: a simulation toolkit for PET and SPECT *Phys. Med. Biol.* **49** 4543–61
Le Duc G *et al* 2000 Feasibility of synchrotron radiation computed tomography on rats bearing glioma after iodine or gadolinium injection *Eur. Radiol.* **10** 1487–92
Llopart X *et al* 2001 Medipix2, a 64k pixel read out chip with 55 μm square elements working in single photon counting mode *IEEE Trans. Nucl. Sci.* **49** 2279–83
Maeda K *et al* 2005 Compton-scattering measurement of diagnostic x-ray spectrum using high-resolution Schottky CdTe detector *Med. Phys.* **32** 1542–7
Mathieson K *et al* 2002 Charge sharing in silicon pixel detectors *Nucl. Instrum. Methods Phys. Res.* A **487** 113–22
Mikulec B 2003 Development of segmented semiconductor arrays for quantum imaging *Nucl. Instrum. Methods Phys. Res.* A **510** 1–23
Pangaud P *et al* 2007 XPAD3: a new photon counting chip for x-ray CT scanner *Nucl. Instrum. Methods Phys. Res.* A **571** 321–4
Pangaud P *et al* 2008 XPAD3-S: a fast hybrid pixel readout chip for x-ray synchrotron facilities *Nucl. Instrum. Methods Phys. Res.* A **591** 159–62
Ponchut C 2008 Correction of the charge sharing in photon-counting pixel data *Nucl. Instrum. Methods Phys. Res.* A **591** 311–3
Shikhaliev P M 2008 Energy-resolved computed tomography: first experiment results *Phys. Med. Biol.* **53** 5595–613
Tumer T O *et al* 2006 High-resolution imaging 1D and 2D solid-state detector systems *Hard X-Ray and Gamma-Ray Detector Physics and Penetrating Radiation Systems VIII*; *Proc. SPIE* **6319** 63190
Yorkston J 2007 Recent developments in digital radiography detectors *Nucl. Instrum. Methods Phys. Res.* A **580** 974–85

Repeated Imaging of Lung Cancer Development Using PIXSCAN, a Low Dose Micro-CT Scanner Based on XPAD Hybrid Pixel Detectors

Franck Debarbieux, Alain Bonissent, Patrick Breugnon, Franca Cassol Brunner, Pierre A. Delpierre, Charles Hemmer, Jean-Claude Clémens, Bernard Dinkespiler, Jonathan Luchino, Fanny Mann, Christophe Meessen, Eric Vigeolas, Geneviève Rougon, and Christian Morel

***Abstract*—PIXSCAN is the first micro-CT prototype based on XPAD hybrid pixel detectors whose properties (high signal to noise ratio and detection efficiency) theoretically allow imaging at low irradiation dose. We have tested the impact of repeated imaging sessions with PIXSCAN on living mice. Mice were subjected on average to 10 imaging sessions over two weeks without any detectable sign of X-ray injuries as assessed by spontaneous activity in the cage, examination of hair and skin, or comparison of lung absorbing properties for X-rays.**

PIXSCAN was therefore used to detect and non-invasively monitor the progression of lung metastasis in a murine model of cancer. Aim was two-fold: i) to provide imaging assistance to decide timing of animal sacrifice for subsequent histological characterization; ii) to optimize imaging protocol to allow direct evaluation of new therapeutic agents to stop cancer progression.

Comparing in vivo tomographic reconstruction of freely breathing mice with post mortem examination of their lungs, we have shown that identification and localization of millimetric tumors was compatible with X-ray imaging protocol delivering only 10 mGy per exam.

***Index Terms*—Biomedical applications, dose rate effects, X-ray detectors, X-ray tomography.**

I. Introduction

ANIMAL models represent valuable tools to get insight into molecular mechanisms of human pathologies such as cancer. However, the medical imaging technologies that provide physicians with useful diagnosis and allow for the follow-up of cancer tumors have to be adapted to the tremendous change of scale of the rodents studied in preclinical research [1]. Cone-beam (CB) CT-scanners count among the most promising modalities for cancer research, as they are fast and easy to operate, relatively low cost, and resolutive in three dimensions [2]. Moreover, they can provide contrasted images of hypervascularized tumors when iodinated contrast agents are injected to highlight blood vessels [3]. Nevertheless, doses delivered to animals during exams represent a caveat for its wide use due to possible interference with biological phenomena of interest [4]. Concern is all the more relevant when dose is dramatically increased in the case of images with high spatial resolution and low level of noise in order to ease interpretation [5].

Whereas X-ray absorption is an intrinsic physical property of biological tissues, the dose delivery that is necessary to get an image can theoretically be lowered by improving the detection efficiency of the scanner. After Centre for Particle Physics of Marseille (C.P.P.M.) had built hybrid pixel detectors for the vertex trackers of the high energy physics experiments DELPHI and ATLAS at CERN [6], it developed the hybrid pixel detector XPAD2 dedicated to X-ray photon counting. The XPAD2 detector was integrated in PIXSCAN, a small animal CB CT-scanner demonstrator [7] built to evaluate the advantage of photon counting detection in the context of longitudinal *in vivo* experiments.

A murine model of cancer known to develop metastatic tumors in the lungs was used to qualify our imaging equipment. This model relied on intravenous injection of highly metastatic murine mammary tumor cells (4T1 cell line) into healthy BALB-c mice [8]. These cells then invaded mice lungs where they quickly proliferated and induced animal death. Due to inter-subject variability, it has been so far challenging to predict evolution of the disease for a given animal. The aim of our study was thus to provide imaging assistance to decide on the timing of either animal treatment or sacrifice for subsequent histological characterization.

We showed here that millimeter tumors can be successfully located in the lungs while delivering doses as low as $\sim$10 mGy in air, at least if using the XPAD2 photon counting detector. Tumor growth kinetics could thus be determined non-invasively.

II. The PIXSCAN CT-Scanner Demonstrator

We used a wide aperture cone beam, Molybdenum target, X-ray tube (60 kV, 30 W, 0.5 mA; RTW, Berlin, Germany)

Manuscript received January 28, 2009; revised August 18, 2009. Current version published February 10, 2010. This work was supported in part by the French National Agency for Research (ANR) under Grant ANR-05-CEXC-013 and by the Provence-Alpes-Côte d'Azur Regional Council.

F. Debarbieux is with the Institute for Developmental Biology of Marseille-Luminy, 13288 Marseille Cedex 9, France, the National Center for Scientific Research, 75794 Paris Cedex 16, France, the Centre for Particle Physics of Marseilles, Marseilles, France, the National Center for Scientific Research-IN2P3, 75016 Paris, France, and also with Aix-Marseille Université, France (e-mail: debarbieux@ibdml.univ-mrs.fr).

A. Bonissent, P. Breugnon, F. Cassol Brunner, P. A. Delpierre, C. Hemmer, J.-C. Clémens, B. Dinkespiler, C. Meessen, E. Vigeolas, and C. Morel are with Aix-Marseille Université, France, and also with the CNRS/IN2P3, 75016 Paris, France.

J. Luchino, F. Mann, and G. Rougon are with the Institute for Developmental Biology of Marseille-Luminy, 13288 Marseille Cedex 9, France, the National Center for Scientific Research, 75794 Paris Cedex 16, France, and also with Aix-Marseille Université, France.

Digital Object Identifier 10.1109/TNS.2009.2037319

whose spectrum was hardened by a 6 mm Aluminum filter. Detector consisted of a tiled assembly of 500 μm thick Silicon pixels bump bonded to XPAD2 circuits. XPAD2 detector had a detection surface of $6.5 \times 6.8\ \mathrm{cm}^2$ for a total of 36,800 pixels. In this configuration, 10,000 photons were counted on average per pixel for flat irradiation conditions (in absence of a mouse) after a 1.2 s exposition time. 360 projection images of mice were acquired every degree in about 15 minutes. Image reconstruction was then performed using modified FDK algorithms either home written or written by Créatis (RecFDK, INSA, Lyon). Given the pixel size of $330 \times 330\ \mu\mathrm{m}^2$ and a geometrical zoom factor of two, $200 \times 200 \times 200$ voxels of 165 μm were reconstructed. Images were then analyzed using either the ImageJ or Amide free software packages.

III. Characterization of Dose Rates

Two different approaches have been used to evaluate the air kerma: (1) by GATE Monte Carlo simulations [9] that were taking into account both the system geometry and the X-ray spectrum of the source; (2) by measurements of the dose rates using a dosimeter Diados (PTW, Freiburg, Germany). Whereas the simulations returned a dose rate of $301 \pm 4.5\ \mu\mathrm{Gy/s}$ at the impinging surface of the mouse, measurements were in agreement and pointed to a dose rate of $290 \pm 23\ \mu\mathrm{Gy/s}$. This indicates that the useful dose per exam remained below 125 mGy for statistics of the order of 10,000 counts per pixel, which is comparable to doses reported for other prototypes [10].

IV. Absence of Deletorious Effects After Repeated Imaging Sessions

Prior to longitudinal study of tumor development, we checked on a few mice $(n = 4)$ that 1–2 Gy cumulative dose ($\sim$10 imaging sessions) over two weeks was neither inducing detectable traumatic lesions in the lungs nor affecting significantly mouse health. Mice were active, did not loose weight and presented neither hair loss nor skin lesions two weeks after the initial imaging session. Moreover, we found no obvious changes of lung attenuating properties between the first and the 9th exam two weeks later (Fig. 1).

V. 3D Detection of Millimeter Lung Tumors

We next checked that both spatial and contrast resolutions of our imaging system were compatible with the localization of lung tumors for biological investigations. Twenty mice were injected intravenously with 4T1 cells [8] and separated into two groups: (1) mice $(n = 8)$ were imaged only once on day 30th after tumor cells injection and were immediately sacrificed for *ex vivo* examination of their lungs; (2) mice $(n = 12)$ were imaged repeatedly at 3–5 days intervals from the beginning of the third week until their lungs were collected for final *ex vivo* examination.

All mice were first diagnosed for tumors based on the tomographic reconstruction of their lungs. Six of our twenty mice were directly diagnosed positive for tumors based on the presence of millimetric compact masses (Figs. 2 and 4) which were absent at corresponding location in the lungs of healthy mice

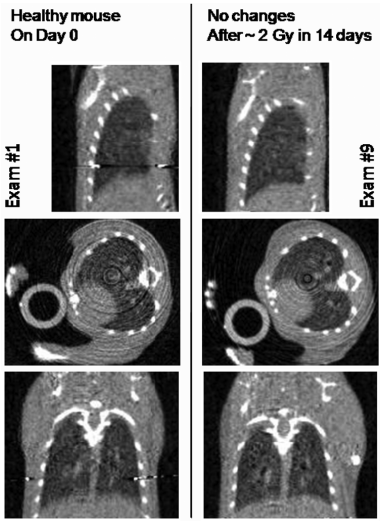

Fig. 1. Corresponding individual slices (thickness: 165 μm) from two image reconstructions of the same healthy mouse at 14 days interval. Between the presented scans, mouse was repeatedly imaged twice a week (in the conditions described in Section II) resulting in a $\sim$2 Gy cumulative dose. Note the absence of changes in lungs anatomy.

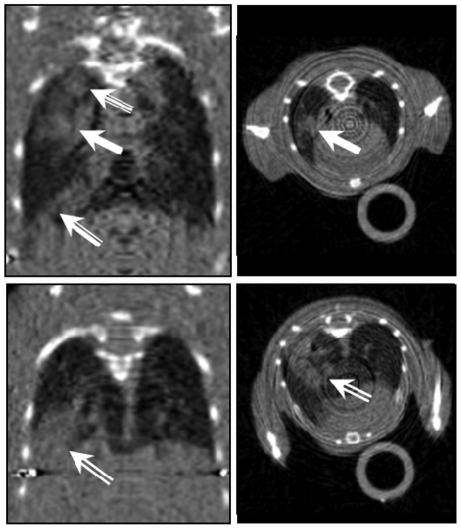

Fig. 2. Different views from the same image reconstruction of a mouse, 21 days after tail vein injection of 4T1 cells. White arrows point to lung tumor masses which were later identified post-mortem on the fixed lungs presented in Fig. 3. Plain arrow locates a tumor at the ventral part of the right middle lobe while double stranded arrow points to a tumor mass at the dorsal part of the right lower lobe.

(Fig. 1). Millimetric size was chosen as a criterium to avoid false positive due to insufficient signal to noise ratio in images.

This first diagnosis was then challenged by an ex-vivo examination of mice lungs. We actually found that only 50% of

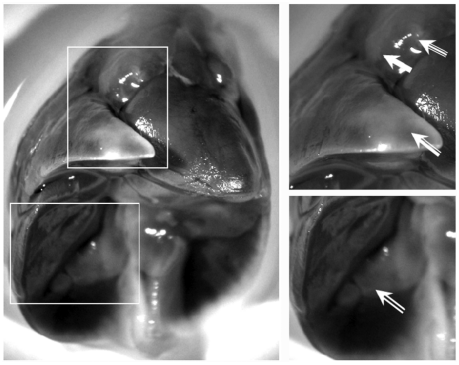

Fig. 3. Lungs whose image reconstruction is presented in Fig. 2 were dissected immediately at the end of X-ray scan and fixed with paraformaldehyde 4%. Tumors were identified as dense bulbous white masses under binocular microscope. Zooms of the regions outlined by white square son the left image are presented on the right panel. Tumors are pointed to with the same arrow types as the ones used in Fig. 2.

group 1 and 67% of group 2 of the mice developed visible tumors on the external surface of their lungs one month after 4T1 cells injection. This result thus points out the need for dedicated imaging protocols in order to assess cancer progression prior to mouse sacrifice because of the large inter-subject variability of metastasis development. As irradiated mice were if at all slightly more prone to develop lung metastasis than the control population of mice, we could rule out a possible impediment of tumors development due to cumulative dose delivery over repeated imaging sessions [4].

In half of the mice ($n = 6$ out of 12) whose lungs turned out to be visibly invaded by superficial tumors after post-mortem inspection, we could clearly identify and locate internal lung tumor masses from image reconstructions (Fig. 2). In some cases, these tumors were sufficiently large to have a superficial extension that allowed their *ex vivo* identification at the surface of the lungs (Fig. 3). Although we could not convincingly identify tumors in the image reconstructions of the remaining mice ($n = 6$), it must be noted that only few tumors (1 or 2) were finally observed at the surface of the corresponding lungs. Moreover, the size of these tumors did not exceed a few hundreds of microns, which probably challenged the spatial resolution of our current XPAD detector.

Our demonstrator nevertheless remained of great use to identify mice with numerous millimeter tumors in the lungs. Actually, such criteria are required for assessing statistically, and hence conclusively, the efficiency of anti-metastatic pharmacological treatments.

VI. Detection of Tumors at Very Low Dose

Mice, for which millimetric lung tumors were successfully identified in the tomographic reconstruction acquired in our standard conditions, were then imaged a second time using six-fold shorter exposure times per projection (200 ms versus 1.2 s). We indeed observed some increase of the noise in the reconstructed images due to reduced statistics (1,200 photons counted per pixel in flat images instead of 10,000 photons).

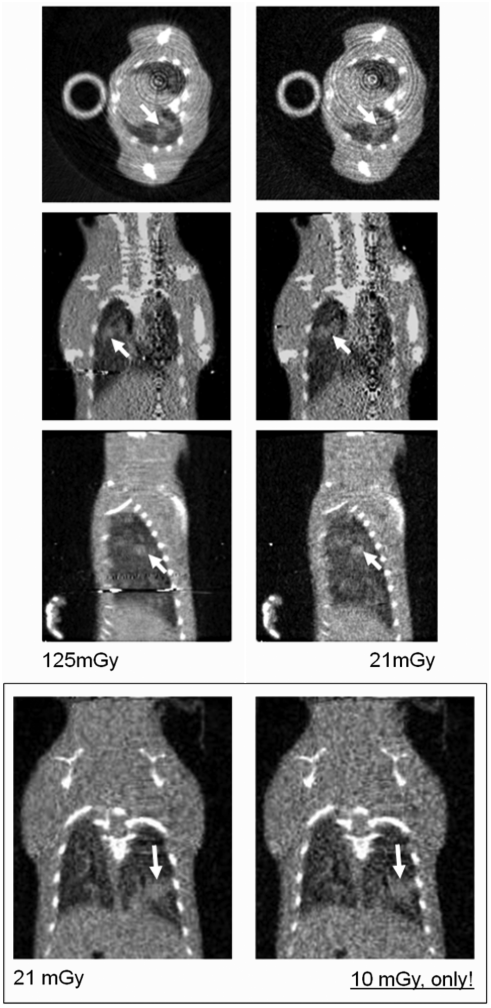

Fig. 4. Examples of lung tumor detection at low dose. (Top panel) Lungs of a mouse were reconstructed from two different sets of 360 projection images, 28 days post-injection of 4T1 cells: Projection images were acquired with exposure times of either 1.2 s or 200 ms per projection resulting in a total dose of 125 and 21 mGy respectively. Arrows point on the same tumors identified on the three different views. (Bottom panel) Lungs of another mouse 21 days post-injection were reconstructed from projections acquired with 200 ms or 100 ms exposure times. Tumor mass (arrow) can be successfully located even with the shortest exposure time, resulting in an only 10 mGy dose for full scan. Presented images are averages over 4 slices (total thickness: 660 μm).

Nevertheless, we were still able to locate all their tumors in reconstructions acquired with doses of 21 mGy instead of 125 mGy (Fig. 4, top).

Impressively, we finally obtained similarly good results with exposure times of 100 ms instead of 200 ms (Fig. 4, bottom). Altogether, these observations indicate that 600 photons per $330 \times 330\,\mu\mathrm{m}^2$ pixel are sufficient to establish meaningful reconstructions of mice lungs and to detect millimetric lung tumors. The

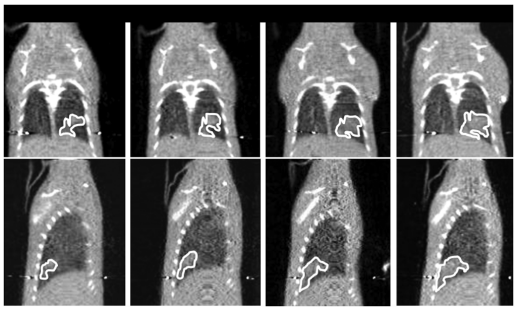

Fig. 5. Monitoring of the tumor mass expansion from repeated imaging sessions every 3–4 days from the second week post-injection (D14 to D24). Selected coronal and sagittal sections from tomographic reconstructions of the same mouse to show evolution of its lung tumor. Tumor maximal section has been outlined manually using a thin white line.

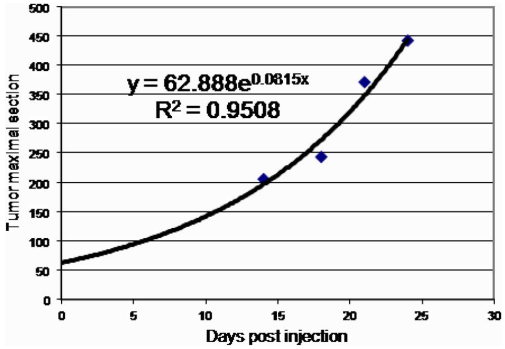

Fig. 6. Area of the maximal section (arbitrary units) for the tumor presented in Fig. 5 was plotted as a function of days after intravenous injection of 4T1 cells. The plot was then nicely fitted by an exponential curve.

corresponding 10 mGy dose delivered per exam then lies 10 to 20 folds lower than the one delivered by regular commercial microCT-scanner and is among the lowest ever reported to date [10].

VII. Monitoring Non Invasively the Time Course of Lung Tumor Development

Growth kinetics of a given lung tumor could be established from repeated low dose imaging sessions with the PIXSCAN demonstrator.

The same tumor mass was identified again on successive reconstructions acquired at 3 to 4 days intervals (Fig. 5). The largest contour of the tumor was manually delimited for every imaging session. Surfaces of these regions of interest were then plotted as a function of time.

Interestingly enough, evolution of the maximum tumor section was reasonably well fitted by an exponential model (correlation coefficient $R^2 = 0.95$, Fig. 6).

Such exponential growth, which resulted in a doubling of the tumor volume within a week, might therefore explain the accelerated countdown to death that is observed once millimeter tumors are formed in the lungs.

VIII. Conclusions and Prospects

We presented a direct biological application for the first CB CT-scanner demonstrator based on hybrid pixel detectors. Reconstructed images are of similar quality to the one published for CB CT-scanners based on charge integration detectors. Nevertheless, we presented evidence that the dose used to obtaining these images could be reduced to levels that were so far unreported. We finally established the number of photons that were required to perform meaningful image reconstructions of mice lungs.

In its current status, the PIXSCAN demonstrator already proved its usefulness for research in biology. However, coming developments are likely to make it even more attractive. A second generation of the PIXSCAN demonstrator will integrate the new XPAD3 detector [11]. This latter has hybrid pixels of 130 μm, which makes it possible for improving spatial resolution by a factor 3. Sub-millimeter tumor detection should therefore not represent a challenge anymore. Moreover, the main advantage of hybrid pixel detectors relies on their ability to optimize their sensor efficiency with regards to the energy of the X-rays. The XPAD3 circuit will also be bump bonded with pixellated CdTe sensors [12] thus allowing for further reducing the dose necessary to obtain meaningful images.

References

[1] R. Weissleder, "Scaling down imaging: Molecular mapping of cancer in mice," *Nature Rev. Cancer*, vol. 2, no. 1, pp. 11–18, 2002.
[2] N. Beckmann *et al.*, "In vivo mouse imaging and spectroscopy in drug discovery," *NMR Biomed.*, vol. 20, no. 3, pp. 154–185, 2007.
[3] F. Kiessling *et al.*, "Volumetric computed tomography (VCT): A new technology for noninvasive, high-resolution monitoring of tumor angiogenesis," *Nature Med.*, vol. 10, no. 10, pp. 1133–1138, 2004.
[4] N. A. Scott *et al.*, "Inhibition of vascular cell growth by X-ray irradiation: Comparison with gamma radiation and mechanism of action," *Int. J. Radiat. Oncol. Biol. Phys.*, vol. 50, no. 2, pp. 485–493, 2001.
[5] N. L. Ford *et al.*, "Fundamental image quality limits for microcomputed tomography in small animals," *Med. Phys.*, vol. 30, no. 11, pp. 2869–2877, 2003.
[6] P. Delpierre *et al.*, "Large scale pixel for DELPHI at LEP 200 and ATLAS at LHC," *Nucl. Instrum. Methods Phys. Res. A*, vol. A342, pp. 233–239, 1994.
[7] P. Delpierre *et al.*, "PIXSCAN: Pixel detector CT-scanner for small animal imaging," *Nucl. Instrum. Methods Phys. Res. A*, vol. A571, pp. 425–428, 2007.
[8] D. L. Dexter *et al.*, "Heterogeneity of tumor cells from a single mouse mammary tumor," *Cancer Res.*, vol. 38, pp. 3174–3181, 1978.
[9] S. Jan *et al.*, "GATE: A simulation toolkit for PET and SPECT," *Phys. Med. Biol.*, vol. 49, no. 19, pp. 4543–4561, 2004.
[10] S. K. Carlson *et al.*, "Small animal absorbed radiation dose from serial micro-computed tomography imaging," *Mol. Imag. Biol.*, vol. 9, no. 2, pp. 78–82, 2007.
[11] P. Pangaud *et al.*, "XPAD3-S: A fast hybrid pixel readout chip for X-ray synchrotron facilities," *Nucl. Instrum. Methods Phys. Res. A*, vol. A591, pp. 159–162, 2008.
[12] J.-C. Clémens *et al.*, "A 20 kpixels CdTe photon-counting imager using XPAD chip," *Nucl. Instrum. Methods Phys. Res. A*, vol. A589, pp. 268–274, 2008.

Imaging neutron beams with hybrid pixels detectors

Franca Cassol Brunner and Christian Morel

January 5, 2009

Abstract

We present a project aiming at testing and optimizing the use of hybrid pixel detectors for high resolution imaging in neutron radiography and tomography. The project will be carried out within a collaboration between the group imXgam of the Centre for Particle Physics of Marseilles, led by Prof. C. Morel, and the Imaging Group of the Helmholtz Zentrum Berlin (HZB), led by Prof. J. Banhart.

1 Introduction

The interdisciplinary group imXgam [1] is developing X-ray imaging detectors based on hybrid pixel detectors [2]. Originally created for tracking particles in high energy physics experiments, hybrid pixels have recently been used in material sciences and macromolecular crystallography. Moreover, their capability to count single photons and to apply a threshold on the photon energy suggests that they can form optimal digital detectors for low energy X-ray beams as used for small animal computed tomography (CT). The group has developed pixels based on the XPAD chip [3] and several results have already been presented on its use as an X-ray imaging device [4]-[6]. Further projects are carried out on definitively test its performance both for material sciences [7] and for pre-clinical imaging [8].
Recently, neutron transmission tomography (NT) has become more and more used as a complementary technique to X-ray tomography. It permits in fact to accessing material properties that cannot be obtained by X-ray imaging, due to the difference of neutron and X-ray interaction in matter. NT can preferably be applied in cases where thick layers of a heavy material have to be transmitted and small amount of light elements like hydrogen, boron, have to be detected. The characteristics of XPAD, as its pixel dimension, dynamic range and readout speed, will permit to qualify it as a

possible performing neutron imaging detector. In particular, the readout speed (< 2 ms/frame) will represent an optimal feature for dynamic studies as those performed by the HZB group (cf. 2.3). A preliminary condition will be the identification of a neutron converter to be added to the XPAD sensor. It must have a high neutron cross-section and convert neutrons into particles easily detectable by the hybrid pixel typical sensor (Si, CdTe).
The goal of the project is the identification of an optimized converter, the characterization of the XPAD chip in a neutron beam and its first application in neutron imaging.

2 Project development

2.1 Converter identification

In order to detect cold or thermal neutrons (E=25 meV or less) with hybrid pixels it is necessary to identify a neutron converter that optimizes the neutron detection without deteriorating the spatial resolution. Two possible ways are at the moment taken into consideration.

2.1.1 Passive converter

The most simple solution is the deposition of a converter layer on the sensor surface: the chip will thus detect charge particles or photons produced by the neutron interaction. First studies have already been done with hybrid pixel chips (Medipix Collaboration [9]) as well as with pin diode semiconductor detectors [10]. Tests on the Medipix chips with commonly used neutron converter materials (^6Li,^{10}B,^{113}Cd,^{155}Gd and ^{157}Gd) have demonstrated that the most suitable converter is ^6LiF. The $^6Li(n,t)^4He$ reaction produces a 2.73 MeV tritium and a 2.05 MeV alpha particle ejected on opposite direction with higher energies than for the other reactions and therefore a higher probability to be detected by the Si/CdTe sensor. Moreover, neither gamma nor conversion electrons are produced. These latter particles degrade substantially the spatial resolution since they can migrate from one pixel to the other [11]. Measurements and Monte Carlo studies demonstrate that the maximal efficiency is reached with a layer thickness of ~ 6 mg/cm^2 and does not exceed 4%. In order to increase this value, it is necessary to optimize the contact between the converter and the sensor to maximizing the passage of alpha and tritium particles down to the sensor. We think this can be realized by an optimized perforation of the silicon. The holes and the de-

tector surface will then be filled with the converter material. Semiconductor diode detectors have already proven an improvement of the efficiency up to values of 30% [12]. This is also suggested by Monte Carlo simulations of hybrid pixels [13]. This number is close to the efficiency of common scintillator converters used in CDD neutron imaging systems.

2.1.2 Active converter

Recent experiments indicate that micro-channel plates (MCPs) could be an attractive alternative solution as neutron converter [14]. Standard MCPs are basically glass disks (~ 1 mm thick) with densely packed cylindrical pores of $5 - 10$ μm in diameter. The MCP glass can be doped with neutron absorbing atoms (^{10}B) in order to be neutron sensitive. The charge particles produced by the neutron interaction induce an electron cascade inside one or two pores. It is estimated that MCPs can reach an efficiency for neutron detection better than 60% and convert a single neutron to a ~ 1 ns wide pulse of $10^4 - 10^7$ electrons preserving the location of the neutron absorption within $10 - 15$ μm. When coupled to a hybrid pixel sensor they could guarantee high rate neutron detection and an exceptionally fast readout.

2.2 Detector characterization

The plan is to test both converter types, possibly in collaboration with authors that already developed some experience with them. Three XPAD3 chips with readout system will be dedicated to the project. Preliminary Monte Carlo studies will be performed by the imXgam group and beam tests will take place at the research nuclear reactor of the HZB h. The principal figures of merit to be estimated are: the detector efficiency, the spatial resolution (modulation transfer function), the noise (noise power spectrum) and the global readout speed.

2.3 Direct applications

The customized chips could be directly tested in several applications developed by the HZB group that require high speed readout with possibly external triggers.

2.3.1 Investigation of fuel cells by neutron radiography [15]

The water management in PEM fuel cells is a key point for the optimization of their performance. The real-time imaging of an operating fuel cell provides information about the dynamics of electro-chemical processes in the cell. The detectors nowadays available for real-time imaging (e.g. CMOS cameras) have high signal-to-noise ratio at fast readout speed. On the other hand the detectors with very low electronic noise (e.g. CCD cameras) have low readout speed of few seconds which makes them unsuitable for observation of dynamic processes. A new detector type will allow for faster readout speed at low noise levels.

2.3.2 Stroboscopic imaging [16]

Dynamic processes in combustion engines can be investigated by stroboscopic technique. For this, the detector should be synchronized with the engine by a trigger signal that is sent at a defined position of the piston (crankshaft). Single shoots are accumulated for a defined state and an average image with a good statistics is obtained. By shifting the trigger pulse, a new measuring time interval can be defined.

2.3.3 High-speed tomography [17]

This new type of detector will allow for high-speed neutron tomography of dynamic systems. The fast readout and low noise of the detector are preconditions for collecting projections in short times at high intensive neutron beam.

2.3.4 Time-of-flight neutron imaging [18]

The use of pulsed source for imaging requires a new type of detector, which can be triggered by narrow gates. The beam can be chopped in such a way way that at a certain distance a narrow spectral interval can be selected by the proper triggering of the detector. The method can be used for energy-selective imaging.

References

[1] imXgam group home page:
http://imxgam.in2p3.fr

[2] Rossi L *et al.*, Pixel Detectors (Springer).

[3] Delpierre P *et al.*, XPAD: A photon counting pixels detector for material sciences and small animal imaging, *Nucl. Instrum. and Methods* A **572** (2007) 250-254.

[4] Cassol Brunner F *et al.*, Measured Imaging Performance of Photon Counting Hybrid Pixel X-Ray Detectors, in Conf. Rec. of "2008 IEEE Med. Imag. Conf.", Dresden, Germany, Oct. 2008, in Press.

[5] Pangaud P *et al.*, XPAD3-S: A fast hybrid pixel readout chip for X-ray synchrotron facilities, *Nucl. Instrum. and Methods* A **591** (2008) 159-162.

[6] Debarbieux F *et al.*, Repeated imaging of lung cancer development using PIXSCAN, a low dose micro-CT scanner based on XPAD hybrid pixel detectors, in Conf. Rec. of "2008 IEEE Med. Imag. Conf.", Dresden, Germany, Oct. 2008, in Press.

[7] Bérar J-F *et al.*, XPAD3, an Hybrid Pixel Detector for Scattering Applications Using Synchrotron Sources, in Conf. Rec. of "2008 IEEE Med. Imag. Conf.", Dresden, Germany, Oct. 2008, in Press.

[8] Chantepie B *et al.*, The XPAD3 detector: a fast hybrid pixel detector for small animal X-ray imaging *Proc. Int. Conf. on Optical Complex Systems (Cannes)* (2008) 107-108.

[9] Medipix collaboration home page:
http://medipix.web.cern.ch/MEDIPIX

[10] McNeil W J *et al.* , Perforated diode fabrication for neutron detection, in Conf. Rec. of "2008 IEEE Med. Imag. Conf.", San Diego, Oct. 2006, 3732-3735.

[11] Jakubek J *et al.*, Neutron imaging with Medipix-2 chip and a coated sensor, *Nucl. Instrum. and Methods* A **560** (2005) 143-147.

[12] McGregor D S *et al.*, Perforated semiconductor neutron modules for detection of spontaneous fission neutrons, in Conf. Rec. of "2008 IEEE Med. Imag. Conf.", Dresden, Germany, Oct. 2008, in Press.

[13] Uher J *et al.*, Characterization of 3D thermal neutron semiconductor detectors, *Nucl. Instrum. and Methods* A **576** (2007) 32-37.

[14] Tremsin A S *et al.*, On the possibility to image thermal and cold neutron with sub-15 μm spatial resolution, *Nucl. Instrum. and Methods* A **592** (2008) 374-384.

[15] Hartnig C*et al.*, Combined neutron radiography and locally resolved current density measurements of operating PEM fuel cells, *Journal of Power Sources* **176** (2008) 452-459.

[16] Schillinger B *et al.*, Detection systems for short-time stroboscopic neutron imaging and measurement on a rotating engine , *Nucl. Instrum. and Methods* A **542** (2005) 142-147.

[17] Dierick *et al.*, High-speed neutron tomography of dynamic processes, *Nucl. Instrum. and Methods* A **542** (2005) 296-301.

[18] Kockelmann W *et al.*, Energy-selective neutron transmission imaging at a pulsed source, *Nucl. Instrum. and Methods* A **578** (2007) 421-434.

IOP PUBLISHING PHYSICS IN MEDICINE AND BIOLOGY

Phys. Med. Biol. **56** (2011) 881–901 doi:10.1088/0031-9155/56/4/001

GATE V6: a major enhancement of the GATE simulation platform enabling modelling of CT and radiotherapy

S Jan[1], D Benoit[2], E Becheva[1], T Carlier[3,4], F Cassol[5], P Descourt[6], T Frisson[7], L Grevillot[7], L Guigues[7], L Maigne[8], C Morel[5], Y Perrot[8], N Rehfeld[2], D Sarrut[7], D R Schaart[9], S Stute[2], U Pietrzyk[10], D Visvikis[6], N Zahra[7] and I Buvat[2]

[1] DSV/I2BM/SHFJ, Commissariat à l'Energie Atomique, Orsay, France
[2] IMNC–UMR 8165 CNRS–Paris 7 and Paris 11 Universities, 15 rue Georges Clémenceau, 91406 Orsay Cedex, France
[3] INSERM U892–Cancer Research Center, University of Nantes, Nantes, France
[4] Nuclear Medicine Department, University Hospital of Nantes, Nantes, France
[5] Centre de physique des particules de Marseille, CNRS-IN2P3 and Université de la Méditerranée, Aix-Marseille II, 163, avenue de Luminy, 13288 Marseille Cedex 09, France
[6] INSERM, U650, Laboratoire du Traitement de l'Information Medicale (LaTIM), CHU Morvan, Brest, France
[7] Université de Lyon, CREATIS, CNRS UMR5220, Inserm U630, INSA-Lyon, Université Lyon 1, Centre Léon Bérard, France
[8] Laboratoire de Physique Corpusculaire, 24 Avenue des Landais, 63177 Aubière Cedex, France
[9] Delft University of Technology, Radiation Detection & Medical Imaging, Mekelweg 15, 2629 JB Delft, The Netherlands
[10] Reseach Center Juelich, Institute of Neurosciences and Medicine and Department of Physics, University of Wuppertal, Germany

E-mail: buvat@imnc.in2p3.fr

Received 6 August 2010, in final form 29 November 2010
Published 19 January 2011
Online at stacks.iop.org/PMB/56/881

Abstract

GATE (Geant4 Application for Emission Tomography) is a Monte Carlo simulation platform developed by the OpenGATE collaboration since 2001 and first publicly released in 2004. Dedicated to the modelling of planar scintigraphy, single photon emission computed tomography (SPECT) and positron emission tomography (PET) acquisitions, this platform is widely used to assist PET and SPECT research. A recent extension of this platform, released by the OpenGATE collaboration as GATE V6, now also enables modelling of x-ray computed tomography and radiation therapy experiments. This paper presents an overview of the main additions and improvements implemented in GATE since the publication of the initial GATE paper (Jan *et al* 2004 *Phys. Med. Biol.* **49** 4543–61). This includes new models available in GATE to simulate optical and hadronic processes, novelties in modelling tracer, organ or detector motion, new options for speeding up GATE simulations, examples illustrating the use of GATE V6 in radiotherapy applications and

0031-9155/11/040881+21$33.00 Printed in the UK

CT simulations, and preliminary results regarding the validation of GATE V6 for radiation therapy applications. Upon completion of extensive validation studies, GATE is expected to become a valuable tool for simulations involving both radiotherapy and imaging.

(Some figures in this article are in colour only in the electronic version)

1. Introduction

GATE (Geant4 Application for Emission Tomography) is a Monte Carlo simulation platform developed by the OpenGATE collaboration since 2001 and first publicly released in 2004. Initially, this platform was dedicated to the modelling of planar scintigraphy, single photon emission computed tomography (SPECT) and positron emission tomography (PET) acquisitions (Santin *et al* 2003, Jan *et al* 2004). Over the years, the features of the platform have been enhanced and new versions of the software have been regularly released, to incorporate well-validated upgrades and to stay consistent with regular GEANT4 public releases. Compared to the functionalities of the platform described in the initial paper of the OpenGATE collaboration (Jan *et al* 2004), the major enhancements consist of additional options for speeding up simulations (Taschereau and Chatziioannou 2008, Rehfeld *et al* 2009, Descourt *et al* 2010), facilities to use GATE for dose calculations in internal dosimetry (Visvikis *et al* 2006a, Taschereau and Chatziioannou 2007, Ferrer *et al* 2007, Thiam *et al* 2008, Grevillot *et al* 2010b), and inclusion of optical physics models for accurate modelling of the detector response (van Der Laan *et al* 2010). All these developments have been incorporated in the new GATE V6 release presented here, but are not described in this paper as they have been explained in the articles listed above. Other developments relating to early GATE versions have been reported (Staelens *et al* 2006, De Beenhouwer *et al* 2007, 2008) but were not included in GATE V6 as they have not yet been made available to the OpenGATE collaboration.

In the same period, GATE has been widely used as a tool to assist SPECT and PET research and developments and a number of conventional SPECT and PET scanners and prototypes have been modelled (e.g., Gonias *et al* 2007, Van Der Laan *et al* 2007, Bruyndonckx *et al* 2007, Karakatsanis *et al* 2006, Lamare *et al* 2006, Schmidtlein *et al* 2006, Visvikis *et al* 2006b, Chung *et al* 2005, Assié *et al* 2005, Jan *et al* 2005). More recently, GATE has also been used to model x-ray computed tomography (CT) scanners (Cassol Brunner *et al* 2009, Nicol *et al* 2009, Chen *et al* 2009).

The GATE V6 version released in February 2010 has been considerably extended to enable modelling of radiation therapy experiments. These developments have been largely motivated by the more and more frequent integration of radiotherapy and imaging. Examples of such integration are the use of PET imaging to delineate the metabolically active tumour to be treated by radiotherapy (Ford *et al* 2009) and the emerging domain of in-beam imaging in proton and ion therapy (Crespo *et al* 2007, Knopf *et al* 2008, Nishio *et al* 2006, Parodi *et al* 2008). These developments create a need for tools that enable simultaneous modelling of imaging and radiotherapy experiments.

In this work we present an overview of the main additions and improvements implemented in GATE since the publication of the initial GATE paper (Jan *et al* 2004). We focus on the functionalities that have not yet been reported upon in the specific papers cited above. In section 2, we briefly describe the main improvements made to GATE's architecture. Section 3 describes the new models available in GATE to simulate optical and hadronic processes. Section 4 presents novelties in modelling tracer, organ and detector motion while section 5

explains how CT scans can be modelled with GATE. In section 6, new options for speeding up GATE simulations are given. Section 7 describes new facilities for handling input and output data. A new benchmark is presented in section 8, and section 9 gives preliminary results regarding the validation of GATE V6 for radiation therapy applications. Additional examples illustrating the use of GATE V6 in radiotherapy applications and CT simulations are provided in section 10 and in a companion paper (Grevillot *et al* 2010b). Section 11 gives an overview of upcoming developments in GATE.

2. New features in the architecture of GATE

The basic architecture of the GATE code remains identical to that described in Jan *et al* (2004). It consists of a Geant4 kernel surrounded by three specific layers: (1) the core layer defining the basic simulation elements such as geometry definition, source definition, physical processes, particle tracking, and time management; (2) the application layer, using the basic elements of the core layer, to model objects and processes specific to the imaging applications and, as of version 6, radiotherapy applications; and (3) the user layer, providing the user with simple mechanisms to set up a simulation using scripts only, without any C++ coding. In GATE V6, major changes have been inserted at the first two levels. No major change has been introduced at the user layer.

2.1. Core layer

The changes introduced in the core layer are meant to facilitate future developments in GATE, by introducing a 'plugin' approach, the so-called *auto-list* mechanism, to manage lists of object types involved in the simulations. An object can, for instance, be a volume or a physics process. As an example, adding a new type of geometrical volume (used to describe part of a phantom or a detector) in GATE now only requires inheriting from a Geant4 base class and putting the new source file in the appropriate directory, while no change in other files is necessary; the new type will be automatically inserted in the list of available types.

The most significant parts of the code benefiting from these changes are the volume management for the definition of the simulation geometry (as in the example given above) and the management of the physics processes—hadronic interactions are now available. Cuts (i.e. criteria specifying when secondary particles should not be produced) can also be controlled in a flexible way. Furthermore, the management of sources is now inherited directly from the Geant4 classes and options are provided to move sources within the simulation scene (see section 4). Last but not least, the initialization mechanisms (cross-section table computation) and the run management (data information related to event collection inside a run) of the code were simplified.

Another important feature introduced into the core layer is the concept of *actor*. An *actor* is similar to a sensitive detector (SD) in Geant4 but has extended capabilities; it can store information at each *step* (similar to an SD), but it can also act on particles at each *step*, *track*, *event* or *run*, where the words *step*, *track*, *event* and *run* have the same meanings as in Geant4. For instance, a *DoseActor* measures the energy deposited in a given volume, the *KillActor* stops the tracking of particles when they reach a given volume, the *SimulationStatisticsActor* gives the number of run, events, track, geometrical and physical steps of the simulation, and the *PhaseSpaceActor* stores information related to incoming particles (see section 7).

The concept of *filter* has furthermore been added to GATE to modify the behaviour of *actors*. *Filters* perform tests on the particle properties (e.g., energy, type, or position) at the *step track*, *event*, or *run* level so as to trigger the *actor* only if the test output is true. For

instance, a *filter* can be used to calculate a dose distribution only for electrons having an energy greater than a certain threshold. *Actors* and *filters* can be combined to get new outputs.

Developers can add new types of *actors* and *filters* easily by using the *auto-list* concept.

2.2. Application layer

Contrary to initial GATE versions in which the application layer only managed imaging applications, the application layer is now organized into three distinct parts.

- The imaging application level includes dedicated input and output management, digitizer modules to model the electronic response of various types of detector and a concept of systems to fit scanners of different modalities such as CT, SPECT and PET.
- The new radiotherapy and dosimetry application level includes a new management of particle interactions and provides a new output format appropriate for dose map computation.
- The new general application level gives the users great flexibility in designing a simulation, in a way close to that offered by Geant4. In this general application level, the user can use GATE using script language only or can modify and extend it via C++ programming.

3. Electromagnetic and hadronic physics

In Geant4, each physics process is described by a model (several models are sometimes available for a given physics process) and a corresponding cross-section table. All Geant4 physics models and cross-sections below 10 GeV are now available in GATE. In particular, models describing the transport of optical photons and hadronic interactions have recently been introduced. New processes can easily be added thanks to the *auto-list* concept.

3.1. Optical and scintillation processes

Optical photons can be considered the primary information carriers in scintillation detectors such as those used in SPECT and PET. However, since a large number of scintillation photons (up to $\sim 10^4$) may be generated per absorbed gamma quantum, it is generally not practical to include optical transport in the simulation of a full SPECT or PET system. Optical simulations can nevertheless be useful, for example at the level of single detectors. Such simulations may help to better understand the performance of existing systems and assist in research on novel detector concepts. GATE has therefore been extended to make it possible to simulate the scintillation process, the transport of scintillation photons through the crystal to the light sensor and the conversion of these photons into electronic signals, using the scintillation and optical transport models available in Geant4.

The Geant4 optical models were originally derived from Detect2000 (Levin and Moisan 1996). For example, they allow for the time- and wavelength-dependent modelling of the scintillation process; absorption and scattering of optical photons within dielectric materials; and reflection, transmission and absorption at various types of material interfaces (dielectric–dielectric, dielectric–metal, etc) with different surface treatment (optically polished, ground, etched).

In general, optical Monte Carlo simulations require knowledge of a relatively large number of input parameters such as the light yield, energy resolution, emission spectrum and decay characteristics of the scintillator; the refractive index, absorption length, scattering length and surface roughness of the crystal, and the reflection and absorption properties of the light sensor

and any other materials surrounding the crystal. Sometimes these parameters can be obtained from published data, and sometimes they need to be determined experimentally.

Van der Laan *et al* (2010) recently published a validation of the GATE optical routines by comparing simulated results with measurements on a prototype monolithic PET detector. That work and the references therein provide more details on the optical models used in GATE. The same work also illustrates how the required optical input parameters can be determined. An example of a GATE script for performing optical simulations is provided with the GATE release. Other examples of GATE optical Monte Carlo simulations have been published (Janecek and Moses 2010, van Der Laan *et al* 2006).

3.2. Electromagnetic processes

In GATE V6, three packages of models/cross-sections are available to simulate electromagnetic processes: the standard package for processes between 1 keV and 100 TeV, the low-energy package for processes between 250 eV and 100 GeV, and the PENELOPE package for processes between 250 eV and 1 GeV. Models and cross-sections are based on theoretical calculations and on experimental data. The standard package relies on the parameterization of experimental data (*Geant4 Physics Reference Manual*), while the low-energy package uses directly the experimental data (Apostolakis *et al* 1999). The PENELOPE package is based on the PENELOPE code (PENetration and Energy LOss of Positrons and Electrons), version 2001 (PENELOPE 2001), where the electron multiple-scattering algorithms of PENELOPE have not yet been implemented.

The energy loss of photons is due to discrete interactions only. The energy loss of electrons, however, is separated into continuous energy loss (soft collisions) and secondary electron production (hard collisions or knock-ons). The production threshold (often referred to as 'cut') is defined as the minimum energy E_{cut} above which secondary particles are produced and tracked. When the electron energy $E < E_{\mathrm{cut}}$, E decreases only by continuous energy loss. When $E > E_{\mathrm{cut}}$, secondary electrons are being produced. This threshold is set as a range cut, internally converted into energy, to avoid the dependence on material.

The user can define four types of cut to limit the tracking of particles: the *maximum total track length*, the *maximum total time of flight*, the *minimum kinetic energy*, and the *minimum remaining range*. When a particle reaches any of these cuts, its remaining energy is deposited locally. Other options (*stepping function*, *maximum allowed step size*, *stepping algorithm*, see Apostolakis *et al* (2009), Agostinelli *et al* (2003), *Geant4 Physics Reference Manual*) are available for controlling the standard electromagnetic processes and allow the user to change the trade-off between accuracy and CPU time. The Geant4 option 3 physics list (*Geant4 Physics Reference Manual*), which has been designed for high-precision simulations in e.g. medical applications, is now available in GATE. The influence of different cut values has been reported upon for not only macro-dosimetry using carbon ions (Zahra *et al* 2010) and protons (Grevillot *et al* 2010a), but also for micro-dosimetry (Frisson *et al* 2009).

3.3. Hadronic processes

Hadronic processes describe the interactions between energetic hadrons/ions and target nuclei. Four main types of nucleon–nucleon collision processes can be distinguished as a function of projectile energy and impact parameter. At low energies, incomplete fusion may occur in central collisions and elastic or inelastic scattering in peripheral collisions. At higher energies, central collisions give rise to fragmentation into several lighter fragments or nucleons, while in peripheral collisions a separation into so-called participant and spectator regions occurs.

In Geant4, fusion, inelastic scattering and fragmentation processes are included in the inelastic process type. Inelastic hadronic interactions allow simulation of the cascade, pre-equilibrium and de-excitation stages of ions interacting with matter. These yield, among other products, prompt-gamma radiations and $\beta+$ emitters. Each process is described through models and sets of interaction data. The different Geant4 models available (Bertini, binary cascade, quantum molecular dynamics model, low-energy parameterized model) offer different levels of complexity for the simulations. Models can be selected as a function of particle type, energy, and material. Most hadronic processes require an explicit choice of models. Several interaction datasets may be available for each hadronic process. The choice of data set as a function of energy is performed with a last-in-first-out method.

GATE does not provide more processes or datasets than the ones available in Geant4, but integrates them for imaging and radiation therapy related applications. Some examples of physics lists are currently provided, based on the Geant4 quark-gluon string precompound—binary cascade (QGSP-BIC) models in the recommended physics list for hadronic interactions. Experienced users can tune any parameter to perform comparisons and choose the options that best describe their data.

4. Modelling of moving sources and generic motion

Moving objects during a simulation is one of the unique original features of GATE compared to other simulation tools used in emission or transmission tomography. This feature is useful for modelling, for instance

- the rotation of image acquisition devices around the patient during acquisition;
- the motion of sources during the simulation, e.g., when the tracer distribution changes during a PET or SPECT acquisition;
- organ motion during SPECT or PET acquisitions;
- CT scans where the x-ray beam performs a complete rotation around the object;
- radiation therapy treatments requiring multiple beam angles to conform the dose to the target.

4.1. Moving sources

The Geant4 architecture is not appropriate for moving or transforming sources during a simulation. Therefore, in previous GATE versions, geometrical (i.e. non-voxelized) sources were moved using the concept of confinement (Jan *et al* 2004). In GATE V6, a new, simple and convenient paradigm is used: each source can be attached to any user-defined geometrical volume. The position and momentum of the source particles are defined relative to the coordinate system of this volume instead of to the world coordinate system. Any source can thus be displaced by moving a geometrical volume with time.

Up to recently, the only way to model dynamic patient processes (due either to changes in radiotracer distribution or in organ positions) in voxelized phantoms was through multiple static simulations corresponding to the patient geometries at fixed time points within a dynamically evolving process (for example respiration, cardiac beating, activity concentration). Although feasible, the problem with this approach was the management of multiple independent simulation processes, which becomes increasingly important when fine temporal sampling of the dynamic process of interest is required.

To facilitate the simulation of complex dynamic processes in the patient, new functionalities have been added to define and manage dynamic voxelized phantoms

(*GateRTPhantom* and *GateRTPhantomMgr*, respectively, where RT stands for real time) (Descourt *et al* 2006). This real-time dynamic phantom simulation approach has been validated in comparison to multiple static simulations at different instances of the respiratory cycle and variable organ time-activity curve simulations using the NCAT voxelized phantom (Segars *et al* 2001, Le Maitre *et al* 2009).

4.2. Modelling motions

A new method for describing complex object motions (*genericMove*) has been introduced in GATE V6. The user can now provide, for each volume of interest, the succession of translations and rotations to be applied as a function of time. Note that the same approach is also used for the *repeater* concept (*genericRepeater*); any volume can now be duplicated at different positions and orientations, at no memory cost, according to a file describing the operations to be followed in the duplication process.

A typical application of these new GATE features is the simulation of intensity modulated radiation therapy (IMRT) treatments. In this application, multiple treatment fields are to be simulated, requiring different beam positions and orientations and different amounts of radiation to be delivered. Moreover, for each beam, a sequence of multi-leaf collimator (MLC) configurations with different time durations is used. GATE now makes it possible to simulate this situation by describing only one leaf that is repeated with the generic repeater and moved according to time. Other applications that require such features are the simulation of arc therapy and other complex treatment systems such as Cyberknife or Tomotherapy devices.

The timing capabilities of GATE have also been enhanced. In GATE, each run is associated with a time slice. Volumes can move in between two time slices only. Simulations can now be split into time slices with durations varying from one time slice to another. According to the source activity, in each time slice a different number of particles can be generated.

5. CT modelling with GATE

CT scanners can be modelled using the CT scanner system. The Geant4 General Particle Source (GPS) allows the user to simulate a realistic x-ray source. Indeed, the GPS can produce particles defined by specific energy, angular and spatial distributions. The energy distribution of the source is defined using an energy histogram (weights against energy bins). The angular distribution is defined using two angles, while the spatial distribution defines the 2D or 3D shape of the source. The CT system is composed of modules that can be linearly repeated along an axis. A module is composed of clusters, each of which corresponds to a set of equally sized pixels (figure 1). This approach enables the modelling of many different types of CT scanner. A complete simulation applies *digitizer* functions at the level of the pixels. The standard output stores 32 bit raw data corresponding to the number of photons detected per CT projection in each pixel. As long as the digitizer model makes sense and is

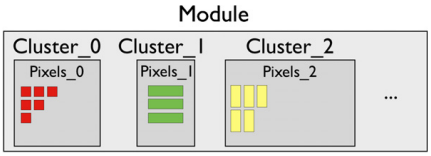

Figure 1. Basic components of the *CT scanner* system.

duly validated against real data, digitizer functions can also be tailored by the user directly at the level of the *module* to avoid time-consuming tracking at the level of the pixels.

6. Variance reduction techniques and other acceleration options

A number of variance reduction techniques (VRTs) appropriate for different types of situations have been introduced in GATE to accelerate simulations. Dedicated publications have already reported and validated the implementation of the regular navigator and fictitious interaction approaches appropriate for SPECT and PET (Rehfeld *et al* 2009), the tabulated modelling of the detector response in SPECT which circumvents the tracking of particles within the collimator/detector pair (Descourt *et al* 2010), and compressed voxel strategies to optimize memory and CPU use (Taschereau and Chatziioannou 2008). In the following, we briefly describe generic VRTs that have recently been added, as well as a simple acceleration option appropriate for CT simulations.

6.1. Classical VRT techniques

Two standard VRTs of Geant4 are now available in GATE, namely splitting and Russian roulette (*Geant4 Physics Reference Manual*). To increase the efficiency of these VR techniques, the user can add selection criteria to be applied to the incident (primary) or secondary particles, using the concept of *filters* (section 2.1). The *filters* for splitting and Russian roulette are the same as those available for *actors*. Using this approach, it is possible to optimize simulations of clinical linear accelerators using selective bremsstrahlung splitting (Kawrakow *et al* 2004).

6.2. Acceleration for CT simulations

To efficiently simulate CT, every photon that reaches the detector surface is split into k clones. Each clone is forced to interact within the CT detector using the direct inversion method, according to the attenuation properties of the detector, and considering the photon cross-section data from the Geant4 standard electromagnetic package. Without acceleration ($k = 1$), the propagation of N photons impinging on the surface of the detector is equivalent to a binomial trial of mean Np, where p is the detection probability. As long as N and p are, respectively, large and small enough, the number of detected photons follows a Poisson distribution of mean and variance equal to Np. Considering the use of k clones, the expectation of the number of detected photons becomes Nkp and its variance is $(Nkp)^2[(k-1)/Nk+1/Nkp]$. As shown in figure 2(a), the relative variance resulting from this acceleration option is perfectly described by this model and increases rapidly when k becomes large. Figure 2(b) shows the acceleration achieved using this approach; obtaining an average count above 10 000 photons/pixel with $k = 10$ clones results in an acceleration of the execution time by a factor around 10 with only a slight increase of the relative variance. Using more clones (e.g. $k = 20$) results in a dramatic increase of the relative variance, although the acceleration factor remains roughly proportional to the number of clones. Indeed, this approach can provide a speedup factor proportional to the number of clones, but it has to be used with caution, since the increase of the relative variance might result in reconstructed images with enhanced noise.

7. Data input and output

It is important that GATE can easily read in data from CT scanners, as such data are often used to design simulations based on realistic patient data, and that it can store data in a format

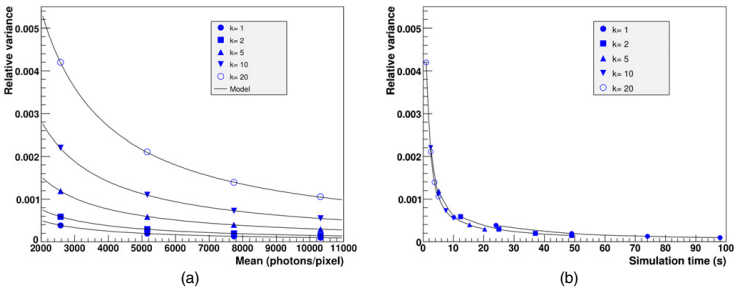

Figure 2. Plot of the relative variance against mean photons/pixel (a) and simulation time (b). The mean and variance of the number of detected photons per pixel are determined from the simulation of a Si pixel detector with 10 000 pixels of 0.5 mm × 0.5 mm × 0.5 mm each irradiated using a flat field of 17.6 keV x-rays. 50 000 realizations were performed to calculate the means and standard deviations. In (a), the relative variance calculated from the simulations is perfectly predicted by the variance given by $(k-1)/Nk+1/Nkp$ derived from the model.

that is readable by other software. New features have been introduced in GATE V6 to comply with these requirements.

7.1. Data input

Using CT images as simulation input requires a method to relate the Hounsfield unit (HU) values in the input image to Geant4 materials. The stoichiometric calibration implemented in GATE V6 is that described by Schneider *et al* (2000). The procedure is based on a user-defined mass density tolerance parameter and two calibration files describing the piecewise linear correspondence between CT numbers and mass density, and a list of material compositions. The tolerance parameter can be used to tune the number of materials depending on the accuracy required in the simulation. The list of materials generated and the correspondence between materials and HU values are stored and can be used for converting any CT image into materials.

7.2. Data output

The *DoseActor* has been added to store 1D, 2D or 3D distributions of dose and/or energy deposited with the associated statistical uncertainty in any volume (Sarrut and Guigues 2008). A user-defined scoring matrix consisting of so-called *dosels* can be attached to any volume, including voxelized geometries. The sizes of the *dosels* can be different from the voxel size (De Smedt *et al* 2005). Every time a particle interacts in the volume, the energy deposited and/or the absorbed dose are recorded in the corresponding *dosel*.

In Geant4, the user has to specify at which location the energy deposited during a *step* is scored, for instance at the beginning or at the end of the *step*. For charged particles, which deposit most of their energy through continuous energy loss, GATE V6 provides a slightly different approach in which the deposited energy is scored at a randomly chosen position along the *step*. This approach ensures that the energy deposited by charged particles is scored correctly on average, even in the vicinity of volume boundaries. Since a *step* is always

interrupted when it crosses a volume boundary, other dose scoring methods may introduce biases.

The *DoseActor* is compatible with variance reduction techniques as the deposited energy is weighted by the particle weight. In addition to the deposited energy, an estimation of the relative statistical uncertainty is computed as proposed by Chetty *et al* (2006). When a simulation is split into multiple jobs, such as when using clusters of workstations, the total uncertainty cannot be computed directly from the uncertainties obtained for each job. In this case the first and second moment of the energy distribution are stored for each job and the uncertainty can be calculated retrospectively.

7.3. Phase-space files

GATE V6 allows the user to record so-called phase-space files containing the essential properties of the simulated particles at a given geometric level.

For imaging applications, particle tracking can be limited to the phantom (or patient). The properties of each particle exiting the phantom are stored in a phase-space file. This output file can then be used as an input file in subsequent GATE simulations (or even in other software), in which the stored particles are further propagated towards the detector. This option can be useful to efficiently study or optimize different detector set-ups, since the simulation of particles within the phantom has to be performed only once.

For radiotherapy applications, the phase-space file can be used, for instance, to first simulate the linear-accelerator head (patient-independent part) and then store the properties of the particles before they enter the MLC. The phase space can subsequently be used to simulate different treatment scenarios (patient-dependent part). In this case, phase-space files are created using an actor (*phaseSpaceActor*) that collects the relevant properties of all particles passing through a given region. The particle properties that can be stored are the energy, type, position, direction, weight, and the process and volume of production. The phase-space data can be stored in ROOT or in a standard IAEA format (Capote *et al* 2006). The IAEA format can be used to produce phase-space files for other MC codes. Conversely, an IAEA file produced by another code can be used in a GATE simulation that considers all particles in the phase-space file as primary particles.

8. New GATE V6 benchmark

GATE benchmarks provide users with relatively easy simulation set-ups that can be run with any GATE release to check the validity of the user's results by comparing them with the results provided on the GATE website and to track changes between versions. A new benchmark related to radiation therapy applications is distributed with GATE V6.

The radiotherapy benchmark consists of a proton beam and a photon beam interacting in a 40 cm $\times$ 40 cm $\times$ 40 cm water phantom. The beam energy is set to 150 MeV for the proton beam and to 18 MV for the photon beam. The physics list used in this benchmark is that recommended by the Geant4 collaboration for the hadrontherapy applications (https://twiki.cern.ch/twiki/bin/view/Geant4/LowePhysicsLists). Three hundred and fifty thousand protons and 2 million photons are generated. The total computing time for this benchmark is about 1 h on an Intel Xeon 5130 CPU at 2.0 GHz.

The simulated energy deposition profile is shown in figure 3. This figure is automatically produced by the analysis code provided with the benchmark. A statistics file containing the number of events, tracks, and steps is also generated. Table 1 shows the mean values and the associated standard deviations obtained by running the benchmark with GATE V6.1 on four

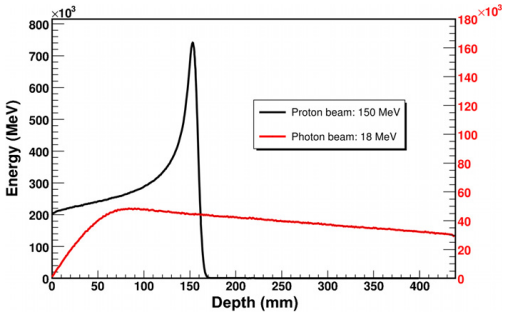

Figure 3. Energy deposition profiles obtained when running the radiation therapy benchmark.

Table 1. Average values ± 1 standard deviation of parameters analysed in the radiation therapy benchmark.

Beam	Number of events	Number of tracks	Number of steps	Number of geometric steps	Number of physical steps
Protons (150 MeV)	350 000	17 851 294 ± 100 047	105 566 062 ± 293 928	588 828 ± 4221	104 977 233 ± 297 892
Photons (18 MV)	2 000 000 ± 0	34 191 416 ± 44 709	127 354 486 ± 173 392	8 166 686 ± 3621	119 187 800 ± 169 779

different sites. These values serve as reference values for checking the integrity of a GATE installation and to track changes from one GATE version to another.

9. Preliminary validation results for radiation therapy applications

The ICRU (1993) definition was used for all materials involved in the studies reported in this section (composition, density, ionization potential).

9.1. Photon beam radiation therapy

A realistic photon beam in a multilayer phantom was modelled. The phantom (30.5 × 39.5 × 30 cm^3) consisted of four layers: water (0–3 cm), aluminium (3–5 cm), lung (5–12 cm) and water (12–30 cm). The phantom was irradiated with a 18 MV photon beam, originating from a uniform point source at 100 cm from the phantom surface and collimated to 1.5 × 1.5 cm^2 at the surface of the phantom using four *KillActors*. The energy spectrum of the point source fitted the configurations of a VARIAN Clinac 2100C as modelled using the BEAM code (Rogers *et al* 1995). The depth–dose distribution was calculated along the central axis with a 1D *DoseActor*. The *dosel* dimensions were 5 mm × 5 mm orthogonally to the beam direction and 2 mm along the beam direction. We used the standard physics list with option 3 (see section 3) for electrons, positrons and photons. The production threshold was set to 1 mm in the world and to 0.1 mm in the phantom for electrons, positrons and photons. A total

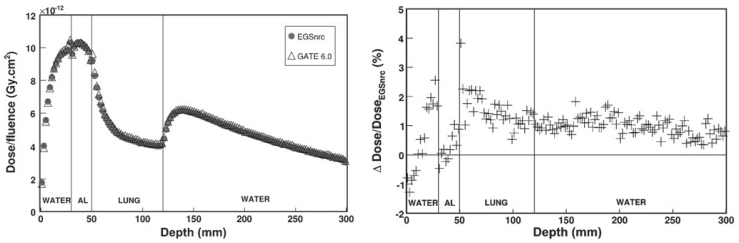

Figure 4. (a) Dose deposited per unit photon fluence as a function of depth in a multilayer phantom for an 18 MV photon beam. Results with GATE V6.0 (open diamonds) are compared with results with EGSnrc (black circles). (b) Relative differences d_r between the depth–dose distributions calculated with EGSnrc and GATE.

of 10^8 incident photons were simulated. The statistical relative uncertainty was below 0.6% in all dosels.

The depth–dose profile calculated with GATE was compared to that obtained with EGSnrc following the configuration reported by Rogers and Mohan (2000) using the PRESTAII stepping algorithm (figure 4). Two relative differences in dose estimates were derived: $d_r = (\text{Dose}_{\text{GATE}} - \text{Dose}_{\text{EGS}})/\text{Dose}_{\text{EGS}}$ and $d_m = (\text{Dose}_{\text{GATE}} - \text{Dose}_{\text{EGS}})/\text{Dose}_{\text{max}}$, where $\text{Dose}_{\text{GATE}}$, Dose_{EGS} and Dose_{max} are the dose values calculated by GATE, EGSnrc, and $\max(\text{Dose}_{\text{GATE}}, \text{Dose}_{\text{EGS}})$, respectively. The results obtained using GATE V6 were in good agreement with EGSnrc results, with d_r less than 3% and d_m less than 1.8%. The computation time was about 3 h on an Intel 2.3 GHz CPU.

9.2. Electron beam radiation therapy

A realistic 20 MeV electron beam was modelled in a multilayer phantom (30.5 cm × 39.5 cm × 8 cm) consisting of four layers: water (0–2 cm), aluminium (2–3 cm), lung (3–6 cm) and water (6–8 cm). A total of 2.5×10^5 electrons were simulated. The *dosel* dimensions were 5 mm × 5 mm orthogonally to the beam direction and 2 mm along the beam direction. The statistical relative uncertainty increased from 0.6% near the phantom entrance surface to 2.6% near the exit surface.

The depth–dose distribution obtained with GATE was compared to the results obtained using EGSnrc following the configuration reported in Rogers and Mohan (2000) using the PRESTAII stepping algorithm (figure 5). The d_r and d_m relative dose differences defined in section 9.1 were calculated. GATE V6.0 yielded results in good agreement with EGSnrc results with d_r less than 4% (except at 8 cm where d_r reaches 7.5% with a statistical uncertainty of ∼7%) and d_m less than 1.1%. The computation time was about 6 h on an Intel 2.3 GHz CPU.

9.3. Proton beam radiation therapy

The depth–dose profile of a 150 MeV mono-energetic proton beam in a 40 cm × 40 cm × 40 cm water phantom was calculated. The proton beam had a Gaussian fluence profile with a

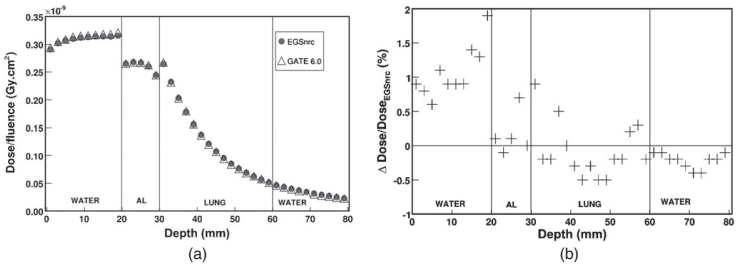

Figure 5. (a) Dose deposited per unit electron fluence as a function of depth in the multilayer phantom for a 20 MeV mono-energetic electron beam. Results with GATE V6.0 (open diamonds) are compared with EGSnrc (black circles). (b) Relative differences d_r between the depth–dose distributions calculated with EGSnrc and GATE.

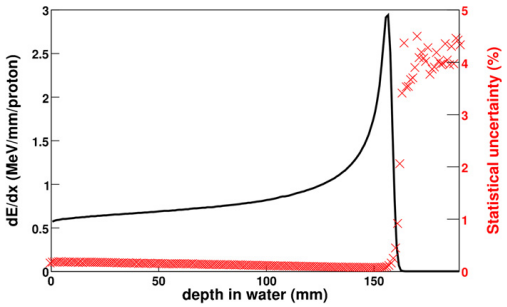

Figure 6. Normalized energy deposited by a 150 MeV proton beam as a function of depth in water (black curve, left-hand axis) and associated relative statistical uncertainty (red curve, right-hand axis).

standard deviation of 3 mm. The *dosel* dimensions were 40 cm × 40 cm orthogonally to the beam and 1 mm along the beam direction. The *hadrontherapyStandardPhys.mac* physics list proposed in GATE was used, with an additional *StepLimiter* of 1 mm and default production thresholds (1 mm range cut for electrons, positrons and photons). A total of 10^6 incident protons were simulated in 57 min on a single 1.66 GHz CPU.

The results shown in figure 6 show that the relative statistical uncertainty is below 0.1% for all dosels before the distal tail of the Bragg peak (oscillations after the peak are due to the near-zero values of deposited energy at the corresponding depths). The proton range, defined as the position of 80% of the maximum dose in the distal fall-off region, is 158 mm. This agrees to within 0.3 mm with the CSDA range of 157.7 mm given by the NIST PSTAR database (http://physics.nist.gov/PhysRefData/Star/Text/PSTAR.html). The peak-to-entrance energy ratio, defined as the ratio between the maximum dose and the dose in the entrance dosel, is 5.15. The peak width, defined as the distance between the points at which the dose equals 80% of the maximum dose at either side of the Bragg peak, is 5.5 mm.

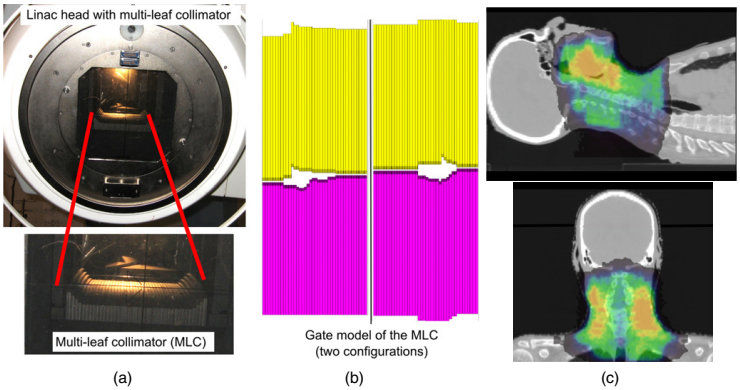

Figure 7. A multi-leaf collimator (a) and two of its modelled configurations (b) during an IMRT treatment plan simulated with GATE. The resulting dose distribution (c) is superimposed on two CT slices.

10. Examples of GATE V6 simulations

10.1. Radiation therapy examples

To illustrate a radiotherapy application of GATE, we exported a head and neck IMRT treatment plan from a XIO (CMS) treatment planning system and converted it into GATE macros. The plan was composed of 5 beams with 20 leaf positions, simulated using 100 GATE runs. The MLC was simulated by describing a single leaf and using the *genericMove* and *genericRepeater* as discussed in section 4.2 (figure 7). The DICOM data of the patient CT scan were converted into a GATE readable file format (Analyze), using the stoichiometric calibration described in section 7. This 3D dose simulation (10^9 particles in about 33 h on a single Intel 2.7 GHz CPU) has not yet been compared to TPS results nor to experimental measurements. Our primary goal here was to illustrate that complex simulations including voxelized phantoms, MLC models, and motion were feasible with GATE. The relative statistical uncertainty is lower than 1% in the high-dose region (i.e. where the dose is $>$ 50% of the maximum dose).

As an example of a hadron therapy application, we simulated a ^{12}C scanning pencil beam irradiation of an artificial spherical target inside a patient CT image. The treatment plan comprised 12 $\times$ 12 spots at 24 different energy layers ($\sim$3500 different pencil beams of which $\sim$2200 with non-zero intensity). The beams were described according to the results of a spread-out Bragg peak (SOBP) optimization performed with the method of Krämer *et al* (2000). Ion ranges were estimated using the water equivalent path length obtained from the CT numbers (Krämer *et al* 2000). The biological dose was estimated using the method of Kase *et al* (2006). Figure 8 illustrates the dose deposition measured using this simulation, which took $\sim$15 min on a one hundred AMD Opteron 2.3 GHz CPU cluster.

10.2. In-beam PET modelling with GATE

To illustrate the ability of GATE to jointly model radiation therapy and emission tomography, a complete in-beam PET set-up was simulated. A 4D CT patient scan was used to define

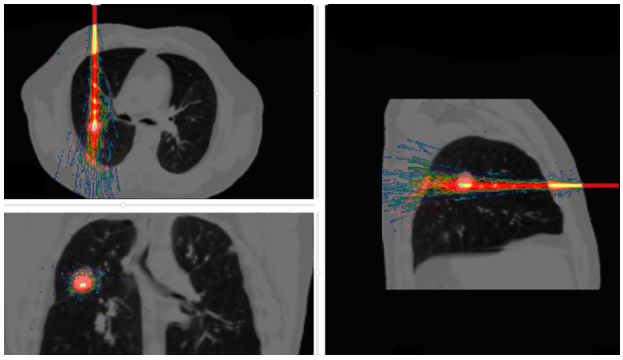

Figure 8. Dose deposited by a carbon ion beam inside a CT image of a thorax. The colour scale is a warm metal scale, with high values (white) corresponding to high-dose deposit and low values (blue) corresponding to low-dose deposit.

the numerical phantom. A three-beam treatment plan was modelled with a total production of 3×10^9 ^{12}C ions. Each beam was composed of 195 independent spots with 42 different incident energies between 175 and 230 MeV/u. All hadronic and electromagnetic processes were included in the simulation, from the ^{12}C ion tracking to the β^+ decay of ^{11}C and ^{15}O produced by nuclear reactions. Positron range and annihilation photon pair acollinearity were taken into account. A model of the Siemens HR+ PET system (Jan *et al* 2005) was used to simulate a 20 min static acquisition starting immediately after the ^{12}C irradiation. PET data were normalized, corrected for attenuation using an attenuation map derived from the CT, and reconstructed using 3D back projection. The simulation was performed in less than 24 h on a cluster of 1000 Intel Nehalem 2.93 GHz CPUs.

The reconstructed PET images (figure 9) suggest that the ^{11}C activity distribution (mainly created by auto-activation) contains most information regarding the location of the SOBP, while the ^{15}O activity (entirely due to target activation) might be relevant to derive information about the dose to normal tissues.

10.3. Example of CT modelling with GATE

As an example, we have tentatively simulated the design of the XPAD3 hybrid pixel detector, a prototype x-ray photon counting detector under development at CPPM (Nicol *et al* 2009) operated with a source emitting a cone beam of x-rays of 12° aperture angle with a typical Mo target energy spectrum. The x-ray detector was composed of five barrettes of seven chips of 80×120 pixels tiled together, corresponding to 336 000 500 μm thick pixels of 130×130 μm^2. The 4D MOBY phantom was used with $435 \times 435 \times 600$ voxels of 60 μm (Segars *et al* 2004). A total of 25 279 488 photons were detected per time slice of 1 s. The complete simulation took 149 min on an Intel Core 2 Duo T9600 processor operating at 2.80 GHz. It took only 14 min with the acceleration option using 10 clones.

Figure 10 shows two cone-beam projections of the MOBY phantom simulated without (figure 10(a)) and with (figure 10(b)) the acceleration option. The projections are shown as

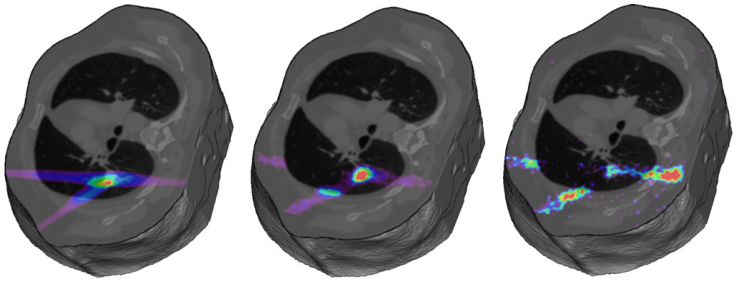

Figure 9. (a) Dose distribution simulated for a ^{12}C irradiation inside a CT image of a thorax. (b) Simulated PET image of the resulting ^{11}C isotope distribution. (c) Simulated PET image of the ^{15}O isotope distribution.

matrices filled with the raw counts of the pixels and do not reproduce the actual geometry of the detector with its tiles. 360 projections per scan are used to reconstruct an image using the FDK algorithm while taking into account the actual geometry of the detector (figure 10(c)). The image reconstructed with projections using the acceleration option with ten clones (figure 10(d)) does not show any structured artefacts but appears of poorer quality compared to the image without the acceleration option, due to the increased variance in the projections.

This example is not intended to be a validation of the CT model but illustrates the feasibility of CT simulations with GATE at a reasonable computational cost.

11. Discussion

The broad use of GATE in detector design, imaging and processing protocol optimization, and even in image reconstruction, motivated the enhancements described in this paper. Based on its new features, GATE should meet the needs of an increasing number of scientists involved in SPECT, PET and CT imaging, and now also in external beam photon and hadron radiotherapy. An important consequence of the use of the same software by many scientists is that it makes it easier to compare, share and understand results.

Of course, this also makes it important that the software is thoroughly validated. GATE has already been validated for a number of PET and SPECT imaging configurations by comparing simulated and experimental data (Lazaro *et al* 2004, Staelens *et al* 2003, Gonias *et al* 2007, Van Der Laan *et al* 2007, Rey *et al* 2007, Karakatsanis *et al* 2006, Lamare *et al* 2006, Schmidtlein *et al* 2006, Visvikis *et al* 2006b, Chung *et al* 2005, Assié *et al* 2005, Jan *et al* 2005, Cassol Brunner *et al* 2009, Chen *et al* 2009). For radiation therapy, the relevant Geant4 models have already been partly studied (Carrier *et al* 2004, Pshenichnov *et al* 2005, 2006, Jiang *et al* 2004, Paganetti 2004, Jarlskog and Paganetti 2008). More extensive validation of GATE V6 and underlying Geant4 models for proton and ion therapy applications is currently ongoing.

Upon completion of these validation studies, GATE V6 will provide a unique tool for simulations involving both radiotherapy and imaging. Examples of approaches in which imaging and therapy are integrated include the use of PET imaging to delineate the

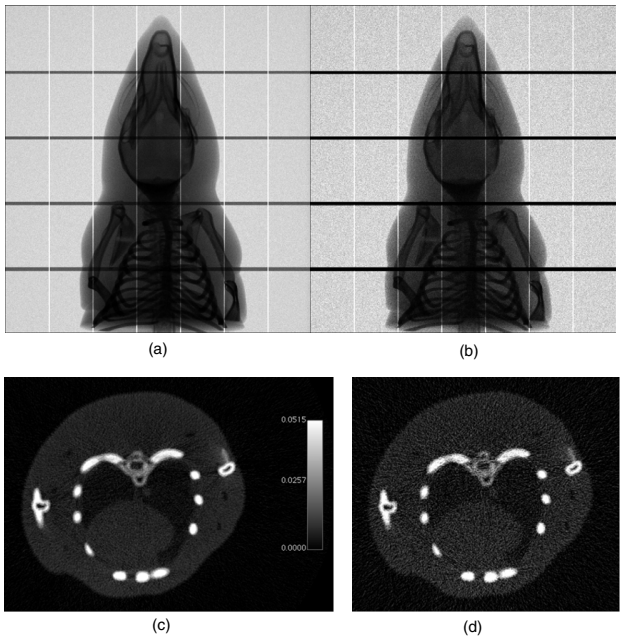

Figure 10. Example of a simulated CT projection of a Moby phantom: without ($k = 1$) (a) and with acceleration ($k = 10$ clones) (b). Transaxial slices reconstructed from the projections without (c) and with acceleration (d).

metabolically active tumour to be irradiated (Ford *et al* 2009), online imaging in external beam therapy, ranging from portal imaging (EPIDs) (van Elmpt *et al* 2008) and integrated x-ray imaging (Mutanga *et al* 2007, Sonke *et al* 2009) to e.g. the Cyberknife (Seppenwoolde *et al* 2007) and Tomotherapy devices (Welsh *et al* 2004), the emerging domain of in-beam imaging in proton and ion therapy (Crespo *et al* 2007, Knopf *et al* 2008, Nishio *et al* 2006, Parodi *et al* 2008), and targeted radiotherapy using radionuclides that can also be imaged (e.g., Kwekkeboom *et al* 2000, Seevinck *et al* 2007). Each of these applications may benefit from the availability of an integrated software supporting both imaging and radiation therapy simulations.

In addition to the recent developments of GATE towards radiotherapy applications, the extension of GATE to optical imaging is also in progress. Optical imaging is of growing importance in the field of preclinical imaging. However, most optical acquisitions are currently limited to 2D projections, without any quantitative analysis of the resulting images. Simulations may help in the design of devices for 3D quantitative optical imaging and associated reconstruction algorithms accounting for optical scattering in tissues. To date, although several approaches have been described in the literature (Wang *et al* 1995, Boas *et al*

2002, Li *et al* 2004), there is no commonly accepted software to perform such simulations. Extending GATE to optical imaging requires us to integrate the relevant physics processes, add databases containing the optical properties of different tissues and materials, and add systems and digitizer options relevant to optical imaging devices.

A weakness of previous GATE versions that many users are aware of is its relatively low computational efficiency. Several options have recently been introduced to speed up GATE in specific situations (section 6) and better manage the trade-off between computation time and accuracy. However, additional options may be worth investigating, especially for applications such as the calculation of system matrices for tomographic image reconstruction (Rehfeld *et al* 2010). Furthermore, the possibility of running GATE on hybrid CPU/GPU architectures is currently under study. At the same time, tools to facilitate the deployment of GATE on grids are being developed (Camarasu *et al* 2010).

Several computer-oriented developments other than those described here have been introduced to facilitate the use of GATE by users and developers, such as the distribution of GATE as an image appropriate for virtual machines, providing the documentation as a wiki, etc. All of these developments aim at making GATE accessible to scientists involved in SPECT, PET, CT and radiotherapy applications, without requiring expertise in computer science or C++ programming.

12. Conclusion

The introduction of a large number of new features in GATE V6 now makes it possible to use GATE as an integrated tool for the modelling of imaging, dosimetry and treatment in the same simulation platform, consistent with current and future needs of the nuclear medicine and radiation therapy communities. Extensive validation studies are currently being performed to establish the role of GATE in the development of image-guided radiation therapy.

References

Agostinelli *et al* 2003 Geant4—a simulation toolkit *Nucl. Instrum. Methods Phys. Res.* **506** 250–303

Apostolakis J, Giani S, Maire M, Nieminen P, Pia M G and Urban 1999 Geant4 low energy electromagnetic models for electrons and photons CERN-OPEN-99-034, INFN/AE-99/18

Apostolakis J *et al* 2009 Geometry and physics of the Geant4 toolkit for high and medium energy applications *Rad. Phys. Chem.* **78** 859–73

Assié K, Gardin I, Vera P and Buvat I 2005 Validation of the Monte Carlo simulator GATE for Indium 111 imaging *Phys. Med. Biol.* **50** 3113–25

Boas D, Culver J, Stott J and Dunn A 2002 Three dimensional Monte Carlo code for photon migration through complex heterogeneous media including the adult human head *Opt. Express* **10** 159–70

Bruyndonckx P, Lemaître C, Schaart D R, van Der Laan D J, Maas M C, Krieguer M, Devroede O and Tavernier S 2007 Towards a continuous crystal APD-based PET detector design *Nucl. Instrum. Methods Phys. Res.* A **571** 182–6

Camarasu-Pop S, Glatard T, Mościcki J T, Benoit-Cattin H and Sarrut D 2010 Dynamic partitioning of GATE Monte-Carlo simulations on EGEE *J. Grid Comput.* **8** 241–59

Capote R, Jeraj R, Ma C P, Rogers D W O, Sanchaez-Doblado F, Sempau J, Seuntjens J and Siebers J V 2006 Phase-space database for external beam radiotherapy *IAEA Technical Report* INDC(NDS)-0484

Carrier J F, Archambault L, Beaulieu L and Roy R 2004 Validation of Geant4, an object-oriented Monte Carlo toolkit, for simulations in medical physics *Med. Phys.* **31** 484–92

Cassol Brunner F, Khoury R, Benoit D, Meessen C, Bonissent A and Morel C 2009 Simulation of PIXSCAN, a photon counting micro-CT for small animal imaging *J. Instrum.* **4** P05012

Chen Y, Liu B, O'Connor J M, Didier C S and Glick S J 2009 Characterization of scatter in cone-beam CT breast imaging: comparison of experimental measurements and Monte Carlo simulation *Med. Phys.* **36** 857–69

Chetty I J *et al* 2006 Reporting and analyzing statistical uncertainties in Monte Carlo-based treatment planning *Inter. J. Radiat. Oncol. Biol. Phys.* **65** 1249–59

Chung Y H, Choi Y, Cho G S, Choe Y S, Lee K H and Kim B T 2005 Optimization of dual layer phoswich detector consisting of LSO and LuYAP for small animal PET *IEEE Trans. Nucl. Sci.* **52** 217–21

Crespo P, Shakirin G, Fiedler F, Enghardt W and Wagner A 2007 Direct time-of-flight for quantitative, real-time in-beam PET: a concept and feasibility study *Phys. Med. Biol.* **52** 6795–811

De Beenhouwer J, Staelens S, Kruecker D, Ferrer L, D'Asseler Y, Lemahieu I and Rannou F R 2007 Cluster computing software for GATE simulations *Med. Phys.* **34** 1926–33

De Beenhouwer J, Staelens S, Vandenberghe S and Lemahieu I 2008 Acceleration of GATE SPECT simulations *Med. Phys.* **35** 1476–85

Descourt P, Carlier T, Du Y, Song X, Buvat I, Frey E C, Bardies M, Tsui B M W and Visvikis D 2010 Implementation of angular response function modeling in SPECT simulations with GATE *Phys. Med. Biol.* **55** N253–66

Descourt P, Segars W P, Lamare F, Ferrer L, Tsui B, Bizais Y, Bardies M and Visvikis D 2006 RTNCAT (Real Time NCAT): implementing real time physiological movement of voxellised phantoms in GATE *IEEE Nucl. Sci. Symp. Conf. Rec.* pp 3163–5

De Smedt B, Vanderstraeten B, Reynaert N, De Neve W and Thierens H 2005 Investigation of geometrical and scoring grid resolution for Monte Carlo dose calculations for IMRT *Phys. Med. Biol.* **50** 4005–19

Ferrer L, Chouin B, Bitar A, Lisbona A and Bardies M 2007 Implementing dosimetry in GATE: dose point kernel validation with GEANT4 4.8.1 *Cancer Biother. Radiopharm.* **22** 125–9

Ford E C, Herman J, Yorke E and Wahl R L 2009 18F-FDG PET/CT for image-guided and intensity-modulated radiotherapy *J. Nucl. Med.* **50** 1655–65

Frisson T, Zahra N, Lautesse P and Sarrut D 2009 Monte-Carlo based prediction of radiochromic film response for hadrontherapy dosimetry *Nucl. Instrum. Methods Phys. Res.* A **606** 749–54

Geant4 Collaboration *Geant4 Physics Reference Manual* http://geant4.cern.ch/G4UsersDocuments/UsersGuides/PhysicsReferenceManual/html/PhysicsReferenceManual.html

Gonias P *et al* 2007 Validation of a GATE model for the simulation of the Siemens PET/CT biograph 6 scanner *Nucl. Instrum. Methods Phys. Res.* A **571** 263–6

Grevillot L, Frisson T, Zahra N, Bertrand D, Stichelbaut F, Freud N and Sarrut D 2010a Optimization of GEANT4 settings for proton pencil beam scanning simulations using GATE *Nucl. Instrum. Methods Phys. Res.* B **268** 3295–305

Grevillot L, Frisson T, Maneval D, Zahra N, Badel J-N and Sarrut D 2010b Simulation of a 6 MV Elekta Precise Linac photon beam using GATE/GEANT4 *Phys. Med. Biol.* **56** 903–18

ICRU 1993 Stopping Powers and Ranges for Protons and Alpha Particles *ICRU Report No 49* (Bethesda, MD: ICRU)

Jan S *et al* 2004 GATE: a simulation toolkit for PET and SPECT *Phys. Med. Biol.* **49** 4543–61

Jan S, Comtat C, Strul D, Santin G and Trébossen R 2005 Monte Carlo simulation for the ECAT EXACT HR+ system using GATE *IEEE Trans. Nucl. Sci.* **52** 627–33

Janecek M and Moses W W 2010 Simulating scintillator light collection using measured optical reflectance *IEEE Trans. Nucl. Sci.* **57** 964–70

Jarlskog C Z and Paganetti H 2008 Physics settings for using the Geant4 toolkit in proton therapy *IEEE Trans. Nucl. Sci.* **55** 1018–25

Jiang H and Paganetti H 2004 Adaptation of GEANT4 to Monte Carlo dose calculations based on CT data *Med. Phys.* **31** 2811–8

Karakatsanis N *et al* 2006 Comparative evaluation of two commercial PET scanners, ECAT EXACT HR+ and Biograph 2, using GATE *Nucl. Instrum. Methods Phys. Res.* A **571** 368–72

Kase Y, Kanematsu N, Kanai T and Matsufuji N 2006 Biological dose calculation with Monte Carlo physics simulation for heavy-ion radiotherapy *Phys. Med. Biol.* **51** N467–75

Kawrakow I, Rogers D W and Walters B R 2004 Large efficiency improvements in BEAMnrc using directional bremsstrahlung splitting *Med. Phys.* **31** 2883–98

Knopf A, Parodi K, Paganetti H, Cascio E, Bonab A and Bortfeld T 2008 Quantitative assessment of the physical potential of proton beam range verification with PET/CT *Phys. Med. Biol.* **53** 4137–51

Krämer M, Jäkel O, Haberer T, Kraft G, Schardt D and Weber U 2000 Treatment planning for heavy-ion radiotherapy: physical beam model and dose optimization *Phys. Med. Biol.* **45** 3299–317

Kwekkeboom D, Krenning E P and de Jong M 2000 Peptide receptor imaging and therapy *J. Nucl. Med.* **41** 1704–13

Lamare F, Turzo A, Bizais Y, Le Rest C C and Visvikis D 2006 Validation of a Monte Carlo simulation of the Philips Allegro/GEMINI PET systems using GATE *Phys. Med. Biol.* **51** 943–62

Lazaro D *et al* 2004 Validation of the GATE Monte Carlo simulation platform for modelling a CsI(Tl) scintillation camera dedicated to small-animal imaging *Phys. Med. Biol.* **49** 271–85

Le Maitre A, Segars W P, Marache S, Reilhac A, Hatt M, Tomei S, Lartizien C and Visvikis D 2009 Incorporating patient specific variability in the simulation of realistic whole body 18F-FDG distributions for oncology applications *Proc. IEEE* **97** 2026–38

Levin A and Moisan C 1996 A more physical approach to model the surface treatment of scintillation counters and its implementation into DETECT *IEEE Nucl. Sci. Symp. Conf. Rec.* **2** 702–6

Li H *et al* 2004 A mouse optical simulation environment (MOSE) to investigate bioluminescent phenomena in the living mouse with the Monte Carlo method *Acad. Radiobiol.* **11** 1029–38

Mutanga T F, de Boer H C J, van der Wielen G J, Wentzler D, Barnhorn J, Incrocci L and Heijmen B J M 2007 Stereographic targeting in prostate radiotherapy: speed and precision by daily automatic positioning corrections using kilovoltage/megavoltage image pairs *Int. J. Radiat. Oncol. Biol. Phys.* **71** 1074–83

Nicol S *et al* 2009 Design and construction of the ClearPET/XPAD small animal PET/CT scanner *IEEE Nucl. Sci. Symp. Conf. Rec.* pp 3311–4

Nishio T, Ogino T, Nomura K and Uchida H 2006 Dose-volume delivery guided proton therapy using beam on-line PET system *Med. Phys.* **33** 4190–7

Paganetti H 2004 Four-dimensional Monte Carlo simulation of time-dependent geometries *Phys. Med. Biol.* **49** N75–81

Parodi K, Bortfeld T and Haberer T 2008 Comparison between in-beam and offline positron emission tomography imaging of proton and carbon ion therapeutic irradiation at synchrotron- and cyclotron-based facilities *Int. J. Radiat. Oncol. Biol. Phys.* **71** 945–56

PENELOPE 2001 PENELOPE: a code system for Monte Carlo simulation of electron and photon transport *Workshop Proc. Issy-les-Moulineaux (AEN-NEA, France, 5–7 November 2001)*

Pshenichnov I, Mishustin I and Greiner W 2005 Neutrons from fragmentation of light nuclei in tissue-like media: a study with the GEANT4 toolkit *Phys. Med. Biol.* **50** 5493–507

Pshenichnov I, Mishustin I and Greiner W 2006 Distributions of positron-emitting nuclei in proton and carbon-ion therapy studied with GEANT4 *Phys. Med. Biol.* **51** 6099–112

Rehfeld N, Vauclin S, Stute S and Buvat I 2010 Multidimensional B-spline parameterization of the detection probability of PET systems to improve the efficiency of Monte Carlo simulations *Phys. Med. Biol.* **55** 3339–61

Rehfeld N S, Stute S, Apostolakis J, Soret M and Buvat I 2009 Introducing improved voxel navigation and fictitious interaction tracking in GATE for enhanced efficiency *Phys. Med. Biol.* **54** 2163–78

Rey M, Jan S, Vieira J M, Mosset J B, Krieguer M, Comtat C and Morel C 2007 Count rate performance study of the Lausanne ClearPET scanner demonstrator *Nucl. Instrum. Methods* A **571** 207–10

Rogers D and Mohan R 2000 Questions for comparison of clinical Monte Carlo codes *13th Int. Conf. on the Use of Computers in Radiation Therapy* ed W Schlegel and T Bortfeld (Heidelberg: Springer) pp 120–2

Rogers D W O, Faddegon B A, Ding G X, Ma C M, We J and Mackie T R 1995 BEAM: a Monte Carlo code to simulate radiotherapy treatment units *Med. Phys.* **22** 503–24

Santin G, Strul D, Lazaro D, Simon L, Krieguer M, Vieira Martins M, Breton V and Morel C 2003 GATE, a Geant4-based simulation platform for PET and SPECT integrating movement and time management *IEEE Trans. Nucl. Sci.* **50** 1516–21

Sarrut D and Guigues L 2008 Region-oriented CT image representation for reducing computing time of Monte Carlo simulations *Med. Phys.* **35** 1452–63

Schmidtlein C R *et al* 2006 Validation of GATE Monte Carlo simulations of the GE Advance/Discovery LS PET scanner *Med. Phys.* **33** 198–208

Schneider W, Bortfeld T and Schlegel W 2000 Correlation between CT numbers and tissue parameters needed for Monte Carlo simulations of clinical dose distributions *Phys. Med. Biol.* **45** 459–78

Seevinck P R, Seppenwoolde J H, de Wit T C, Nijsen J F W, Beekman F J, van het Schip A D and Bakker C J G 2007 Factors affecting the sensitivity and detection limits of MRI, CT, and SPECT for multimodal diagnostic and therapeutic agents anti-cancer agent *Med. Chem.* **7** 317–34

Segars W P, Lalush D S and Tsui B M W 2001 Modeling respiratory mechanics in the MCAT and spline-based MCAT phantoms *IEEE Trans. Nucl. Sci.* **48** 89–97

Segars W P, Tsui B M W, Frey E C, Johnson G A and Berr S S 2004 Development of a 4-D digital mouse phantom for molecular imaging research *Mol. Imag. Biol.* **6** 149–59

Seppenwoolde Y, Berbeco R I, Nishioka S, Shirato H and Heijmen B 2007 Accuracy of tumor motion compensation algorithm from a robotic respiratory tracking system: a simulation study *Med. Phys.* **34** 2774–84

Sonke J J, Rossi M, Wolthaus J, van Herk M, Damen E and Belderbos J 2009 Frameless stereotactic body radiotherapy for lung cancer using four-dimensional cone beam CT guidance *Int. J. Radiat. Oncol. Biol. Phys.* **74** 567–74

Staelens S, De Beenhouwer J, Kruecker D, Maigne L, Rannou F, Ferrer L, D'Asseler Y, Buvat I and Lemahieu I 2006 GATE: improving the computational efficiency *Nucl. Instrum. Methods Phys. Res.* A **569** 341–5

Staelens S, Strul D, Santin G, Vandenberghe S, Koole M, D'Asseler Y, Lemahieu I and Van de Walle R 2003 Monte Carlo simulations of a scintillation camera using GATE: validation and application modelling *Phys. Med. Biol.* **48** 3021–42

Taschereau R and Chatziioannou A F 2007 Monte Carlo simulations of absorbed dose in a mouse phantom from 18-fluorine compounds *Med. Phys.* **34** 1026–36

Taschereau R and Chatziioannou A F 2008 Compressed voxels for high-resolution phantom simulations in GATE *Mol. Imaging Biol.* **10** 40–7

Thiam C O, Breton V, Donnarieix D, Habib B and Maigne L 2008 Validation of a dose deposited by low energy photons using GATE/GEANT4 *Phys. Med. Biol.* **53** 3039–55

Van Der Laan D J, Maas M C, de Jong H W A M, Schaart D R, Bruyndonckx P, Lemaitre C and van Eijk C W E 2007 Simulated performance of a small-animal PET scanner based on monolithic scintillation detectors *Nucl. Instrum. Methods Phys. Res.* A **571** 227–30

Van Der Laan D J, Maas M C, Schaart D R, Bruyndonckx P, Léonard S and van Eijk C W E 2006 Using Cramér–Rao theory combined with Monte Carlo simulations for the optimization of monolithic scintillator PET detectors *IEEE Trans. Nucl. Sci.* **53** 1063–70

Van Der Laan D J, Schaart D R, Maas M C, Beekman F J, Bruyndonckx R and van Eijk C W E 2010 Optical simulation of monolithic scintillator detectors using GATE/GEANT4 *Phys. Med. Biol.* **55** 1659–75

Van Elmpt W, McDermott L, Nijsten S, Wendling M, Lambin P and Mojnheer B 2008 A literature review of electronic portal imaging for radiotherapy dosimetry *Radiat. Oncol.* **88** 289–309

Visvikis D, Bardies M, Chiavassa S, Danford C, Kirov A, Lamare F, Maigne L, Staelens S and Taschereau R 2006a Use of the GATE Monte Carlo package for dosimetry applications *Nucl. Instrum. Methods Phys. Res.* A **569** 335–40

Visvikis D, Lefevre T, Lamare F, Kontaxakis G, Santos A and Darambaravan D 2006b Monte Carlo based performance assessment of different animal PET architectures using pixellated CZT detectors *Nucl. Instrum. Methods Phys. Res.* A **569** 225–9

Wang L, Jacques S L and Zheng L 1995 MCML—Monte Carlo modeling of light transport in multi-layered tissues *Comput. Methods Prog. Biomed.* **47** 131–46

Welsh J S, Bradley K, Ruchala K J, Mackie T R, Mañjon R, Patel R, Wiederholt P, Lock M, Hui S and Mehta M P 2004 Megavoltage computed tomography imaging: a potential tool to guide and improve the delivery of thoracic radiation therapy *Clin. Lung Cancer* **5** 303–6

Zahra N, Frisson T, Grevillot L, Lautesse P and Sarrut D 2010 Influence of Geant4 parameters on dose distribution and computation time for carbon ion therapy simulation *Phys. Medica* **26** 202–8

Nuclear Instruments and Methods in Physics Research A 633 (2011) S111–S113

Contents lists available at ScienceDirect

Nuclear Instruments and Methods in Physics Research A

journal homepage: www.elsevier.com/locate/nima

Study of the charge sharing effect in the photon-counting pixel detector XPAD3-S

F. Cassol Brunner [a,*], D. Benoit [a], J.-F. Bérar [b], J.-C. Clémens [a], C. Morel [a]

[a] CPPM, Aix-Marseille Université, CNRS/IN2P3, Marseille, France
[b] D2AM-CRG, ESRF and Institut Néel, CNRS, Grenoble, France

ARTICLE INFO

Available online 19 June 2010

Keywords:
Hybrid pixel detectors
Charge sharing
X-ray imaging

ABSTRACT

The charge sharing effect in the single photon counting hybrid pixel detector XPAD3-S is studied. Several figures of merit are measured, both in the case of Si and CdTe sensors. Data are compared to a Monte Carlo simulation that models the main sources of charge migration.

1. Introduction

Hybrid pixel detectors developed originally for particle tracking in high energy physics experiments are very promising X-ray detectors for material science and micro-computed tomography. Hybrid pixel detectors are, however, affected by charge sharing between neighboring pixels [1]. This effect influences not only the spatial resolution and the measured energy spectrum, but also the detector count rate. Good knowledge of its role in the detector response is a precondition for correct interpretation of the detector data. We present a study of the charge sharing effect in the XPAD3-S module. Several figures of merit are measured as a function of the pixel energy threshold and compared to Monte Carlo predictions that include the modelling of the main charge sharing sources, such as the diffusion and the repulsion of the signal charges during their drift within the sensor.

2. Materials and methods

2.1. Detectors and X-ray sources

The XPAD3-S circuits are either connected to a Si (XPAD3-S/Si) or to a CdTe sensor (XPAD3-S/CdTe). The sensor thicknesses amount to 500 and 700 μm, respectively. A detailed description of the XPAD3-S chip can be found in Refs. [2,3]. The chips are composed of 9600 pixels with a 130 μm × 130 μm pixel pitch, organized in a 80 × 120 matrix, and allow the setting of an energy threshold for the detection of the photons. The used X-ray sources are either diffused monochromatic synchrotron beams of given energies (ESRF D2AM beam line) or a wide cone beam aperture X-ray tube.[1]

2.2. Monte Carlo simulation

In the case of the Si sensor, data are compared to Monte Carlo simulations. First, photon interactions in Si are simulated with a program based on the Geant4 package [4]. The energy along the electron tracks is recorded in steps of about 1 μm. Next, the production of electron–hole pairs inside the sensor and their repulsion and diffusion during the drift towards the cathode are simulated following the model proposed in Ref. [5]. These effects are indeed the main causes of charge sharing. Their introduction permits to correctly reproduce the measured data. Fig. 1 shows the simulated spectrum as it would be measured by a pixel in case of simple charge drift (full histogram), or of drift plus charge repulsion and diffusion (crossed line histogram), and the same with a pixel noise of 100 e^- (empty histogram).

3. Measurements and results

3.1. Charge sharing estimation

We estimate the charge sharing probability in the XPAD3-S detector, following the formulation proposed in Ref. [6]. The measured spectrum, for an incident energy E_0, is the sum of an unsplit charge component $n_p(E,E_0)$ and of a charge sharing component $n_{cs}(E,E_0)$

$$n(E,E_0) = (1-k)n_p(E,E_0) + kn_{cs}(E,E_0). \quad (1)$$

* Corresponding author.
E-mail address: cassol@cppm.in2p3.fr (F. Cassol Brunner).

0168-9002/$ - see front matter © 2010 Elsevier B.V. All rights reserved.
doi:10.1016/j.nima.2010.06.139

[1] MCBM 65 B-50, RTW (Germany) with a Molybdenum target and a 50 μm × 50 μm emission spot.

A Gaussian distribution is assumed with a width w (associated to energy dispersion due to the pixel noise) for $n_p(E,E_0)$, and $n_{cs}(E,E_0)$ ends to be constant and equal to $\Delta E/E_0$. Finally, k represents the charge sharing probability. The energy spectrum is indirectly measured by an energy threshold scan, giving the integral of the spectrum. Fig. 2 shows the scan results for one pixel irradiated with a 20 keV beam. The fit permits to estimate the parameters k and w. The spectrum obtained with the simulation is also shown and is in good agreement with the derivative of the data fit. Similar results are obtained for 14 and 22 keV radiations. The average value of k and w on 100 pixels are summarized in Table 1 for the two types of sensors exposed to 14 keV radiation.

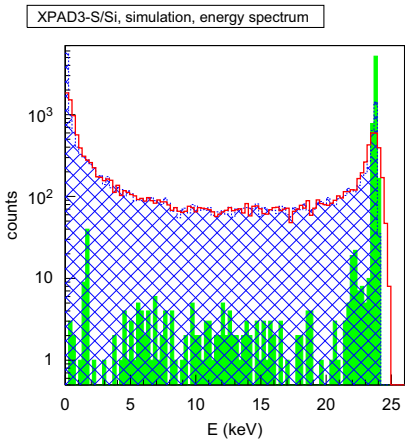

Fig. 1. Simulated spectrum as measured by XPAD3-S/Si for a monochromatic 24 keV beam. See the text for detailed explanations.

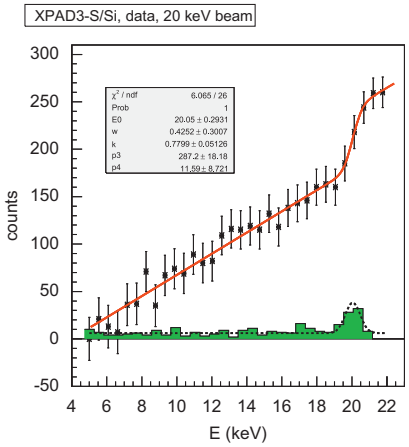

Fig. 2. Counts of one pixel for an energy threshold scan (star points) with a beam of 20 keV. The derivative (dashed line) of the fit (solid line) gives the energy spectrum as measured by XPAD3-S/Si. The simulated spectrum (green histogram) reproduces the flat energy component at low energies due to charge sharing between pixels. (For interpretation of the references to colour in this figure legend, the reader is referred to the web version of this article.)

3.2. Spatial uniformity

The charge sharing effect is responsible for nonuniformities in the pixel response. In fact, close to the pixel borders, charges migrate partially to the neighboring pixels, thus resulting in

Table 1
Charge sharing probability (k) and average energy resolution (w) with a 14 keV beam.

Sensor	Si	CdTe
k	0.75(0.76)	0.85
w (keV)	0.37(0.45)	0.45

The values in brackets correspond to the simulation results.

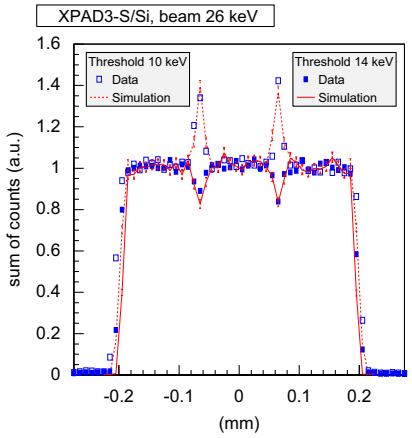

Fig. 3. Sum of counts on three pixels for a 26 keV beam scan centered on one pixel row of XPAD3-S/Si.

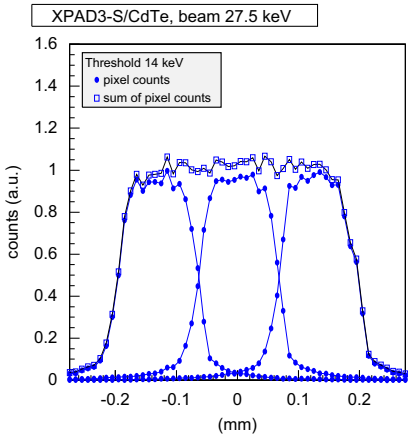

Fig. 4. Counts and sum of counts on three pixels of XPAD3-S/CdTe for a 27.5 keV beam scan. The threshold, which is close to one half of the beam energy, guarantees uniform global response between the pixels.

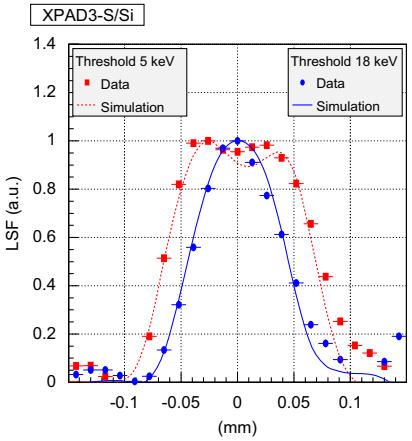

Fig. 5. LSF of XPAD3-S/Si at two different energy thresholds and comparison with the simulation results.

double signals in case of low thresholds, or in a loss of signal with high thresholds. We studied this effect by performing narrow pencil beam ($\sim 15\,\mu m \times 15\,\mu m$) scans with steps of $\sim 10\,\mu m$ at different pixel thresholds. The simulation reproduces correctly the data. Fig. 3 shows for XPAD3-S/Si the loss of signal between the pixels for a threshold above one half of the beam energy and the so-called double count effect otherwise. Fig. 4 presents, in the case of XPAD3-S/CdTe, the global uniformity that can be reached if the threshold is close to one half of the beam energy. In this case, the fact that the signal tails in the neighboring pixels are very pronounced is also due to the fluorescence effect associated to the Cd K-shell (26.7 keV).

3.3. *Spatial resolution*

The spatial resolution of XPAD3-S has been already presented in Ref. [7]. It is shown that the Line Spread Function (LSF) and the Modulation Spread Function (MTF) are independent of the sensor and mostly affected by the pixel energy threshold.[2] In fact, the effective pixel size is increased due to the charge sharing effect close to the pixel borders for lower thresholds. This work compares the results with the Monte Carlo simulation where correct modelling of the sources of charge sharing permits to reproduce the data, as shown in Fig. 5 for the LSF in the case of the XPAD3-S/Si detector and the IEC standard mammography radiation quality RQA3-M.

4. Conclusions

Several figures of merit are studied in order to estimate the effects of charge sharing in the XPAD3-S detector. A simple simulation that models the main sources of charge migration is sufficient to reproduce the data. For energies under the Cd K-shell, both types of sensors have a charge sharing probability of around 80%. The detector efficiency is uniform for an energy threshold equal to one half of the beam energy. For lower or higher thresholds, either double counts or count losses appear close to the border of the pixels. The spatial resolution dependence on the energy threshold is also correctly reproduced by the Monte Carlo simulation.

References

[1] K. Mathieson, Nucl. Instr. and Meth. A 487 (2002) 113.
[2] P. Pangaud, et al., Nucl. Instr. and Meth. A 591 (2008) 159.
[3] S. Basolo, et al., Nucl. Instr. and Meth. A 589 (2008) 268.
[4] J. Allison, Nucl. Phys. News 12 (2) (2007) 20.
[5] J. Durst, Ph.D. Thesis, Erlangen University, 2008.
[6] C. Ponchut, Nucl. Instr. and Meth. A 591 (2008) 311.
[7] F. Cassol Brunner, et al., Phys. Med. Biol. 54 (2009) 1773.

[2] 10% MTF at about 6.5(9.5) lp/mm for a 5(18) keV threshold, respectively.

Nuclear Instruments and Methods in Physics Research A 634 (2011) 85–90

Contents lists available at ScienceDirect

Nuclear Instruments and Methods in Physics Research A

journal homepage: www.elsevier.com/locate/nima

Neutron imaging with the XPAD3-S hybrid pixel detector

F. Cassol Brunner [a,b,*], N. Kardjilov [b], J.-C. Clémens [a], C. Morel [a]

[a] CPPM, Aix-Marseille Université, CNRS/IN2P3, Marseille, France
[b] Helmholtz Centre Berlin for Materials and Energy, Berlin, Germany

ARTICLE INFO

Article history:
Received 3 November 2010
Received in revised form
3 January 2011
Accepted 15 January 2011
Available online 26 January 2011

Keywords:
Hybrid pixel detectors
Neutron imaging

ABSTRACT

The X-ray photon counting hybrid pixel camera XPAD3-S is a promising detector for small animal X-ray radiography and tomography. The increasing interest in neutron imaging as a complementary approach to X-ray imaging motivates the study of the potentialities of this device for neutrons. To investigate this issue, we have studied the response of XPAD3-S to alpha particles and cold neutrons. The neutron detection was obtained with passive converters placed in front of the sensor. This choice permits to easily assemble 2D neutron sensitive imagers without size constraints; it penalizes however the detector efficiency with respect to other solutions. In this paper, we first analyze the detector response to alpha particles under several conditions, then we investigate its imaging performances and its detection efficiency for cold neutrons. Finally, we present the first XPAD3-S neutron tomography. Most of the results are validated by Monte Carlo simulations that will also permit to extrapolate the detector response to thermal neutrons.

1. Introduction

The photon counting hybrid pixel detector XPAD is a promising two-dimensional (2D) X-ray imaging technology for material science and micro-computed tomography [1–4]. Recently several authors have proposed the use of solid state detectors for imaging neutron beams [5–8]. Neutron tomography (NT) is indeed more and more considered as a complementary technique to X-ray tomography. In fact, due to the difference between the interactions of neutrons and X-rays in matter, NT permits to access material properties that cannot be observed with X-ray imaging. The characteristics of XPAD3-S such as its readout speed, dynamic range and fast gate, makes it an excellent candidate for neutron imaging.

We present a first study aiming at verifying the use of XPAD3-S to detect neutrons. The sensitivity to neutrons is obtained through conversion of incoming neutron flux into detectable particles by a passive ^{6}LiF layer, which converts neutrons to tritium and alpha particles easily detectable by the XPAD3-S sensor. The choice of a flat passive converter limits the detection efficiency to less than 10% [5], but it has the advantage to permit an easy conversion of this X-ray sensitive detector to a neutron sensitive detector. Actually, a removable converter can be easily designed whose size can be adapted to the detector surface without constraints.

First, we analyze the response of XPAD3-S to alpha particles. Then, we study the signal in response to cold neutrons. The detection efficiency was measured as a function of the converter thickness and the results are compared to Monte Carlo simulations that will also permit estimation of the detector response to different neutron energies. Finally, we present a first example of neutron tomography using XPAD3-S.

2. Materials and methods

2.1. Detectors

We consider XPAD3-S circuits connected to a 500 μm thick Si sensor. The chips are composed of 9600 pixels with a 130 μm × 130 μm pixel pitch, organized in a 80 × 120 matrix. A threshold can be set on the detected signal, corresponding to a linear energy threshold in case of X-ray detection. Table 1 summarizes the main characteristics of the XPAD3-S chip, of which a detailed description can be found in Ref. [9].

2.2. Neutron converters

In order to detect neutrons with hybrid pixels, we have to add to the device a converter that must optimize the neutron detection without deteriorating spatial resolution. Following the results of Jakubek et al. [5], the best passive neutron converter for this type of detectors is ^{6}LiF. The induced nuclear reaction is

$$^{6}\mathrm{Li} + \mathrm{n} \rightarrow \alpha(2.05\ \mathrm{MeV}) + {}^{3}\mathrm{H}(2.72\ \mathrm{MeV}) \quad (1)$$

* Corresponding author. Permanent address: CPPM, 163 Av. Luminy, 13288 Marseille, France. Tel.: +33 491827248; fax: +33 491827299.
E-mail address: cassol@cppm.in2p3.fr (F. Cassol Brunner).

0168-9002/$ - see front matter © 2011 Elsevier B.V. All rights reserved.
doi:10.1016/j.nima.2011.01.077

Table 1
Main characteristics of the XPAD3-S circuits.

Number of pixels	9600 (120 × 80)
Pixel size	130 μm × 130 μm
Selectivity mode	Single threshold
Counting rate	10^6 photons/pixel/s
Minimum pulse recovery time	500 ns
Readout time	2 ms
Global electronic noise	130 electrons

Table 2
Thickness and size of the ^{6}LiF converters.

Number	Thickness (mg/cm^2)	Thickness (μm)	Size (cm^2)
1	1.1	4	1 × 1
2	6.7	25	1 × 1
3	16.4	62	1 × 1
4	23.4	89	1 × 1
5	6.9	26	2 × 2

The produced alpha and tritium particles have a very short range in the Si sensor (see Section 3.1)

$R_\alpha = 8.6\ \mu m, \quad R_{^3H} = 44.1\ \mu m.$

Moreover, the absence of energetic gammas and conversion electrons guarantees that the signal remains local, and hence provides a good spatial resolution. We produced several converter sheets, each including a substrate of 500 μm thick polished silicon, on which a layer of ^{6}LiF was deposited. More precisely, the ^{6}LiF was mixed in a water solution of polyvinylalcohol, which acts as a glue, and painted with a fine brush on the substrate. The quantity of polyvinylalcohol was chosen so that the solution contains less than 5% atomic mass of polyvinylalcohol with respect to ^{6}LiF. The average thickness of the ^{6}LiF layer was estimated from the change in weight of the substrate for a given layer surface. Its homogeneity was assessed by the change in efficiency over the surface. For this, the active surface was divided into four areas and the uncertainty of the layer thickness was derived from the spread of the efficiencies determined within the four sub-areas. All layers have an efficiency variation of around 10%. Table 2 summarizes the characteristics of the used converters.

2.3. Radiation beams

Alpha particles of ~5.5 MeV are produced by an ^{241}Am source. The source has a surface of 0.5 × 0.5 cm^2. The distance between the source and the sensor can be varied and it is known with a precision of about 1 mm.

The neutrons used to measure the detector efficiency came from the V17 monochromatic beam line of the BER II reactor at the Helmholtz Zentrum Berlin (HZB). The beam energy is 7.3 meV ($\lambda = 3.35$ Å) and the absolute fluency is $(1.7 \pm 0.1)\ 10^4$ neutrons/(cm^2 s). This latter was measured with a ^{3}He monitor positioned in front of the detector. Finally, NT was performed at the V7 cold beam of the HZB. Its energy spectrum is shown in Fig. 1 and its fluency is equal to 10^7 neutrons/(cm^2 s). Fig. 1 also presents the spectrum of the thermal neutron beam of the BER II reactor. This spectrum was used in the Monte Carlo simulations to estimate the detector efficiency at higher neutron energies.

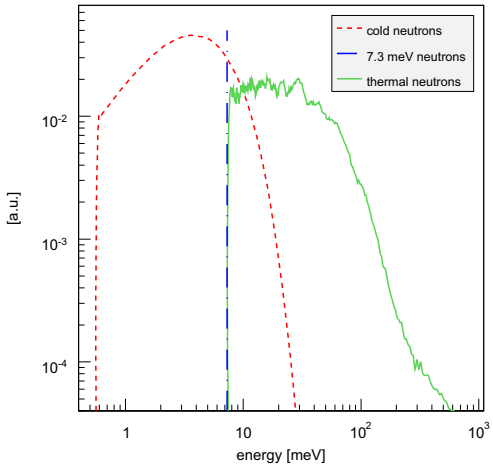

Fig. 1. Cold, thermal and monochromatic neutron energy spectra of the BER II reactor at HZB.

2.4. Monte Carlo simulations

In order to compare the detector response with Monte Carlo simulations, two simulation codes were used. The interactions of thermal and cold neutrons in ^{6}LiF and the subsequent production rates of alpha and tritium particles were simulated with MCNP [10], whereas the particle tracking in the converter and its energy deposition in the Si sensor were studied with Geant4 [11,12]. We estimated the total production of alpha/tritium particles per interacting neutron in successive conversion layers of 5 μm thickness each.[1] Fig. 2 presents the production rate as a function of the converter thickness for the three beams described in Fig. 1. The detector counting rate is then estimated as follows: we considered the converter as a source of alpha/tritium particles and we simulated with Geant4 several converters composed of one or more layers, each with an activity corresponding to the alpha/tritium production rate estimated by MCNP. The Geant4 simulation models all interaction processes of particles in matter, it describes therefore correctly the escape probability of the alpha and tritium particles from the ^{6}LiF layer. More precisely, electromagnetic processes are simulated with the "Standard" Geant4 physics list, whereas hadronic processes with the "LHEP_PRECO_HP" physics list which performs a parametrized modeling of hadronic interactions. The converter was placed in close contact with the silicon sensor and every alpha/tritium particle that reaches the detector was assumed to be detected. The results of the simulation are presented together with measurements.

3. Measurements and results

3.1. Response to alpha particles

We placed the ^{241}Am source in front of the detector and vary its distance to the detector from 1 to 4 cm in order to study its

[1] For the sake of precision the first 5 μm layer was further subdivided into steps of 1 μm.

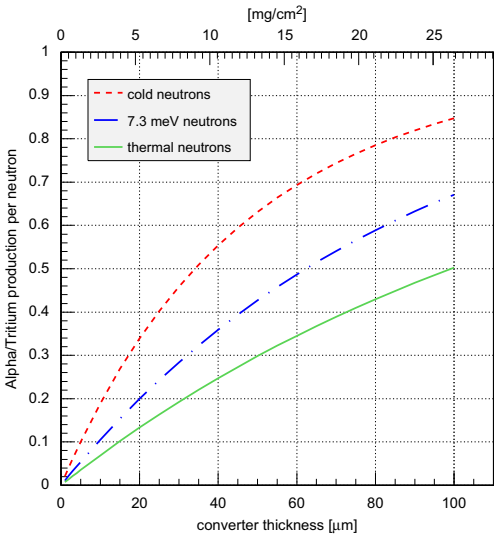

Fig. 2. Production of alpha/tritium particles simulated with MCNP as a function of the ^{6}LiF converter thickness for the cold, thermal and 7.3 meV neutron beams of Fig. 1.

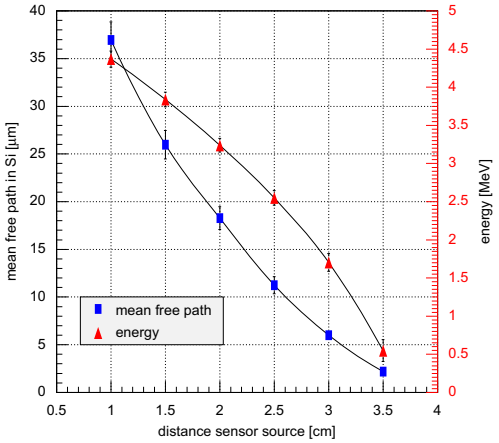

Fig. 3. Mean free path in Si (left vertical axis) and average energy at the sensor surface (right vertical axis) of simulated alpha particles emitted by a ^{241}Am source as a function of its distance to the detector.

response as a function of the alpha energy. The alphas emitted by the ^{241}Am source have an energy of 5.5 MeV. After traveling 2.8 cm in air, their energy is close to 2.0 MeV, corresponding to the energy of the alphas emitted by the ^{6}LiF converter. Fig. 3 presents the expected energy at the sensor surface and the corresponding mean free path (MFP) in the silicon sensor estimated by the simulation. It is less than 10 μm for 2.05 MeV alphas, and remains quite short for alpha energies below 5 MeV.

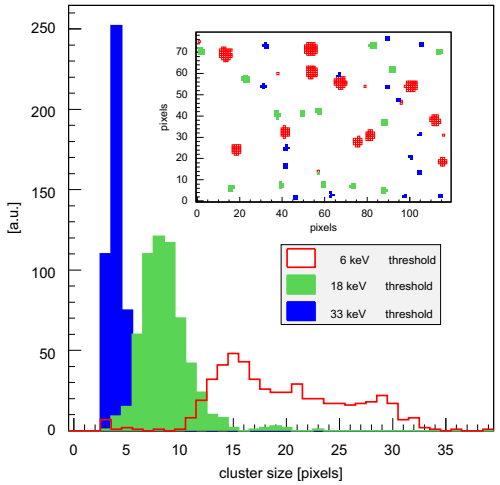

Fig. 4. Alpha signal and its size distribution for 1.7 MeV alphas measured at three different signal thresholds.

The signal associated to the detection of an alpha particle is a cluster of counting pixels. We employed a simple cluster algorithm to select isolated clusters far from the borders. Fig. 4 presents the clusters produced by 1.7 MeV alphas at three different signal thresholds[2] and the corresponding cluster size distributions. In the case of the lower threshold (6 keV), we observe an asymmetry in the cluster sizes (up-down in the insert of Fig. 4) that explains the broader distribution for this threshold. This effect is likely to be due to a different threshold adjustment in the top and in the bottom of the chip. The mean cluster size as a function of the alpha energy can be seen in Fig. 5, where the error bars correspond to the root mean square (RMS) of the distributions. The mean size increases linearly with the energy and can reach more than 30 pixels with the lower threshold. Hence, a certain amount of the charges are shared not only with adjacent but also with more distant pixels. The shared charges correspond however to a small fraction of the total particle signal. Indeed, a small increase of the threshold of a few tenths of keV reduces considerably the cluster sizes.

If we look at the detection rate, we observe that increasing the threshold does not change the detection efficiency, except for the 0.5 MeV alphas. In this case in fact, the detection rate is reduced by 10% and 53%, with a 18 keV and a 33 keV threshold, respectively. This is probably due to the very short MFP in Si at this energy (2.2 μm), giving a reduced charge collection, as well as to some energy loss in the Al contact of the sensor.

The signal does not present a strong dependence on the applied bias voltage for values higher than the total depletion voltage (80 V). Fig. 6 shows the results for 4.4 and 1.7 MeV alphas for two different signal thresholds. At lower voltages, we see first an increase of the mean cluster size, probably due to the reduced strength of the electric field, which results in an increase of charge sharing. Then, a decrease of the mean cluster size can be observed, due to a general reduction of the charge collection. For voltages under 10 V, we see also a loss of efficiency.

[2] Here and later on in this paper the value in keV of the signal threshold is meant for X-ray detection.

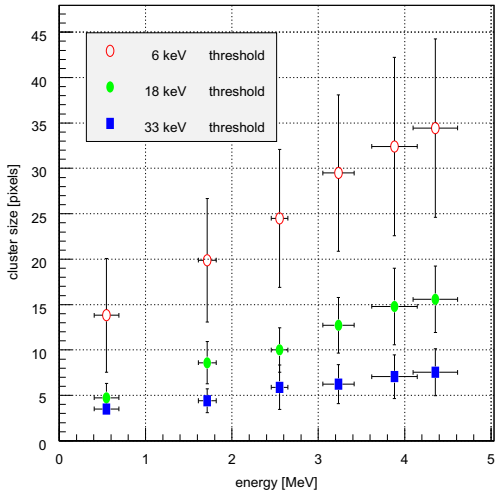

Fig. 5. Mean cluster size as a function of the alpha energy measured at three signal thresholds.

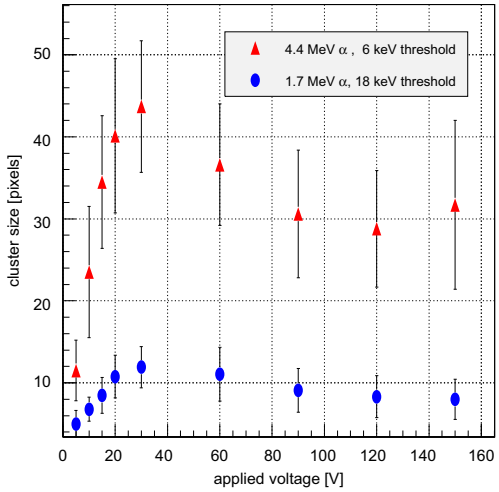

Fig. 6. Mean cluster size as a function of the bias voltage for two different alpha energies and signal thresholds.

The spatial resolution associated to alphas is verified by measuring the Line Spread Function (LSF) of the system. This is derived by the image of the sharp edge of a razor blade positioned at 2 mm from the sensor. Fig. 7 presents the smoothed edge profile and the derived LSF in the case of 1.7 MeV alphas and a 33 keV signal threshold. The full width at half maximum of the LSF is equal to 1.8 pixels and degrades to 2.5 pixels for a 6 keV threshold.

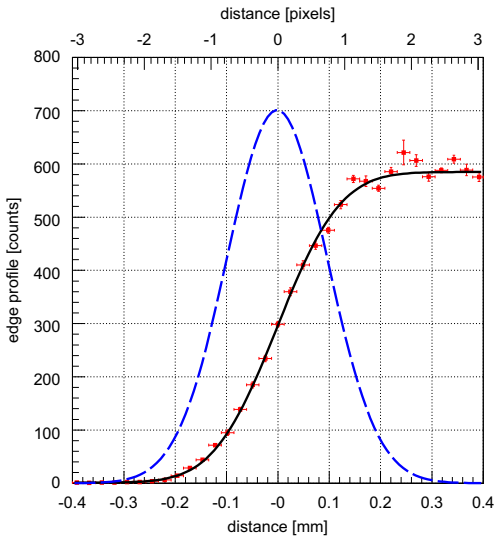

Fig. 7. Smoothed profile of the image of a sharp edge (points) and derived LSF (dashed line) in case of 1.7 MeV alphas detected with a 33 keV signal threshold.

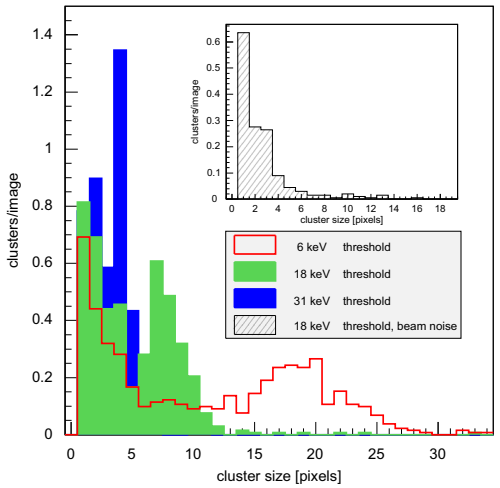

Fig. 8. Cluster size distributions of neutron induced signals at three different signal thresholds and cluster size distribution of the beam noise.

3.2. Response to cold neutrons

We studied the detector response at the V17 monochromatic cold neutron beam. The converter was placed in close contact with the silicon sensor. As deduced from the study of the detector response to alpha particles, each neutron induced signal corresponds to a cluster of pixels. Fig. 8 presents the cluster size distribution measured with three different signal thresholds. The

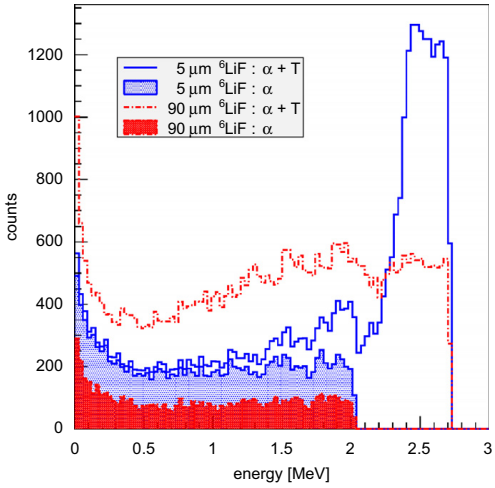

Fig. 9. Energy spectra of simulated alpha and tritium particles reaching the sensor after being generated in converters of 5 and 90 µm thickness, respectively.

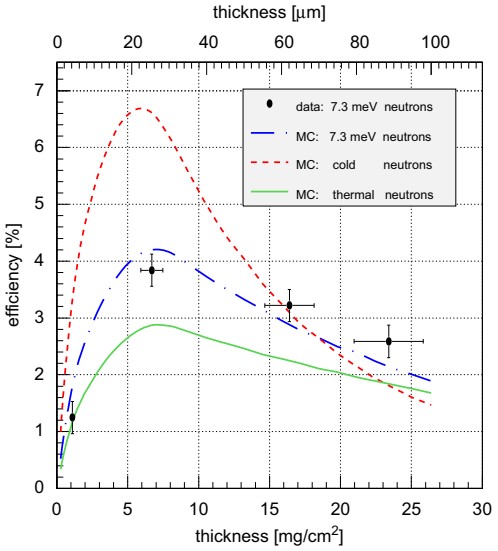

Fig. 10. Neutron detection efficiency as a function of the ^{6}LiF thickness for measured and simulated data.

distributions are similar to those obtained with alpha particles (Fig. 4), except for the presence of a peak at cluster sizes smaller than 4 pixels. This is mainly due to a noise of gammas and electrons coming from the beam, which can be measured by removing the converter (dashed histogram in Fig. 8). The remaining clusters at smaller sizes are related to signals coming from the converter, they are probably associated to particles that have reached the sensor after a loss of energy in the ^{6}LiF layer (see Fig. 9 for two examples of energy spectrum as given by the Monte Carlo simulation).

Like for alpha particles, the spatial resolution is estimated with a razor blade edge placed in front of the sensor. For the LSF measured with a 31 keV signal threshold, we confirm the result of 1.8 pixels obtained for alpha particles.

The detector efficiency is estimated as follows. We select 50×50 pixels placed in the center of the converter. The acquisition time was preset to 50 ms in order to avoid the superposition of clusters in the same image. For each configuration, we acquired 100 images and estimated the average number of clusters per second and per surface unit. The measured efficiency as a function of the converter thickness (converters Nb. 1–4 as from Table 2) is presented in Fig. 10 together with the Monte Carlo results for three different beams. Measured and simulated data are in fairly good agreement. In all cases, the efficiency is maximal for a converter thickness of 6–7 mg/cm^2. The same converter will therefore be optimal both for thermal and cold neutrons.

3.3. Tomographic reconstruction

We performed a first tomography of a tooth using the V7 cold beam line. For this, we had to use a new beta version of the detector (XPAD3.2-S) with gating capabilities, together with the converter Nb. 5 (as from Table 2) that covers the whole sensor. The object was placed on a rotating table just in front of the chip. The reconstruction is based on 180 acquisitions of 10 s each, for a total rotation of 180°. We observe a rather large distribution in the flat field pixel counting rate due to the converter inhomogeneities, but also to the approximative threshold calibration performed with the test pulse of the circuit. We estimate that the applied signal threshold was equivalent to 8 keV for X-rays, still too low for an optimal result with neutrons. Fig. 11a shows an example of a raw projection. The white pixels correspond to defective pixels. Before reconstruction, we rejected the first 12 columns on the left, which count less events due to a thinner converter thickness. We also performed a flat field correction (Fig. 11b) and set a value to the defective pixels by using a linear interpolation between the neighboring pixels of the same column (Fig. 11c). The reconstruction was then performed with a standard FBP algorithm for parallel beams. Three slices of the reconstructed image are shown in Fig. 12.

4. Conclusions

The potentialities of the XPAD3-S detector for 2D neutron imaging have been investigated using a simple passive neutron converter. The optimal converter thickness is 6–7 mg/cm^2 for cold and thermal neutrons. The signal threshold must be set to high values (>30 keV) in order to reduce the charge sharing effect, which strongly affects ion detection. The imaging system reaches a spatial resolution close to 200 µm with an efficiency of 7% in the case of cold neutrons. The results are in general agreement with Monte Carlo simulations, which allowed to estimate an efficiency of less than 3% for thermal neutrons. We expect an improvement of image quality by the use of better converters with a more uniform thickness and by better control of the signal threshold setting.

Finally, we like to observe that an external passive converters permits easy transformation of the XPAD3-S from X-ray detection to detection of neutrons. The converter can be removable, modular and easily adaptable to any detection surface.

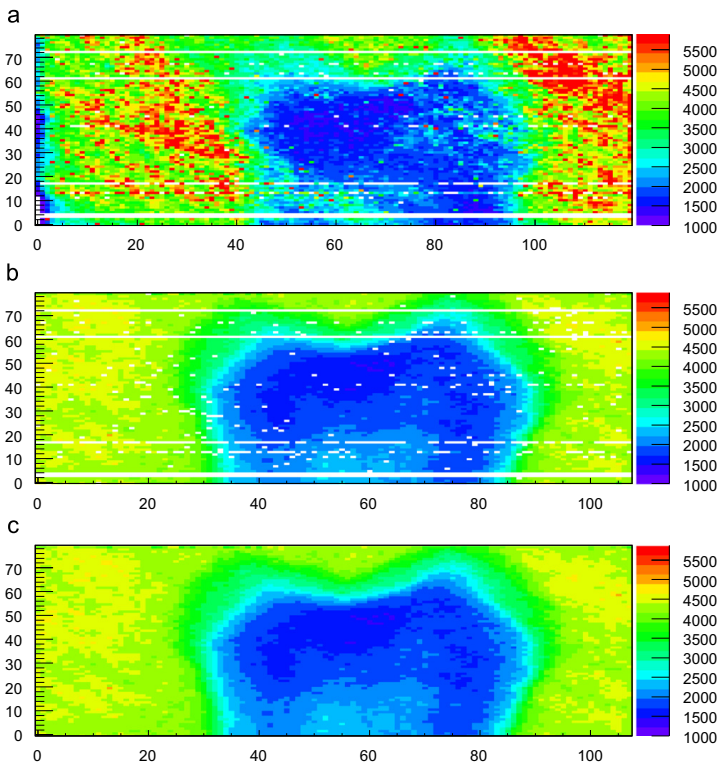

Fig. 11. Neutron radiography of a tooth with XPAD3.2-S under a cold neutron beam: raw data (a), corrected for flat field (b), and corrected for defective pixels (c).

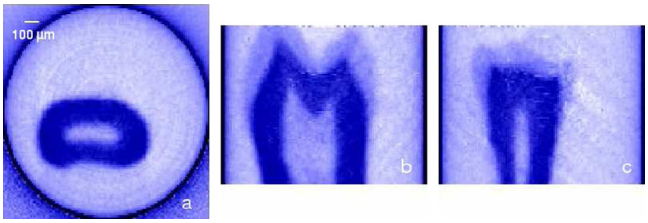

Fig. 12. Transverse (a), coronal (b) and sagittal (c) slices of the reconstructed image of a tooth with the XPAD3.2-S detector irradiated by a cold neutron beam.

Acknowledgements

The authors are grateful to Dr. Ingo Manke for the stimulating discussions. They would like to thank Svyatoslav Alimov and Christian Schulz for the support at the HZB neutron beam lines. Finally, they thank Dr. Burkhard Schillinger for kindly providing the ^{6}LiF powder.

References

[1] F. Cassol Brunner, et al., Phys. Med. Biol. 54 (2009) 1773.
[2] F. Debarbieux, et al., IEEE Trans. Nucl. Sci. NS-57 (2010) 242.
[3] P. Pangaud et al., First results of XPAD3, a new photon counting chip for X-ray CT-scanner with energy discrimination, in Conference Records of "2007 IEEE Medical Imaging Conference", Honolulu, Hawaii, October 2007, pp. 14–18.
[4] J.-F. Bérar, et al., Nucl. Instr. and Meth. A 607 (2009) 233.
[5] J. Jakubek, et al., Nucl. Instr. and Meth. A 560 (2005) 143.
[6] D.S. McGregor, et al., Nucl. Instr. and Meth. A 606 (2009) 608.
[7] J. Uher, et al., Nucl. Instr. and Meth. A 576 (2007) 32.
[8] A.S. Tremsin, et al., Nucl. Instr. and Meth. A 592 (2008) 374.
[9] P. Pangaud, et al., Nucl. Instr. and Meth. A 591 (2008) 159.
[10] MCNP—A General Monte Carlo N-Particle Transport Code—Version 5 〈http://mcnp-green.lanl.gov/〉.
[11] F. Cassol Brunner, et al., Nucl. Instr. and Meth. A (2010). doi:10.1016/j.nima.2010.06.139.
[12] J. Allison, Nucl. Phys. News 12 (2) (2007) 20.

First K-Edge Imaging With a Micro-CT Based on the XPAD3 Hybrid Pixel Detector

Franca Cassol Brunner, Mathieu Dupont, Christophe Meessen, Yannick Boursier, Hamid Ouamara, Alain Bonissent, Carine Kronland-Martinet, Jean-Claude Clémens, Franck Debarbieux, and Christian Morel

***Abstract*—We investigate the capability to perform K-edge imaging with the newly developed micro-CT PIXSCAN based on the XPAD3 hybrid pixel detector. The XPAD3 detector surface of $8\ \mathrm{cm} \times 11\ \mathrm{cm}$ makes it possible to perform whole body mouse imaging. We present a proof of principle of K-edge imaging of mouse-size phantoms filled with Silver and Iodine solutions. Results are compared with standard X-ray absorption tomography for several solution densities.**

***Index Terms*—Hybrid integrated circuits, image enhancement, pixel sensors, X-ray tomography.**

I. Introduction

HYBRID pixel detectors are a new generation of digital X-ray detectors used for photon counting instead of charge integration. This novel approach involves several advantages [1], among which the absence of dark noise and the ability to set an energy threshold for the detected photons are of uppermost importance for the development of X-ray imaging modalities that will exploit spectral information on the detected X-rays. In the past, several authors have indeed pointed out the benefits of photon spectral information in computed tomography, see e.g., [2]–[4]. Energy resolving detectors, with two or more energy bins, permit material decomposition thanks to the dependency of the attenuation coefficient on the X-ray energy, which is specific to each element. The increase of contrast to noise ratio (CNR) for a given material can be maximized by choosing the optimal energy bins and/or performing proper image weighting, either at the projection [5] or at the reconstruction image stage [6]. In the case of elements presenting their K-edge within the X-ray tube energy spectrum, two energy bins, one below and one above a given K-edge value, are sufficient to permit the identification of the selected contrast material and to increase its CNR. If more than two materials have to be quantified, more energy bins must then be taken into consideration [3], [7], [8].

Manuscript received February 13, 2012; revised June 18, 2012; accepted August 30, 2012. Date of publication August 30, 2012; date of current version February 06, 2013.

F. Cassol Brunner, M. Dupont, C. Meessen, Y. Boursier, H. Ouamara, A. Bonissent, C. Kronland-Martinet, J.-C. Clémens, and C. Morel are with the CPPM, Aix-Marseille Université, CNRS/IN2P3, Marseille 13288, France (e-mail: cassol@cppm.in2p3.fr; mdupontcassol@cppm.in2p3.fr; boursiercassol@cppm.in2p3.fr; ouamaracassol@cppm.in2p3.fr; bonissencassol@cppm.in2p3.fr; kronlandcassol@cppm.in2p3.fr; clemenscassol@cppm.in2p3.fr; morel}cppm.in2p3.fr; meessen@cppm.in2p3.f).

F. Debarbieux is with the IBDML, Aix-Marseille Université, CNRS, Marseille 13288, France (e-mail: debarbieux@cppm.in2p3.fr).

Color versions of one or more of the figures in this paper are available online at http://ieeexplore.ieee.org.

Digital Object Identifier 10.1109/TNS.2012.2217753

TABLE I
Characteristics of the XPAD3 Chip.

Number of pixels	9600 (80 × 120)
Pixel size	130 μm × 130 μm
Input polarity	Hole collection
Selectivity mode	Single threshold
Counting rate	Up to 10^6 photons/pixel/s
Readout time	2 ms/frame
Global electronic noise	130 e^- rms
Threshold adjustment resolution	200 e^- rms
Threshold adjustment dispersion	57 e^- rms
Minimum threshold	4 keV

We investigate the capability to perform K-edge imaging with the newly developed micro-CT PIXSCAN, based on the XPAD3 hybrid pixel detector [9]–[11]. The detector surface of $8\ \mathrm{cm} \times 11\ \mathrm{cm}$ (500 kpixels of 130 $\mu\mathrm{m} \times 130\ \mu\mathrm{m}$) permits to perform whole mouse K-edge imaging without any detector translation, as it is indeed required for smaller hybrid pixel scanners with similar spectrometric capabilities [12]–[14]. After proper pixel calibration, K-edge imaging is obtained by changing the pixel threshold around the K-edge value of the selected contrast agents. We image mouse-size phantoms filled with Silver and Iodine solutions. In order to appreciate the basic detector capabilities, we have just considered the difference of the images in the selected energy bands, without applying any specific energy weighting algorithm. Results are compared with standard absorption tomography.

II. Imaging System

The XPAD3 circuits are connected to a $500\ \mu\mathrm{m}$ thick Si sensor and form hybrid pixels of $130\ \mu\mathrm{m} \times 130\ \mu\mathrm{m}$. Table I summarizes the main characteristics of the XPAD3 chip, a more detailed description can be found in [9]. The high counting rate (10^6 photons/pixel/s) and the fast read out (up to 2 ms/frame) make this device very suitable for computed tomography and imaging in high flux synchrotron beams. Its photon counting mode allows for diagnostic CT imaging at low photon statistics, hence low irradiation dose [15]. However, the main feature that concerns this study is the possibility to set a lower threshold on the energy of the detected photons (cf. Section III).

The whole detector consists of 8 modules of 7 XPAD3 chips of 80×120 pixels tiled to form an overall sensitive surface of $8\ \mathrm{cm} \times 11\ \mathrm{cm}$. The imaged object is placed on a rotating plate in between the detector and the X ray source, which provides a wide aperture cone beam (Fig. 1). The distance between the detector and the tube is 437 mm and the distance between the rotation table and tube is 235 mm. Two X-ray tubes are used for this study: a Molybdenum target tube RTW-MCBM 65B-Mo (RTW,

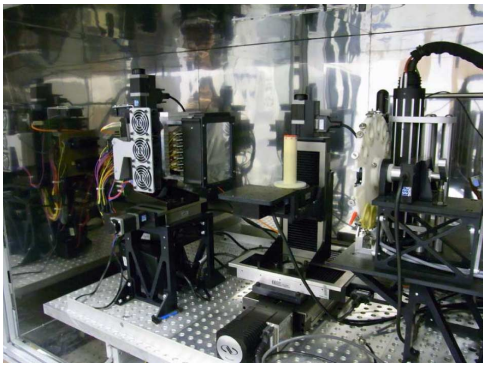

Fig. 1. Picture of the PIXSCAN micro-CT prototype. The XPAD3 detector can be seen on the left side; at the center, the cylindrical phantom used in this study is set on the rotating table; the RTW Mo target X-ray tube, together with the wheel holding different filters are located on the right side.

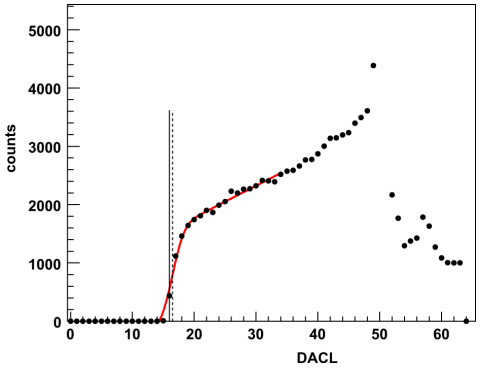

Fig. 2. Counting rate of one pixel for a DACL scan with a monochromatic beam of 25.5 keV. The dashed line indicates the float value corresponding to the beam energy as suggested by the fit, the plain line shows the most closed available DACL value.

Berlin, Germany) with a $50\ \mu\mathrm{m} \times 50\ \mu\mathrm{m}$ emission spot and a Tungsten target tube Microfocus 90KV TGT (Oxford Instruments, Scotts Valley CA, U.S.A.) with a $30\ \mu\mathrm{m} \times 30\ \mu\mathrm{m}$ emission spot. Geometrical alignment of the micro-CT is obtained from the scan of steal-balls glued inside a hollow cylinder. Geometrical parameters are derived form the trajectories of the shadows of the balls on the detector [16].

III. Pixel Energy Calibration

The energy of the single threshold of each pixel results from a global 8-bit DAC (ITH) set for all pixels of a chip and from a local 6-bit DAC (DACL) individually set per pixel. This latter is used to recover the dispersion of the thresholds within the chip [10]. For this, two methods of calibration have been developed. The first one is using monochromatic X-ray beams delivered by synchrotron light sources. The second one is based on K-edge values of metallic filters used with polychromatic X-ray tubes. Both calibration methods are described in the next two subsections.

A. Calibration Using Monochromatic X-ray Beams

Calibration of pixel thresholds is generally performed at synchrotron beam lines, which can provide monochromatic X-ray beams. Each chip of the detector is calibrated at a given energy the following way. First, a scan on ITH with DACL fixed to its middle range value $(\mathrm{DACL} = 32)$ allows for determining the global threshold level of each chip defined as the minimum ITH value for which more than half of the pixels are counting. Then, a second scan on DACL, with ITH fixed to the resulting value of the first scan, allows for setting precisely the threshold value corresponding to the energy of the beam. This value is determined from a fit of the typical S-curve response function of the pixel, as shown in Fig. 2 for a 25.5 keV beam delivered by the ESRF D2AM beam line. Contrary to ITH, increasing DACL values correspond to decreasing threshold energies with steps of around 0.6–0.7 keV. The pixel starts to count when the threshold value approaches the beam energy, which corresponds to the center of the S-curve. In Fig. 2, the calibrated DACL value (full line) is the closest integer of the floating point DACL (dashed line) resulting from the fit. It is worth noticing that the linear increase of the counts beyond the S-curve is due to the charge sharing between neighbor pixels as shown in [18]. Above this part, the highest point of the response function corresponds to the noise level of the pixel.

B. Calibration on K-edge Values of Filters

The procedure described in the previous subsection requires to move the scanner to a synchrotron facility and does not permit to easily perform a periodic check of the threshold settings. Therefore, we developed a new calibration method based on the use of filters of the same material as the contrast agents we want to study using K-edge tomography. The K-edge value of a given contrast agent, which consists in a sudden increase of its attenuation coefficient with energy, is responsible for a fall of the number of photons passing through the filter. Fig. 3 shows the measured energy spectrum of X-rays that have passed through $50\ \mu\mathrm{m}$ of Ag using the W target tube operated at 60 kVp. The difference between measured and Geant4 simulated data is due to the energy resolution of the spectrometer XR-100T-CdTe (Amptek, Bedford MA, U.S.A) that we used to measure the X-ray energy spectrum. In this case, ITH and DACL threshold scans allows for identifying the threshold levels that corresponds to the energy of the K-edge value of the metallic filter. The K-edge search algorithm looks for a steep change in the count slope. The same search algorithm is used for both the ITH and the DACL scans. First the ITH scan is performed with DACL set to 32, which provides a different ITH value for each pixel. The mean of these ITH values over the chip is used for the DACL scan, which provides the final threshold settings of each pixel. As an example, Fig. 4 shows a DACL scan of the spectrum displayed on Fig. 3 for all pixels of one column of a chip. Each pixel response is translated by the DACL value determined by the search algorithm, which is

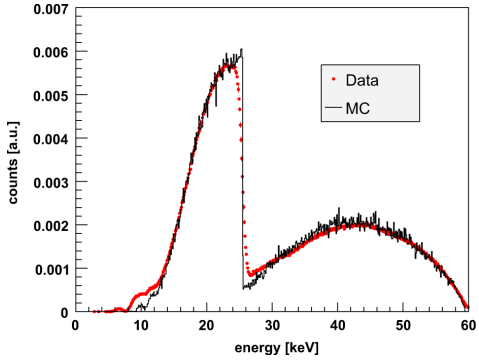

Fig. 3. X-ray energy spectrum after 50 μm Ag attenuation (W target, 60 kVp).

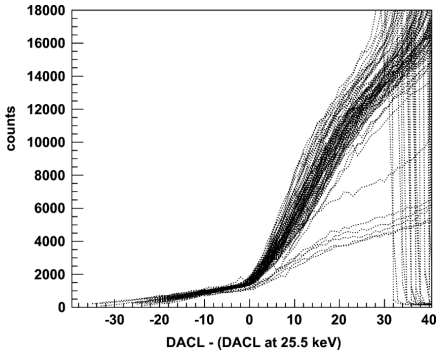

Fig. 4. Response curves resulting from DACL scans of individual pixels irradiated with the X-ray spectrum displayed in Fig. 3. The curves are shifted by the DACL value determined at the K-edge of the filter (25.5 keV).

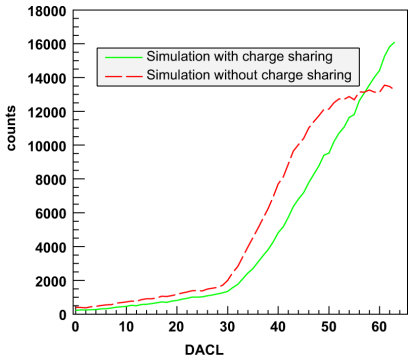

Fig. 5. Simulated DACL scans of the spectrum displayed in Fig. 3 with (full line) or without (dashed line) charge sharing with a DACL value at the Ag K-edge (25.5 keV) equal to 29.

assumed to correspond to the K-edge energy of the filter (25.5 keV).

In order to evaluate the precision of the K-edge search algorithm, we simulated DACL scans with a Monte Carlo code based on Geant4 [17]. The code includes the modelisation of

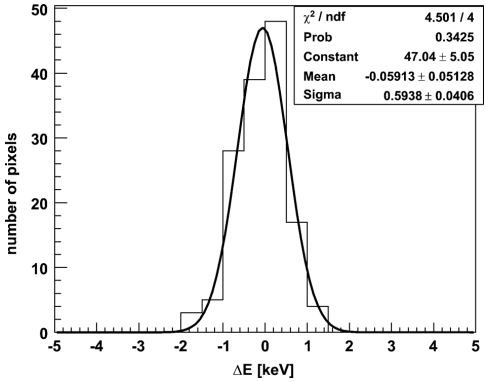

Fig. 6. Energy dispersion of the pixel threshold calibration at the Ag K-edge energy (25.5 keV) as estimated by the Monte Carlo simulation.

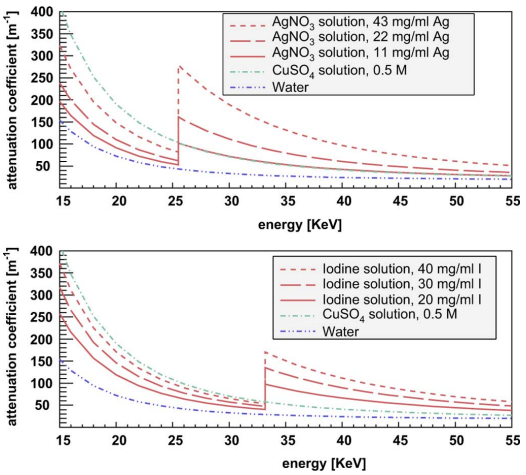

Fig. 7. Expected attenuation coefficients for the solutions filling the inserts of the cylindrical phantom.

repulsion and diffusion of electron-hole pairs during the drift towards the cathode inside the Si sensor and correctly reproduces the charge sharing between neighbor pixels [18]. In fact, this effect modifies the shape of the DACL scan curves, as shown in Fig. 5 by comparing two Monte Carlo curves simulated with and without charge sharing. For this, the simulated DACL for 25.5 keV was equal to 29. Hence, the search algorithm must take into account the effect of charge sharing in order to return the correct calibrated DACL. We apply the K-edge search algorithm to simulated DACL scans in a matrix of 12×12 pixels. A threshold energy dispersion of 0.6 keV is estimated after calibration from the difference between the calibrated threshold energy and 25.5 keV (Fig. 6).

IV. K-Edge Imaging if Iodine and Silver Solutions

K-edge imaging is obtained by changing the pixel threshold around the K-shell binding energy of the selected contrast

TABLE II
LIST OF IMAGED SOLUTIONS.

Nr.	Solution	Concentration
1	Water	-
2	$AgNO_3$	118 mg/ml Ag
3	$AgNO_3$	43 mg/ml Ag
4	$AgNO_3$	22 mg/ml Ag
5	$AgNO_3$	11 mg/ml Ag
6	Iomeron	95 mg/ml I
7	Iomeron	40 mg/ml I
8	Iomeron	30 mg/ml I
9	Iomeron	20 mg/ml I
10	$CuSO_4$	0.5 M
11	$CuSO_4$	1.0 M

TABLE III
ENERGY VALUES CHOSEN TO DEFINE THE INTERVALS AROUND THE K-SHELL ENERGY OF SILVER AND IODINE.

Silver	Iodine
$E_{1Ag} = 21.0$ keV	$E_{1I} = 25.5$ keV
$E_{2Ag} = 25.5$ keV	$E_{2I} = 33.2$ keV
$E_{3Ag} = 33.2$ keV	$E_{3I} = 40/50$ keV

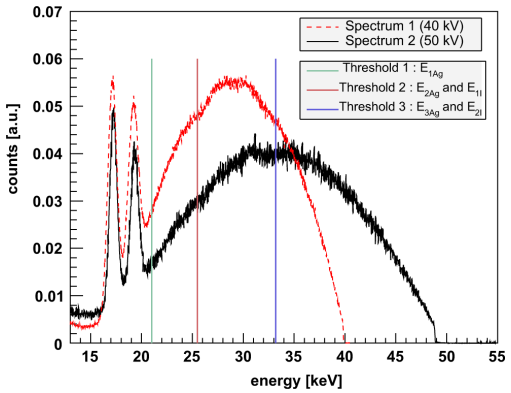

Fig. 8. X-ray energy spectra used for the K-edge imaging generated from a RTW Mo target tube operated at 40 kVp (Spectrum 1) or 50 kVp (Spectrum 2) through a Cu filter of 100 μm.

agents. For a given binding energy E_K, we acquired images at three different thresholds: $E_1 = (E_K - \Delta E_1)$, $E_2 = E_K$ and $E_3 = (E_K + \Delta E_3)$ with ΔE_i of a few keV. The comparison of the differences $(E_1 - E_2)$ and $(E_2 - E_3)$ permits to enhance the contrast of the selected contrast agent, thanks to the increase in absorption right above its K-edge value.

We selected Iodine and Silver for demonstrating simultaneous contrast agents identification with respect to other similarly absorbing materials. Table II lists the solutions under study. The expected attenuation coefficients calculated using NIST [19] for some of the solutions of Table I are shown in Fig. 7 as a function of the photon energy. The K-edge value of Ag and I are 25.5 and 33.2 keV respectively. The energy

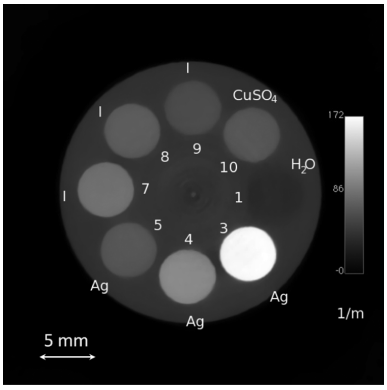

Fig. 9. Transverse slice of data acquired with Threshold 2 (25.5 keV) and reconstructed with MAP-TV. The numbers aside the inserts correspond to the solutions listed in Table II.

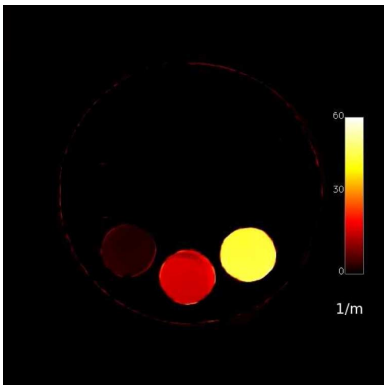

Fig. 10. Silver solutions appear as positive CT numbers on the subtraction of the windowed slices $(E_{2Ag} - E_{3Ag}) - (E_{1Ag} - E_{2Ag})$.

interval that we chose for the two materials are defined by the energies listed in Table III.

We imaged two phantoms, a "cylindrical phantom" with eight inserts and a "twisted phantom" given by three twisted rubber pipes. The inserts and the pipes were filled with the solutions listed in Table II. We used the X-ray energy spectra shown in Fig. 8, which are given by a Mo tube operated at 40 or 50 kVp and a Cu filter 100 μm thick. In all cases, one CT scan corresponds to 360 projections (10 s/frame) spaced by a 1 degree rotation step. For each phantom, three CT scans were performed at the three energy thresholds shown in Fig. 8: Threshold 1 = 21.0 keV, Threshold 2 = 25.5 keV and Threshold 3 = 33.2 keV. The photon statistics in the flat field depends strongly on the applied threshold. A minimum statistics of about 600 photons/pixel was acquired for the first spectrum with Threshold 3 and a maximum statistics of about 11,000 photons/pixel for the second spectrum with Threshold 1.

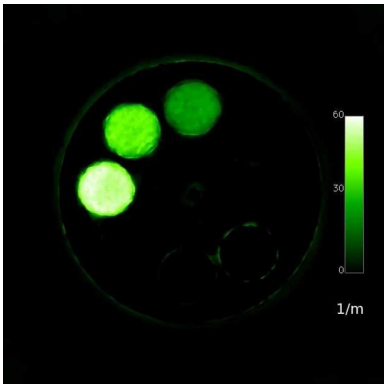

Fig. 11. Iodine solutions appear as positive CT on the subtraction of the windowed slices $(E_{2I} - E_{3I}) - (E_{1I} - E_{2I})$.

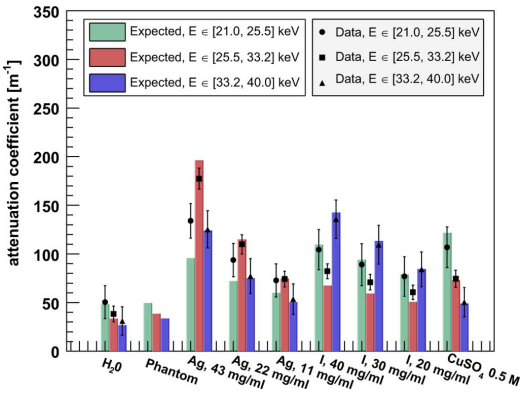

Fig. 12. Calculated and FDK reconstructed attenuation coefficients within the considered energy windows.

Image reconstructions were performed both using the FDK [20] and the iterative MAP-TV [21] algorithms.

A. Cylindrical Phantom

The cylindrical phantom (10 cm height and 2.8 cm external diameter) is made of epoxy resin and has eight inserts of 5 mm diameter filled with the solutions Nr. 1, 3, 4, 5, 7, 8, 9, 10 listed in Table II. The first spectrum was used to image this phantom. Fig. 9 shows a transverse slice of data acquired with Threshold 2 (25.5 keV) and reconstructed with the MAT-TV algorithm. Indeed, the Silver, Iodine and Copper solutions cannot be identified on this image right on the base of standard absorption CT. For instance, inserts Nr. 5 and 10 have almost the same CT number despite they are filled with two different materials. In K-edge imaging the contrast of Silver or alternately of Iodine is enhanced by subtracting the slices reconstructed from data acquired within the energy bands[1] $(E_2 - E_3)$ and $(E_1 - E_2)$. Figs. 10 and 11 show that Silver and Iodine appear with

[1]In the case of Iodine, E_3 is given by the end of the spectrum, in this case the energy interval $(E_2 - E_3)$ is obtained without any subtraction.

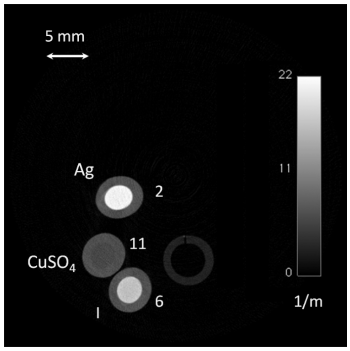

Fig. 13. Transverse slice of data acquired with Threshold 2 (25.5 keV) and reconstructed with FDK. The numbers aside the rubber tubes correspond to the solutions listed in Table II.

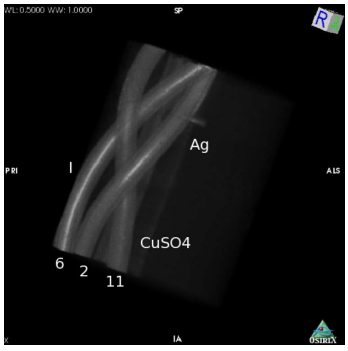

Fig. 14. 3D volume rendering of the slices acquired with Threshold 2 (25.5 keV) and reconstructed with FDK.

positive CT numbers in the subtracted slices $(E_{2Ag} - E_{3Ag}) - (E_{1Ag} - E_{2Ag})$ and $(E_{2I} - E_{3I}) - (E_{1I} - E_{2I})$, respectively. They are in fact the only materials that present an increase of the absorption coefficient in the second energy interval, with respect to the first one. All the other materials (water, the phantom resin and the $CuSO_4$ solution) have negative CT numbers and are therefore suppressed in the image, according to the used colour scale that is restricted to positive values. A comparison between the measured CT numbers and the NIST [19] expected attenuation coefficient for each insert is given in Fig. 12. The behavior of CT numbers is in reasonable agreement with the expectations, given the fact that these latter are calculated from the beam spectrum only and do not include neither the model of the detector nor the bias resulting from reconstruction of data acquired with a polychromatic instead of a monochromatic beam. The systematic effect observed between the data and the theoretical expectations in the energy window under the K-edges needs further investigations to understand the very origin of the effect.

B. Twisted Phantom

The twisted phantom is formed of three twisted rubber pipes, 16 cm long, of 3 mm inner diameter, filled with the solutions Nr. 2, 6 and 11 listed in Table II. Data were acquired with the second

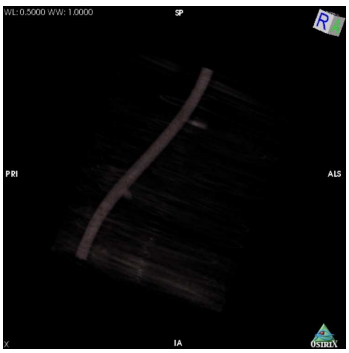

Fig. 15. 3D volume rendering of the subtracted windowed slices $(E_{2A_g} - E_{3A_g}) - (E_{1A_g} - E_{2A_g})$ magnifying the Silver content of the twisted phantom.

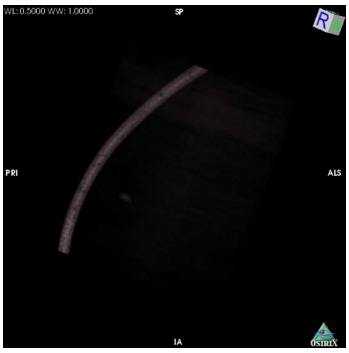

Fig. 16. 3D volume rendering of the subtracted windowed slices $(E_{21} - E_{31}) - (E_{11} - E_{21})$ magnifying the Iodine content of the twisted phantom.

spectrum. Figs. 13 and 14 show the results of standard absorption CT acquired with Threshold 2 and reconstructed using the FDK algorithm. Fig. 13 shows a transverse slice though the twisted phantom and Fig. 14 represents a 3D volume rendering of the reconstructed slices. Figs. 15 and 16 demonstrate spectral identification of the Silver and Iodine solutions, respectively, represented as 3D volume renderings of the subtracted energy windowed slices.

V. Conclusions

We have demonstrated the capability of the micro-CT PIXSCAN, based on the photon counting hybrid pixel detector XPAD3, to perform whole body mouse-like K-edge imaging on two contrast agents. The possibility to set an energy threshold on the detected photons allows for identifying Silver and Iodine solutions among other materials by acquiring three CT scans with appropriate energy thresholds. Solutions with a Silver density greater than 11 mg/ml or a Iodine density greater than 20 mg/ml appear to be easily identifiable. For this, a new pixel threshold calibration method has been developed, based on filters of the same material as the contrast agents to be imaged. More sophisticated approaches [8] are under investigation in order to achieve a better quantitative accuracy. Further developments will involve both the development of a large surface CdTe hybrid pixel prototype based on the present XPAD3 chip, and the design of a new chip with two independent thresholds in the longer term.

References

[1] J. Yorkston, "Recent developments in digital radiography detectors," *Nucl. Instrum. Meth. A*, vol. 580, pp. 974–985, 2007.
[2] R. E. Alvarez and A. Macovsky, "Energy-selective reconstruction in X-ray computerized tomography," *Phys. Med. Biol.*, vol. 21, pp. 733–744, 1976.
[3] S. J. Riederer and C. A. Mistretta, "Selective iodine imaging using K-edge energies in computerized x-ray tomography," *Med. Phys.*, vol. 4, pp. 474–481, 1977.
[4] M. J. Tapiovaara and R. F. Wagner, "SNR and DQE analysis of broad spectrum x-ray imaging," *Phys. Med. Biol.*, vol. 30, pp. 519–529, 1985.
[5] P. M. Shikhaliev, "Energy-resolved computed tomography: First experimental results," *Phys. Med. Biol.*, vol. 53, pp. 5595–5613, 2008.
[6] T. G. Schmidt, "Optimal imaged-based weighting for energy-resolved CT," *Med. Phys.*, vol. 36, pp. 3018–3027, 2009.
[7] E. Roessl and R. Proksa, "K-edge imaging in x-ray computed tomography using multi-bin photon counting detectors," *Phys. Med. Biol.*, vol. 52, pp. 4679–4696, 2007.
[8] J. P. Schlomka *et al.*, "Experimental feasibility of multi-energy photon-counting K-edge imaging in pre-clinical computed tomography," *Phys. Med. Biol.*, vol. 53, pp. 4031–4047, 2008.
[9] P. Pangaud *et al.*, "XPAD3-S: A fast hybrid pixel readout chip for X-ray synchrotron facilities," *Nucl. Instrum. Meth. A*, vol. 591, pp. 159–162, 2008.
[10] P. Pangaud *et al.*, "First results of XPAD3, a new photon counting chip for X-Ray CT-Scanner with energy discrimination," in *Proc. 2007 IEEE Nucl. Sci. Symp. Conf. Rec., IEEE Press*, Honolulu, Hawaii, Nov. 3, 2007, pp. 14–18.
[11] F. Cassol Brunner *et al.*, "Imaging performance of the hybrid pixel detectors XPAD3-S," *Phys. Med. Biol.*, vol. 54, pp. 1773–1789, 2009.
[12] S. M. Jorgensen *et al.*, "Biomedical spectral x-ray imaging; promises and challenges," *Proc. of SPIE Med. Applicat. Radiation Detectors*, vol. 8143, 2011.
[13] M. Firsching *et al.*, "Contrast agent recognition in small animal CT using the Medipix2 detector," *Nucl. Instrum. Meth. A*, vol. 607, pp. 179–182, 2009.
[14] N. G. Anderson *et al.*, "Spectroscopic (multi-energy) CT distinguishes iodine and barium contrast material in mice," *Eur. Radiol.*, vol. 20, pp. 2126–2134, 2010.
[15] F. Debarbieux *et al.*, "Repeated imaging of lung cancer development using PIXSCAN, a low dose micro-CT scanner based on XPAD hybrid pixel detectors," *IEEE Trans. Nucl. Sci.*, vol. 57, pp. 998–1007, 2010.
[16] R. Khoury *et al.*, "A geometrical calibration method for the PIXSCAn micro-CT scanner," *JINST*, vol. 4, p. 07016, 2009.
[17] J. Agostinelli *et al.*, "Geant4—A simulation toolkit," *Nucl. Instrum. Meth Phys.*, vol. 506, pp. 250–303, 2003.
[18] F. Cassol Brunner *et al.*, "Study of the charge sharing effect in the photon counting pixel detector XPAD3-S," *Nucl. Instrum. Meth. A*, vol. 633, pp. 111–113, 2011.
[19] [Online]. Available: http://physics.nist.gov/PhysRefData/Xcom/html/xcom1.html.
[20] L. Feldkamp, L. Davis, and J. Kress, "Practical cone-beam algorithm," *J. Opt. Soc. Amer. A.*, vol. 6, pp. 612–619, 1984.
[21] S. Anthoine, J.-F. Aujol, Y. Boursier, and C. Melot, "On the efficiency of proximal methods in CBCT and PET," in *Proc. IEEE Int. Conf. Image Process.*, Brussels, Belgium, 2011, pp. 1365–1368.

Jinst

Published by IOP Publishing for Sissa Medialab

Received: *October 1, 2015*
Accepted: *October 27, 2015*
Published: *November 25, 2015*

17TH International Workshop on Radiation Imaging Detectors
28 June – 2 July 2015,
DESY, Hamburg, Germany

A large surface X-ray camera based on XPAD3/CdTe single chip hybrids

F. Cassol,[a,1] **N. Blanc,**[c,d] **F. Bompard,**[e] **N. Boudet,**[c,d] **Y. Boursier,**[a] **C. Buton,**[b] **J.-C. Clémens,**[a] **A. Dawiec,**[b] **F. Debarbieux,**[f] **P. Delpierre,**[e] **M. Dupont,**[a] **J. Graber-Bolis,**[a,f] **S. Hustache,**[b] **C. Morel,**[a] **H. Perez-Ponce,**[e] **L. Portal**[a] **and E. Vigeolas**[a]

[a] *Aix Marseille Université, CNRS/IN2P3, CPPM UMR 7346*
13288, Marseille, France
[b] *Synchrotron SOLEIL,*
L'Ormes des Merisiers, Saint-Aubin BP 48 91192, Gif-sur-Yvette Cedex, France
[c] *Université Grenoble Alpes, Institut NÉEL,*
F-38042 Grenoble, France
[d] *CNRS, Institut NÉEL,*
F-38042 Grenoble, France
[e] *imXPAD SAS,*
Espace Mistral, Athélia IV, 297 avenue du Mistral, 13600 La Ciotat, France
[f] *Aix Marseille Université, CNRS, INT,*
Marseille, France

E-mail: cassol@cppm.in2p3.fr

Abstract: The XPAD3 chip bump-bonded to a Si sensor has been widely used in preclinical micro-computed tomography and in synchrotron experiments. Although the XPAD3 chip is linear up to 60 keV, the performance of the XPAD3/Si hybrid detector is limited to energies below 30 keV, for which detection efficiencies remain above 20%. To overcome this limitation on detection efficiency in order to access imaging at higher energies, we decided to develop a camera based on XPAD3 single chips bump-bonded to high-Z CdTe sensors. We will first present the construction of this new camera, from the first tests of the single chip hybrids to the actual mechanical assembly. Then, we will show first images and stability tests performed on the D2AM beam line at ESRF synchrotron facility with the fully assembled camera.

Keywords: Computerized Tomography (CT) and Computed Radiography (CR); Instrumentation for synchrotron radiation accelerators

[1] Corresponding author.

doi:10.1088/1748-0221/10/11/C11010

2015 JINST 10 C11010

Contents

2015 JINST 10 C11010

1 Introduction

Hybrid pixels detectors, originally developed for high energy physics experiments, are nowadays widely exploited in X-ray imaging applications [1, 2]. The XPAD3 circuit [3] bump-bonded to Si sensors has been the building block for several photon counting X-ray cameras of different sizes. The smallest camera is composed of a single chip (1.6 cm × 1.1 cm, a matrix of 120 × 80 pixels of 130 μm × 130 μm), an other intermediate-size module is based on a single Si sensor (7.5 cm × 1.6 cm) bump-bonded to 7 contiguous chips, and a large surface camera (7.5 cm × 11.4 cm) is formed of 8 modules tiled one above the others, as shown in figure 1. These devices have been successfully employed both for synchrotron research [4] and biomedical imaging [5], for which their particular strength lays is in the possibility of performing spectral imaging by using the K-edge method [6].

The main limitation of the XPAD3/Si detectors is the reduced efficiency of the 500 μm thick Si sensor, particularly critical in the case of preclinical applications, where the measured Detection Quantum Efficiency (DQE) amounts to less than 40% [7]. Moreover, K-edge imaging is limited to elements with K-shell binding energies below 35 keV, as the efficiency becomes too low for higher energies (< 10%). Therefore, in order to reduce the dose delivered to the animals in longitudinal studies and to access elements like Gd and Au with K-shell binding energy of 50.2 and 80.7 keV,

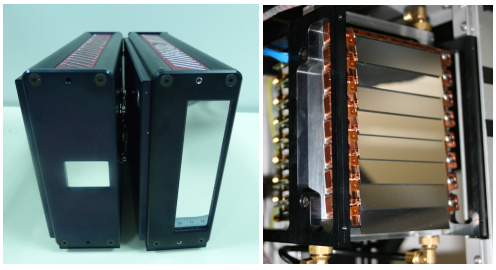

Figure 1. Pictures of X-ray cameras based on the XPAD3/Si detector.

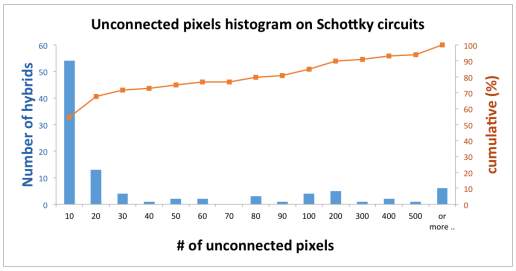

Figure 2. Number of hybrids as function of the number of disconnected pixels. The right axis indicates the cumulative percentage.

respectively, we have designed and built a new camera based on the XPAD3 chip bump-bonded to CdTe sensors: XPAD3/CdTe. Exploratory studies have shown that, if Si sensors are replaced by 750 μm CdTe sensors a DQE larger than 80% can be reached in the case of common micro-CT radiations [7]. Moreover, the efficiency is expected to remain above 50% up to the Au K-shell binding energy.

Since the production of CdTe sensors is still limited to wafer of few inches, since the robustness of the bump-bonding in large sensors appeared rather weak to peeling stress and since the aging of the detector is still uncertain, we decided conservatively to build a camera by assembling mechanically single chips in a 7×8 matrix. In such a way, the mechanical and the thermal stress is kept as low as possible for each one of the hybrids and, in case of failure, each detector can be easily replaced. The main challenge of such a strategy remains in the mechanical assembly which must guarantee a precision of at least 20 μm in order to minimize dead spaces and ensure a correct alignment between the chips. The global surface of the camera is $7.8\,\text{cm} \times 15.1\,\text{cm}$, large enough to image a whole-body mouse.

In the following, we will first describe the different steps of the conception and of the assembling of the camera (section 2), then we will show results from preliminary images taken with the completed detector at the at the D2AM beam line of the ESRF synchrotron facility (section 3). Finally, we will present some conclusion and outlooks.

2 Conception and assembling of the camera

The XPAD3.2/CdTe hybrids (Schottky contacts, hole collection) have been selected after a preliminary test campaign in which also electron collection both with Ohmic and with Schottky contacts was taken into consideration [8]. We then went through the production of 100 hybrids, 70 of which were selected by requiring less than 25 disconnected pixels out of 9600 pixels ($< 0.2\%$). Figure 2 shows the global statistics related to the unconnected pixel study.

The camera conception is based on mono-blocks of graphite, which hold the hybrids (graphite was chosen for its good thermal conductivity). Figure 3 presents the CAD design of a mono-block and a picture of the mechanical tool that has been developed to position the hybrid precisely on the graphite block during the gluing phase. In order to verify the assembling procedure and its precision,

2015 JINST 10 C11010

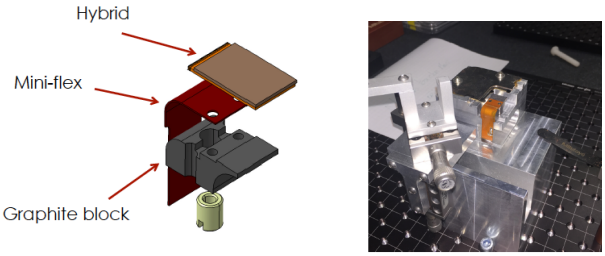

Figure 3. CAD design of the graphite block holding a hybrid (left) and picture of the mechanical tool developed to provide metrological assistance during the gluing of the hybrids on the graphite block.

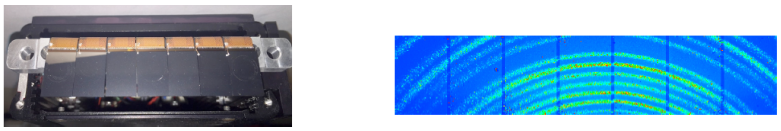

Figure 4. Picture of the first assembled module (left) and one image taken with a 16.6 keV beam, diffracted on LaB_6 crystals.

some of the less performing hybrids were first assembled in two modules for test, which have been exposed on the Psiché beam line at the SOLEIL synchrotron facility. Figure 4 shows one of the two modules, together with an image taken with a 16.6 keV beam, diffracted on LaB_6 crystals. The first produced hybrids were also used to assess the expected improvements for preclinical K-edge imaging by performing a direct comparison with a XPAD3/Si detector [9]. The results, obtained in the case of a common iodine contrast agent, were very encouraging, indicating an increase of the efficiency of around a factor 11, for energies close to the Iodine K-shell binding energy (33.2 keV), and an increase of the contrast-to-noise ratio of around a factor 3 in K-edge images (figure 5). We then assembled

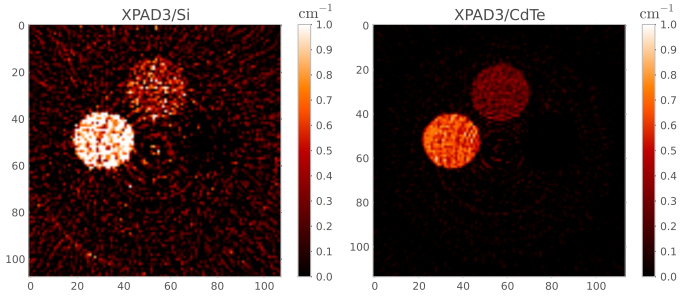

Figure 5. K-edge images of iodine solutions (0.315 M and 0.630 M) acquired with the XPAD3/Si detector (left) and the XPAD3/CdTe detector (right) at equivalent dose [9].

2015 JINST 10 C11010

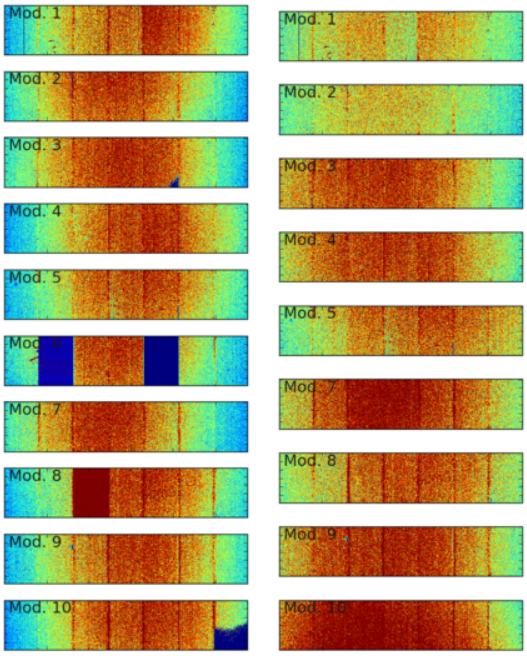

Figure 6. Acquisitions under irradiation with a ^{241}Am source of the assembled modules, before (left) and after (right) the HV contact fixing and the replacement of the two defected hybrids.

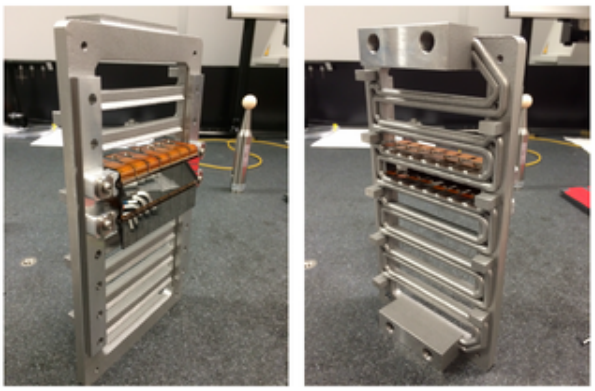

Figure 7. Assembling of the modules on the Aluminum frame, which also embeds the water cooling pipes.

2015 JINST 10 C11010

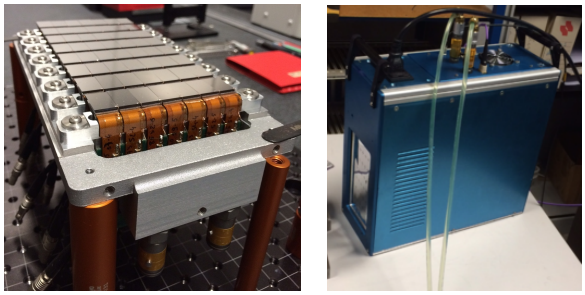

Figure 8. Picture of the complete camera outside (left) and inside (right) its box.

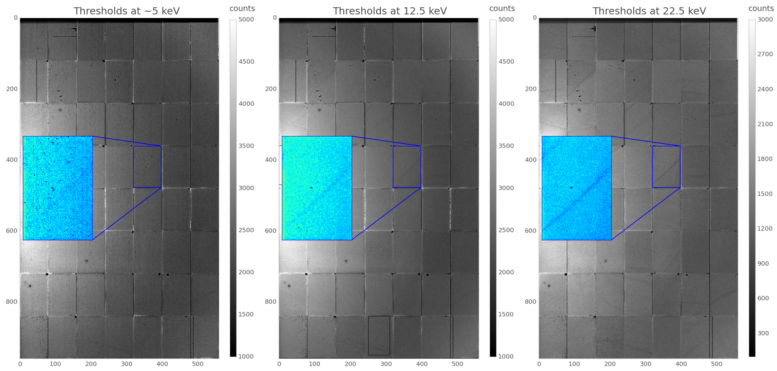

Figure 9. Flat images taken with a diffused 25.5 keV beam, for three different threshold values.

10 more modules, 8 of them to be used for the new camera. A consecutive test with a ^{241}Am source showed that some of the hybrids were not responding correctly. Problems due to defective high voltage (HV) contacts could be easily repaired, but for two chips the bump-bonding of several pixels was damaged and not recoverable anymore. In this case, we could replace the faulty hybrids with spare parts of module 6, which was sacrificed, and obtain 9 good modules, as it can be seen in figure 6. The modules were then integrated in the Al frame of the camera, which also embeds the cooling pipes used to stabilize the temperature of the detector to around 20 degree by circulating water from a chiller (figure 7). Finally, the complete camera was inserted in its external box (figure 8).

3 First images

The first images with the full camera were taken at the D2AM beam line of the ESRF synchrotron facility. We used a beam of 25.5 keV and three energies of pixel threshold calibrations: 5 keV (just above noise), 12.5 keV (half of the beam energy) and 22.5 keV (just below the beam energy). At first, we took flat images with the beam diffused by a block of Teflon. Figure 9 compares the results

2015 JINST 10 C11010

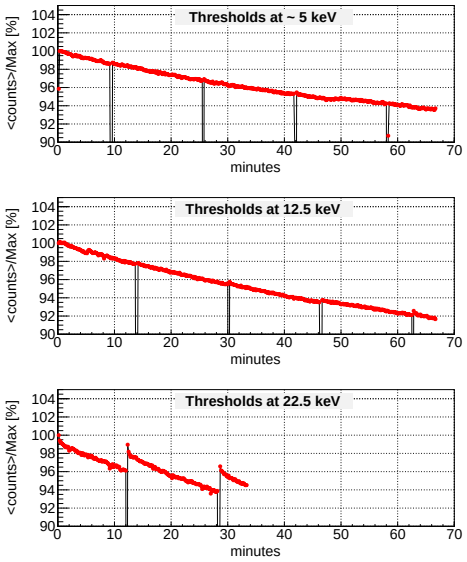

Figure 10. Average counting drift with time, for three different threshold values.

obtained with the three threshold values: the uniformity is quite satisfactory and similar in all cases, even if some patterns can be noticed. Then, we tested the counting stability with time, which, in the case of CdTe sensors, is known to be influenced by charge space accumulations along the crystal defects. We took sequences of images (10 s each) applying HV resets every 1000 seconds (HV= 700 V). In the case of efficiency changes, we expect to observe a counting rate recovery after each reset. Figure 10 presents the average counting drift with time for the three threshold values. It is actually dominated by the beam life time, which unfortunately could not be corrected. In the case of the 5 keV threshold, no significant counting recover is observed after the HV resets, but for the higher threshold values some effect can be seen, which amounts to around 2% in the case of the 22.5 keV threshold. These results are rather encouraging, though if we plot the difference between the first image after a reset and the last image before it (figure 11-left), we can recognize, for all the threshold values, the dislocation walls inside the crystals. This means that even if the average efficiency is not changing, the space charge accumulations along the sensor defects induce in all cases efficiency inhomogeneities, although they grow rather slowly and can be kept at a reasonable level providing the HV is reset on time. In fact, the difference of two consecutive acquisitions is quite uniform (figure 11-right).

The internal geometry of the camera has been measured with micro-metric precision and, on average, the dead space is 0.7 mm between the hybrids along a module and 4.7 mm between the modules. Figure 12 shows the effect of the geometry correction on the image of a 25.5 keV beam diffracted by Cr_2O_3 crystals.

2015 JINST 10 C11010

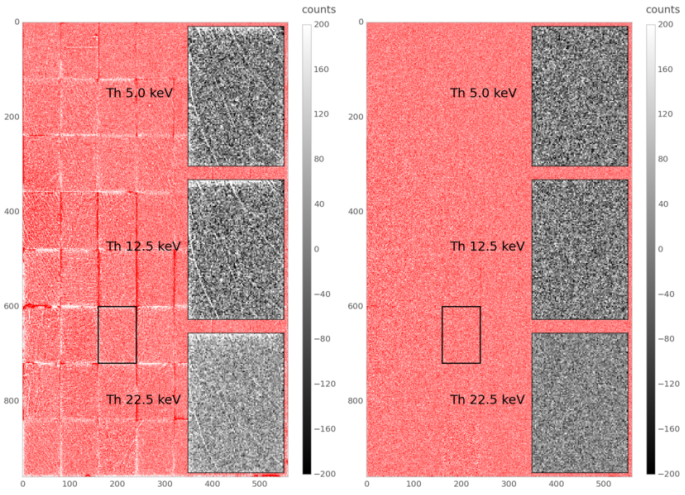

Figure 11. Difference of images: after and before a reset (left) and for two consecutive acquisitions (right).

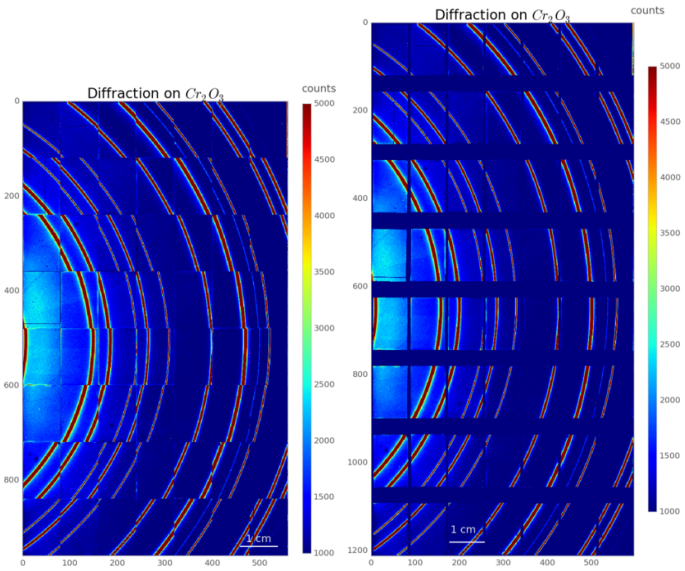

Figure 12. Beam diffraction by Cr_2O_3 crystals: raw image (left), image after correction of the camera internal geometry (right).

2015 JINST 10 C11010

4 Conclusions

A 537 600 pixel camera based on the XPAD3.2/CdTe single hybrids has been integrated. The precision of the mechanical assembly is below 20 μm. Preliminary tests showed quite uniform images, but with spatial inhomogeneities related to CdTe crystal defects that appear after several seconds of data taking. Further studies will be performed in order to define the optimal working conditions. The camera will then be employed in preclinical research for tumor development studies with standard and spectral tomography and in synchrotron radiation researches at the SOLEIL and ESRF facilities.

Acknowledgments

This work was supported by the ITMO Cancer within the Plan Cancer 2009-2013 under Grant no. PC201235 and the European project Calipso, Grant agreement no. 312284. The authors are also indebted and grateful to the CRG-BM02-D2AM and Métrologie beamlines at ESRF and SOLEIL, respectively.

References

[1] N. Wermes, *Pixel detectors for tracking and their spin-off in imaging applications*, *Nucl. Instrum. Meth.* **A 541** (2005) 150.

[2] K. Taguchi and J.S. Iwanczyk, *Vision 20/20: Single photon counting x-ray detectors in medical imaging*, *Med. Phys.* **40** (2013) 100901.

[3] P. Pangaud et al., *XPAD3: a new photon counting chip for small animal imaging*, *Nucl. Instrum. Meth.* **A 571** (2007) 321.

[4] K. Medjoubi et al., *Performance and applications of the CdTe- and Si-XPAD3 photon counting 2D detector*, 2011 *JINST* **6** C01080.

[5] F. Cassol et al., *Performances of a micro-CT system based on the photon counting XPAD3/Si hybrid pixel detectors*, submitted to *Phys. Med. Biol.* (2015).

[6] F. Cassol et al., *First K-edge imaging with a micro-CT based on the XPAD3 hybrid pixel detector*, *IEEE Trans. Nucl. Sci.* **60** (2013) 103.

[7] F. Cassol et al., *Imaging performance of the hybrid pixel detectors XPAD3-S*, *Phys. Med. Biol.* **54** (2009) 1773.

[8] C. Buton et al., *Comparison of three types of XPAD3.2/CdTe single chip hybrids for hard X-ray application in material science and biomedical imaging*, *Nucl. Instrum. Meth.* **A 758** (2014) 44.

[9] F. Cassol et al., *K-edge imaging with the XPAD3 hybrid pixel detector, direct comparison of CdTe and Si sensors*, *Phys. Med. Biol.* **60** (2015) 5497.

2015 JINST 10 C11010

IOP Publishing | Institute of Physics and Engineering in Medicine Physics in Medicine & Biology

Phys. Med. Biol. **60** (2015) 5497–5511 doi:10.1088/0031-9155/60/14/5497

K-edge imaging with the XPAD3 hybrid pixel detector, direct comparison of CdTe and Si sensors

F Cassol[1], L Portal[1], J Graber-Bolis[6], H Perez-Ponce[5], M Dupont[1], C Kronland[1], Y Boursier[1], N Blanc[3,4], F Bompard[5], N Boudet[3,4], C Buton[2], J C Clémens[1], A Dawiec[2], F Debarbieux[6], P Delpierre[5], S Hustache[2], E Vigeolas[1] and C Morel[1]

[1] Aix Marseille Université, CNRS/IN2P3, CPPM UMR 7346, 13288, Marseille, France
[2] Synchrotron SOLEIL, L'Orme des Merisiers, Saint-Aubin BP 48 91192, Gif-sur-Yvette Cedex, France
[3] Université Grenoble Alpes, Institut NEEL, F-38042 Grenoble, France
[4] CNRS, Institut NEEL, F-38042 Grenoble, France
[5] imXPAD SAS Espace Mistral, Athelia IV, 297 avenue du Mistral, 13600 La Ciotat, France
[6] Aix Marseille Université, CNRS, INT, 13284 Marseille, France

E-mail: cassol@cppm.in2p3.fr

Received 28 January 2015, revised 26 March 2015
Accepted for publication 4 June 2015
Published 2 July 2015

Abstract

We investigate the improvement from the use of high-Z CdTe sensors for pre-clinical K-edge imaging with the hybrid pixel detectors XPAD3. We compare XPAD3 chips bump bonded to Si or CdTe sensors in identical experimental conditions. Image performance for narrow energy bin acquisitions and contrast-to-noise ratios of K-edge images are presented and compared. CdTe sensors achieve signal-to-noise ratios at least three times higher than Si sensors within narrow energy bins, thanks to their much higher detection efficiency. Nevertheless Si sensors provide better contrast-to-noise ratios in K-edge imaging when working at equivalent counting statistics, due to their better estimation of the attenuation coefficient of the contrast agent. Results are compared to simulated data in the case of the XPAD3/Si detector. Good agreement is observed when including charge sharing between pixels, which have a strong impact on contrast-to-noise ratios in K-edge images.

Keywords: K-edge imaging, hybrid pixels, spectral CT

(Some figures may appear in colour only in the online journal)

0031-9155/15/145497+15$33.00

1. Introduction

For the last decade, hybrid pixels detectors have been widely studied in the field of x-ray imaging for pre-clinical studies and for synchrotron radiation research. Indeed, their capability to perform direct photon counting permits not only to free images from the electronic noise, but also to reach fast read-out times (∼ms/frame) and high counting rates (∼10^6 photons/pixel/s) (Pangaud *et al* 2008, Henrich *et al* 2009, Ballabriga *et al* 2011). Moreover, the possibility to set energy thresholds on the counted photons paves the way to spectrometric imaging of the photon flux. Spectral information, in turn, allows to access material composition thanks to the dependence of the material attenuation coefficient on the incident photon energy (Alvarez and Macovski 1976). This capability increases intrinsic contrast of metallic or lanthanide ions used as contrast agents such as Iodine, Gadolinium or Gold that will turn x-ray computed tomography to a native anatomo-functional imaging modality. For instance, Gold nanoparticles attached to antibodies can be targeted to specific tumor cells and be readily identified by their K-edge signature at 80 keV (Jorgensen *et al* 2011). In the case of a single threshold per pixel, the so-called 'K-edge imaging' is the most promising spectral imaging method. Actually, it permits to identify contrast agents having their K-edge within the x-ray energy spectrum by performing two acquisitions in energy bins just below and above the K-edge energy (Riederer and Mistretta 1977).

This paper describes results obtained with the single threshold hybrid pixel detector XPAD3 (Pangaud *et al* 2008), which can be bump-bonded to Si or to CdTe sensors. The Si version of the detector (XPAD3/Si) has already been intensively characterized and used in pre-clinical micro-computed tomography (micro-CT) and in many synchrotron experiments. In particular, we assessed its capability of performing K-edge imaging in the context of the micro-CT PIXSCAN devoted to small animal studies (Cassol *et al* 2013). In order to increase its detection efficiency[7] and to access materials with K-edge at higher energies, like Gadolinium (E_K = 50.2 keV), we explored in the past the imaging performances of some prototypes of the XPAD3 detector bump-bonded to high-Z sensors based on CdTe (XPAD3/CdTe). The studies, performed both at synchrotrons (Medjoubi *et al* 2010) and for pre-clinical imaging (Cassol *et al* 2009), were very encouraging, indicating an efficiency of 80% at 35 keV and the possibility to reach a detective quantum efficiency close to 1 in the case of low dose micro-CT imaging. In this work, we further investigate the XPAD3/CdTe chips by comparing their K-edge imaging performance against the usual XPAD3/Si chips at energies still accessible to both detectors, i.e. the K-shell of Iodine (E_K = 33.2 keV), widely used in clinical and pre-clinical studies. We first investigate the response of both detectors in energy bins close to E_K, then we compare contrast-to-noise ratios (CNR) of K-edge images obtained with both the Si and the CdTe detectors. A comparison with simulated expectations is done in the case of the XPAD3/Si chip. Results are presented both at equivalent transmitted dose and at equivalent detected photon statistics.

2. Materials and methods

2.1. Imaging system

We consider two XPAD3 chips of version 3.2. The XPAD3/CdTe (Schottky contacts, hole collection) is a single chip, while the XPAD3/Si data are taken considering the central chip of a 7 chip module (figure 1). Each circuit is composed of 80×120 pixels of $130\,\mu m \times 130\,\mu m$.

[7] The XPAD3/Si efficiency rapidly decreases below 20% at energies greater than 30 keV, mainly due to the rapid decrease of the photoelectric effect.

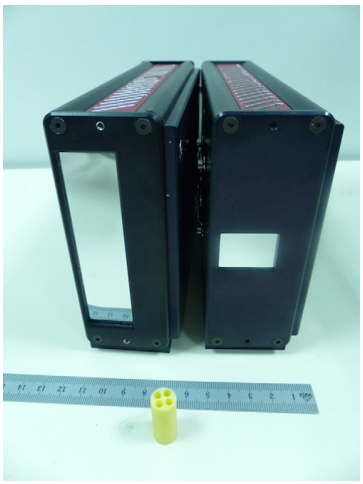

Figure 1. Picture of the XPAD3/Si (left) and XPAD3/CdTe (right) detectors, in front of them is shown the imaged phantom.

Table 1. Characteristics of the XPAD3 chip.

Number of pixels	9600 (80 × 120)
Pixel size	130 μm × 130 μm
Chip size	1.56 cm × 1.04 cm
Input polarity	Hole collection
Selectivity mode	Single threshold
Counting rate	10^6 photons/pixel/s
Readout time	1 ms/frame
Global electronic noise	100 e^- rms
Threshold step	135 e^- rms

Table 2. Main characteristics of the Si and CdTe sensors.

	Si	CdTe
Density (g · cm^{-3})	2.3	6.2
e^-/h^+ energy (eV)	3.6	4.4
Thickness (μm)	500	750
Applied bias voltage (V)	200	500

We suggest Buton *et al* (2014) for a detailed description of the newly produced XPAD3/CdTe chips, table 1 summarizes the main characteristics of the XPAD3 circuit and table 2 compares the main characteristics of the Si and CdTe sensors.

Each pixel detects photons above a threshold adjusted by a global 8-bits DAC and equalized pixel to pixel by a local 6-bits DAC, called DACL. To calibrate the thresholds at the

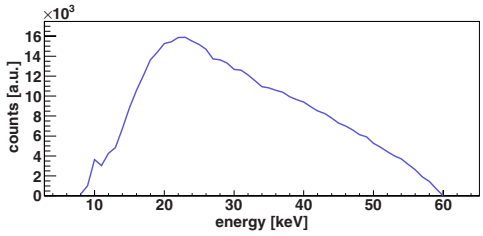

Figure 2. X-ray energy spectrum after 0.5 mm Al attenuation (W target, 60 kVp).

K-edge energy of a given contrast agent, DACL values are scanned while irradiating the pixels with an x-ray beam passing through a filter made of the contrast agent (e.g. Iodine). Photon counts resulting from the DACL scan are then analyzed to identify the DACL values that correspond to the sharp transition in counts expected around the K-edge energy of the contrast agent (Cassol *et al* 2013).

Tomographic acquisitions are performed with a Tungsten target x-ray tube (Microfocus 90 KV TGT, Oxford Instruments, Scotts Valley CA, USA). The tube has a $30\,\mu\text{m} \times 30\,\mu\text{m}$ emission spot and it works at 60 kVp, filtered by 0.5 mm of Aluminum. Figure 2 shows the employed spectrum, as measured by a XR-100T-CdTe (Amptek, Bedford MA, USA) spectrometer.

The source-detector distance is around 25 cm and the imaged objects are placed on a rotating table at a minimal distance from the detector (a few millimeters). This configuration has been chosen in order to avoid the magnification of the imaged objects, given the already small dimension of the chip. Moreover, it permits to perform tomographic reconstruction in the parallel beam approximation, which does not demand a precise estimation of the system geometry. Each tomographic acquisition consists of 360 projections (one degree spaced) followed by 100 flat and 100 dark field projections. Before each tomographic reconstruction the images are normalized with the flat field acquisitions and corrected for defectives or dead pixels by a linear interpolation with the neighboring pixels.

We imaged cylindrical phantoms of 1 cm diameter with four cylindrical inserts of 3 mm diameter, as shown in figure 1. The inserts were filled with: water, two different solutions of iodine (0.630 M and 0.315 M, obtained from the dilution of IOMERON 400) and one solution of $CuSO_4$ (1 M) in order to compare with a material having an equivalent density, but without K-edge in the considered energy range.

2.2. K-edge imaging

The principle of K-edge imaging is based on the comparison of images taken in energy bins close to the energy E_K corresponding to the K-shell binding energy of the material to be investigated. In fact, at this energy, the attenuation coefficient presents a sharp increase, behaving differently than for every other surrounding material, as it can be seen in figure 3, which presents the attenuation coefficients of the imaged solutions, as calculated by NIST data (Berger *et al* 1990).

Since the XPAD3 detector has a single threshold per pixel, one energy bin image ($\mathcal{I}$) is defined by subtracting two acquisitions ($\mathcal{A}$) taken with the thresholds set at the lower and the upper bound of the bin. In our case, three acquisitions with the pixel thresholds set at the energies ($E_K - |\Delta E|$), E_K and ($E_K + |\Delta E|$) are performed and then subtracted

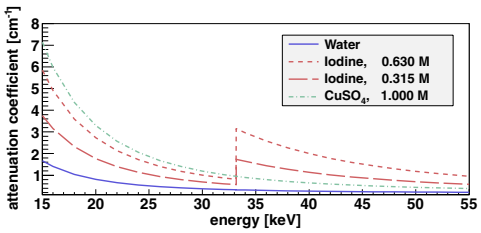

Figure 3. Attenuation coefficients of the imaged solutions as function of the incident photon energy.

$$\mathcal{I}_{+}(\Delta E) = \mathcal{A}(E_K) - \mathcal{A}(E_K + |\Delta E|) \tag{1}$$

$$\mathcal{I}_{-}(\Delta E) = \mathcal{A}(E_K - |\Delta E|) - \mathcal{A}(E_K) \tag{2}$$

The standard FDK tomographic reconstruction of $\mathcal{I}$ gives an average estimation of the attenuation coefficient in the two adjacent energy bins, $\mu_{+}(\Delta E)$ and $\mu_{-}(\Delta E)$. We finally define the K-edge image as the subtraction of these two images, hence resulting in positive values only in presence of the K-edge material

$$\mu_{K-edge}(\Delta E) = \mu_{+}(\Delta E) - \mu_{-}(\Delta E) \tag{3}$$

In practice, we calibrate the detector at the energy E_K, as described in section 2.1, and define the other thresholds by decreasing or increasing the DACL values by a fixed number of DACL steps. In this way we avoid the use of a mono-energetic beam to calibrate the detector at all the considered thresholds. The DACL steps have been measured and amount to 0.45 ± 0.10 keV and 0.55 ± 0.08 keV for the Si and the CdTe sensors respectively.

For what concerns the energy bin width, figure 3 suggests that the narrower the bin, the higher the spectral contrast will be. However, a compromise has to be taken in order to keep a satisfying counting statistics per pixel without increasing too much the delivered dose. Moreover, the energy bin width must be larger than the dispersion of the threshold, which is about 110 e^{-}. In order to evaluate influence of the bin width on the results, we perform acquisitions with bins of 3, 6 and 9 steps of DACL, corresponding approximately to 1.5, 3 and 4.5 keV.

Finally, we compare the two detectors both at equivalent dose, fixing a common acquisition time of 1 s/projection, which corresponds to a total dose of 120 mGy pretty common with preclinical micro-CTs, and at equivalent statistics per pixels[8] by reducing the acquisition time for the XPAD/CdTe detector to 0.09 s/projection, as a consequence of its higher efficiency. This involves the reduction of the delivered dose by a factor 11.

2.3. Simulation

We obtain a preliminary estimation of the results by modeling the chosen K-edge method in the case of the XPAD3/Si chip, for which we have a Monte Carlo simulation of the detector response.

[8] For thresholds set at $E_K = 33.2$ keV.

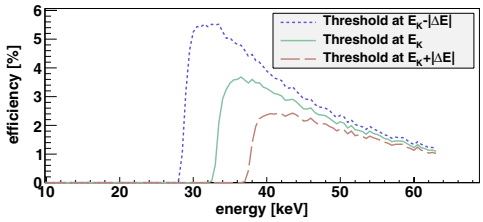

Figure 4. XPAD3/Si simulated efficiency for thresholds set around the Iodine K-edge energy ($|\Delta E| = 4.5$ keV). The fluctuations are purely statistical.

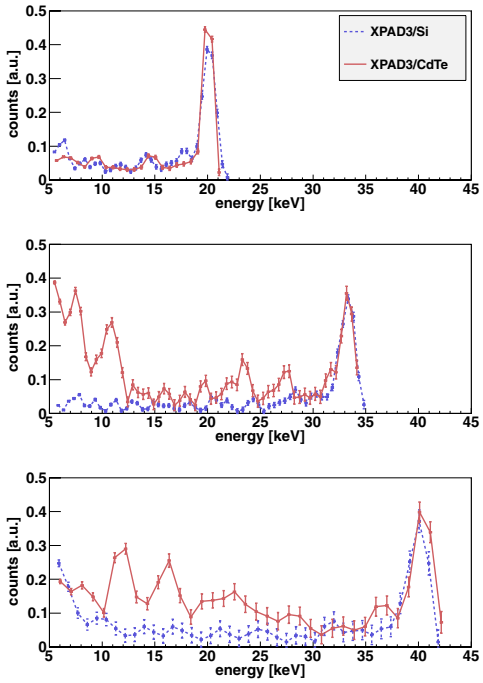

Figure 5. Detector responses at 20, 33.2 and 40 keV as obtained by the numerical differentiation of threshold scans.

Given the input spectrum $N_0(E)$ of figure 2 and assuming a homogenous imaged object of thickness L and an attenuation coefficient μ, the number of detected photons per pixel with threshold set to E_T is calculated as

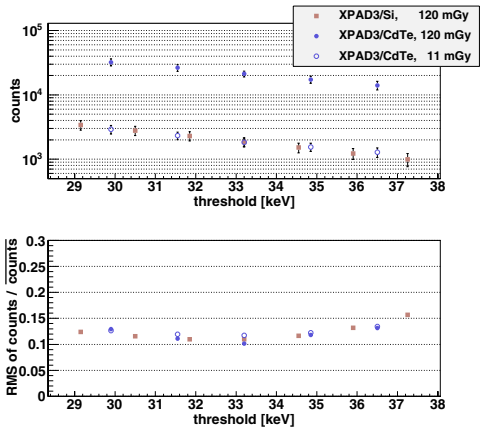

Figure 6. Counted photons per pixel (top) and relative counting dispersion (bottom) in flat images.

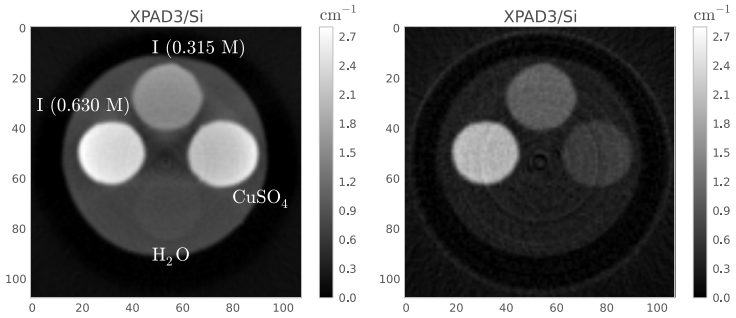

Figure 7. Tomographic slices measured by the XPAD3/Si detector with two different thresholds: noise level (left) and at E_K (right).

$$\mathcal{A}(E_T) = \int_{E_T}^{\infty} N_0(E)\varepsilon_{E_T}(E)e^{-\mu(E)L}dE \tag{4}$$

where $\varepsilon_{E_T}(E)$ is the detection efficiency function. The estimated number of detected photons in the energy windows of width ΔE is given by equations (1) and (2) as for data, while the average attenuation coefficient is calculated by the logarithm of the Beer–Lambert law

$$\mu_{\pm}(\Delta E) = -\ln[\mathcal{I}_{\pm}(\Delta E)/\mathcal{I}_{0\pm}(\Delta E)] \tag{5}$$

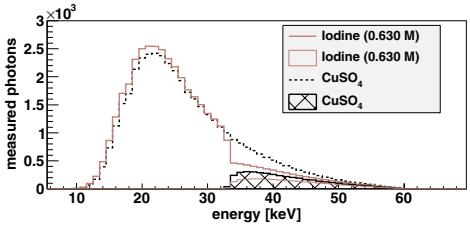

Figure 8. Detected photon spectra behind 3 mm of Iodine and of $CuSO_4$ with pixel thresholds set at noise level (empty histograms) and E_K (filled histograms). Simulated data.

The efficiency $\varepsilon_{E_T}(E)$ is estimated with the Monte Carlo code described in Cassol *et al* (2011), which models the repulsion and diffusion of electron-hole pairs during their drift towards the cathode, and appears to be dependent on the energy threshold E_T due to the charge sharing effect, as can be seen in figure 4 for three thresholds close to the Iodine K-edge energy. In fact, the sharing of charges between pixels reduces the efficiency for thresholds close to the detected photon energy (due to the loss of charges in the neighboring pixels) and artificially increases the efficiency for lower thresholds (due to possible double counts in the neighboring pixels). This dependence implies that the number of counted photons inside an energy bin is no more rigorously given by equations (1) and (2) and the higher the charge sharing effect, the higher the induced uncertainty (see appendix A for a mathematical formulation of this deviation).

For what concerns the XPAD3/CdTe detector, we do not have a simulation of the energy detector response yet. However, we expect that the fluorescence photons from the K-shell of Te and Cd at 23 keV and 27 keV, respectively, add to the charge sharing effect inducing a further uncertainty of equations (1) and (2). In order to visualize the fluorescence component and to compare the energy response of both detectors, we performed some threshold scans with synchrotron monochromatic beams that are presented in section 3.1.

Finally, we notice that charge summing schemes between pixels could reduce the impact of charge sharing and of fluorescence photons on the image quality (Koenig *et al* 2014). Unfortunately the XPAD3 circuit does not permit to apply this feature.

3. Measurements and results

3.1. Detector response

Figure 5 presents the responses of both detectors to monochromatic x-rays of 20, 33.2 and 40 keV for some arbitrarily chosen pixels. The points are obtained by numerical differentiation of DACL scans performed at the Psiché beam line of the synchrotron SOLEIL (Saint-Aubin, France) and are normalized to the beam peak integral. As expected, the detectors present a similar response at 20 keV while the signal component associated to the fluorescence photons at 23 and 27 keV (together with the corresponding escape peaks) add to the CdTe response for the higher beam energies[9]. As already said, this component is expected to further increase the dependence of the efficiency function on the pixel threshold for XPAD3/CdTe detectors.

[9] The low amplitude peaks visible in all the scans of figure 5 are due to local non-linearity of the DACL bit weights impacting some of the DACL values.

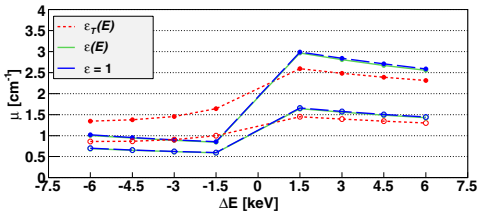

Figure 9. Attenuation coefficients expected for three types of detectors with $\varepsilon_T(E)$, $\varepsilon(E)$ and $\varepsilon = 1$ for the Iodine solutions (full markers: 0.630 M, empty markers: 0.315 M). Simulated data.

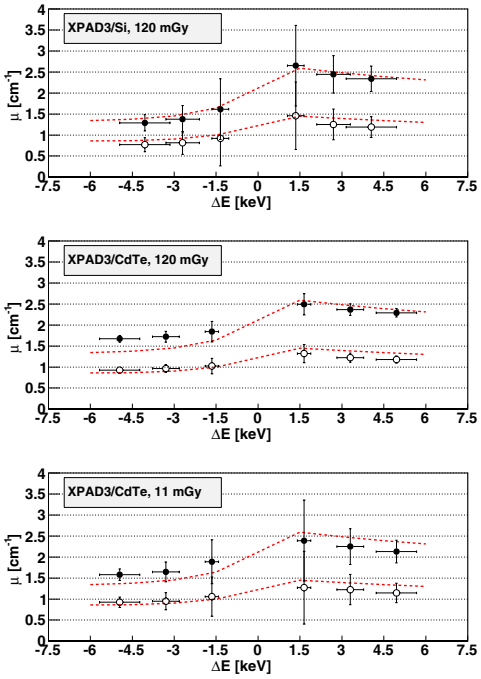

Figure 10. Attenuation coefficients of the Iodine solutions (full markers: 0.630 M, empty markers: 0.315 M) as measured by the XPAD3/Si (top) and the XPAD3/CdTe at equivalent dose (middle) and equivalent counting statistics per pixel (bottom). The lines corresponds to the XPAD3/Si simulated response.

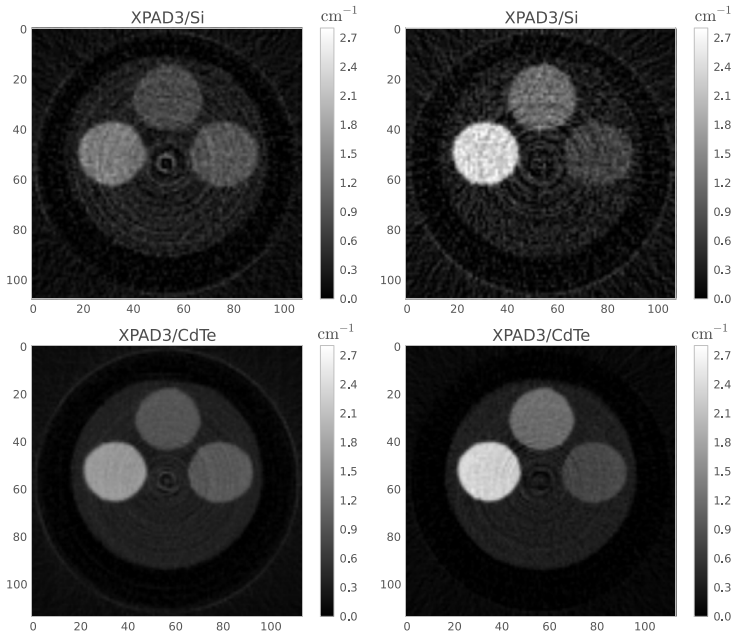

Figure 11. Transverse slices reconstructed from data acquired with energy bins $\Delta E_- \simeq -4.5$ keV (left) and $\Delta E_+ \simeq +4.5$ KeV (right) at equivalent dose for both detectors (top: XPAD3/Si, bottom: XPAD3/CdTe).

The counting statistics and relative counting dispersion for flat images, which are taken for all acquisition conditions, are presented in figure 6 for both detectors. The counting statistics reflects the factor 11 between the efficiencies of the two sensors used with the employed photon spectrum. The dispersion, which is similar for both detectors, slowly increases for thresholds far from E_K, reflecting the fact that our threshold energy is affected by the dispersion of the DACL step (around 0.1 keV).

The influence of the pixel threshold on the contrast between materials can be appreciated in figure 7, which shows transverse slices reconstructed from data acquired by the XPAD3/Si with thresholds set at 5 keV (just above noise) and 33.2 keV (E_K). We notice that the Iodine (0.630 M) and the $CuSO_4$ solutions have almost the same reconstructed value with the lower threshold, while they differ significantly with the higher threshold. This is due to the different impact of the K-edge effect on the detected photons, as it can be seen in figure 8, which shows the detected spectra as given by the simulation. Between Iodine and $CuSO_4$, the total numbers of detected photons differ by 2% in the first case (thresholds set just above noise) and 50% in the second case (thresholds set at E_K).

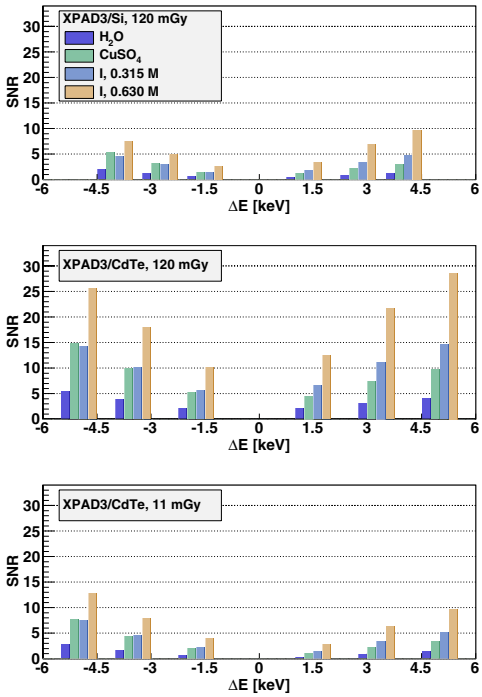

Figure 12. SNR in the selected ROIs for all bin energies. Data are from the XPAD3/Si detector (top), the XPAD3/CdTe detector at equivalent dose (middle), the XPAD3/CdTe detector at equivalent counting statistics (bottom).

3.2. Imaging in energy bins around E_K

Following the procedure described in section 2.3, we simulate the values of μ measured by three different types of detectors: the XPAD3/Si detector (efficiency $\varepsilon_T(E)$ depending on the threshold), a detector having an efficiency independent of the threshold ($\varepsilon(E)$ equal to the efficiency estimated with the thresholds set just above noise) and finally an ideal detector having a constant efficiency equal to one. We present in figure 9 the results obtained for the Iodine solutions. It can be seen that, while an efficiency independent of the threshold value (even when it is quite low like with Si) is not influencing the estimation of the μ values, the real detector is affected by a noticeable reduction of contrast between the negative and positive bins and no gain can be expected for bin widths smaller than 3 keV. This is a direct consequence of the charge sharing, as described in appendix A.

The real measurements for both the Si and CdTe detectors are presented in figure 10. The μ values and their errors correspond to the mean and the standard deviation (σ) of a Gaussian

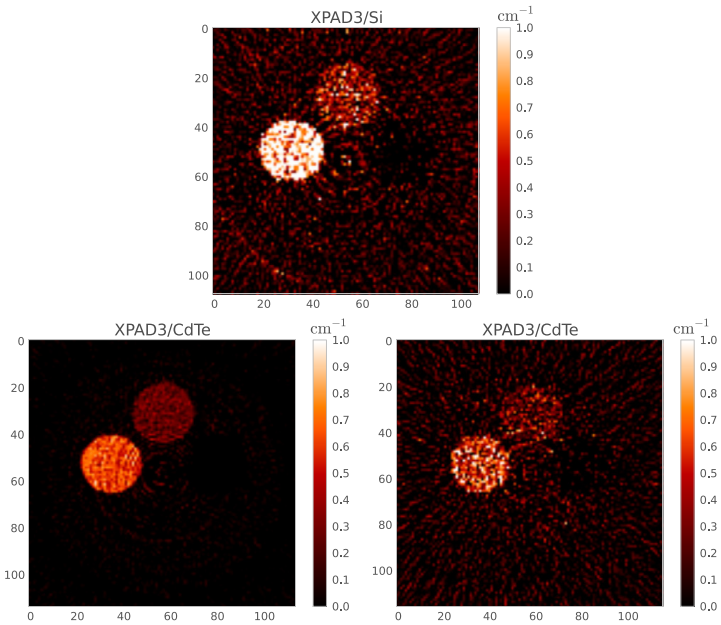

Figure 13. K-edge transverse slices reconstructed from data acquired with the $\Delta E_{\pm} \simeq \pm 4.5$ keV energy bins in the case of the XPAD3/Si detector (top), the XPAD3/CdTe detector at equivalent dose (bottom-left), the XPAD3/CdTe detector at equivalent counting statistics (bottom-right).

fit on the reconstructed attenuation coefficients in a Region of Interest (ROI)[10] inside the Iodine inserts. An example of transverse slices reconstructed from data acquired for the largest energy bins ($\Delta E_{\pm} \simeq \pm 4.5$ keV) can be seen in figure 11, where the signal enhancement in the iodine solutions is clearly visible despite the higher statistical noise of the XPAD3/Si data. Generally, XPAD3/Si data fit rather well the simulation expectations, confirming a reduction of contrast in the narrower bins. The XPAD3/CdTe has a similar behavior, but it presents a more pronounced deviation from the ideal detector possibly due to a different impact of charge sharing and/or fluorescence escape, which is expected to penalize CNR of K-edge images. The detectors have an equivalent increment of noise for the narrower energy bins, reflecting the same statistics driven uncertainty.

A complete overview of the results can be deduced from figure 12, which presents the signal-to-noise ratio (SNR) of all the ROIs for all the measurements, defined as $\mathrm{SNR} = \mu_{\mathrm{ROI}}/\sigma_{\mathrm{H_2O}}$. We recognize the higher performances of the XPAD3/CdTe at equivalent dose (figure 12 middle) which reflects the higher counting statistics and the corresponding noise reduction of around a factor 3. In the case of acquisitions at equivalent statistics, the two detectors perform rather similarly, except for the slightly higher SNR of the XPAD3/CdTe in the negative energy

[10] Cylinder of 10 pixels radius and 20 slices height.

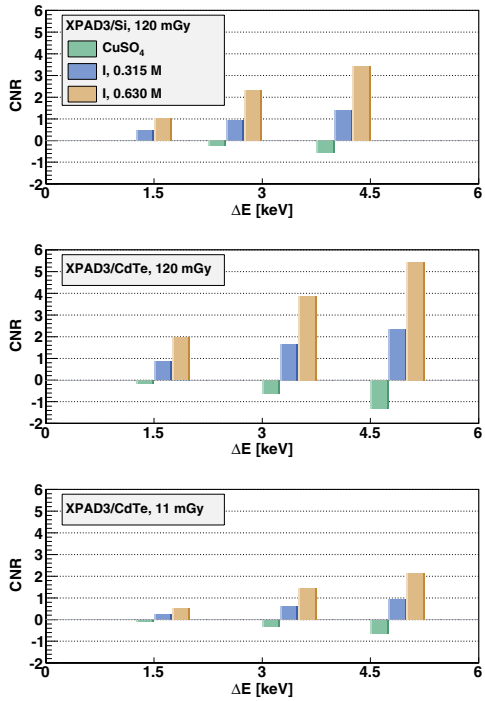

Figure 14. CNR of the K-edge images for all energy bins. Data are from the XPAD3/Si detector (top), the XPAD3/CdTe detector at equivalent dose (middle), the XPAD3/CdTe detector at equivalent counting statistics (bottom).

bins, due to the higher values of μ, as already observed in figure 10. Comparing the ROIs, we can appreciate the K-edge effect which induces a contrast between the $CuSO_4$ and the iodine solutions in the positive energy bins, not always distinguishable in the negative ones.

3.3. K-edge imaging

Figure 13 presents K-edge transverse slices obtained by equation (3) for both detectors and for the largest energy bin $\Delta E_{\pm} \simeq \pm 4.5$ keV. As expected, only the Iodine solutions are visible, i.e. their $\mu_{\mathrm{K-edge}}$ is positive thanks to the K-edge effect. The images confirm the higher contrast capability of the Si sensor for acquisitions at equivalent counting statistics. A more quantitative estimation is given by the CNR, defined as $\mathrm{CNR} = (\mu_{\mathrm{ROI}} - \mu_{H_2O})/\sigma_{H_2O}$, and presented in figure 14, where in turn the far better performance of XPAD3/CdTe at equivalent dose can be seen (figure 14 middle). Clearly, the largest energy bins have to be preferred, even though a further increase of ΔE would at a certain point decrease CNR as shown in He *et al* (2012).

4. Conclusions

We presented a direct comparison of the spectral performance of the XPAD3 hybrid pixel detector with Si or CdTe sensors. XPAD3/Si data are in agreement with simulations and demonstrate a satisfactory comprehension with regards of the detector response and of the factors that limit its spectral imaging performance. In particular, the charge sharing effect is the main cause for spectral contrast reduction. The XPAD3/CdTe confirms its clear superiority in terms of detection efficiency and CNR of K-edge images acquired at equivalent doses (the CNR being incremented by around a factor 3 in our case). It is slightly less performing than the XPAD3/Si detector when working at equivalent statistics, due to an higher deviation from the ideal detector response in energy bin imaging. Though, this is largely compensated by the dose reduction, which amounts to a factor 11 at energies around 33 keV. This makes the XPAD3/CdTe detector a very suited instrument for long term pre-clinical studies, while XPAD3/Si remains preferable for high contrast, high dose studies at energy lower than 30 keV.

Acknowledgments

This work was supported by the ITMO Cancer within the Plan Cancer 2009–2013 under Grant no. PC201235 and the European project Calipso, Grant agreement no. 312284. The authors are also indebted and grateful to the CRG-BM02-D2AM beamline at ESRF and the Métrologie and the Psiché beamlines at SOLEIL.

Appendix A

In the case of charge sharing, the pixels efficiency depends on the threshold. From figure 4 we can define

$$\Delta\varepsilon(E) = \varepsilon_{E_\mathrm{K}}(E) - \varepsilon_{E_\mathrm{K}+\Delta E}(E) \tag{A.1}$$

Hence, equation (1) (similarly equation (2)) does not give the number of photons measured in the energy interval ΔE, $\mathcal{I}_+(\Delta E)$, but instead

$$\begin{aligned}
&\mathcal{A}(E_\mathrm{K}) - \mathcal{A}(E_\mathrm{K} + \Delta E)\\
&= \int_{E_\mathrm{K}}^{\infty} N(E)\ \varepsilon_{E_\mathrm{K}}(E)\mathrm{d}E - \int_{E_\mathrm{K}+\Delta E}^{\infty} N(E)\ \varepsilon_{E_\mathrm{K}+\Delta E}(E)\ \mathrm{d}E\\
&= \int_{E_\mathrm{K}}^{\infty} N(E)\ \varepsilon_{E_\mathrm{K}}(E)\ \mathrm{d}E - \int_{E_\mathrm{K}+\Delta E}^{\infty} N(E)\ (\varepsilon_{E_\mathrm{K}}(E) - \Delta\varepsilon(E))\ \mathrm{d}E\\
&= \int_{E_\mathrm{K}}^{E_\mathrm{K}+\Delta E} N(E)\ \varepsilon_{E_\mathrm{K}}(E)\ \mathrm{d}E + \int_{E_\mathrm{K}+\Delta E}^{\infty} N(E)\ \Delta\varepsilon(E)\,\mathrm{d}E\\
&= \mathcal{I}_+(\Delta E) + \int_{E_\mathrm{K}+\Delta E}^{\infty} N(E)\ \Delta\varepsilon(E)\ \mathrm{d}E
\end{aligned} \tag{A.2}$$

This induces an intrinsic uncertainty in the results equal to the integral of $\Delta\varepsilon(E)$ weighted by the incident photon spectrum $N(E)$.

References

Alvarez R E and Macovski A 1976 Energy-selective reconstructions in x-ray computerized tomography *Phys. Med. Biol.* **21** 733–44

Ballabriga R *et al* 2011 Medipix3: a 64 thinsp;k pixel detector readout chip working in single photon counting mode with improved spectrometric performance *Nucl. Instrum. Methods* A **633** 15–8

Berger M J *et al* 1990 XCOM Photon cross section data base *NIST Standard Reference Data Base 8 (XGAM)* (www.nist.gov/pml/data/xcom/)

Buton C *et al* 2014 Comparison of three types of XPAD3.2/CdTe single chip hybrids for hard x-ray application in material science and biomedical imaging *Nucl. Instrum. Methods* A **758** 44–56

Cassol B F *et al* 2009 Imaging performance of the hybrid pixel detectors XPAD3-S *Phys. Med. Biol.* **54** 1773–89

Cassol B F *et al* 2011 Study of the charge sharing effect in the photon counting pixel detector XPAD3-S *Nucl. Instrum. Methods* A **633** 111–3

Cassol B F *et al* 2013 First K-edge imaging with a Micro-CT based on the XPAD3 hybrid pixel detector *IEEE Trans. Nucl. Sci.* **60** 103–8

He P *et al* 2012 Optimization of K-edge imaging with spectral CT *Med. Phys.* **39** 6572–9

Henrich B *et al* 2009 PILATUS: a single photon counting detector for x-ray applications *Nucl. Instrum. Methods* A **607** 247–9

Jorgensen S M *et al* 2011 Biomedical spectral x-ray imaging; promises and challenges *Medical Applications of Radiation Detectors Proc. SPIE* ed H B Barber, H Roehrig and D J Wagenaar **8143** 814302

Koenig T *et al* 2014 How spectroscopic x-ray imaging benefits from inter-pixel communication *Phys. Med. Biol.* **59** 6195–213

Medjoubi K *et al* 2010 Detective quantum efficiency, modulation transfer function and energy resolution comparison CdTe and silicon sensors bump-bonded to XPAD2S *J. Synchrotron Radiat.* **17** 486–95

Pangaud P *et al* 2008 XPAD3-S: a fast hybrid pixel readout chip for x-ray synchrotron facilities *Nucl. Instrum. Methods* A **591** 159–62

Riederer S J and Mistretta C A 1977 Selective iodine imaging using K-edge energies in computerized x-ray tomography *Med. Phys.* **4** 474–81

IOP Publishing Biomed. Phys. Eng. Express 2 (2016) 025003 doi:10.1088/2057-1976/2/2/025003

Biomedical Physics & Engineering Express

PAPER

Characterization of the imaging performance of a micro-CT system based on the photon counting XPAD3/Si hybrid pixel detectors

RECEIVED
23 October 2015

REVISED
1 February 2016

ACCEPTED FOR PUBLICATION
4 February 2016

PUBLISHED
24 February 2016

F Cassol[1], M Dupont[1], C Kronland-Martinet[1], H Ouamara[1,4], A Dawiec[1,3], Y Boursier[1], A Bonissent[1], J-C Clémens[1], L Portal[1], F Debarbieux[2] and C Morel[1]

[1] Aix Marseille Université, CNRS/IN2P3, CPPM UMR 7346, 13288, Marseille, France
[2] Aix Marseille Université, CNRS, INT UMR 7289, Marseille, France
[3] *Present address:* Synchrotron SOLEIL, L'Orme des Merisiers, Saint-AubinBP 48 91192, Gif-sur-Yvette Cedex, France.
[4] *Present address:* EOS imaging, France.

E-mail: cassol@cppm.in2p3.fr

Keywords: hybrid pixel detectors, preclinical imaging, micro-CT

Abstract

We characterize the imaging performance of the micro computed tomography (micro-CT) prototype PIXSCAN equipped with an x-ray photon counting camera based on XPAD3/Si hybrid pixel detectors. The camera, which is composed of eight distinctive horizontal modules, permits the performance of whole-body mouse scans. Photon counting supplied by hybrid pixels guarantees acquisitions at a Poisson noise level exclusively determined by the detected photon statistics. First, we characterize the performance of the imaging system while assessing its linearity, noise, spatial resolution and low contrast detectability estimated from scans of appropriate phantoms. Then, we show CT images of mice data acquired either *in vivo* or *post mortem*, without or with an injection of iodine as a contrast agent. Although hybrid pixels guarantee a minimal noise to the images, the limited detection efficiency of Si sensors impairs detected photon statistics and therefore the improvement in contrast-to-noise ratio for standard tomographic imaging. Indeed, the most innovative potential of the PIXSCAN prototype is its capacity to perform spectral tomographic imaging and fast dynamic imaging. The first is thanks to the possibility of setting an energy threshold on the detected photons, and the second is thanks to its fast acquisition rate (till 500 images/s). We present some examples of these imaging methods applied to mice and discuss their main limiting factors.

1. Introduction

Hybrid pixels detectors, originally invented for high energy physics experiments, are nowadays widely developed as x-ray detectors for imaging applications (Wermes 2005). The most innovative characteristic of hybrid pixels is the digital conversion of the photon signal through one or more minimum thresholds: only photons giving a signal higher than predefined values are counted. As a consequence, hybrid pixels provide photon counting instead of integrating the overall signal charge. This feature not only allows a linear detector response and provides the acquisition of images free from electronic noise, potentially with an infinite counting range, but also permits the realization of spectral imaging (Alvarez and Macovsky 1967) by acquiring data with different energy thresholds (Jorgensen *et al* 2011).

During the last decade, several research groups and companies have developed hybrid pixel detectors coupled to various sensor materials (e.g. Si, CdTe, GaAs) for x-ray imaging in preclinical and, more recently, clinical applications (Delpierre 2014, Taguchi and Iwanczyk 2013). In this regard, the construction of large surface detectors (in the case of preclinical imaging $\geqslant 100\text{cm}^2$) is particularly challenging, due to the difficulty of producing large semiconducting sensors or of assembling several readout chips without dead areas.

In this paper, we characterize the micro computed tomography (micro-CT) prototype PIXSCAN equipped with a hybrid pixel camera based on the XPAD3 chip bump-bonded to silicon sensors (XPAD3/Si). XPAD3 chips have a single threshold per pixel that can be set from few keV to about 35 keV (Pangaud *et al* 2007). In the case of standard preclinical

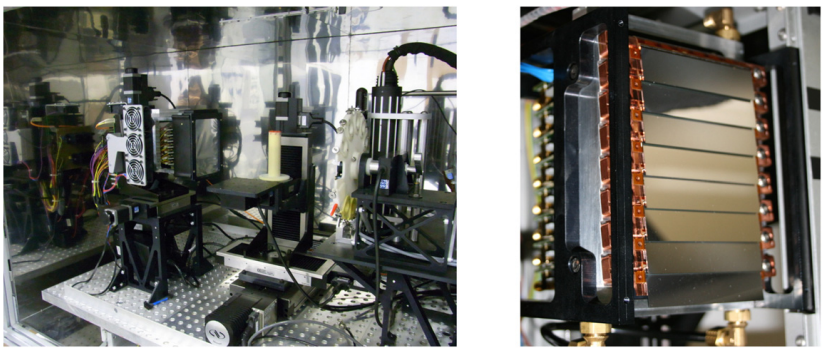

Figure 1. Picture of the micro-CT prototype PIXSCAN (left) and of the XPAD3/Si camera (right). Inside the lead/steel box (from left to right): the camera, the rotating table supporting a cylindrical phantom, the wheel holding different types of filters and the x-ray tube (MCBM 65 B-50, RTW in this case).

Table 1. Employed x-ray beam qualities.

Quality	Target	Tension (kV)	Current (μA)	Filter	HVL[a] (mm Al)	Dose rate (mGy/s)
RQA[b]	Mo	30	600	0.03 mm Mo + 2 mm Al	0.64	0.043
RQ1	Mo	50	600	6 mm Al	2.56	0.067
RQ2	Mo	50	600	1 mm Al	0.66	1.168
RQ3	Mo	50	600	0.1 mm Cu	1.18	0.201
RQ4	W	90	890	0.2 mm Nb	—	1.150

[a] Half value layer.
[b] Standard mammography radiation RQAM-3 (IEC 61267).

radiations, the XPAD3/Si detector behaves like a pure Poisson detector and its detection quantum efficiency (DQE) is mainly limited by the silicon sensor efficiency (Cassol *et al* 2009). The pixels have a size of 130μm × 130 μm and the camera has a global surface of 7.5 cm × 11.4 cm, sufficient for the imaging of a whole mouse chest without dead areas.

We present the imaging performances of the micro-CT and provide some examples of its application to preclinical imaging. After the description of the system, of the calibration procedures and of the data processing/reconstruction in section 2, we estimate in section 3.1 standard figures of merit through tomographic imaging of specific phantoms using the standard IEC mammography radiation RQA3-M (IEC 61267). Then, in section 3.2, we present some examples of mice imaging, also using other x-ray beam qualities. In particular, we present examples of *in vivo* and *post mortem* standard tomographic imaging, without or with the injection of a iodinated contrast agent; further, we use the capability of the XPAD3/Si detectors to adjust their pixel threshold to perform spectral imaging via the K-edge method (Riederer and Mistretta 1977); finally, we show fast radiography imaging to study the dynamic bio-distribution of an iodinated contrast agent injected intravenously. We finish the paper with some discussions and conclusions.

2. Materials and methods

2.1. Imaging system

The micro-CT prototype PIXSCAN (figure 1) is contained in a lead/steel box of dimensions 80 cm × 130 cm × 90 cm (L × W × H). It is composed of two x-ray tubes which can be easily interchanged: a molybdenum target x-ray tube with a 50 μm × 50 μm emission spot (MCBM 65 B-50, RTW, Berlin, Germany) and a tungsten target tube with a 20 μm × 20 μm emission spot (Microfocus 90KV TGT, Oxford Instruments, Scotts Valley CA, USA). In front of the tube, a wheel holding different types of filters permits further modulatation of the x-ray beams.

Table 1 lists the radiation qualities considered in this paper and figure 2 shows their emission spectrum as measured by a XR-100 T-CdTe (Amptek, Bedford MA, USA) spectrometer. The source-detector distance is 447 mm and 437 mm in the case of the molybdenum and tungsten anode tube, respectively. The imaged object is placed on a rotating table located between the

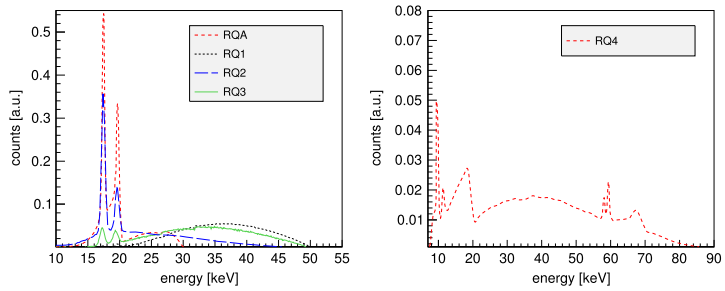

Figure 2. Spectra of the radiation qualities listed in table 1, delivered by the molybdenum (left) and the tungsten (right) target x-ray tube.

Table 2. Main characteristics of the XPAD3 circuit.

Number of pixels	9600 (80 × 120)
Pixel size	130 μm × 130 μm
Chip size	1.56 cm × 1.04 cm
Input polarity	Hole collection
Selectivity mode	Single threshold
Counting rate	10^6 photons/pixel/s
Readout time	1 ms/frame
Global electronic noise	100 e^- rms

source and the detector at a distance corresponding to a magnification factor of 1.85.

The camera is composed of eight contiguous horizontal modules which are slightly tilted vertically (7.5 degrees) and overlapped by about 3 mm in order to avoid dead areas. Each module has a size of 7.5 cm × 1.6 cm and consists of a silicon sensor, 500 μm thick, with 560 × 120 pixels at 130 μm pitch bump-bonded to 7 XPAD3 chips. Table 2 summarizes the main characteristics of the XPAD3 circuit, which reads a matrix of 80 × 120 pixels, each associated with an analog stage, with charge detection and current comparison for the energy discrimination, and a digital stage, with a 12-bits counter associated with an overflow mechanism. The camera has a total of 537,600 pixels.

2.1.1. Pixel threshold calibration

The energy threshold of the XPAD3 chip can be set pixel per pixel through two digital-to-analog converters (DACs): one global 8-bits DAC, called ITH (intensity threshold), common to every pixel of a chip and one local 6-bits DAC, called DACL, which permits the fine-tuning of the threshold of each pixel independently. The step size of both DACs is regulated by a common register and can be varied from 0.5 to 2 keV, 0.7 keV being the typical used value.

Standard tomographic images are acquired after setting the thresholds just above the electronics noise in order to count all the photons impinging on the camera. In this case, the threshold calibration is performed in two steps. A first calibration is obtained in the absence of radiation by performing ITH and DACL scans and by setting the threshold just above noise (i.e. the lowest threshold value for which pixels are not counted). However, a flat image acquired with such a calibration shows a counting dispersion per chip much higher than is expected for a single pixel, which is known to follow the Poisson law (Cassol *et al* 2009). This is mainly due to two concurrent factors. First, the electronic noise is not exactly the same for each pixel. Second, hybrid pixels are affected by charge sharing between pixels, which adds a tail of low energy signals to the original x-ray spectrum (Cassol *et al* 2011). Hence, the mentioned slight difference in the threshold setting implies a measurable difference in terms of counts between the pixels. In order to further equalize the response of the pixels, we proceed with a second calibration step, which takes into account the employed radiation and consists in an iterative process. We start by applying the previously obtained calibration and acquire a flat image with the desired radiation. Then, we decrease or increase the DACL of each pixel if it counts more or less than three sigma ($\sigma = \sqrt{\overline{N}}$) far from the average pixel counts of the chip, $\overline{N}$. We apply the new calibration and repeat the procedure until less than 5% of the DACL moves. Generally, five iterations are sufficient to reach almost a Poisson distribution of the counts, as can be seen in figure 3, where we compare the count histograms of an image before and after a calibration performed with the radiation RQA. The remaining discrepancy from the theoretical Poisson dispersion has to be associated with the DACL step, which intrinsically limits the equalization.

In the case of K-edge tomography or other non standard tomographic methods, calibration of the thresholds at higher energies is required. In this case, either monochromatic synchrotron radiations or polychromatic x-ray tubes with suitable filters are chosen for irradiating the chips during the ITH and the DACL scans. The calibration values are then identified

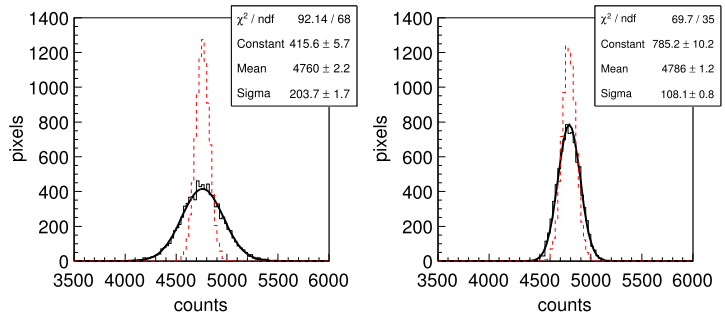

Figure 3. Histograms of the pixel counts in a chip, before (left) and after (right) equalization of the pixel thresholds with an incident radiation. The red-dashed histograms show the distributions expected in the case of Poisson dispersion of the counts in a chip.

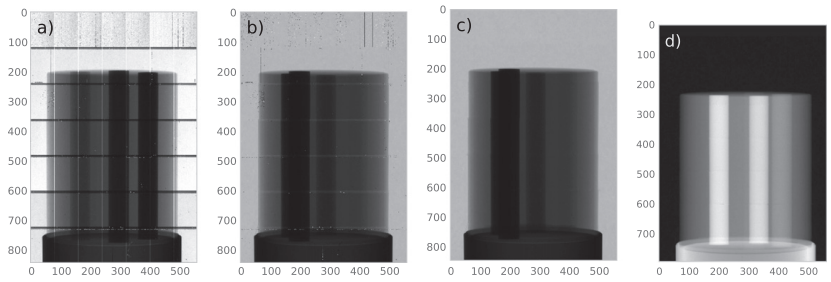

Figure 4. Sequential steps of data processing before tomographic reconstruction. From left to right: (a) raw projection, (b) calibrated projection, (c) projection corrected from defective pixels, (d) logarithm of the projection corrected from the pixels masked by the upper adjacent module.

by looking at the variation of the pixel counts when the scan moves through to the desired calibration energy (Cassol *et al* 2013).

2.1.2. Image processing and tomographic reconstruction

Each tomographic acquisition includes 360 projections, each acquired after the rotation of the imaged object by one degree, 100 flat images (no object in front of the source) and 100 black images (x-ray source off). Figure 4(a) shows the raw projection of a cylindrical phantom. The dark horizontal rows correspond to the pixels of each module that are covered by the module placed just above it; these rows do not enter the final image (around 6% of the total pixels). The vertical bright columns correspond to the pixels at the edges of each chip, which are by construction 2.47 times larger. It has to be noticed that the first module on top is not working properly, this will consequently affect the top part of all our tomographic images. Finally, we can also observe some defective pixels (around 1% in the top module and 0.1% in the other modules).

Before any tomographic reconstruction, raw projections are processed in the following way: normalization of the images to the average counts of the 100 flat images (figure 4(b)); identification of defective pixels (pixels which count in black images or count more than 3 σ away from the mean value in flat images) replaced by bilinear interpolation of good neighboring pixels (figure 4(c)); and finally, suppression from the images of the rows corresponding to the pixels masked by the module located just above it and computation of the logarithm of the resulting image (figure 4(d)). Image reconstruction is processed on GPUs[5] using a voxel-driven implementation of the FDK algorithm (Feldkamp *et al* 1984), with non-apodized ramp filtering. The back projection core of the code incorporates the internal tiled geometry of the detector and the cone-beam acquisition setup.

The output of the image reconstruction, μ, is given in units of cm^{-1} as the attenuation coefficient. However, in order to compare our tomographic results from different radiation qualities (and eventually from different imaging systems) we convert μ into a CT number expressed in Hounsfield units according to

[5] The reconstruction is performed on two AMD/ATI FirePro V8800 graphic cards simultaneously.

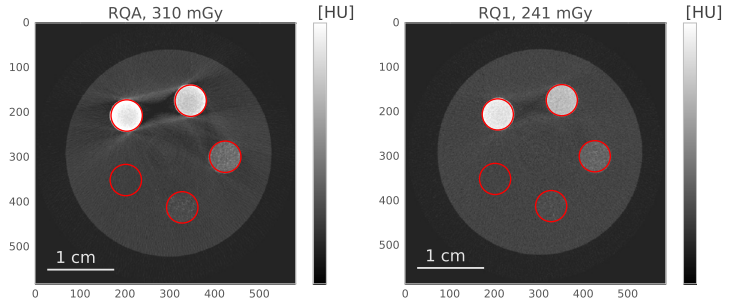

Figure 5. Transverse slices of a linearity phantom acquired with a soft and a hard radiation quality: RQA (left) and RQ1 (right). The red circles indicate the position of the inserts with different calcium hydroxyapatite densities.

equation (1)

$$HU = 1000 \times \frac{\mu - \mu_{\text{water}}}{\mu_{\text{water}}} \quad (1)$$

3. Measurements and results

3.1. Imaging with phantoms

We assess in this section the technical quality of the scanner. We employ mainly the standard mammography radiation RQA, already used for assessing the radiological performances of the detector (Cassol *et al* 2009). When pertinent, we consider three delivered doses: 31, 155 and 310 mGy, defined by changing the acquisition time from 2 to 10, and 20 s/projection and corresponding to counting statistics in flat images of approximately 1000, 5000 and 10,000 photons/pixel, respectively.

3.1.1. Linearity

The linearity of CT numbers with respect to the attenuation coefficients of the imaged materials is verified using a phantom QRM-MicroCT-HA (QRM, Germany) of epoxy resin with five inserts of calcium hydroxyapatite of different density (the diameters of the phantom and of the inserts are 32 and 5 mm, respectively). Figure 5 shows two reconstructed transverse slices acquired with the soft and the hard radiation qualities RQA and RQ1, which have a HVL of 0.62 and 2.56 mm of Al, respectively. The increase of the beam hardening effect in correspondence to the softer radiation is well visible for the heavier inserts. This effect implies a loss of linearity at higher densities, as can be seen in figure 6, where we present the calibration curves for the two radiation qualities. Still, it has to be noticed that CT numbers can be considered linear for soft tissue densities (−1000 HU to 1000 HU). The attenuation coefficients of the inserts, μ, are calculated, for each radiation quality, by estimating the mean free path of the radiation, $1/\mu$, with the Geant4 simulation code (Allison 2007).

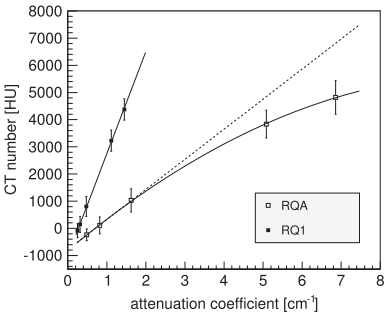

Figure 6. CT calibration curves for the two radiation qualities RQA and RQ1. The full lines correspond to a second order polynomial fit of all points, while the dashed lines show the linear fit of the three points at lower density. The error bars correspond to the RMS of the CT numbers calculated in cylindrical regions of interest (4.5 mm diameter and 5 mm height) inside the inserts.

3.1.2. Noise

We study the noise of the tomographic images by imaging a cylindrical phantom filled with water using the radiation RQA. Figure 7 presents, for each dose employed, an example of a reconstructed transverse slice, together with the average standard deviation, σ, calculated inside the indicated regions of interest (ROIs). The results can be better quantified using the variance σ^2. In fact, in the case of a cylindrical object, if the detector is affected only by statistical noise, the variance of a tomographic image is inversely proportional to the number of photons detected per pixel in the central region of the phantom, $\overline{N}$, and can be approximated by equation (2) (Faulkner and Moores 1984)

$$\text{var}(\mu) = \frac{\pi^2}{12\, m\overline{N} d^2}\ [\text{cm}^{-2}] \quad (2)$$

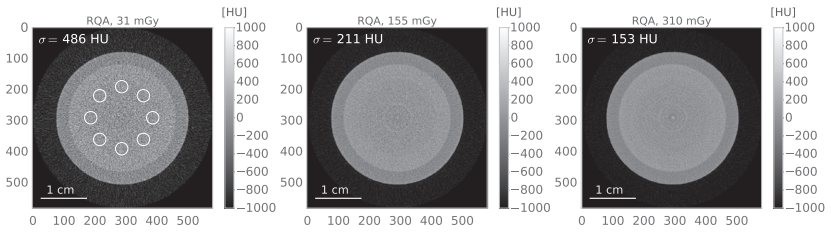

Figure 7. Transverse slices of a cylindrical phantom with plastic walls filled with water, from projections acquired with three different doses. The left image shows the ROIs used to estimate the mean standard deviation, σ.

Table 3. Comparison of measured, σ^2, and expected, var(μ), variances in CT images at three different doses.

Dose [mGy]	var(μ) [cm^{-2}]	σ^2 [cm^{-2}]	Dose$_{(31\ mGy)}$/Dose	$\sigma^2/\sigma^2_{(31\,mGy)}$
310	0.014	0.015 ± 0.001	0.10	0.10 ± 0.01
155	0.029	0.029 ± 0.002	0.20	0.19 ± 0.02
31	0.144	0.155 ± 0.011		

where m is the number of projections and d^2 the detector pixel size. Table 3 shows the good agreement between var(μ), calculated using equation (2), with $\overline{N}$ measured on the projections, and σ^2, estimated from the reconstructed images. It shows also that the ratio of the variances scales inversely proportional to the dose, as is implicit in equation (2).

Finally, we verify the noise behavior as a function of spatial frequency, i.e. the spatial correlation between CT numbers in the reconstructed images, by estimating the noise power spectrum (NPS), which is the Fourier transform of the auto-correlation function. The two-dimensional NPS is calculated from an ROI of 50 × 50 pixels selected in traverse slices of the water phantom reconstructed image. It is defined as

$$\mathrm{NPS}(u, v) = \frac{|FFT(\delta(x, y))|^2}{M^2} R^2 \qquad (3)$$

where u and v denote the spatial frequency along the horizontal and vertical axis, $M^2 = 50 \times 50$ is the area of the ROI, $R^2 = 0.07 \times 0.07\,\mathrm{mm}^2$ is the reconstructed image pixel size and FFT the fast Fourier transform of $\delta(x, y)$, which represents the normalized variation of $\mu(x, y)$ with respect to a third order polynomial fit $f(x, y)$ of the chosen ROI defined as

$$\delta(x, y) = \frac{\mu(x, y) - f(x, y)}{f(x, y)} \qquad (4)$$

The subtraction of the polynomial fit is applied in order to remove from the spectrum the low frequency components induced by counting modulations that are constant from image to image, like for instance beam hardening effects (Foley Kijewski and Judy 1987). Figure 8 shows the two-dimensional NPS averaged over 70 adjacent frames and along the radial component. The results are fairly close to the model developed by Foley Kijewski and Judy (1987), which considers detectors presenting only statistical noise and propagates the noise to tomographic images, taking into account filtering, interpolation and discrete sampling, but in the case of a parallel beam instead of a cone beam configuration.

3.1.3. Spatial resolution

We estimate the spatial resolution by studying the system response to an edge and to a point like object (figure 9). In the first case, we image a half cylinder of polyvinyl chloride with the radiation RQ3 in order to reduce the beam hardening effect. We derive the system response by fitting (with a Gaussian error function) the projection of the CT numbers of a transverse slice in the direction perpendicular to the edge. The slight inclination of the edge with respect to the slice pixel matrix provides oversampling of the data. We obtain the line spread function (LSF) of the system by differentiating the edge function and the modulation transfer function (MTF) by performing a discrete Fourier transform of the LSF. Results are shown in figure 10. The full width at half maximum (FWHM) of the LSF is ~94 μm, slightly larger than the reconstructed pixel size (70 μm). In fact, it is known that charge sharing between pixels slightly reduces the spatial resolution of the XPAD3 detector when using low pixel thresholds (Cassol *et al* 2009), moreover the x-ray tube spot size (50μm × 50 μm) and the interpolation processes involved in the FDK reconstruction contribute also to the width of the LSF. Nevertheless, the MTF at 20% is close to the Nyquist frequency of the images (7.1 lp/mm). Similar results are obtained with the estimation of the point spread function (PSF). In this case, we image a phantom QRM-microCT-wire, which is an empty cylinder containing two

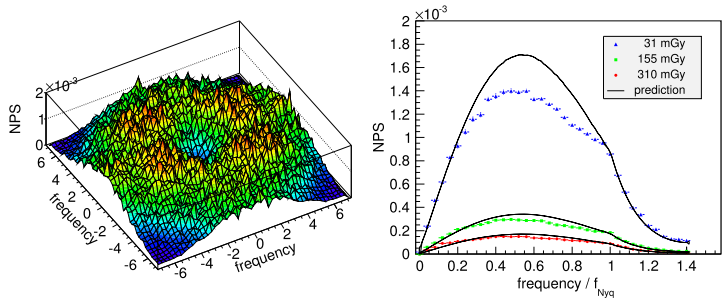

Figure 8. Two dimensional NPS (RQA radiation, 310 mGy) (left) and NPS averaged along the radial component, for three different doses (right). The lines show the NPS value predicted by the model developed by Foley Kijewski and Judy (1987).

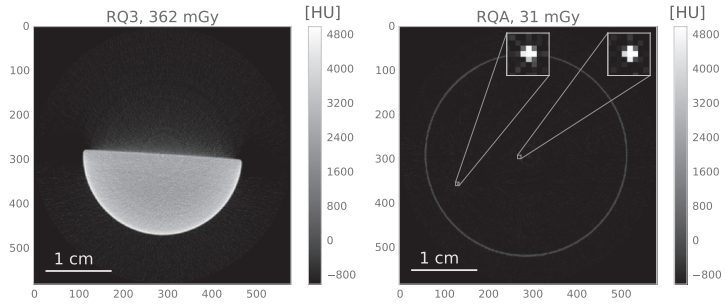

Figure 9. Transverse tomographic slices of the phantoms used for the estimation of the line spread function (LSF) (left) and of the point spread function (PSF) (right) of the system.

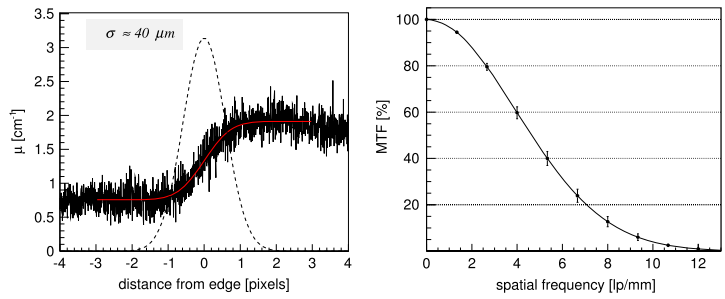

Figure 10. Left: fit of the edge response (red fill line) and its derivative which gives the LSF of the system (black dashed line). Right: MTF obtained from the discrete Fourier transform of the LSF.

tungsten wires of 25 μm diameter, almost parallel to the rotation axis, and placed at two different distances from it. The fact that the wires are not perfectly parallel to the rotation axis provides over-sampling of the PSF. We sum the response of 400 consecutive slices, each one being correctly shifted to superimpose all PSF centers (estimated by a two-dimensional Gaussian fit in each slice). Figure 11 shows the two PSFs, which are pretty symmetric along X and Y and have a fitted FWHM of 92 μm and 93 μm for the central and the peripheral wires, respectively, quite close to the LSF result.

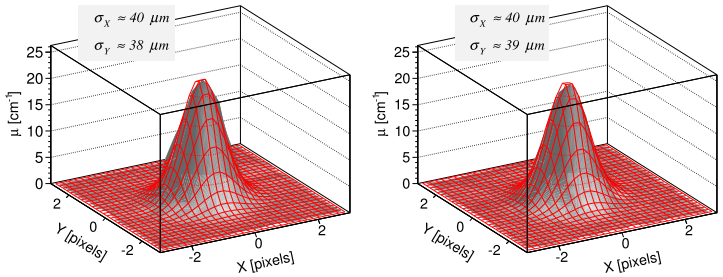

Figure 11. Oversampled PSF and its two-dimensional Gaussian fit (red lines) of the central (left) and the peripheral (right) wire of the QRM-microCT-wire phantom.

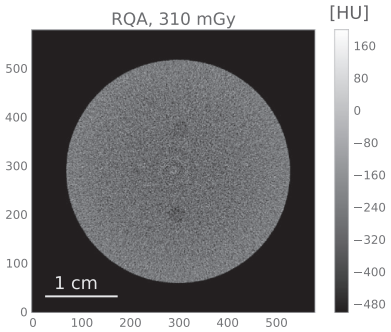

Figure 12. Transverse slice of the QRM low contrast phantom (RQA radiation).

3.1.4. Low contrast detectability

Detectability of low contrast inserts in tomographic imaging systems is influenced by several factors. It depends on the intrinsic contrast of the imaged object ($\Delta HU = |HU_{object} - HU_{environment}|$) and on the object dimensions. Further, it is also impacted by the noise of the system (Hanson 1979), which, in the case of the micro-CT prototype PIXSCAN, is only related to the counting statistics, hence to the delivered dose.

We quantify the low contrast detectability of our system using a QRM-microCT-LC phantom, including four cylindrical inserts with two different diameters (1 mm and 2.5 mm) and contrasts, $\Delta HU1 \approx 49$ HU and $\Delta HU2 \approx 25$ HU, estimated for the RQA radiation using the photon cross section tables of the Geant4 code. Figure 12 presents a reconstructed transverse slice imaged with the above radiation.

In the extreme case for which only a single transverse slice is accessible (slice thickness 0.07 mm), we estimate the visibility of the inserts by asking five different observers to recognize, in identical conditions, the four cylindrical inserts in 40 different slices. Figure 13 summarizes the results. It can be seen that the visibility strongly depends on all the parameters (intrinsic contrast, dimensions and absorbed dose). A 100% visibility is obtained only for the biggest insert in the case of the highest contrast (~49 HU) and for the highest dose (~10,000 photons/pixel). When thicker slices are considered, calculating the average on several transverse slices can result in a 100% visibility of all the inserts. To achieve it, we estimate that we need 20, 40 and 200 original slices for doses of 310, 155 and 31 mGy, corresponding to an overall thickness of 1.4, 2.8 and 14 mm, respectively. This can be seen in figure 14, where we indicate also the contrast of the inserts with respect to an equivalent size ROI located nearby (the average CT number values are obtained by a Gaussian fit of the CT numbers inside the ROIs). The measured values are fairly close to the above estimated $\Delta HU1$ and $\Delta HU2$, even if they are slightly higher for the biggest inserts and systematically lower for the smallest one, most probably due to the partial volume effect.

3.2. Imaging with mice

The main goal of micro-CTs is to image *in vivo* and *post mortem* small animals for biomedical research. In this section, we present several examples of preclinical imaging, with more emphasis on qualitative than quantitative results.[6]

3.2.1. Standard tomographic imaging

Since the DQE of the XPAD3/Si detector is not particularly competitive with respect to commonly used charge integration cameras (Cassol *et al* 2009), standard tomography results are not expected to be particularly outstanding. More precisely, we have seen in section 3.1.4 that images with good contrast-to-noise ratio need statistics of at least 10,000 photons/

[6] All experimental procedures were performed in accordance with the French legislation and in compliance with the European Community Council Directive of November 24, 1986 (86/609/EEC) for the care and use of laboratory animals. The research on animals was authorized by the Direction Départementale des Services Vétérinaires des Bouches-du-Rhône (license 13-300) and approved by the National Committee for Ethic in Animal Experimentation (Section N14; project 87-04122012b).

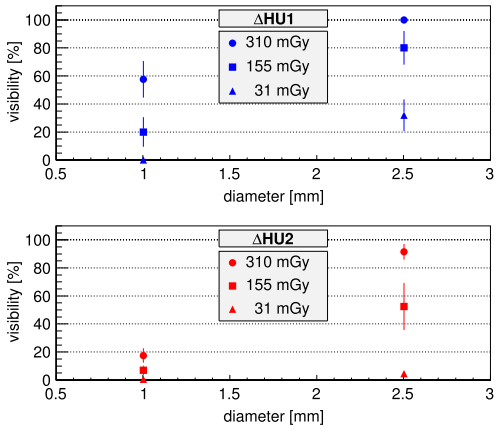

Figure 13. Visibility of low contrast inserts in one tomographic slice as a function of their diameter and contrast for three different doses.

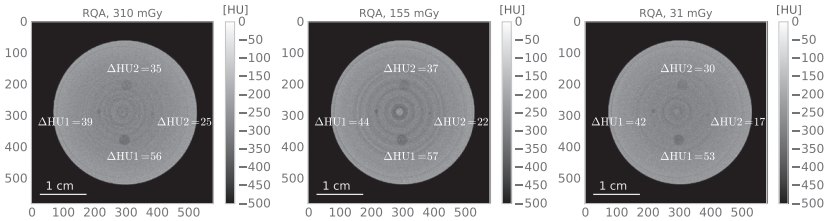

Figure 14. Transverse slices with a 100% visibility of all the inserts obtained by averaging 20 (left), 40 (middle) and 200 (right) slices for doses of 310, 155 and 31 mGy, respectively. The contrast of the inserts with respect to an equivalent size ROI located nearby is also indicated.

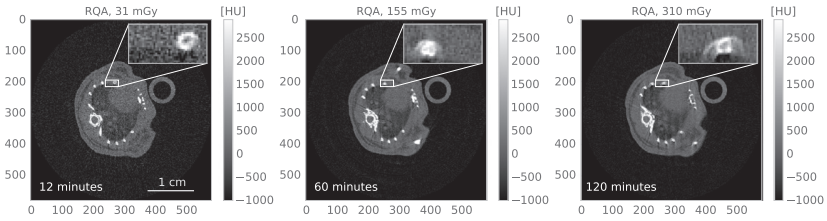

Figure 15. Transverse reconstructed slices of data acquired *in vivo* for three different acquisition times of 12, 60 and 120 min (from left to right). The rectangles show the zoom of a rib.

pixels, which corresponds to doses of hundreds of mGy.

The first example we discuss is obtained with the RQA radiation used until now. Figure 15 shows transverse slices of an anesthetized mouse[7] acquired for doses of 31, 155 and 310 mGy, corresponding to total acquisition times of 12, 60 and 120 minutes, respectively. Such long acquisitions, both due to the limited DQE of the detector and the low dose rate of the radiation, are actually not suitable for *in vivo* mice imaging. In fact, small physiological movements are always present and induce some blurring with time, as can be seen by looking at the zoom of a rib in figure 15.

[7] Anesthesia was obtained by intra-venous injection of a mixing of Ketamine and Xylazine.

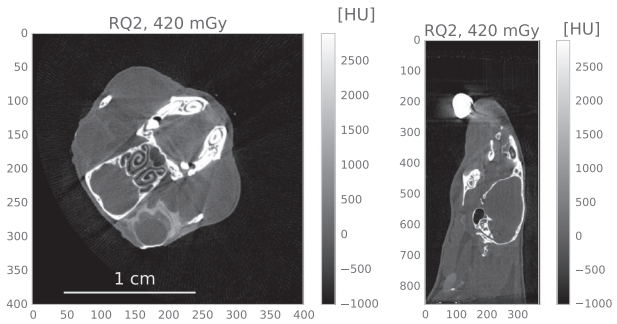

Figure 16. Transverse (left) and sagittal (right) slice of a mouse head acquired in zoomed configuration (magnification of 2.60 instead of 1.85). The white spot visible in the sagittal slice is the dough in which are inserted the teeth of the mouse in order to keep the animal in a vertical position.

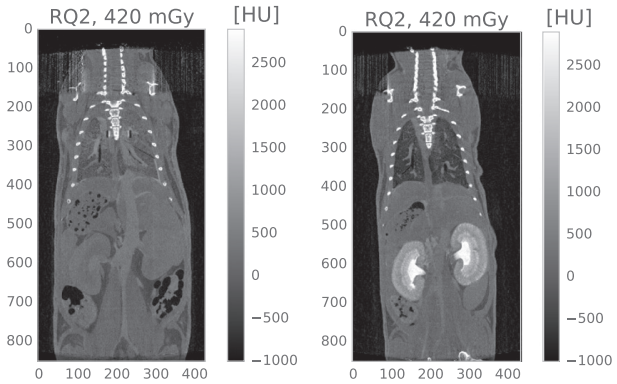

Figure 17. Coronal slices of mice sacrificed shortly after the injection of an iodinated contrast agent.

Therefore, in order to better estimate the potential of the micro-CT prototype PIXSCAN, we will employ in the following sections other radiation qualities with higher dose rates. Moreover, we will present only *post mortem* tomographic results, that are less impaired by longer acquisition times.

The magnification of the system can be varied from 1.4 to 2.8 by changing the distance between the rotation axis and the source. Figure 16 presents an example of a mouse head scanned with a magnification of 2.6, which permits us to better distinguish the details of the nasal septum and of the skull (RQ2 radiation, 420 mGy, 6 min acquisition duration).

In order to increase the visibility of the vascular system and/or of individual organs, tomographic imaging can profit nowadays from great progress in the development of specific contrast agents, which enhance significantly the potentialities of micro-CTs in biological studies (Li *et al* 2014). Figure 17 shows two imaging examples performed with an iodinated contrast agent (Iomeron 350). The images are acquired *post mortem* with animals sacrificed either immediately or 15 min following the injection of 300 μl of the contrast agent. In the left image, the iodine is still diffused by blood perfusion, particularly evident in the lung where the little vessels have a much higher contrast than usual, whereas in the right image the iodine is already mostly accumulated in the kidneys.

3.2.2. K-edge tomographic imaging

Contrary to standard tomography, the use of photon counting detectors is fully justified for spectral tomography, which cannot be addressed by charge integration devices. K-edge imaging exploits the dependence of the photon attenuation coefficient on the photon energy. In particular, for values close to the K-shell binding energy of a given material (E_K), the attenuation coefficient behaves significantly differently than for the surrounding materials and it presents in fact a sharp increase, due to the opening of the new

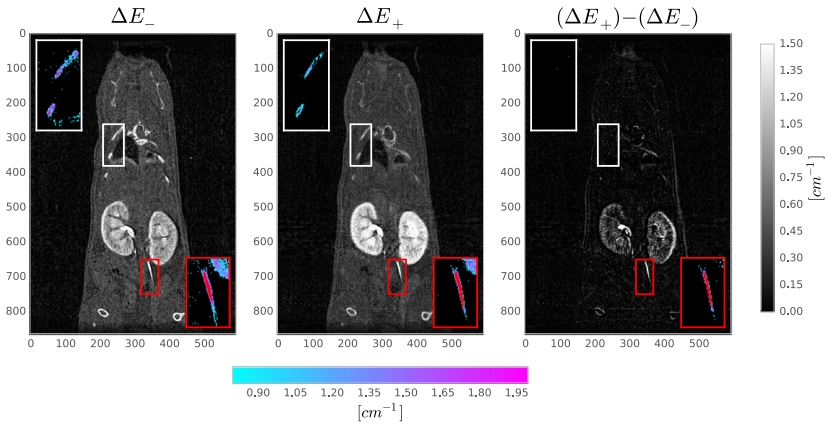

Figure 18. Coronal slices of a sacrificed mouse after injection of an iodinated contrast agent. From left to right: slice reconstructed in the energy window ΔE_-, in the energy window ΔE_+ and K-edge image (subtraction of the first slice from the second one, $(\Delta E_+) - (\Delta E_-)$). Zooms of two ribs and the ureter are also shown.

photoelectric interaction channel. In the case of the micro-CT prototype PIXSCAN, K-edge imaging consists in the comparison of images taken in two different energy windows, one below and the other above E_K. Since the XPAD3 chip is supplied with only one threshold, we obtain an energy window of width ΔE by subtracting two acquisitions taken with the pixel thresholds set at two different values: $E_1 = E$ and $E_2 = E + \Delta E$, hence resulting in $\Delta E = E_2 - E_1$. This procedure has already been successfully tested on phantoms (Cassol *et al* 2013). We present here its application to a mouse sacrificed after the injection of 200 μl of Visipaque 320. We perform two successive acquisitions while setting the pixel thresholds at 25.5 and 33.2 keV. Then, the energy windows are defined as $\Delta E_- = (25.5–33.2)$ keV and $\Delta E_+ = (33.2–50.0)$ keV, 50.0 keV being the end point of the x-ray energy spectrum. We use the radiation RQ3 with an acquisition duration of 30 min, corresponding to a delivered dose of 362 mGy per scan and a total dose of 724 mGy for the K-edge result. Figure 18 shows a coronal slice for ΔE_- and ΔE_+ and their subtraction, $(\Delta E_+) - (\Delta E_-)$, here named 'K-edge image', which permits the identification of the iodine content that appears with positive values. For example, a comparison of two ribs and the ureter shows a similar aspect in each one of the ΔE slices, whereas the ribs are absent in the K-edge image because their attenuation coefficient decreases with energy, hence they appear with negative values after the subtraction of the two windows.

This result represents an undeniable proof of principle of the method, but calls for further improvements. In fact, the images reconstructed within restricted energy windows are pretty noisy, due to a strong reduction in photon statistics induced by the energy windowing and due to the large variance in the window images resulting from the sum of the variance of the single acquisitions. Moreover, since the acquisitions are performed successively, adjustments of the animal (even if dead) induce false signals in the K-edge image (see for example the shadows at the femur positions). Concerning noise, an increase of the total photon flux is not suitable since it would further increase the delivered dose, which is already doubled by the need of two acquisitions. Therefore, the most appropriate solution would be an increase of the detection efficiency. Indeed, the next generation of XPAD3 cameras is conceived with CdTe sensors instead of silicon sensors (Buton *et al* 2014). Preliminary studies have shown that the higher efficiency of CdTe induces an improvement of contrast-to-noise ratio in K-edge images of iodine by a factor of around three (Cassol *et al* 2015a). Concerning the animal movements observed between images, we explore the possibility of performing only one acquisition with pixels set at different thresholds along an alternate pattern to form bigger composite pixels and to obtain images reconstructed within energy windows directly from this single scan (Kronland–Martinet *et al* 2014). This solution, which would also have the advantage of reducing the delivered dose by a factor of two, is at the expense of degrading the spatial resolution.

3.2.3. Fast dynamic radiography

The last imaging example we want to present takes advantage of the fast acquisition rate achievable with the camera XPAD3, which permits us to follow the perfusion of an iodinated contrast agent through the venous and arterial system of a living mouse. In this

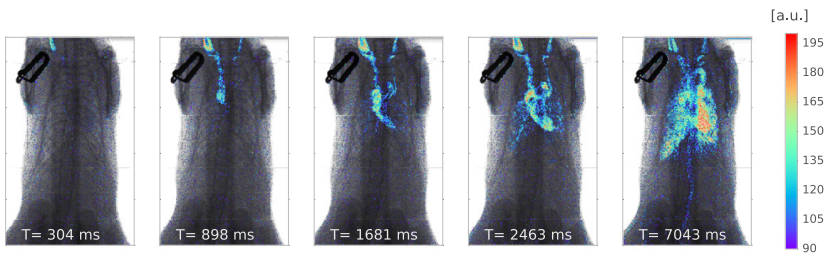

Figure 19. Perfusion of an iodinated contrast agent through the venous and arterial system of a living mouse. The iodine component (colored pixels) is superimposed to the usual gray-level projections.

case, images are simple projections[8] and are performed with the radiation RQ4. The contrast agent (200 μl of Iomeron 350) is injected retro-orbitally while images are acquired with 10 ms pose duration at a frame rate of 69 images/s, corresponding to counting statistics in flat images of around 1500 photons/pixel. The contrast induced by iodine is identified in each frame by subtracting a frame acquired before injection of iodine and applying a threshold to the resulting image. Figure 19 shows some projections selected at different times after the injection. The iodine component (colored pixels) is superimposed to usual gray-level projections. It can be seen how iodine is transported via the veins (i.e. superior vena cava) to the right atrium and to the right ventricle of the heart. It perfuses then to the lungs and returns to the left part of the heart from which it is pumped toward other organs via arteries (the aortic arch becomes clearly visible together with the descending aorta).

This study, which constitutes only a preliminary test, clearly indicates the potential of such a camera for angioscopy or similar studies.

4. Discussion and summary

We characterized the imaging performance of the micro-CT prototype PIXSCAN equipped with an x-ray camera based on photon counting XPAD3/Si hybrid pixel detectors. The dimensions of the camera permit us to image whole-body mice without dead area. Studies on phantoms show: (i) a linear tomographic response for material densities of interest for preclinical studies, (ii) an uncorrelated tomographic noise, exclusively affected by the counting statistics, (iii) a spatial resolution close to the pixel size, marginally affected by charge sharing between pixels. Finally, the detectability at low contrast is such that an object with a contrast of ~25 HU can be detected if its size is of the order of a millimeter for a delivered dose above 300 mGy that corresponds to a counting statistic of around 10,000 photons/pixel, recognized as a reference value for good quality imaging.

Standard tomographic imaging of *in vivo* mice shows the importance of performing short acquisitions (~minute) in order to not be affected by animal movements. This fact, together with the general effort of reducing the delivered dose (particularly important for longitudinal studies), suggests the development of cameras with improved detection efficiency. The use of contrast agents turns out to be a reliable tool in standard imaging and opens the door to less standard methods such as K-edge imaging and fast dynamic imaging, which are demonstrated to be accessible to the XPAD3 chip. However, a higher detection efficiency appears again a fundamental condition to reduce noise sufficiently for obtaining fully satisfying results. Therefore, a more efficient camera based on the XPAD3 chip bump-bonded to CdTe sensors is presently under commission and it will be thoroughly assessed for biomedical imaging applications with x-rays (Cassol *et al* 2015b). Nonetheless, the future of spectral imaging with photon counting detectors relies on the development of hybrid pixel chips with more than one threshold, ensuring a significant improvement on the signal-to-noise ratio, the delivered dose and the acquisition time.

[8] Projections are corrected for defective pixels and masked rows of pixels. No correction of the tiled geometry is applied, since the vertical pixel dimension is marginally affected by the 7.5 degrees tilt (<1%).

Acknowledgments

The authors would like to thank all the members of the XPIX collaboration (CPPM, SOLEIL, D2AM-ESRF) involved in the development of the XPAD3 detector.

References

Allison J 2007 Geant4 — A simulation toolkit *Nucl. Phys. News* **17** 20–4

Alvarez R E and Macovsky A 1967 A energy-selective reconstruction in x-ray computerized tomography *Phys. Med. Biol.* **21** 733–44

Buton C *et al* 2014 Comparison of three types of XPAD3.2/CdTe single chip hybrids for hard x-ray application in material

science and biomedical imaging *Nucl. Instrum. Methods* A **758** 44–56
Cassol B F *et al* 2009 Imaging performance of the hybrid pixel detectors XPAD3-S *Phys. Med. Biol.* **54** 1773–89
Cassol B F *et al* 2011 Study of the charge sharing effect in the photon counting pixel detector XPAD3-S *Nucl. Instrum. Methods* A **633** 111–3
Cassol B F *et al* 2013 First K-edge imaging with a Micro-CT based on the XPAD3 hybrid pixel detector *IEEE Trans. Nucl. Sci.* **60** 103–8
Cassol F *et al* 2015a K-edge imaging with the XPAD3 hybrid pixel detector, direct comparison of CdTe and Si sensors *Phys. Med. Biol.* **60** 5497–511
Cassol F *et al* 2015b A large surface x-ray camera based on XPAD3/CdTe single chip hybrids, iWoRID 2015 *JINST* submitted (doi:10.1088/1748-0221/10/11/C11010)
Kronland-Martinet C *et al* 2014 Development of K-Edge spectral tomography using XPAD3 composite pixels *Conf. Rec. of the IEEE Med. Imag. Conf.* (*8–15 Nov, Seattle, USA*)
Delpierre P 2014 A history of hybrid pixel detectors, from high energy physics to medical imaging *JINST* **9** C05059
Faulkner K and Moores B M 1984 Noise and contrast detection in computed tomography imges *Phys. Med. Biol.* **29** 329–39
Feldkamp L A *et al* 1984 Practical cone-beam algorithm *J. Opt. Soc. Am.* A **1** 612–9
Foley Kijewski M and Judy P F 1987 The noise power spectrum of CT images *Phys. Med. Biol.* **32** 565–75
Hanson K M 1979 Detectability in computed tomographic images *Med. Phys.* **6** 441–51
IEC 61267 2005 Medical diagnostic x-ray equipment—radiation conditions for use in the determination of characteristics p 85
Li X *et al* 2014 Contrast agents for preclinical targeted x-ray imaging *Advanced Drug Delivery Reviews* **76** 116–33
Jorgensen S M *et al* 2011 Biomedical spectral x-ray imaging; promises and challenges, in Medical Applications of Radiation Detectors *Proc. SPIE* **8143** 814302
Pangaud P *et al* 2007 XPAD3: a new photon counting chip for small animal imaging *Nucl. Instrum. Methods* A **571** 321–4
Riederer S J and Mistretta C A 1977 Selective iodine imaging using K-edge energies in computerized x-ray tomography *Med. Phys.* **4** 474–81
Taguchi K and Iwanczyk J S 2013 Vision 20/20: Single photon counting x-ray detectors in medical imaging *Med. Phys.* **40** 100901
Wermes N 2005 Pixel detectors for tracking and their spin-off in imaging applications *Nucl. Instrum. Methods* A **541** 150–65

Appendices

A. Semiconductor physics

The electrical properties of solids can be described by the energy band model. In this model, the electron energy levels of a solid are localized inside two energy bands, the lower *valence band* and the upper *conduction band*, separated by the *forbidden band*. The band gap energy, equal to the difference between the minimum energy of the conduction band and the maximum energy of the valence band, $E_g = E_C - E_V$, defines the conduction properties of the materials, as shown in Figure A.1.

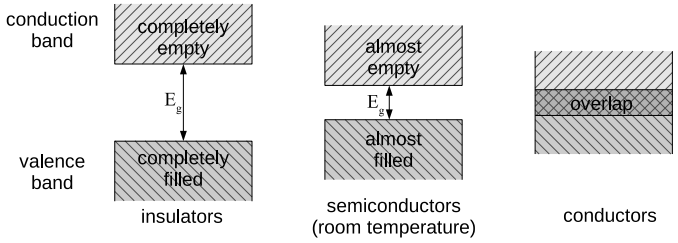

Figure A.1: Energy band model of solid materials (Dawiec 2010). The energy gap is $E_g \sim 1\ eV$ in semiconductors and $E_g > 5\ eV$ in insulators.

Semiconductors are characterized by a pretty narrow gap, $\sim 1\ eV$, in such a way that thermal excitation can move some electrons from the valence band to the conduction band, leaving a hole behind. It follows that in completely pure semiconductors[o], called *intrinsics*, the density of electrons in the conduction band, n_i, and of holes in the valence band, p_i, must be equal

$$n_i \quad = \quad p_i \tag{A.1}$$

These charges can be considered free and are responsible of the weak conductivity of intrinsic semiconductors. The density of free electrons and holes (calculated as the integral of the product of the density of states and their probability of occupation in the conduction and valence band, respectively) depends, for a given material, exclusively on the temperature

$$\begin{aligned} n_i &= N_C\ e^{-\frac{E_C - E_F}{kT}} \\ p_i &= N_V\ e^{-\frac{E_F - E_V}{kT}} \end{aligned} \tag{A.2}$$

where E_F is the Fermi level of that material, k the Boltzmann constant and N_C and N_V are the *effective density of state* in the conduction and valence band,

[o]In practice, a semiconductor can be considered pure if its density of impurities is much lower than the free charge density due to the thermal excitation.

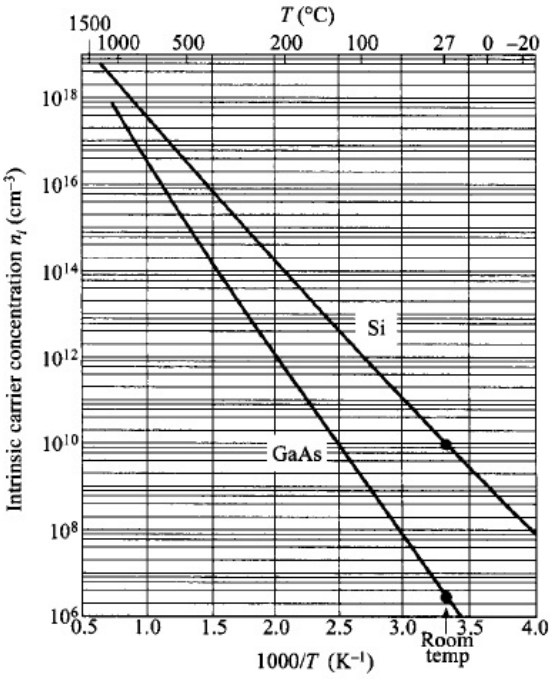

Figure A.2: Intrinsic carriers concentration in Si and GaAs as function of the temperature (Sze and Ng 2006).

respectively

$$N_C = 2\left(\frac{2\pi m_n kT}{h^2}\right)^{\frac{3}{2}} \tag{A.3}$$
$$N_V = 2\left(\frac{2\pi m_p kT}{h^2}\right)^{\frac{3}{2}}$$

where m_n (m_p) are the effective mass of electrons (holes)[p] and h is the Plank constant. In the case of silicon at 300 K, the electron and hole density is $1.45 \cdot 10^{10}\ cm^{-3}$ (Rossi et al. 2006) and decreases with the temperature as shown in Figure A.2. From equation A.2, it follows that the product of hole and electron concentrations does not depend on the Fermi level, hence on the semiconductor purity, but exclusively on E_g

$$n \cdot p = n_i^2 = N_C\, N_V\, e^{-\frac{E_g}{kT}} \tag{A.4}$$

which is known as the *mass-action law*. From equations A.1 and A.2, we can

[p] In silicon at 300 K, $m_n = 1.09\ m_0$ and $m_p = 1.15\ m_0$, being m_0 the free electron mass.

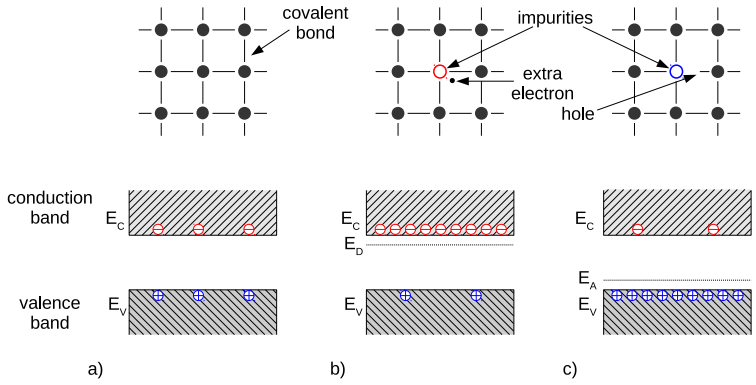

Figure A.3: Crystal lattice bond structure (top) and energy band model (bottom) of (a) an intrinsic, (b) n-type, (c) p-type semiconductor (Dawiec 2010).

derive the Fermi level E_i of an intrinsic semiconductor

$$E_i = \frac{E_C + E_V}{2} + \frac{3kT}{4} \ln\left(\frac{m_p}{m_n}\right) \tag{A.5}$$

which lies very close to the middle of the band gap at room temperature since $\frac{3kT}{4} \ln\left(\frac{m_p}{m_n}\right) \sim 0.01\ eV$.

Transport of charges

After the formation, electrons and holes move randomly away from the creation point, this random motion is called *diffusion*. The mean kinetic energy is that of free particles, $\frac{3}{2}kT$, with a mean thermal velocity of around 10^5 m/s at room temperature

$$v_{th} = \sqrt{\frac{3kT}{m_{n,p}}} \tag{A.6}$$

The average path between collisions with atoms and impurities of the crystals is $\lambda_c \sim 0.1\ \mu\text{m}$, which gives an average time between collisions equal to $\tau_c \sim 10^{-12}\ s$. Diffusion induces a current density proportional to the gradient of the carrier concentration, $\boldsymbol{\nabla} n$ and $\boldsymbol{\nabla} p$

$$\begin{aligned} \boldsymbol{J}_{n,diff} &= -e\ D_n \boldsymbol{\nabla} n \\ \boldsymbol{J}_{p,diff} &= \ \ e\ D_p \boldsymbol{\nabla} p \end{aligned} \tag{A.7}$$

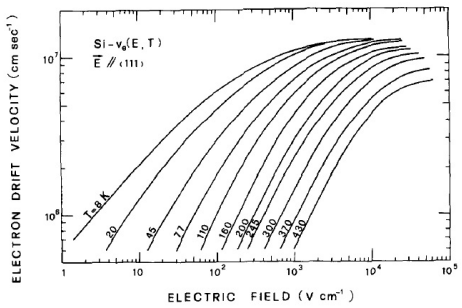

Figure A.4: Measured electron drift velocities as function of the electric field applied parallel to a $< 111 >$ crystallographic direction (Jacoboni et al. 1977).

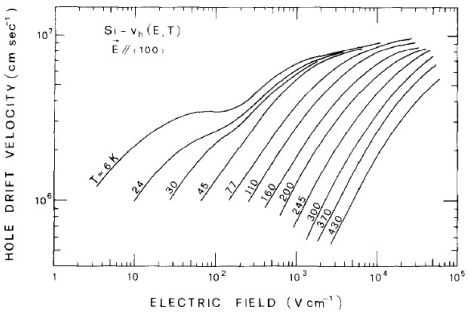

Figure A.5: Measured hole drift velocities as function of the electric field applied parallel to a $< 100 >$ crystallographic direction (Jacoboni et al. 1977).

where D_n and D_p are the *diffusion constant* for n and p carriers, respectively, and e is the positive elementary charge. The end effect of diffusion is to reduce the charge gradient overall the volume.

If an electric field, $\boldsymbol{E}$, is applied, charges start to drift parallel to the field lines acquiring an average *drift velocity* $\boldsymbol{v}$. The drift current density for carriers of charge q is given by the number of carriers N that drift through the cross-sectional area A in a time t

$$J = \frac{qN}{At} \tag{A.8}$$

where N is the number of charges in a volume $A \cdot l$, with the length l such that all the particles have the time to drift outside the volume in the time t, $l = v \cdot t$. Therefore, in term of charge density n_q we can set

$$J = \frac{qN}{At} = \frac{qn_qAl}{At} = \frac{qn_qAvt}{At} = qn_qv \tag{A.9}$$

which, in the case of electrons and holes, gives the vectorial notation

$$\begin{aligned} \boldsymbol{J}_{n,drift} &= -en\boldsymbol{v}_n \\ \boldsymbol{J}_{p,drift} &= ep\boldsymbol{v}_p \end{aligned} \tag{A.10}$$

then, if we consider the Ohm's law, the current density is defined as

$$J = \frac{I}{A} = \frac{V}{RA} = \frac{l}{RA}E = \sigma E \tag{A.11}$$

where V is the applied voltage, R the resistance and $\sigma = l/RA$ is the specific *conductivity* of the volume. Hence, considering equation A.10

$$\begin{aligned} \boldsymbol{J}_{n,drift} &\equiv -en\boldsymbol{v}_n = \sigma_n \boldsymbol{E} \\ \boldsymbol{J}_{p,drift} &\equiv ep\boldsymbol{v}_p = \sigma_p \boldsymbol{E} \end{aligned} \tag{A.12}$$

which says that the average drift velocity of the carriers is proportional to the electric field

$$\begin{aligned} \boldsymbol{v}_n &= -\mu_n \boldsymbol{E} \\ \boldsymbol{v}_p &= \mu_p \boldsymbol{E} \end{aligned} \tag{A.13}$$

the proportionality coefficient is called *mobility* and is defined as

$$\begin{aligned} \mu_p &= \frac{\sigma_n}{en} \\ \mu_n &= \frac{\sigma_p}{ep} \end{aligned} \tag{A.14}$$

For not to high $\boldsymbol{E}$, till the velocity gain due to the electric field is negligible with respect to the thermal velocity, the average time between collisions does not significantly change from $\tau_c = \lambda_c / v_{th}$, the mobility can therefore be estimated considering the Newton law ($m_{n,p} v_{th}/\tau_c = eE$) and equation A.6

$$\begin{aligned} \mu_n &= \frac{e\tau_c}{m_n} = \frac{e\lambda_c}{\sqrt{3kTm_n}} \\ \mu_p &= \frac{e\tau_c}{m_p} = \frac{e\lambda_c}{\sqrt{3kTm_p}} \end{aligned} \tag{A.15}$$

Notice that $\mu_{n,p}$ depends on τ_c and therefore on the temperature and the crystal imperfections and impurities. At field values for which the acceleration significantly increases the charge velocity with respect to the thermal velocity, the average time between collisions, τ_c, decreases inducing a mobility degradation with a consequent saturation of $v_{n,p}$ to around 10^7 m/s, as can be seen in Figures A.4 and A.5 which show the drift velocity of electrons and holes as function of the electric field for different temperatures in silicon. Figure A.6 presents also the mobility at 300 K as function of the electric field, from calculations of Jacoboni et al. Jacoboni et al. 1977. At low electric fields the mobility is constant, $\mu_n = 1,415\ cm^2/(Vs)$ and $\mu_p = 480\ cm^2/(Vs)$.

When the system reaches the equilibrium, the sum of the diffusion current and

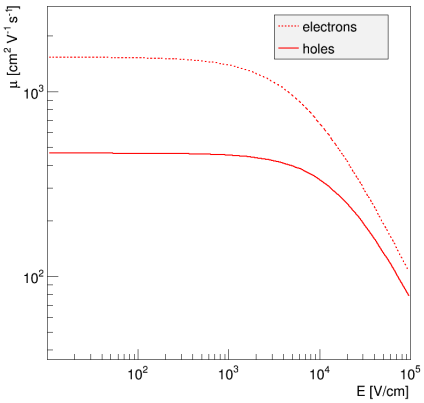

Figure A.6: Mobility values calculated in the case of silicon at 300 K (after Ref. Jacoboni et al. 1977).

of the drift current of all the charge carriers must be zero

$$\begin{aligned} e\, D_n \boldsymbol{\nabla} n + en\mu_n \boldsymbol{E} &= 0 \\ e\, D_p \boldsymbol{\nabla} p - ep\mu_p \boldsymbol{E} &= 0 \end{aligned} \tag{A.16}$$

which permits to relate the diffusion constant to the mobility. In fact, considering the case of electrons, the assumption of free distinguishable particles permits to consider the Boltzmann statistics in a potential given by the electric field

$$n = n_0 e^{\frac{eV}{kT}} \tag{A.17}$$

the gradient $\boldsymbol{\nabla} n$ is

$$\begin{aligned} \boldsymbol{\nabla} n &= n_0 \frac{e}{kT} e^{\frac{eV}{kT}} \boldsymbol{\nabla} V \\ &= n \frac{e}{kT} \boldsymbol{\nabla} V \\ &= n \frac{e}{kT} \boldsymbol{E} \end{aligned} \tag{A.18}$$

which, together with equation A.16, gives the so called *Einstein relation*

$$\begin{aligned} D_n &= \mu_n \frac{kT}{e} \\ D_p &= \mu_p \frac{kT}{e} \end{aligned} \tag{A.19}$$

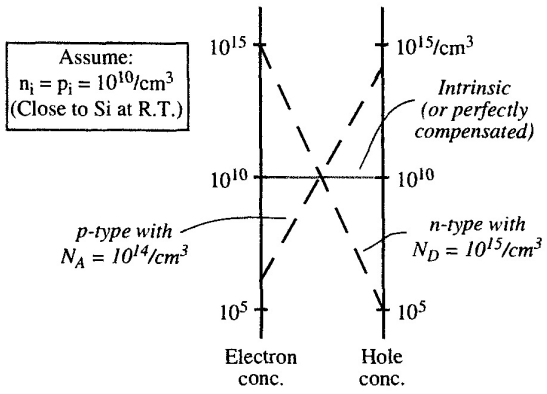

Figure A.7: Scheme of the relationship between electron and hole concentrations, as given by the mass-action law (Equation A.23). For a given concentration in one axis, the concentration in the other axes is given by the line passing by the center. The scales are logarithmic. (Knoll 2010)

Extrinsic semiconductors

In order to increase the conductivity, semiconductors are doped with small quantities of impurities. Impurity atoms take the place of the original atoms inside the crystal lattice and introduce new energy levels inside the forbidden band. Doped semiconductors are called *extrinsic*. In the case of silicon, elements of the fifth group (e.g phosphor) or of the third group (e.g. boron) of the periodic table are added, see Figure A.3. The first group of elements have an extra valence electron, which is easily released in the conduction band because its energy level is just below E_C, the density of electrons is therefore dominated by the impurity concentration N_D

$$n \simeq N_D \tag{A.20}$$

and the doped semiconductor is called of *n-type*. The second group of elements has an electron less than silicon in the outer shell, therefore it tend to trap electrons from the valence band in order to fill the covalent bond with the neighbouring atoms, these impurities are therefore called *acceptors*. Trapped electrons cumulate in an energy level just above E_V and generate holes in the valence band, therefore acceptor doped semiconductors are called of *p-type*. In this case, the density of holes is dominated by the impurity concentration, N_A

$$p \simeq N_A \tag{A.21}$$

The Fermi level of doped semiconductors is shifted towards the conduction or the valence bands for donors or acceptors, respectively. In fact, equating Equation

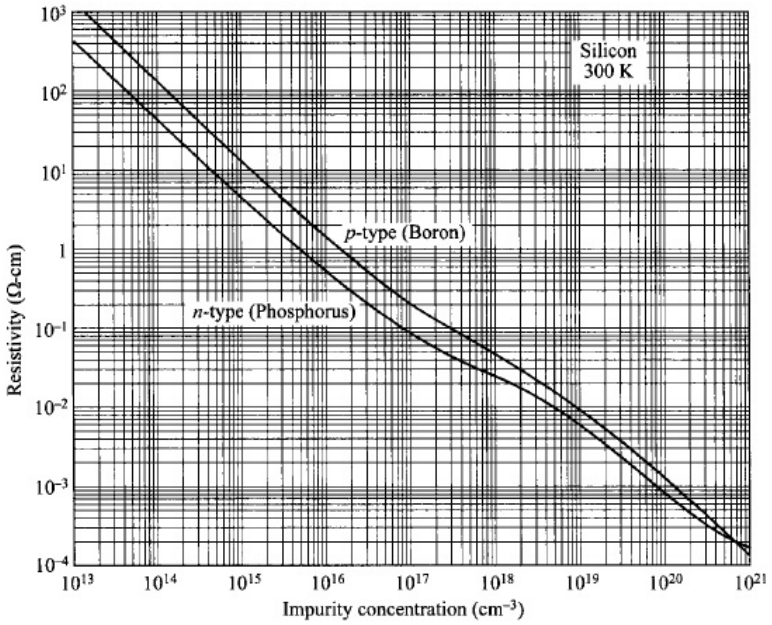

Figure A.8: Resistivity versus impurity concentration in Si at 300 K (Sze and Ng 2006).

A.2 with N_D and N_A, we can easily derive

$$E_F = E_i + kT \ln \frac{N_D}{n_i} \qquad for \quad donors \tag{A.22}$$
$$E_F = E_i - kT \ln \frac{N_A}{n_i} \qquad for \quad acceptors$$

where E_i is the Fermi level of intrinsic semiconductors. In n-type semiconductors the higher density of electrons, will induce a filling of holes till the equilibrium stated by the mass-action law is again established

$$n \cdot p = n_i \cdot p_i \tag{A.23}$$

since $n \simeq N_D \gg n_i$ the density of holes, p, will be much less than p_i and the conductivity will be mainly due to electrons, called *majority carriers*, while holes are *minority carriers*. Vice versa, in p-doped semiconductors holes are majority carriers and electrons minority carriers. Figure A.7 nicely illustrates the relationship between minority and majority carriers in intrinsic and extrinsic semiconductor. In general, the number of charges and therefore their conductivity is much higher in extrinsic semiconductors than in instrinsic ones. The resistivity,

$\rho = 1/\sigma$, is dominated by the majority carriers concentration and mobility

$$\begin{aligned} \rho_n &= \frac{1}{e(\mu_n n + \mu_p p)} \sim \frac{1}{e\mu_n N_D} \\ \rho_p &= \frac{1}{e(\mu_n n + \mu_p p)} \sim \frac{1}{e\mu_p N_A} \end{aligned} \tag{A.24}$$

as can be seen in Figure A.8. For example, in the case of a donor concentration of $10^{13}\ cm^{-3}$

$$\begin{aligned} \rho &= \frac{1}{e\mu_p N_A} \\ \rho &= \frac{1}{(1.6 \cdot 10^{-19}\ C)(1350\ cm^2/Vs)(10^{13}\ cm^{-3})} \\ \rho &= 463\ \Omega\ cm \end{aligned} \tag{A.25}$$

to be compared with a the resistivity of an intrinsic material

$$\begin{aligned} \rho &= \frac{1}{e(\mu_n n + \mu_p p)} \\ \rho &= \frac{1}{(1.6 \cdot 10^{-19}\ C)(450 + 1350\ cm^2/Vs)(1.5 \cdot 10^{10}\ cm^{-3})} \\ \rho &= 230,000\ \Omega\ cm \end{aligned} \tag{A.26}$$

B. Blocking contacts

p-n junctions

Reversed biased diodes based on a *p-n* junction are schematically shown in Figure B.1. When p-doped silicon gets in contact with n-doped silicon, free charge carriers diffuse from each side of the junction and the remaining ionized impurities create a space charge distribution that induces a build-in potential V_{bi} given, at equilibrium, by the difference of the Fermi level of the p and the n side

$$V_{bi} \approx \frac{kT}{e} \ln\left(\frac{N_D N_A}{n_i^2}\right) \tag{B.1}$$

where n_i is the intrinsic free charge concentration, N_D and N_A are the donor and the acceptor concentration[q], k is the Boltzmann constant and T the temperature. The build-in potential V_{bi} is $\sim 1\ eV$. The electric field associated to V_{bi} prevents that charges further migrate across the junction, the space charge region is depleted from free carriers and called *depletion zone*. This region is very suitable for radiation detection because, due to the high resistivity induced by the electric field, it behaves like a *blocking contact* with a very low leakage current, which permits to detect the motion of electrons-holes eventually produced by the interaction of a particle. The electric field, E(x), the potential, V(x) and the width of the depletion region can be calculated, with some simplifying assumptions[r], by

[q] Equation B.1 neglects the contribution of the minority carriers.

[r] The case of an abrupt one dimensional p-n junction is considered and the contribution of the minority carriers to the charge density ρ is neglected.

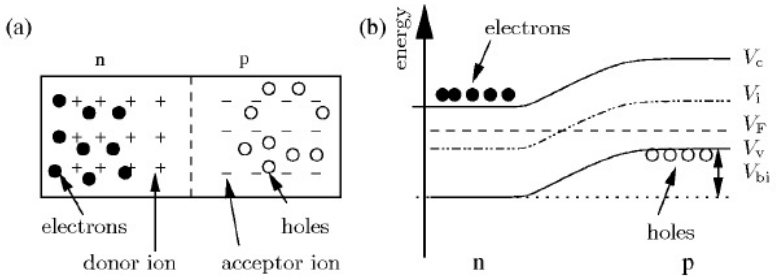

Figure B.1: Schematic illustration of a *p-n* junction (a) and of the formation of the build-in potential V_{bi} in the energy band model (b), V_C is the lower energy of the conduction band and V_V the higher energy of the valence band. (Rossi et al. 2006)

.

solving the Poisson equation

$$\frac{d^2V(x)}{dx^2} = -\frac{\rho(x)}{\epsilon} \tag{B.2}$$

where ϵ is the dielectric constant of the medium and $\rho(x)$ the density of charges. Figure B.1 illustrates the solution in the case of a charge density given by

$$\rho(x) = \begin{cases} -qN_A & -W_p < x < 0 \\ +qN_D & 0 < x < W_n \end{cases} \tag{B.3}$$

The electric field, $E(x) = -dV(x)/dx$, is obtained by integrating equation B.2 with the boundary conditions $E(-W_p) = 0$ and $E(W_n) = 0$

$$\begin{aligned} E(x) &= -\frac{qN_A}{\epsilon}(x + W_p) && -W_p < x \leq 0 \\ E(x) &= +\frac{qN_D}{\epsilon}(x - W_n) && 0 \leq x < W_n \end{aligned} \tag{B.4}$$

A second integration permits to obtain the potential with the boundary conditions $V(-W_p) = 0$ and $V(W_n) = V_{bi}$

$$\begin{aligned} V(x) &= +\frac{qN_A}{2\epsilon}(x + W_p)^2 && -W_p < x \leq 0 \\ V(x) &= -\frac{qN_D}{2\epsilon}(x - W_n)^2 + V_{bi} && 0 \leq x < W_n \end{aligned} \tag{B.5}$$

and, equating the equations B.5 at $x = 0$, we obtain

$$\frac{qN_AW_p^2}{2\epsilon} = V_{bi} - \frac{qN_DW_n^2}{2\epsilon} \tag{B.6}$$

which permits to easily estimate the width $d = W_p + W_n$ of the depletion zone in the case in which one of the junction sides has a much higher doping concentration, as it is generally the case. If $N_A \gg N_D$, then $W_p \ll W_n$ in order to guarantee charge neutrality ($N_AW_p = N_DW_n$). Then, W_p can be neglected in equation B.6 and the depletion region width d can be estimated as

$$d = W_p + W_n \approx W_n = \sqrt{\frac{2\epsilon V_{bi}}{eN_D}} \tag{B.7}$$

In order to further increase the depletion region, active in the particle detection, an external potential V ($\simeq 50 - 100\ V$) is generally applied in the same direction

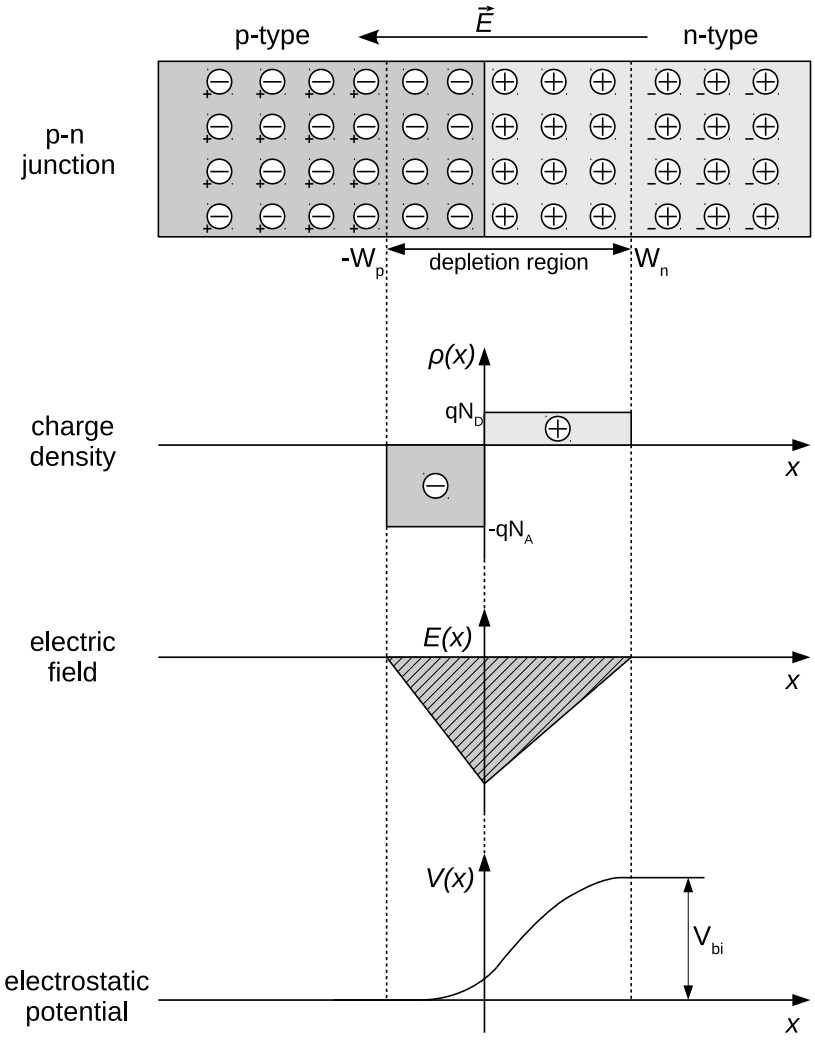

Figure B.2: Electric characteristic functions of an typical abrupt p-n junction (Dawiec 2010).

of V_{bi}

$$d \approx \sqrt{\frac{2\epsilon(V + V_{ib})}{eN_D}} \approx \sqrt{\frac{2\epsilon V}{eN_D}} \tag{B.8}$$

The junction is then said *reversely biased* and *fully depleted* in the case that d corresponds to the full width of the sensor. Notice that the concentration N of the dopant in the less doped side plays an important role in the determination of d: the lower the doping, i.e. the higher the resistivity of the material ($\rho = 1/\mu eN$), the wider the depletion region for a given bias voltage. Moreover, due

to the fixed space charge in the depletion region, the p-n junction behaves like a capacitor with capacitance per unit area

$$C = \frac{\epsilon}{d} \approx \sqrt{\frac{e\epsilon N}{2V}} \tag{B.9}$$

Therefore, fully depleted junctions permit to reduce the detector capacitance and to reach a better signal to noise ratio, with a consequent improvement in energy resolution. Figure B.3 presents a schematic view of the correlations between resistivity, capacitance, depletion width and bias voltage in a p-n junction.

Metal-semiconductor junctions

In the case of high resistivity semiconductors, like CdTe, it is possible to use metal-semiconductor junctions, which act as rectifying contacts, like the p-n junction. In fact, when a metal gets in contact with a semiconductor with a

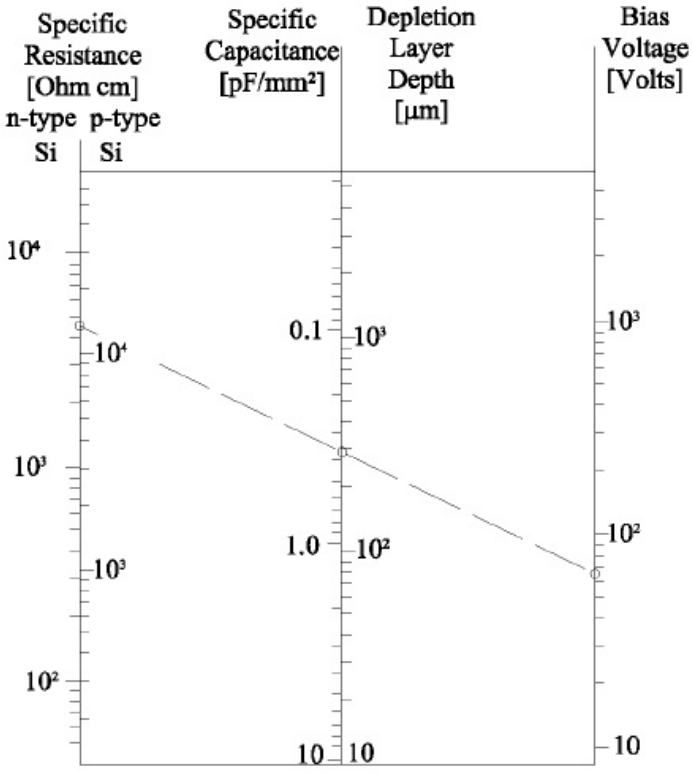

Figure B.3: Diagram of the correlations between several parameters that characterize a p-n junction (Rossi et al. 2006).

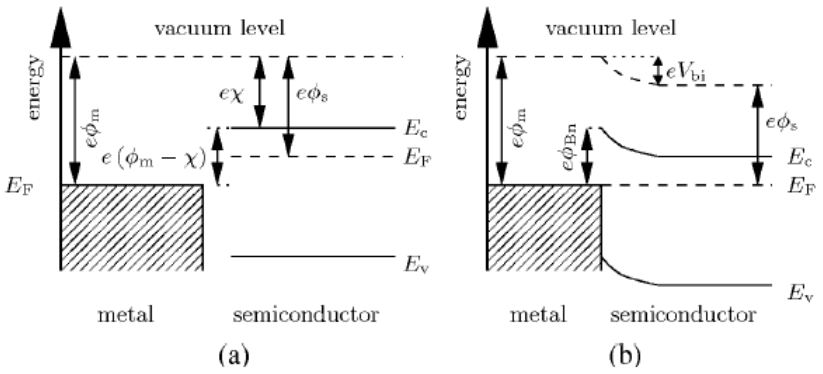

Figure B.4: Band diagram of a junction between a metal and a n-doped semiconductor: (a) both material are isolated. (b) materials are in contact (Rossi et al. 2006).

lower work function[s], $e\phi$, electrons diffuse into the metal side and create a surface barrier which permits to equalize the Fermi levels of the two materials. The induced build-in potential V_{bi} is equal to the difference of the two work functions

$$V_{bi} = \phi_m - \phi_s \tag{B.10}$$

while the potential barrier seen by the metal, called *Schottky barrier*, is equal to the difference between the work function of the metal and the affinity[t] χ of the semiconductor

$$\phi_{Bn} = \phi_m - \chi \tag{B.11}$$

Figure B.4 illustrates the metal-semiconductor junction in the case of n-type semiconductors. A depletion region is formed in the semiconductor side, which can be increased with an external potential, like in the case of the p-n junction.

[s]The work function is the energy necessary to remove an electron from the Fermi level to the vacuum.

[t]The affinity is energy necessary to move an electron from the lower level of the conduction band, E_C, to the vacuum.

Acronyms

AMS Austria Mikro Systeme. 23

ANTARES Astronomy with a Neutrino Telescope and Abyss environmental RE-Search project. 11

ASIC Application Specific Integrated Circuit. 14, 20

ATLAS A Toroidal LHC ApparatuS. 3, 11, 19, 22

CCD Charge-Coupled Devices. 22

CERIMED Centre Européen de Recherche en Imagerie MEDicale. 12

CERN European Organization for Nuclear Research. 3, 11, 14, 16, 19, 20, 22

CHORUS CERN Hybrid Oscillation Research apparatUS. 11

CMOS Complementary Metal-Oxide Semiconductor. 14

CNRS Centre National de la Recherche Scientifique. 11

CPPM Centre de Physique de Particules de Marseille. 3, 11–13, 20, 22, 27

CREATIS Centre de Recherche en Acquisition et Traitement de l'Image pour la Santé. 31

DAC Digital-to-Analog Converter. 27

DELPHI Detector with Lepton, Photon and Hadron Identification. 3, 16, 22–24

DQE Detection Quantum Efficiency. 4, 5

ESRF European Synchrotron Radiation Facility. 22, 24

FDK Feldkamp-Davis-Kress. 31

FWHM Full Width at Half Maximum. 34

HERA Hadron Elektron Ring Anlage. 11

HU Hounsfield Unit. 4

HZB Helmholtz Zentrum Berlin. 12

IBDM Institut de Biologie du Développement de Marseille. 29

imXgam imagerie X et gamma. 11

IN2P3 Institut National de Physique Nucléaire et de Physique des Particules. 11

LEP Large Electron Positron Collider. 16

LHC Large Hadron Collider. 11, 16

LSF Line Spread Function. 31

micro-CT micro-Computed Tomography. 12, 13, 20, 22, 29

MIP Maximum Intensity Projection. 4, 6

MSc Master of Science. 29

MTF Modulation Transfer Function. 4, 31, 33, 34

NIST National Institute of Standards and Technology. 3, 25

PET Positron Emission Tomography. 33

PhD Doctor of Philosophy. 29

PSF Point Spread Function. 5

R&D Research and Development. 11, 14, 16

SOLEIL Source Optimisée de Lumière d'Energie Intermédiaire du LURE. 22, 27

XPAD X-ray pixel chip with Adaptable Dynamics. 12, 13, 20, 22

List of Figures

List of Tables

Bibliography

[1] R E Alvarez and A Macovski. “Energy-selective reconstructions in X-ray computerised tomography”. In: *Physics in Medicine & Biology* 21.5 (1976), p. 733. URL: http://stacks.iop.org/0031-9155/21/i=5/a=002 (cit. on p. 51).

[2] R Ballabriga et al. “The Medipix3RX: a high resolution, zero dead-time pixel detector readout chip allowing spectroscopic imaging”. In: *Journal of Instrumentation* 8.02 (2013), p. C02016. URL: http://stacks.iop.org/1748-0221/8/i=02/a=C02016 (cit. on p. 54).

[3] R. Ballabriga et al. “Review of hybrid pixel detector readout ASICs for spectroscopic X-ray imaging”. In: *Journal of Instrumentation* 11.01 (2016), P01007. URL: http://stacks.iop.org/1748-0221/11/i=01/a=P01007 (cit. on pp. 13, 53).

[4] S. Basolo et al. “XPAD: pixel detector for material sciences”. In: *IEEE Transactions on Nuclear Science* 52.5 (2005), pp. 1994–1998. ISSN: 0018-9499. DOI: 10.1109/TNS.2005.856818 (cit. on p. 16).

[5] S. Basolo et al. “A 20 kpixels CdTe photon-counting imager using {XPAD} chip”. In: *Nuclear Instruments and Methods in Physics Research Section A: Accelerators, Spectrometers, Detectors and Associated Equipment* 589.2 (2008), pp. 268 –274. ISSN: 0168-9002. DOI: http://dx.doi.org/10.1016/j.nima.2008.02.042. URL: http://www.sciencedirect.com/science/article/pii/S0168900208002234 (cit. on p. 18).

[6] K.H. Becks et al. “Proceedings of the 5th International Workshop on Vertex Detectors The DELPHI pixels”. In: *Nuclear Instruments and Methods in Physics Research Section A: Accelerators, Spectrometers, Detectors and Associated Equipment* 386.1 (1997), pp. 11 –17. ISSN: 0168-9002. URL: http://www.sciencedirect.com/science/article/pii/S0168900296010893 (cit. on p. 9).

[7] R.O. Bell et al. “Time-dependent polarization of CdTe gamma-ray detectors”. In: *Nuclear Instruments and Methods* 117.1 (1974), pp. 267 –271. ISSN: 0029-554X. DOI: https://doi.org/10.1016/0029-554X(74)90408-X. URL: http://www.sciencedirect.com/science/article/pii/0029554X7490408X (cit. on p. 17).

[8] R Bellazzini et al. “Chromatic X-ray imaging with a fine pitch CdTe sensor coupled to a large area photon counting pixel ASIC”. In: *Journal of Instrumentation* 8.02 (2013), p. C02028. URL: http://stacks.iop.org/1748-0221/8/i=02/a=C02028 (cit. on p. 52).

[9] R. Bellazzini et al. “PIXIE III: a very large area photon-counting CMOS pixel ASIC for sharp X-ray spectral imaging”. In: *Journal of Instrumentation* 10.01 (2015), p. C01032. URL: http://stacks.iop.org/1748-0221/10/i=01/a=C01032 (cit. on p. 54).

[10] D. Benoit. *Modélisation de la fonction de réponse d'un détecteur à pixel hybrides dans GATE*. 2007 (cit. on pp. 5, 21).

[11] J.-F. Berar et al. “A pixel detector with large dynamic range for high photon counting rates”. In: *Journal of Applied Crystallography* 35 (2002), pp. 471–476. URL: http://hal.in2p3.fr/in2p3-00011848 (cit. on pp. 14, 16).

[12] W. Beusch et al. *R&D proposal: development of hybrid and monolithic silicon micropattern detectors*. Tech. rep. CERN-DRDC-90-81. DRDC-P-22. Geneva: CERN, 1990. URL: http://cds.cern.ch/record/292598 (cit. on pp. 7, 8).

[13] L. Blanquart et al. “Pixel readout electronics for LHC and biomedical applications”. In: *European Symposium on Semiconductor Detectors - 8*. Vol. 439. Schloss Elmau, Germany: Elsevier, June 1998, pp. 403–412. URL: http://hal.in2p3.fr/in2p3-00012130 (cit. on p. 11).

[14] L. Blanquart et al. “XPAD, a new read-out pixel chip for X-ray counting”. In: *Nuclear Science Symposium, 2000. IEEE*. 2000, 92–97–191 vol. 3 (cit. on p. 15).

[15] D. Bluemke. “Experience with photon counting CT at the National Institute Health”. In: *4th Workshop on Medical Applications of Spectroscopic X-ray Detectors, CERN 2017*. 2017 (cit. on p. 54).

[16] N. Boudet et al. “XPAD: a hybrid pixel detector for X-ray diffraction and diffusion”. In: *Nuclear Instruments and Methods in Physics Research Section A: Accelerators, Spectrometers, Detectors and Associated Equipment* 510.1–2 (2003). Proceedings of the 2nd International Symposium on Applications of Particle Detectors in Medicine, Biology and Astrophysics, pp. 41 –44. ISSN: 0168-9002. DOI: http://dx.doi.org/10.1016/S0168-9002(03)01676-0. URL: http://www.sciencedirect.com/science/article/pii/S0168900203016760 (cit. on p. 16).

[17] Ch. Brönnimann et al. “A pixel read-out chip for the PILATUS project”. In: *Nuclear Instruments and Methods in Physics Research Section A: Accelerators, Spectrometers, Detectors and Associated Equipment* 465.1 (2001). SPD2000, pp. 235 –239. ISSN: 0168-9002. DOI: https://doi.org/10.1016/S0168-9002(01)00396-5. URL: http://www.sciencedirect.com/science/article/pii/S0168900201003965 (cit. on p. 51).

[18] C. Buton et al. “Comparison of three types of XPAD3.2/CdTe single chip hybrids for hard X-ray applications in material science and biomedical imaging”. In: *Nuclear Instruments and Methods in Physics Research Section A: Accelerators, Spectrometers, Detectors and Associated Equipment* 758 (2014), pp. 44 –56. ISSN: 0168-9002. DOI: http://dx.doi.org/10.1016/j.nima.2014.04.067. URL: http://www.sciencedirect.com/science/article/pii/S016890021400480X (cit. on pp. 19, 45).

[19] R. N. Cahn et al. “Detective quantum efficiency dependence on x-ray energy weighting in mammography”. In: *Medical Physics* 26 (Dec. 1999), pp. 2680–2683. DOI: 10.1118/1.598807 (cit. on p. 51).

[20] M. Campbell et al. “A 10 MHz micropower CMOS front end for direct readout of pixel detectors”. In: *Nuclear Instruments and Methods in Physics Research Section A: Accelerators, Spectrometers, Detectors and Associated Equipment* 290.1 (1990), pp. 149 –157. ISSN: 0168-9002. URL: http://www.sciencedirect.com/science/article/pii/016890029090355A (cit. on p. 9).

[21] M. Campbell et al. “Readout for a 64×64 pixel matrix with 15-bit single photon counting”. In: *Nuclear Science Symposium, 1997. IEEE*. 1997, 189–191 vol.1 (cit. on pp. 11, 12).

[22] M Campbell et al. “A Readout Chip for a 64 x 64 Pixel Matrix with 15-bit Single Photon Counting”. In: CERN-ECP-97-010. CERN-ECP-97-10 (1998), 3 p. URL: https://cds.cern.ch/record/350115 (cit. on p. 51).

[23] Michael Campbell. “10 years of the Medipix2 Collaboration”. In: *Nuclear Instruments and Methods in Physics Research Section A: Accelerators, Spectrometers, Detectors and Associated Equipment* 633 (2011). 11th International Workshop on Radiation Imaging Detectors (IWORID), S1 –S10. ISSN: 0168-9002. DOI: https://doi.org/10.1016/j.nima.2010.06.106. URL: http://www.sciencedirect.com/science/article/pii/S0168900210012969 (cit. on p. 52).

[24] F. Cassol and C. Morel. *Imaging neutron beams with hybrid pixels detectors*. Tech. rep. Demade de mise à disposition. 2009 (cit. on p. 48).

[25] F. Cassol et al. “Imaging performance of the hybrid pixel detectors XPAD3-S”. In: *Physics in Medicine and Biology* 54 (2009), pp. 1773–1789. DOI: 10.1088/0031-9155/54/6/024. URL: http://hal.in2p3.fr/in2p3-00388318 (cit. on pp. 29–31, 33).

[26] F Cassol et al. “Simulation of PIXSCAN, a photon counting micro-CT for small animal imaging”. In: *Journal of Instrumentation* 4.05 (2009), P05012. URL: http://stacks.iop.org/1748-0221/4/i=05/a=P05012 (cit. on pp. 25, 26).

[27] F. Cassol et al. “Neutron imaging with the XPAD3-S hybrid pixel detector”. In: *Nuclear Instruments and Methods in Physics Research Section A: Accelerators, Spectrometers, Detectors and Associated Equipment* 634.1 (2011), pp. 85 –90. ISSN: 0168-9002. DOI: http://dx.doi.org/10.1016/j.nima.2011.01.077. URL: http://www.sciencedirect.com/science/article/pii/S0168900211001550 (cit. on pp. 48–50).

[28] F. Cassol et al. “Study of the charge sharing effect in the photon-counting pixel detector XPAD3-S”. In: *Nuclear Instruments and Methods in Physics Research Section A: Accelerators, Spectrometers, Detectors and Associated Equipment* 633, Supplement 1 (2011). 11th International Workshop on Radiation Imaging Detectors (IWORID), S111 –S113. ISSN: 0168-9002. DOI: http://dx.doi.org/10.1016/j.nima.2010.06.139. URL: http://www.sciencedirect.com/science/article/pii/S016890021001329X (cit. on pp. 31–33).

[29] F. Cassol et al. “First K-Edge Imaging With a Micro-CT Based on the XPAD3 Hybrid Pixel Detector”. In: *IEEE Transactions on Nuclear Science* 60.1 (2013), pp. 103–108. ISSN: 0018-9499. DOI: 10.1109/TNS.2012.2217753 (cit. on pp. 37–39).

[30] F. Cassol et al. “A large surface X-ray camera based on XPAD3/CdTe single chip hybrids”. In: *Journal of Instrumentation* 10.11 (2015), p. C11010. URL: http://stacks.iop.org/1748-0221/10/i=11/a=C11010 (cit. on pp. 19, 44, 45).

[31] F Cassol et al. “K-edge imaging with the XPAD3 hybrid pixel detector, direct comparison of CdTe and Si sensors”. In: *Physics in Medicine and Biology* 60.14 (2015), p. 5497. URL: http://stacks.iop.org/0031-9155/60/i=14/a=5497 (cit. on pp. 41, 42).

[32] F Cassol et al. “Characterization of the imaging performance of a micro-CT system based on the photon counting XPAD3/Si hybrid pixel detectors”. In: *Biomedical Physics & Engineering Express* 2.2 (2016), p. 025003. URL: http://stacks.iop.org/2057-1976/2/i=2/a=025003 (cit. on pp. 34–36, 39).

[33] CERN, ed. *The CERN OMEGA spectrometer 25 years of physic*. 97-02. Geneva: CERN, 1997, p. 54. URL: https://cds.cern.ch/record/330556 (cit. on p. 8).

[34] HM Cho et al. “Characteristic performance evaluation of a photon counting Si strip detector for low dose spectral breast CT imaging”. In: *Medical Physics* 41 (Sept. 2014) (cit. on p. 54).

[35] D.P. Clark and C.T. Badea. “Micro-CT of rodents: State-of-the-art and future perspectives”. In: *Physica Medica* 30.6 (2014), pp. 619 –634. ISSN: 1120-1797. DOI: https://doi.org/10.1016/j.ejmp.2014.05.011. URL: http://www.sciencedirect.com/science/article/pii/S1120179714001008 (cit. on p. 52).

[36] The Cherenkov Telescope Array Consortium et al. “Science with the Cherenkov Telescope Array”. Version 1. In: (Sept. 23, 2017). arXiv: http://arxiv.org/abs/1709.07997v2 [astro-ph.IM, astro-ph.HE, hep-ex]. URL: http://arxiv.org/abs/1709.07997v2 (cit. on p. 55).

[37] A. Dawiec. “Development of an ultra-fast X-ray camera using hybrid pixels”. PhD thesis. Université de la Méditerranée Aix-Marseille II, 2010 (cit. on pp. 168, 170, 179).

[38] F. Debarbieux et al. “Repeated Imaging of Lung Cancer Development Using PIXSCAN, a Low Dose Micro-CT Scanner Based on XPAD Hybrid Pixel Detectors”. In: *IEEE Transactions on Nuclear Science* 57.1 (2010), pp. 242–245. ISSN: 0018-9499. DOI: 10.1109/TNS.2009.2037319 (cit. on p. 27).

[39] P. Delpierre et al. “X-ray pixel detector for crystallography”. In: *IEEE Transactions on Nuclear Science* 48.4 (2001), pp. 987–991. ISSN: 0018-9499 (cit. on p. 15).

[40] P. Delpierre et al. “Large Surface X-Ray Pixel Detector”. In: *IEEE Transactions on Nuclear Science* 49.4 (2002), pp. 1709–1711. ISSN: 0018-9499 (cit. on p. 15).

[41] P. Delpierre et al. “PIXSCAN: Pixel detector CT-scanner for small animal imaging”. In: *Nuclear Instruments and Methods in Physics Research Section A: Accelerators, Spectrometers, Detectors and Associated Equipment* 571.1–2 (2007). Proceedings of the 1st International Conference on Molecular Imaging TechnologyEuroMedIm 2006, pp. 425 –428. ISSN: 0168-9002. DOI: http://dx.doi.org/10.1016/j.nima.2006.10.126. URL: http://www.sciencedirect.com/science/article/pii/S0168900206019243 (cit. on p. 21).

[42] P. Delpierre et al. “XPAD: A photons counting pixel detector for material sciences and small-animal imaging”. In: *Nuclear Instruments and Methods in Physics Research Section A: Accelerators, Spectrometers, Detectors and Associated Equipment* 572.1 (2007). Frontier Detectors for Frontier PhysicsProceedings of the 10th Pisa Meeting on Advanced Detectors, pp. 250 – 253. ISSN: 0168-9002. DOI: http://dx.doi.org/10.1016/j.nima.2006.10.315. URL: http://www.sciencedirect.com/science/article/pii/S0168900206020821 (cit. on p. 16).

[43] M. Dupont. “Tomographie spectrale à comptage de photons: développement du prototype PIXSCAN et preuve de concept”. PhD thesis. Aix-Marseille Université, 2014 (cit. on pp. 5, 29).

[44] S. Faby et al. “Performance of today’s dual energy CT and future multi energy CT in virtual non-contrast imaging and in iodine quantification: A simulation study”. In: *Medical Physics* 42 (July 2015), pp. 4349–4366. DOI: 10.1118/1.4922654 (cit. on p. 53).

[45] Y. Fan et al. “Tissue-Specific Gain of RTK Signalling Uncovers Selective Cell Vulnerability during Embryogenesis.” In: *PLOS Genetics* 11.(9) (2015). ISSN: 0018-9499. DOI: 10.1371/journal.pgen.1005533 (cit. on p. 43).

[46] J.-L. Ferrer et al. “D2AM, a Beamline with a High-Intensity Point-Focusing Fixed-Exit Monochromator for Multiwavelength Anomalous Diffraction Experiments”. In: *Journal of Synchrotron Radiation* 5.6 (1998), pp. 1346–1356. ISSN: 1600-5775. DOI: 10.1107/S0909049598004257. URL: http://dx.doi.org/10.1107/S0909049598004257 (cit. on p. 14).

[47] P. Fischer et al. “A counting pixel readout chip for imaging applications”. In: *Nuclear Instruments and Methods in Physics Research Section A: Accelerators, Spectrometers, Detectors and Associated Equipment* 405.1 (1998), pp. 53 –59. ISSN: 0168-9002. URL: http://www.sciencedirect.com/science/article/pii/S0168900297011467 (cit. on p. 12).

[48] M. Hamonet. “Tomographie hybride simultanée TEP/TDM combinant détecteurs à pixels hybrides et modules phoswich à scintillateurs”. PhD thesis. Aix-Marseille Université, 2016 (cit. on pp. 5, 29).

[49] E.H.M. Heijne et al. “The silicon micropattern detector: A dream?” In: *Nuclear Instruments and Methods in Physics Research Section A: Accelerators, Spectrometers, Detectors and Associated Equipment* 273.2 (1988), pp. 615 –619. ISSN: 0168-9002. URL: http://www.sciencedirect.com/science/article/pii/0168900288900654 (cit. on p. 6).

[50] C. Hemmer. *Evaluation de la dose délivrée par un micro-tomodensitomètre*. 2008 (cit. on pp. 5, 21, 24).

[51] C. Jacoboni et al. “A review of some charge transport properties of silicon”. In: *Solid-State Electronics* 20.2 (1977), pp. 77 –89. ISSN: 0038-1101. URL: http://www.sciencedirect.com/science/article/pii/0038110177900545 (cit. on pp. 171–173).

[52] S Jan et al. “GATE V6: a major enhancement of the GATE simulation platform enabling modelling of CT and radiotherapy”. In: *Physics in Medicine and Biology* 56.4 (2011), p. 881. URL: http://stacks.iop.org/0031-9155/56/i=4/a=001 (cit. on p. 25).

[53] R. Khoury. “PIXSCAN : Micro-Tomodensitomètre à pixel hybrides pour le petit animal”. PhD thesis. Université de la Méditerranée, 2008 (cit. on pp. 5, 21, 22, 27).

[54] R Khoury et al. “A geometrical calibration method for the PIXSCAN micro-CT scanner”. In: *Journal of Instrumentation* 4.07 (2009), P07016. URL: http://stacks.iop.org/1748-0221/4/i=07/a=P07016 (cit. on p. 22).

[55] G. F. Knoll. *Radiation detection and measurement; 4th ed.* New York, NY: Wiley, 2010. URL: https://cds.cern.ch/record/1300754 (cit. on pp. 8, 174).

[56] K. Kronland-Martinet. “Développement de la tomographie intra-vitale au K-edge avec la caméra à pixels hybrides XPAD3”. PhD thesis. Aix-Marseille Université, 2015 (cit. on pp. 5, 29, 36, 37, 40).

[57] Xiang Li et al. “Contrast agents for preclinical targeted X-ray imaging”. In: *Advanced Drug Delivery Reviews* 76 (2014). Targeted imaging, pp. 116 –133. ISSN: 0169-409X. DOI: https://doi.org/10.1016/j.addr.2014.07.013. URL: http://www.sciencedirect.com/science/article/pii/S0169409X14001549 (cit. on p. 52).

[58] G. Lutz. *Semiconductor radiation detectors*. Spring-Verlag Berlin Heidelberg, 2007 (cit. on p. 8).

[59] Daniela Muenzel et al. “Spectral Photon-counting CT: Initial Experience with Dual–Contrast Agent K-Edge Colonography”. In: *Radiology* 283.3 (2017). PMID: 27918709, pp. 723–728. DOI: 10.1148/radiol.2016160890. eprint: https://doi.org/10.1148/radiol.2016160890. URL: https://doi.org/10.1148/radiol.2016160890 (cit. on pp. 52, 54).

[60] H. Ouamara. “Comparaison de la micro-tomodensitométrie par comptage de photons et par intégration de charges avec le dispositif d’irradiation PIXSCAN”. PhD thesis. Aix-Marseille Université, 2013 (cit. on pp. 5, 29).

[61] P. Pangaud et al. “First results of XPAD3, a new photon counting chip for X-ray CT-scanner with energy discrimination”. In: *2007 IEEE Nuclear Science Symposium Conference Record*. Vol. 1. 2007, pp. 14–18. DOI: 10.1109/NSSMIC.2007.4436281 (cit. on p. 18).

[62] P. Pangaud et al. “XPAD3-S: A fast hybrid pixel readout chip for X-ray synchrotron facilities”. In: *Nuclear Instruments and Methods in Physics Research Section A: Accelerators, Spectrometers, Detectors and Associated Equipment* 591.1 (2008). Radiation Imaging Detectors 2007Proceedings of the 9th International Workshop on Radiation Imaging Detectors, pp. 159 – 162. ISSN: 0168-9002. DOI: http://dx.doi.org/10.1016/j.nima.2008.03.047. URL: http://www.sciencedirect.com/science/article/pii/S0168900208004257 (cit. on p. 19).

[63] P. Pangaud et al. *Semiconductor radiation detection system*. K. Iniewski, CRS Press, 2010 (cit. on pp. 14, 19).

[64] Patrick Pangaud et al. “XPAD3: A new photon counting chip for X-ray CT-scanner”. In: *Nuclear Instruments and Methods in Physics Research Section A: Accelerators, Spectrometers, Detectors and Associated Equipment* 571.1–2 (2007). Proceedings of the 1st International Conference on Molecular Imaging TechnologyEuroMedIm 2006, pp. 321 –324. ISSN: 0168-9002. DOI: http://dx.doi.org/10.1016/j.nima.2006.10.092. URL: http://www.sciencedirect.com/science/article/pii/S0168900206018894 (cit. on p. 18).

[65] T Poikela et al. “Timepix3: a 65K channel hybrid pixel readout chip with simultaneous ToA/ToT and sparse readout”. In: *Journal of Instrumentation* 9.05 (2014), p. C05013. URL: http://stacks.iop.org/1748-0221/9/i=05/a=C05013 (cit. on p. 54).

[66] L. Portal. “Développement de la tomodensitométrie spectrale à rayons X avec un détecteur à pixels hybrides en tellurure de cadmium”. Underway. PhD thesis. Aix-Marseille Université, 2014- (cit. on p. 29).

[67] L. Portal. *Premières études en imagerie spectrale avec le détecteur à pixels hybrides XPAD3 en Tellurure de Cadmium,* 2014 (cit. on pp. 5, 29, 42).

[68] L. Portal et al. “First in-vivo monitoring of hepatocellular carcinoma in mice with a photon counting detector for micro-CT imaging”. In: *European Molecular Imaging Meeting - EMIM 2017, Cologne, 5- 7 April*. 2017 (cit. on p. 43).

[69] L. Portal et al. “First in-vivo monitoring of hepatocellular carcinoma in mice with a photon counting detector for micro-CT imaging”. In: *XII ième Journée Scientifique Biologistes Chimistes Physiciens - BCP13, Marseille, 7 December*. 2017 (cit. on pp. 44–47).

[70] A. Pourmorteza et al. “Photon-Counting CT of the Brain: In Vivo Human Results and Image-Quality Assessment”. In: *American Journal of Neuroradiology* 38.12 (2017), pp. 2257–2263. ISSN: 0195-6108. DOI: 10.3174/ajnr.A5402. eprint: http://www.ajnr.org/content/38/12/2257.full.pdf. URL: http://www.ajnr.org/content/38/12/2257 (cit. on pp. 53, 54).

[71] S. J. Riederer and C. A. Mistretta. “Selective iodine imaging using K-edge energies in computerized x-ray tomography”. In: *Medical Physics* 4 (Nov. 1977), pp. 474–481. DOI: 10.1118/1.594357 (cit. on pp. 37, 51).

[72] E Roessl and R Proksa. “K-edge imaging in x-ray computed tomography using multi-bin photon counting detectors”. In: *Physics in Medicine & Biology* 52.15 (2007), p. 4679. URL: http://stacks.iop.org/0031-9155/52/i=15/a=020 (cit. on pp. 37, 51).

[73] L. Rossi et al. *Pixel detectors, from fundamentals to applications*. Spring-Verlag Berlin Heidelberg, 2006 (cit. on pp. 8, 10, 169, 177, 180, 181).

[74] Roger Steadman et al. “ChromAIX2: A large area, high count-rate energy-resolving photon counting ASIC for a Spectral CT Prototype”. In: *Nuclear Instruments and Methods in Physics Research Section A: Accelerators, Spectrometers, Detectors and Associated Equipment* 862 (2017), pp. 18 –24. ISSN: 0168-9002. DOI: https://doi.org/10.1016/j.nima.2017.05.010. URL: http://www.sciencedirect.com/science/article/pii/S0168900217305399 (cit. on p. 54).

[75] S.M. Sze and K.K. Ng. *Physics of semiconductor devices*. Wiley, 2006 (cit. on pp. 169, 175).

[76] K. Taguchi and J. S. Iwanczyk. “Vision 20/20: Single photon counting x-ray detectors in medical imaging”. In: *Medical Physics* 40.10 (2013), p. 100901. DOI: 10.1118/1.4820371 (cit. on p. 53).

[77] S. Valton. “3D cone beam tomographie reconstruction from circular trajectory for small animal bimodal scanner prototypes”. PhD thesis. INSA, 2007 (cit. on p. 23).

[78] C. Da Via et al. “Proceedings of the Fourth International Workshop on GaAs Detectors and Related Compounds Gallium arsenide pixel detectors for medical imaging”. In: *Nuclear Instruments and Methods in Physics Research Section A: Accelerators, Spectrometers, Detectors and Associated Equipment* 395.1 (1997), pp. 148 –151. ISSN: 0168-9002. URL: http://www.sciencedirect.com/science/article/pii/S0168900297006311 (cit. on p. 12).

[79] N. Wermes. “Pixel detectors for particle physics and imaging applications”. In: *Nuclear Instruments and Methods in Physics Research Section A: Accelerators, Spectrometers, Detectors and Associated Equipment* 512.1–2 (2003). Proceedings of the 9th European Symposium on Semiconductor Detectors: New Developments on Radiation Detectors, pp. 277 –288. ISSN: 0168-9002. URL: http://www.sciencedirect.com/science/article/pii/S0168900203019053 (cit. on pp. 10, 11).

[80] Cheng Xu et al. “Evaluation of Energy Loss and Charge Sharing in Cadmium Telluride Detectors for Photon-Counting Computed Tomography”. In: *IEEE Transactions on Nuclear Science* 58.3 (2011), pp. 614–625. ISSN: 0018-9499. DOI: 10.1109/TNS.2011.2122267 (cit. on p. 54).

[81] Zhicong Yu et al. “Evaluation of conventional imaging performance in a research whole-body CT system with a photon-counting detector array”. In: *Physics in Medicine & Biology* 61.4 (2016), p. 1572. URL: http://stacks.iop.org/0031-9155/61/i=4/a=1572 (cit. on p. 54).